# Advanced Characterization of Defects in Silicon Wafers and Solar Cells

## Yan Zhu

A thesis in fulfilment of the requirements for the degree of

Doctor of Philosophy



School of Photovoltaics and Renewable Energy Engineering

Faculty of Engineering

August 2019

# Thesis/Dissertation Sheet

| | | |
|---|---|---|
| Surname/Family Name | : | **Zhu** |
| Given Name/s | : | **Yan** |
| Abbreviation for degree as give in the University calendar | : | **PhD** |
| Faculty | : | **Faculty of Engineering** |
| School | : | **School of Photovoltaic and Renewable Energy Engineering** |
| Thesis Title | : | **Advanced Characterization of Defects in Silicon Wafers and Solar Cells** |

## Abstract

Understanding the recombination properties of bulk defects in silicon wafers is essential for further improvement of performance and stability of silicon solar cells. This thesis focuses on the characterization of the electrical properties of bulk defects in silicon. Injection dependent lifetime spectroscopy, a technique characterizes defects from the measured charge carrier lifetime, is the main technique investigated and ameliorated in this thesis. However, other techniques are also applied together with injection dependent lifetime spectroscopy for a more reliable defect characterization.

The thesis first presents an injection dependent lifetime measurement system. This system allows measurement of charge carrier lifetime with a wide injection range and temperature range. The charge carrier lifetime can be measured using both photoconductance and photoluminescence detectors.

The methodology of injection dependent lifetime spectroscopy analysis is then investigated. A new approach of defect parameterization is proposed. In this new approach, the equation correlating injection dependent lifetime and defect parameters is inversely solved using the Newton-Raphson method. Apart from this new approach, this thesis expands injection dependent lifetime spectroscopy from single-level defects to two-level defects.

The developed methods are then applied to investigate the newly discovered recombination active defects in float-zone silicon. Injection dependent lifetime spectroscopy together with deep-level transient spectroscopy are applied to extract the recombination parameters of these defects. A combination of these two techniques is demonstrated to be very beneficial for accurate defect parameterization.

Apart from recombination active defects, trap-like defects are also investigated in this thesis. Although traps might be less harmful for the performance of solar cells, they can cause artefacts to photoconductance based injection dependent lifetime measurements and impede accurate lifetime spectroscopy analysis. The properties of both minority carrier traps and majority carrier traps in *n*-type Czochralski are investigated using photoconductance measurements.

At the end of this thesis, a new approach of photoluminescence imaging using non-uniform illumination is developed in order to achieve accurate quantitative charge carrier lifetime image for non-uniform samples. This approach can potentially be combined with injection dependent lifetime spectroscopy for a spatially resolved characterization of non-uniformly distributed defects in silicon wafers or solar cells.

# ORIGINALITY STATEMENT

'I hereby declare that this submission is my own work and to the best of my knowledge it contains no materials previously published or written by another person, or substantial proportions of material which have been accepted for the award of any other degree or diploma at UNSW or any other educational institution, except where due acknowledgement is made in the thesis. Any contribution made to the research by others, with whom I have worked at UNSW or elsewhere, is explicitly acknowledged in the thesis. I also declare that the intellectual content of this thesis is the product of my own work, except to the extent that assistance from others in the project's design and conception or in style, presentation and linguistic expression is acknowledged.'

Signed…………………….…………………….............

Date.……………………………….……………..........

# INCLUSION OF PUBLICATIONS STATEMENT

UNSW is supportive of candidates publishing their research results during their candidature as detailed in the UNSW Thesis Examination Procedure.

**Publications can be used in their thesis in lieu of a Chapter if:**
- The student contributed greater than 50% of the content in the publication and is the "primary author", ie. the student was responsible primarily for the planning, execution and preparation of the work for publication
- The student has approval to include the publication in their thesis in lieu of a Chapter from their supervisor and Postgraduate Coordinator.
- The publication is not subject to any obligations or contractual agreements with a third party that would constrain its inclusion in the thesis

Please indicate whether this thesis contains published material or not.

☐ *This thesis contains no publications, either published or submitted for publication*

☒ *Some of the work described in this thesis has been published and it has been documented in the relevant Chapters with acknowledgement*

☐ *This thesis has publications (either published or submitted for publication) incorporated into it in lieu of a chapter and the details are presented below*

**CANDIDATE'S DECLARATION**

I declare that:

- I have complied with the Thesis Examination Procedure

- where I have used a publication in lieu of a Chapter, the listed publication(s) below meet(s) the requirements to be included in the thesis.

| Name | Signature | Date (dd/mm/yy) |
|------|-----------|-----------------|
|      |           |                 |

# COPYRIGHT STATEMENT

# AUTHENTICITY STATEMENT

# Acknowledgement

I gratefully thank my supervisor, Ziv Hameiri for his guidance. He is always able to give me useful and constructive suggestions while keeping enough freedom for me to explore different research topics that interest me. Looking back, I'm delightful for my decision of choosing him as my supervisor.

Thanks to my joint supervisor Gianluca Coletti and co-supervisors Thorsten Trupke. Both of them are extremely knowledgeable and always patient and willing to share their knowledge and wisdom with me.

I would like to thank Alison Lennon, Ivan Perez-Wurfl from University of New South Wales for being the panel of my PhD annual reviews. Their suggestions and feedbacks are valuable for the progress of my PhD. I also want to thank my colleagues, Jack Cowell and Robert Dumbrell for the help of proof-reading this thesis, Kyung Kim, Carlos Castrillon, Fiacre Rougieux, Daniel Chung, Anastasia Soeriyadi, Chang-Yeh Lee, Anh Le, Iskra Zafirovska, Craig Johnson, Moonyong Kim, the Solar Industrial Research Facility team for their help with sourcing and preparing samples used in this thesis, Oliver Kunz, David Payne, Catherin Chan, Alison Ciesla, Michael Pollard, Appu Paduthol, Robert Lee-Chin, Henner Kampwerth, Johannes Seif, Yoann Buratti, Arman Soufiani, the whole Photoluminescence team, the whole Defect team, for their fruitful discussions, proof-reading my manuscripts, and wiping out any obstacles in my PhD. A special thanks to Mattias Juhl, who works closely with me throughout my PhD. Without his intelligence, counseling and preaching of Python, my PhD won't be as smooth as it was.

Thanks to our external collaborators, Mallory Jensen from MIT, Friedemann Heinz, Tim Niewelt and Martin Schubert from Fraunhofer ISE, Nicholas Grant and John Murphy from University of Warwick, Jack Mullins, Joyce Ann De Guzman, Vladimir Markevich and Anthony Peaker from University of Manchester, Baochen Liao from Solar Energy Research Institute of Singapore, Simone Bernardini and Mariana Bertoni from Arizona State University for their contributions to the works in this thesis. I would also like to thank Chang Sun and Daniel Macdonald from Australian National University, Ronald

# Contents

# Abbreviations and Symbols

## Abbreviations

| | |
|---|---|
| 4PP | Four-point probe |
| AC | Alternating current |
| $Au_s$ | Substitutional gold |
| a-Si | Amorphous silicon |
| BO | Boron-oxygen complex |
| BSF | Back surface field |
| CCD | Charge-coupled device |
| CMOS | Complementary metal–oxide–semiconductor |
| Co | Cobalt |
| Cr | Chromium |
| $Cr_i$ | Interstitial chromium |
| Cz | Czochralski |
| c-Si | Crystalline silicon |
| DAQ | Data acquisition card |
| DCE | Dichloroethane |
| DLTS | Deep level transient spectroscopy |
| DMD | Digital micromirror device |
| DPCM | Defect parameter contour map |
| DPSS | Defect parameter solution surface |
| DRM | Depletion region modulation |
| EL | Electroluminescence |
| EQE | External quantum efficiency |
| FeB | Iron-boron pair |
| FTIR | Fourier transform infrared spectroscopy |
| FZ | Float zone |
| HF | Hydrofluoric |
| HH | Hornbeck and Haynes |
| IDLS | Injection dependent lifetime spectroscopy |
| InGaAs | Indium gallium arsenide |
| LCD | Liquid crystal display |

| | |
|---|---|
| LED | Light emitting diode |
| MCTS | Minority carrier transient spectroscopy |
| MMPL | Ratio between the maximum and minimum photoluminescence counts |
| mc-Si | Multi-crystalline silicon |
| $N_{dop}$-IDLS | Doping and injection dependent lifetime spectroscopy |
| NPC | Negative photoconductance |
| ODLTS | Optical deep level transient spectroscopy |
| OSF | Oxygen induced stacking fault |
| PC | Photoconductance |
| PECVD | Plasma enhanced chemical vapor deposited |
| PERC | Passivated emitter rear cell |
| PL | Photoluminescence |
| PLCE | Photoluminescence with current extraction |
| $Pt_s$ | Substitutional platinum |
| PV | Photovoltaic |
| QSS | Quasi-steady-state |
| RCA | Radio Corporation of America |
| RF | Radio frequency |
| SBD | Schottky barrier diode |
| $SiN_x$ | Silicon nitride |
| SRH | Shockley-Read-Hall |
| SRV | Surface recombination velocity [cm/s] |
| SS | Steady state |
| SD | Standard deviation |
| TFSI | bis(trifluoromethane)sulfonimide |
| TIDLS | Temperature and injection dependent lifetime spectroscopy |
| Ti | Titanium |
| UHP | Ultra high performance |
| μ-PCD | Microwave photoconductance decay |

## Roman Symbols

| | |
|---|---|
| $A$ | Area [cm$^2$] |
| $A_r$ | Normalization factor for the radial sensitivity of photoconductance coil |
| $a$ | Quadratic calibration constant of coil [siemens·V$^{-2}$] |
| $B$ | Radiative recombination coefficient [cm$^3$/s] |
| $b$ | Linear calibration constant of coil [siemens·V$^{-1}$] |

| | |
|---|---|
| $C_b$ | Base capacitance [pF] |
| $C_n$ | Auger recombination coefficient for two electrons and one hole [cm$^6$/s] |
| $C_p$ | Auger recombination coefficient for two holes and one electron [cm$^6$/s] |
| $C_{samp}$ | Sample dependent calibration factor for generation rate [cm$^{-1}$] |
| $C_{sys}$ | System dependent calibration factor for generation rate [cm$^{-2}$·s$^{-1}$·V$^{-1}$] |
| $\Delta C$ | Change of capacitance [pF] |
| $c$ | Constant term of calibration constants of coil [siemens] |
| $c_n$ | Electron capture rate per volume [cm$^{-3}$·s$^{-1}$] |
| $c_p$ | Hole capture rate per volume [cm$^{-3}$·s$^{-1}$] |
| $D$ | Diffusivity [cm$^2$·s$^{-1}$] |
| $D_{it}$ | Interface defect density [cm$^{-2}$·eV$^{-1}$] |
| $E_a$ | Activation energy/Apparent energy level [eV] |
| $E_C$ | Conduction band edge [eV] |
| $E_f$ | Fermi level [eV] |
| $E_i$ | Intrinsic level [eV] |
| $E_n$ | Electron emission rate [s$^{-1}$] |
| $E_{na}$ | Activation energy for electron emission signal, or apparent energy level of a defect reference to conduction band edge [eV] |
| $E_p$ | Hole emission rate [s$^{-1}$] |
| $E_{pa}$ | Activation energy for hole emission signal, or apparent energy level of a defect reference to valence band edge [eV] |
| $E_t$ | Defect energy level [eV] |
| $E_t^R$ | Energy level of a recombination active defect [eV] |
| $E_t^T$ | Energy level of a trap like defect [eV] |
| $E_V$ | Valence band edge [eV] |
| $E_\infty$ | Energy barrier for the exponential temperature dependency of capture cross section [eV] |
| $e_n$ | Electron emission rate per volume [cm$^{-3}$·s$^{-1}$] |
| $e_p$ | Hole emission rate per volume [cm$^{-3}$·s$^{-1}$] |
| $F_{samp}$ | Sample dependent calibration factor for photoluminescence [cm] |
| $F_{sys}$ | System dependent calibration factor for photoluminescence [cm$^2$·s·V] |
| $f_p$ | Fraction of the most positive charge state of a two-level defect |
| $f_m$ | Fraction of the middle charge state of a two-level defect |
| $f_n$ | Fraction of the most negative charge state of a two-level defect |
| $G$ | Carrier generation rate [cm$^{-3}$/s] |
| $g_{eeh}$ | Auger enhancement factor for two electrons and one hole |

| | |
|---|---|
| $g_{ehh}$ | Auger enhancement factor for two holes and one electron |
| $h$ | Intercept of a linear fit |
| $J_L$ | Photo-generation current density [A·cm$^{-2}$] |
| $k$ | Ratio of electron and hole capture cross sections |
| $k_B$ | Boltzmann constant, $8.617 \times 10^{-5}$ eV·K$^{-1}$ |
| $L_{eff}$ | Effective diffusion length [cm] |
| $m$ | Slope of a linear fit |
| $N_d$ | Donor concentration [cm$^{-3}$] |
| $N_{dop}$ | Doping concentration [cm$^{-3}$] |
| $N_M$ | Number of measurement data points |
| $N_{maj}$ | Majority carrier concentration [cm$^{-3}$] |
| $N_{minor}$ | Minority carrier concentration [cm$^{-3}$] |
| $N_t$ | Defect concentration [cm$^{-3}$] |
| $n$ | Electron concentration in the conduction band [cm$^{-3}$] |
| $n_0$ | Electron concentration in thermal equilibrium [cm$^{-3}$] |
| $n_1$ | Electron concentration when Fermi level is at the defect level [cm$^{-3}$] |
| $n_i$ | Intrinsic carrier concentration [cm$^{-3}$] |
| $n_s$ | Electron concentration at the surface [cm$^{-3}$] |
| $n_t$ | Electron concentration in the defect states, or concentration of the occupied defect states [cm$^{-3}$] |
| $\Delta n$ | Excess electron concentration [cm$^{-3}$] |
| $\Delta n_{app}$ | Apparent excess electron concentration [cm$^{-3}$] |
| $p$ | Hole concentration in the valence band [cm$^{-3}$] |
| $p_0$ | Hole concentration in thermal equilibrium [cm$^{-3}$] |
| $p_1$ | Hole concentration when Fermi level is at the defect level [cm$^{-3}$] |
| $p_s$ | Hole concentration at the surface [cm$^{-3}$] |
| $p_t$ | Hole concentration in the defect states, or concentration of the unoccupied defect states [cm$^{-3}$] |
| $\Delta p$ | Excess hole concentration [cm$^{-3}$] |
| $q$ | Elementary charge $1.602 \times 10^{-19}$ A·s |
| $R$ | Radius of circular wafer [mm] |
| $R_{Auger}$ | Auger recombination rate [cm$^{-3}$/s] |
| $R_{ext}$ | Extrinsic recombination rate [cm$^{-3}$/s] |
| $R_{rad}$ | Radiative recombination rate [cm$^{-3}$/s] |
| $R_{SRH}$ | Shockley-Read-Hall recombination rate [cm$^{-3}$/s] |
| $R_s$ | Series resistance [Ω·cm] |
| $R_{surface}$ | Surface recombination rate [cm$^{-2}$/s] |
| $R_{tot}$ | Total recombination rate [cm$^{-3}$/s] |

| | |
|---|---|
| $r$ | Distance to the center of photoconductance coil [mm] |
| $r_0$ | Expected value of Gaussian sensitivity function of photoconductance coil [mm] |
| $S$ | Conductance [siemens] |
| $S_{air}$ | Air conductance [siemens] |
| $S_{dark}$ | Dark conductance [siemens] |
| $S_{sample}$ | Sample conductance [siemens] |
| $\Delta S$ | Photoconductance [siemens] |
| $s_r$ | Radial sensitivity of photoconductance coil |
| $T$ | Temperature [K] |
| $T_{sample}$ | Actual sample temperature [K] |
| $T_{set}$ | Set temperature of cryostat [K] |
| $t$ | Time [s] |
| $t_p$ | Filling pulse length [s] |
| $U_b$ | Reverse bias voltage [V] |
| $U_p$ | Filling pulse voltage [V] |
| $V_{cali}$ | Output voltage of amplifier connected to calibration photodiode [V] |
| $V_{PC,air}$ | Output voltage of coil with no sample [V] |
| $V_{PC,cali}$ | Output voltage of coil with calibration sample [V] |
| $V_{PC,dark}$ | Output voltage of coil with sample in the dark [V] |
| $V_{PC,light}$ | Output voltage of coil with sample under illumination [V] |
| $V_{PL}$ | Output voltage of amplifier connected to photoluminescence photodiode [V] |
| $V_{ref}$ | Output voltage of reference cell [V] |
| $V_S$ | Voltage drop due to series resistance [V] |
| $V_{term}$ | Terminal voltage [V] |
| $W$ | Thickness [cm] |
| $X$ | Ratio of electron and hole concentrations |

## Greek Symbols

| | |
|---|---|
| $\alpha$ | Coefficient of power law temperature dependency of capture cross section |
| $\varepsilon$ | Damping factor for adaptive photoluminescence imaging method |
| $\lambda$ | Wavelength [nm] |
| $\mu_n$ | Electron mobility [cm$^2\cdot$V$^{-1}\cdot$s$^{-1}$] |
| $\mu_p$ | Hole mobility [cm$^2\cdot$V$^{-1}\cdot$s$^{-1}$] |
| $\rho_{she}$ | Sheet resistance [$\Omega$/sq] |

| | |
|---|---|
| $\sigma_0$ | Pre-factor for capture cross section with power law temperature dependency [$cm^2$] |
| $\sigma_a$ | Apparent capture cross section [$cm^2$] |
| $\sigma_n$ | Electron capture cross section [$cm^2$] |
| $\sigma_n^R$ | Electron capture cross section of a recombination active defect [$cm^2$] |
| $\sigma_n^T$ | Electron capture cross section of a trap like defect [$cm^2$] |
| $\sigma_p$ | Hole capture cross section [$cm^2$] |
| $\sigma_n^R$ | Hole capture cross section of a recombination active defect [$cm^2$] |
| $\sigma_n^T$ | Hole capture cross section of a trap like defect [$cm^2$] |
| $\sigma_s$ | Deviation of Gaussian sensitivity function of photoconductance coil |
| $\sigma_\infty$ | Pre-factor for capture cross section with exponential temperature dependency [$cm^2$] |
| $\tau$ | Charge carrier lifetime [s] |
| $\tau_{Auger}$ | Auger lifetime of charge carriers [s] |
| $\tau_{app}$ | Apparent lifetime [s] |
| $\tau_{decay}$ | Decay time constant [s] |
| $\tau_{eff}$ | Effective lifetime of charge carriers [s] |
| $\tau_{ext}$ | Extrinsic lifetime of charge carriers [s] |
| $\tau_G$ | Decay time constant of generation light [s] |
| $\tau_{NPC}$ | Time constant of negative photoconductance during the recovery process [s] |
| $\tau_{n0}$ | Electron capture time constant [s] |
| $\tau_{n0\_300K}$ | Electron capture time constant at 300 K [s] |
| $\tau_{p0}$ | Hole capture time constant [s] |
| $\tau_{p0\_300K}$ | Hole capture time constant at 300 K [s] |
| $\tau_r$ | Minority carrier lifetime [s] |
| $\tau_{rad}$ | Radiative lifetime of charge carriers [s] |
| $\upsilon_n$ | Electron thermal velocity [cm/s] |
| $\upsilon_p$ | Hole thermal velocity [cm/s] |
| $\Phi$ | Photon flux [$cm^{-2}s^{-1}$] |
| $\Phi_{PL}$ | Photon flux of photoluminescence [$cm^{-2}s^{-1}$] |

# List of publications

## Journal publications

C. Vargas, **Y. Zhu**, G. Coletti, C. Chan, D. Payne, M. A. Jensen and Z. Hameiri, "Recombination parameters of lifetime-limiting carrier-induced defects in multicrystalline silicon for solar cells," *Appl. Phys. Lett.*, vol. 110, no. 9, p. 092106, 2017. **(Equal contribution with C. Vargas)**

**Y. Zhu**, Q. T. Le Gia, M. K. Juhl, G. Coletti, and Z. Hameiri, "Application of the Newton–Raphson method to lifetime spectroscopy for extraction of defect parameters," *IEEE J. Photovoltaics*, vol. 7, no. 4, pp. 1092–1097, 2017.

**Y. Zhu**, M. K. Juhl, T. Trupke, and Z. Hameiri, "Photoluminescence imaging of silicon wafers and solar cells with spatially inhomogeneous illumination," *IEEE J. Photovoltaics*, vol. 7, no. 4, pp. 1087–1091, 2017.

**Y. Zhu**, M. K. Juhl, G. Coletti, and Z. Hameiri, "On the transient negative photoconductance in $n$-type Czochralski silicon," *IEEE J. Photovoltaics*, vol. 8, no. 2, pp. 421–427, 2018.

**Y. Zhu**, F. D. Heinz, M. K. Juhl, M. C. Schubert, T. Trupke, and Z. Hameiri, "Photoluminescence imaging at uniform excess carrier density using adaptive nonuniform excitation," *IEEE J. Photovoltaics*, vol. 8, no. 6, pp. 1787–1792, 2018. **(Invited journal paper and this study won the Best student Award at the *7th World Conference on Photovoltaic Energy Conversion*)**

F. D. Heinz, **Y. Zhu**, Z. Hameiri, M. K. Juhl, T. Trupke, and M. C. Schubert, "The principle of adaptive excitation for photoluminescence imaging of silicon: theory," *Phys. Status Solidi - Rapid Res. Lett.*, vol. 12, no. 7, p. 1800137, 2018.

**Y. Zhu**, M. K. Juhl, G. Coletti, and Z. Hameiri, "Reassessments of minority carrier traps in silicon with photoconductance decay measurements," *IEEE J. Photovoltaics*, vol. 9, no. 3, pp. 652–659, 2019.

## Conference publications

**Y. Zhu**, C. Vargas, M. A. Jensen, M. K. Juhl, G. Coletti, and Z. Hameiri, "Defect characterization via temperature and injection dependent lifetime spectroscopy," in *9th International Workshop on Crystalline Silicon for Solar Cells and 3rd Silicon Materials Workshop*, 2016.

**Y. Zhu**, M. K. Juhl, Z. Hameiri, and T. Trupke, "Applications of DMD-based inhomogeneous illumination photoluminescence imaging for silicon wafers and solar cells," in *44th IEEE Photovoltaic Specialist Conference (PVSC)*, 2017, pp. 66–69.

**Y. Zhu**, M. K. Juhl, G. Coletti, and Z. Hameiri, "Impact of transient trapping on steady state photoconductance lifetime measurements," in *27$^{th}$ International Photovoltaic Science and Engineering Conference*, 2017.

**Y. Zhu**, M. K. Juhl, F. D. Heinz, M. C. Schubert, T. Trupke, and Z. Hameiri, "Photoluminescence imaging at uniform excess carrier density using non uniform illumination," in *27$^{th}$ International Photovoltaic Science and Engineering Conference*, 2017.

**Y. Zhu**, M. K. Juhl, G. Coletti, and Z. Hameiri, "Reassessment of minority carrier traps in silicon during 'quasi-steady-state' photoconductance measurements," in *7$^{th}$ World Conference on Photovoltaic Energy Conversion (WCPEC)*, 2018, pp. 0077–0088.

**Y. Zhu**, F. E. Rougieux, N. Grant, J. Mullins, J. Ann De Guzman, J. Murphy, V. Markevich, G. Coletti, A. Peaker, and Z. Hameiri, "New insights into the thermally activated defects in n-type float-zone silicon," in *9$^{th}$ International Conference on Silicon Photovoltaics*, 2019, vol. 140014, p. 140014.

**Y. Zhu**, G. Coletti, and Z. Hameiri, "Injection dependent lifetime spectroscopy for two level defects in silicon," in *46$^{th}$ IEEE Photovoltaic Specialist Conference (PVSC)*, 2019.

M. A. Jensen **Y. Zhu**, E. E. Looney, A. E. Morishige, C. V. Castrillon, Z. Hameiri, and T. Buonassisi, "Assessing the defect responsible for LeTID: temperature- and injection-dependent lifetime spectroscopy," in *44$^{th}$ IEEE Photovoltaic Specialist Conference (PVSC)*, 2017, pp. 3290–3294.

S. Nie, **Y. Zhu**, S. Bernardini, M. Bertoni, and Z. Hameiri, "Advanced temperature characterization of silicon nitride surface passivation layer," in *27$^{th}$ International Photovoltaic Science and Engineering Conference*, 2017.

M. A. Jensen, **Y. Zhu**, K. Nakajima, M. K. Juhl, A. Youssef, E. E. Looney, Z. Hameiri, R. Sander, and T. Buonassisi, "Defect engineering for material-quality improvements in low-capex crystalline silicon—an application of temperature- and injection-dependent lifetime spectroscopy," in *MRS Fall Meeting,* 2017.

R. L. Chin, **Y. Zhu**, G. Coletti, S. Binetti, M. Pollard, and Z. Hameiri, "Insights into striations in n-type Czochralski wafers investigated via low-temperature hyperspectral and temperature-dependent spectral photoluminescence," in *10$^{th}$ International Workshop on Crystalline Silicon for Solar Cells*, 2018.

M. C. Schubert, F. Schindler, W. Kwapil, F. D. Heinz, T. Niewelt, R. Eberle, **Y. Zhu**, M. K. Juhl, Z. Hameiri, T. Trupke, F. E. Rougieux, and D. Macdonald, "Understanding the efficiency limitation of silicon material for solar cells," in *10$^{th}$ International Workshop on Crystalline Silicon for Solar Cells*, 2018.

R. L. Chin, **Y. Zhu**, G. Coletti, S. Binetti, M. Pollard, and Z. Hameiri, "Insights into bulk defects in n-type monocrystalline silicon wafers via temperature-dependent micro-photoluminescence spectroscopy," in *7$^{th}$ World Conference on Photovoltaic Energy Conversion (WCPEC)*, 2018, pp. 2524–2527.

F. E. Rougieux, C. Sun, **Y. Zhu**, and D. H. Macdonald, "Accurate defect recombination parameters: What are the limitations of current analyses?" in *7$^{th}$ World Conference on Photovoltaic Energy Conversion (WCPEC)*, 2018, pp. 2520–2523.

M. Jensen, H. S. Laine; **Y. Zhu**; C. V. Castrillon; Z. Liu. J. B. Li, Z. Hameiri, and T. Buonassisi, "Investigating the different degradation behavior of multicrystalline silicon PERC and Al-BSF solar cells," in *7th World Conference on Photovoltaic Energy Conversion (WCPEC)*, 2018, pp. 2528–2532.

S. Bernardini, **Y. Zhu**, S. Nie, Z. Hameiri, and M. Bertoni, "Analysis of SiNx SRV injection- and temperature-dependence and its degradation via TIDLS measurements," *7th World Conference on Photovoltaic Energy Conversion (WCPEC)*, 2018.

S. Bernardini, S. Nie, **Y. Zhu**, Z. Hameiri, and M. Bertoni, "Surface photovoltage spectroscopy as a characterization technique for surface passivation quality assessment," *7th World Conference on Photovoltaic Energy Conversion (WCPEC)*, 2018.

M. Siriwardhana, **Y. Zhu**, Z. Hameiri, F. D. Heinz, D. Macdonald, and F. E. Rougieux, "Temperature dependence of slow minority carrier de-trapping in Czochralski silicon with high concentrations of thermal donors," in *35th European Photovoltaic Solar Energy Conference and Exhibition*, 2018, pp. 337–341.

Z. Hameiri, R. Bhoopathy, D. Chung, R. Dumbrell, M. K. Juhl, O. Kunz, R. L. Chin, A. Paduthol, I. Zafirovska, **Y. Zhu**, and T. Trupke, "Progress in photoluminescence-based characterization of silicon bricks, wafers and modules," in *European Advanced Energy Materials and Technology Congress*, 2018.

# Chapter 1
# Introduction

## 1.1 The future with photovoltaic

Although some suspicions and myths still exist in the media and general public, there is a consensus in the scientific community that human activity over the past 50 years has had a significant and even consequential impact on the climate of our only Earth [1]. The carbon dioxide level in the atmosphere today (August 2019) is more than 35% higher than the historical highest level found over the last 800,000 years [2]–[4]. The associated consequences of the raised carbon dioxide level are: the global warming that cannot be explained by natural cyclical variations [5], [6], rise of sea level [7], retreat of glaciers [8], increase of extreme weather and abnormal climate [9], etc. To fight against this crisis of climate change, transition from traditional fossil fuel energy to clean and renewable energy such as solar and wind is imperative, and it requires immediate and global action.

Among all the renewable energy resources, solar energy has a reserve exceeding the sum of the others by orders of magnitude [10]. The yearly solar potential on earth is one order of magnitude larger than the sum of all the fossil fuels plus fission nuclear [10]. Considering the current global energy use (18.5 TWy, [11]) and assuming a continuing increase of energy demand, solar should be considered to be the major source of our energy within the next decade. Since the global consumption of electricity has been continuously increasing by around 2.9% since 1990 [11], a large part of the solar energy will be used in the form of photovoltaic (PV), where the solar energy is directly transferred to electricity. It is clear that if an environmentally friendly and sustainable future is what we are pursuing, PV will play a vital role in the energy supply of our near future.

Another more compelling reason for embracing PV is the continuous reduction of cost achieved by the PV industry over the past decades [12]. In certain regions, for example Australia, where this thesis has been written, the levelized cost of electricity of PV is already lower than the that of coal, without any subsidy [13]. Therefore, the adoption of

PV is also economically viable. It is thus reasonable to assume a continuous bloom of PV industry and imagine a future with PV as our main energy source.

## 1.2 Thesis objectives

Currently the global PV market is dominated by crystalline silicon (c-Si) based technologies [14]. The industry is relatively mature with an impressive yearly learning rate of around 22% for the PV module selling price over the past 40 years [12]. The c-Si industry and research are still largely focusing on the improvement of device efficiency as well as reliability, and continuing reduction of the cost [15].

The silicon PV industry is moving from conventional back surface filed (BSF) technology [16] towards more advanced solar cell architectures such as passivated emitter and rear cell (PERC) [17], and passivated contacts [18]. These advanced architectures feature reduced carrier recombination at the surface and contacts of the solar cell. Maximizing the advantages of these advanced architectures requires improved bulk quality of silicon. A deep understanding of bulk defects in silicon and their recombination properties is thus essential for the development of PV industry.

Bulk defects are well known to enhance the recombination of photo-generated carriers and reduce the device performance [19]. Characterization of the electrical properties of defects is beneficial for: (1) identification of the defects, and thus better elimination of the defects; and (2) evaluation of their impact on the device efficiency. Conventionally the characterization of defects' electrical properties was widely done via deep level transient spectroscopy (DLTS) techniques [20]. More recently, an emerging technique, injection dependent lifetime spectroscopy (IDLS) [21] has gained popularity in the PV community for defect characterization. This technique extracts the electrical properties of defects directly from the measured recombination of photo-generated carriers, and thus has an ultimately high sensitivity to recombination active defects [21]. Nevertheless, as a relatively new technique, IDLS is less mature compared to DLTS. This thesis aims to improve characterization of bulk defects via IDLS-based techniques. The objectives of this thesis include:

1.  To develop a reliable measurement system for IDLS;

2.  To improve the analysis method of IDLS-based techniques;

3. To apply the improved IDLS techniques for the characterization of newly discovered defects in float-zone (FZ) silicon [22];

4. To extend to investigation from recombination active defects to traps, which could be harmful for the characterization of recombination active defects [23]; and

5. To development accurate quantitative technique for spatially resolved lifetime measurements such that IDLS techniques can be applied to defects with non-uniform distribution.

## 1.3 Thesis outline

In Chapter 2, the basic concepts of carrier recombination and carrier lifetime will be reviewed. These concepts form the base for the IDLS techniques that are investigated and applied in this thesis. A brief introduction of the principles of IDLS and the other characterization techniques used in this thesis will be given. The advantages and disadvantages of different techniques will be discussed.

In Chapter 3, the measurement system developed during this thesis will be presented. It allows IDLS measurements with temperature variation which is used in the recombination active defect investigation in Chapter 5. The capability of measuring photoconductance (PC) at various conditions is also suitable for the investigation of traps in Chapter 6. The working principle and details of the calibration process will be described.

In Chapter 4, the methods of extracting the electrical properties of defects from IDLS measurements will be presented. The conventional approach will be reviewed, and a new method will be proposed. Furthermore, an extension of IDLS technique from single-level defects to two-level defects will be presented.

In Chapter 5, the methods described in Chapter 4 will be applied to investigate recently discovered recombination active defects in FZ silicon. The aim is to identify the dominant defect level and extract the defect parameters. Apart from the IDLS technique, DLTS is also applied for more reliable results. From this concrete example, the advantages of combining different techniques for defect characterization will be highlighted.

Different from the investigation of recombination active defects in Chapter 5, Chapter 6 focuses on the investigation of carrier traps. Traps might be less detrimental to PV

device performance. However, they could impede accurate IDLS measurements, and thus impact the analysis of recombination active defects. Meanwhile, the unique properties of traps are themselves interesting to study. Chapter 5 summarizes the methods used in previous studies of traps and proposes new methods. These methods will then be applied to study the traps in Czochralski (Cz) silicon.

In Chapter 7, the non-uniform distribution of defects is considered. Non-uniform distribution of defects within the sensor area of the lifetime measurement system leads to inaccurate IDLS measurement, and thus inaccurate defect parameterization. Conventional spatially resolved techniques often suffer from the impact of lateral carrier flow. In Chapter 7, a non-uniform illumination photoluminescence (PL) imaging method is developed. This method eliminates the lateral carrier flow by adaptively adjusting illumination intensity at different locations on the sample. Proof of concept measurements have been made to demonstrate the feasibility and advantage of this method for spatially resolved defect characterization.

At the end, the major findings of this thesis are summarized in Chapter 8. Future plans for further improvements of current methods and better understanding of the investigated defects are also outlined.

# Chapter 2
# Literature Review

Defects facilitate recombination of charge carriers, leading to a reduction in the carrier lifetime, and the performance of final PV devices. In this chapter, the basic concepts of recombination, carrier lifetime and the impact of defects on them will be reviewed. The correlation between carrier lifetime and the electrical properties of defect then leads to lifetime spectroscopy, which is the main defect characterization technique used in this thesis. The basic principle of lifetime spectroscopy will be reviewed, together with the principles of other defect characterization techniques.

It should be noted that this chapter only gives a review of the basic principles that applies to the whole thesis. In the following chapters, more detailed reviews will be provided regarding the content relevant to each chapter.

## 2.1 Recombination and lifetime

Solar cells generate electricity relying on the production of electron-hole pairs. In the context of this thesis, unless otherwise specified, the term "electron" refers to the electron in the conduction band of a semiconductor and the term "hole" refers to the hole in the valence band. Electron-hole pairs can be generated when energy higher than the bandgap of the semiconductor is provided, and this can be done, for example, by absorption of photons.

The inverse process of generation is recombination, where an electron and a hole annihilate, and the free energy is released by emission of either photons or phonons, or both. Recombination can be classified into intrinsic recombination and extrinsic recombination [24]. Intrinsic recombination refers to the type of recombination which occurs even in the pure semiconductor crystal with a perfect lattice structure [24]. Extrinsic recombination refers to the type of recombination which occurs via the electron states in the semiconductor bandgap induced by defects [24].

When no defect state is involved, intrinsic recombination of electron-hole pairs occurs via transition of the charge carriers directly from one energy band to the other band where the excess energy can be released via emission of a photon [25]. This type of intrinsic recombination is called radiative recombination. The excess energy can also be transferred to another electron or another hole, which is then lost to the lattice via thermalization. This type of intrinsic recombination is named Auger recombination [26].

Radiative recombination is the reserve process of optical generation. As an electron and a hole are involved, the rate of radiative recombination for the excess charge carriers can be calculated as:

$$R_{rad} = B(np - n_i^2) \tag{2.1}$$

where $B$ is the coefficient of radiative recombination which characterizes the possibility of the occurrence of radiative recombination, $n$ and $p$ are respectively the electron and hole concentration, and $n_i$ is the intrinsic carrier concentration. The term $Bn_i^2$ accounts for the radiative recombination of the thermally generated carriers.

The radiative recombination coefficient $B$ is enhanced by the Coulomb attractions between electrons and holes [27]. Therefore, it is impacted by the charge carrier concentration. The value of $B$ has been determined in a few studies [25], [27]–[31].

Auger recombination is the reverse process of impact ionization, where an electron or a hole with high enough kinetic energy knocks out an electron in the valence band and create an electron-hole pair [19]. Auger recombination involves three particles: two electrons and one hole; or two holes and one electron. The rate of Auger recombination for excess charge carriers can be calculated as [32]–[35]:

$$R_{Auger} = C_n(n^2p - n_0^2p_0) + C_p(np^2 - n_0p_0^2) \tag{2.2}$$

where $C_n$ and $C_p$ are respectively the Auger recombination coefficients for two electrons and one hole process, and two holes and one electron process [36], and $n_0$ and $p_0$ are respectively the electron and hole concentration in thermal equilibrium.

The values of $C_n$ and $C_p$ have been determined by Dziewior and Schmid [36], and Sinton and Swanson [37], however, Dziewior and Schmid also found that the lifetime measured on samples with low doping concentration deviated from the lifetime predicted by the determined values [36]. This was explained by Coulomb interactions between the

involved particles [38]. This Coulomb enhanced effect can be accounted by multiplying $C_n$ and $C_p$ by empirically dependent factors $g_{eeh}$ and $g_{ehh}$ [39] which modifies Eq. (2.2) to:

$$R_{Auger} = C_n g_{eeh}(n^2 p - n_0^2 p_0) + C_p g_{ehh}(np^2 - n_0 p_0^2) \tag{2.3}$$

Nevertheless, apart from the Coulomb enhanced effect, Auger recombination is also found to be determined by other factors, such as phonon participation [40], [41]. Considering the complicity of describing all the physical effect theoretically, empirical parameterization of Auger recombination is often used [39], [42]–[45].

Extrinsic recombination which involves electron states within the bandgap induced by defect, is a two-step process. A charge carrier is first captured by the defect level, then recombined with a carrier with the opposite charge captured by the same defect. The rate of extrinsic recombination $R_{ext}$ is more complex and will be discussed in the next section.

In silicon, the overall recombination rate is usually dominated by the extrinsic recombination rate. Due to the cubic correlation with carrier density, Auger recombination is usually dominating in high injection or highly doped silicon [46]. Radiative recombination is usually less dominant, however, it is the basis of all the PL based measurements [47].

A term closely related to recombination rate is charge carrier lifetime, which is often simplified as lifetime. Lifetime is defined as the average time a charged carrier can exist in the excited state before recombination. As in steady state (SS) condition the generation rate via external excitation $G$ is constant and equals the total recombination rate $R_{tot}$, lifetime $\tau$ can be calculated as [48]:

$$\tau = \frac{\Delta n}{R_{tot}} = \frac{\Delta n}{G} \tag{2.4}$$

where $\Delta n$ is the excess electron concentration, which equals $n - n_0$.

The lifetime in Eq. (2.4) is often referred to as "effective lifetime" as it involves all the recombination rate. Sometimes lifetime due to different recombination types can be calculated separately [48]:

$$\frac{1}{\tau_{eff}} = \frac{R_{tot}}{\Delta n} = \frac{R_{rad} + R_{Auger} + R_{ext}}{\Delta n} = \frac{1}{\tau_{rad}} + \frac{1}{\tau_{Auger}} + \frac{1}{\tau_{ext}} \tag{2.5}$$

where $\tau_{rad}$, $\tau_{Auger}$, and $\tau_{ext}$ are respectively the radiative lifetime, Auger lifetime and extrinsic lifetime.

In transient condition ($G = 0$), the reduction rate of excess carrier concentration $-\frac{d\Delta n}{dt}$ equals total recombination rate. Lifetime can be calculated as the decay time constant of excess carriers [48]:

$$\tau = \frac{\Delta n}{R_{tot}} = \frac{\Delta n}{-\frac{d\Delta n}{dt}} \tag{2.6}$$

In more general cases where $G$ changes with time, the excess carrier density follows the rate equation:

$$\frac{d\Delta n}{dt} = G(t) - R_{tot} \tag{2.7}$$

The carrier lifetime can be calculated as [49]:

$$\tau = \frac{\Delta n}{R_{tot}} = \frac{\Delta n}{G(t) - \frac{d\Delta n}{dt}} \tag{2.8}$$

In the equations above, the lifetimes are calculated for excess electrons. The lifetime for excess holes can be calculated in a similar way. For intrinsic recombination, an electron annihilates directly with a hole; therefore, the intrinsic lifetimes for electron and hole are the same. For extrinsic recombination, electrons and holes can be captured in the defect for different periods of time. Therefore, $\tau_{ext}$ for electrons and holes can be different. This is usually the case for trap-like defect (named trap herein) [50]. For recombination-active defects where electron and hole annihilate with the same rate, the extrinsic lifetimes of electrons and holes are equal. Therefore, without the presence of trap, the effective lifetime for electron is the same as the effective lifetime for holes, and $\Delta n = \Delta p = p - p_0$. In most parts of this thesis, $\Delta n$ is used to denote the general excess carrier concentration. In the parts where traps are investigated, $\Delta n$ is used to denote excess electron concentration specifically and $\Delta p$ is for excess hole concentration.

Carrier lifetime is an important parameter for solar cell performance [24]. Higher carrier lifetime means: (a) at a given external generation rate, the carrier concentration is higher which implies a higher output voltage of the device; and (b) the extraction of carriers out of the device is easier, which implies a higher output current of the device [48], [51].

## 2.2 Defects and SRH recombination statistics

As mentioned before, defects induce available electron states within the bandgap and lead to extrinsic recombination of carriers. There are various types of defects: impurities [52]; crystallographic imperfections such as dislocations [53]; self-interstitials [54]; and many others [55]–[57]. Defects can present in the bulk, as well as at the surface, for example, dangling bonds [58]. Extrinsic recombination statistics can be complicated. First, extrinsic recombination of the simplest case will be introduced and then the discussion extends to more complicated cases.

The simplest case of extrinsic recombination is based on the following assumptions:

1. The defect has only two charge states and a single energy level for the transition between these states;

2. The defect is a bulk defect and not a surface defect;

3. The defect is a point defect and not an extended defect; and

4. The defect is a recombination-active defect and not a trap.

If the above assumptions are valid, the recombination rate in a SS condition due to the defect can be calculated using the statistics derived by Shockley, Read [59] and Hall [60] (SRH):

$$R_{SRH} = \frac{(np - n_i^2)N_t}{\dfrac{(p + p_1)}{\sigma_n v_n} + \dfrac{(n + n_1)}{\sigma_p v_p}} \tag{2.9}$$

where $N_t$ is the defect concentration, $\sigma_n$ and $\sigma_p$ are respectively the capture cross sections for electrons and holes, where $v_n$ and $v_p$ are respectively the thermal velocity for electrons and holes, $n_1$ and $p_1$ are defined as:

$$n_1 = n_i \exp\left[\frac{E_t - E_i}{k_B T}\right] \tag{2.10.1}$$

$$p_1 = n_i \exp\left[-\frac{E_t - E_i}{k_B T}\right] \tag{2.10.2}$$

where $E_t$ is the energy level of the defect, and $E_i$ is the intrinsic Fermi level, $k_B$ is the Boltzmann constant and $T$ is the temperature. The derivation of Eq. (2.9) is based on a detailed balance of the capture and emission of electrons and holes in the defect level.

If we further assume that there is no *other* defect that behaves as a trap so that $\Delta n = \Delta p$ is valid, the extrinsic recombination lifetime can be calculated as:

$$\tau_{SRH} = \frac{\Delta n}{R_{SRH}} = \frac{\tau_{n0}(p_0 + p_1 + \Delta n) + \tau_{p0}(n_0 + n_1 + \Delta n)}{(n_0 + p_0 + \Delta n)} \tag{2.11}$$

where $\tau_{n0}$ and $\tau_{p0}$ are defined as:

$$\tau_{n0} = \frac{1}{\sigma_n v_n N_t} \tag{2.12.1}$$

$$\tau_{p0} = \frac{1}{\sigma_p v_p N_t} \tag{2.12.2}$$

Equation (2.11) is the famous SRH lifetime equation, which is the base of the main characterization technique used in this thesis - injection dependent lifetime spectroscopy [21].

Although the above equations were originally derived in a SS condition, it can be easily proven that if the Assumption (4) above is valid, the equations are valid in transient condition as well.

Let us now investigate the previous assumptions for the SRH lifetime equation. If Assumption (1) is not valid, *i.e.*, the defect has more than one energy levels, the recombination statistics of the defect can be derived using a similar approach as the derivation of SRH recombination rate, although a more complicated equation will be obtained. The recombination rate of a two-level defect has been derived [61]:

$$R_{two-level} = \frac{N_t(np - n_i^2)[\left(\frac{\sigma_{n1}\sigma_{p1}v_nv_p}{\sigma_{p1}v_pp_1 + \sigma_{n1}v_nn}\right) + \left(\frac{\sigma_{n2}\sigma_{p2}v_nv_p}{\sigma_{n2}v_nn_2 + \sigma_{p2}v_pp}\right)]}{1 + \left(\frac{\sigma_{n1}v_nn_1 + \sigma_{p1}v_pp}{\sigma_{p1}v_pp_1 + \sigma_{n1}v_nn}\right) + \left(\frac{\sigma_{p2}v_pp_2 + \sigma_{n2}v_nn}{\sigma_{n2}v_nn_2 + \sigma_{p2}v_pp}\right)} \qquad (2.13)$$

where the subscript "1" and "2" are for the 1st and 2nd level respectively.

Assumption (2) restricts the application of the SRH equation to bulk defect. For surface defect, an extended formulization for the recombination rate needs to be used [62]:

$$R_{surface} = (n_sp_s - n_i^2)\int_{E_V}^{E_C} \frac{D_{it}(E_t)}{\frac{(p_s + p_1)}{\sigma_n(E_t)v_n} + \frac{(n_s + n_1)}{\sigma_p(E_t)v_p}} dE_t \qquad (2.14)$$

where the subscript "$s$" represents the quantity at the surface and $D_{it}$ is the interface defect concentration.

The surface defect usually has a continuum of energy levels, instead of a single or a few distinct energy levels. Therefore, an integral of the recombination rate of all the energy levels is needed. Meanwhile, the carrier concentrations near the surface $n_s$, $p_s$ can be different from the bulk concentration as they are impacted by the charge in the dielectric layer deposited on the surface of silicon [63]. A numerical approach to solve the carrier concentrations at the surface has been proposed [62]–[64].

Assumption (3) restricts the application of SRH equation to point defects whose geometry does not impact the recombination. In the case of extended defect, such as dislocations, grain boundaries, precipitates etc., the geometry of the defect can impact the carrier distribution near the defect, as well as the formulization of the recombination statistics. Several literatures have investigated the recombination statistics for precipitates in silicon [65]–[67].

Assumption (4) is also important for the derivation of SRH equation. When a defect is a trap-like defect which leads to an imbalance of $\Delta n$ and $\Delta p$, the carrier lifetime for electron and hole will be different and the SRH equation cannot be simply used to calculate the lifetime [50]. It should be noted that whether a defect is a trap or not, depends not only on the defect's electrical properties, but also on its concentration and the doping of the sample [50], [68]. Previous studies have investigated the validity of Assumption (4) under SS condition [50]. The recombination statistics of trap can also be impact by the measurement condition. Traps in SS condition can behave different from being in

transient condition [69], [70]. More detailed investigation of traps can be found in Chapter 6 of this thesis.

Given that previous assumptions are valid, the SRH equation builds up the correlation between the defect's electrical properties and the carrier lifetime. The principle of IDLS is to use the measured lifetime and this correlation to inversely solve the defect's electrical properties [21]. The implication of these four assumptions for IDLS will be discussed in the next section.

## 2.3 Characterization of defects

In this section, the principle of IDLS, the main defect characterization technique investigated and applied in this thesis, will be reviewed. The assumptions implied behind conventional IDLS analysis will be outlined. Important factors of reliable IDLS analysis will be discussed.

Additionally, two other characterization techniques used in this thesis will also be reviewed. The first one is DLTS [71], one of the most widely used techniques to characterize defects' electrical properties. The advantages and disadvantages of DLTS and IDLS will be discussed. The second one is PL imaging, one of most widely used spatially characterization techniques for silicon wafers and solar cells [72]. Both techniques will be applied together with IDLS for the characterization of a newly discovered thermally activated defects in FZ silicon in Chapter 5. PL imaging is also the base of a new technique developed in Chapter 7 for characterizing of spatially non-uniform distributed defects.

### *2.3.1 Injection dependent lifetime spectroscopy*

### 2.3.1.1 Basic principles of IDLS

In this section, the basic principle and the development of IDLS will be reviewed. The methods of defect parameterization using IDLS will be reviewed in more detail in Chapter 4 of this thesis.

Lifetime spectroscopy is a technique to extract the defect's electrical properties from the measured lifetime [21]. Back to the 1950s, investigations have been made to extract trap parameters from transient PC lifetime measurement [73], [74]. The first usages of lifetime spectroscopy for recombination active defects were back in the 1990s [75], [76].

At the beginning, only the temperature dependency of the lifetime was used and this type of lifetime spectroscopy is referred to as TDLS [56], [77]. Later on, the information regarding the injection dependency of lifetime was used and this type of lifetime spectroscopy is referred to as IDLS [78]–[81]. With the development of QSSPC technique [82], [83], which makes injection dependent lifetime measurements easy to be done, IDLS has gained a wider popularity in the field of defect characterization for PV [84]. Moreover, the development of high quality surface passivation techniques, such as plasma enhanced chemical vapor deposited (PECVD) silicon nitride (SiN$_x$) [85] made characterization of bulk defect easier. IDLS with doping variation ($N_{dop}$-IDLS) [79] or temperature variation (TIDLS) have also been used [86].

Nevertheless, the spectroscopic potential of lifetime spectroscopy was not fully discussed until the systematic investigation by Rein [21]. It has been shown that IDLS provides only a constraint of the defect parameters instead of the actual values. Infinite solutions of the defect parameters can be found to reproduce the measured lifetime curve. $N_{dop}$-IDLS and TIDLS can minimize the number of solutions from infinity to two. One is in the upper half of the bandgap, and the other in the lower half of the bandgap [21]. If the defect has a capture cross section ratio $k$ ($\sigma_n/\sigma_p$) deviating far from unity and temperature independent, it is possible to further differentiate the two solutions in TIDLS. By combining TDLS and IDLS, it is also possible to obtain a unique solution as in TIDLS [21].

Meanwhile, a method named defect parameter solution surface (DPSS) was proposed by Rein [21] for analyzing lifetime spectroscopy data. DPSS provides a good visualization of all the possible solutions of defect parameters that can fit the measured IDLS or TDLS data. For TIDLS, $N_{dop}$-IDLS, or the combination of TDLS and IDLS, the intersections of DPSS curves measured at different conditions indicate the exact value of the defect parameters. As DPSS is closely related to the analysis methods used in this thesis, the details of DPSS method will be reviewed in Chapter 4.

With the systematic study by Rein [21], lifetime spectroscopy has been used to investigate more and more defects, from intentionally induced defects [87]–[92], to unknown defects dominating the effective lifetime of a sample [93]–[98]. More recently, a method to linearize SRH equation has been proposed [99]. This method has been adopted to simplify the procedure of generating DPSS curves [93]. Alternative methods

of DPSS, such as defect parameter contour map (DPCM) [100], [101], were also proposed. In Chapter 4 a new approach based on the Newton-Raphson method will be presented.

### 2.3.1.2 Assumptions behind IDLS

As mentioned previously, most of the previous lifetime spectroscopy studies are based on the SRH equation, whose assumptions are listed in previous section. As this thesis focus on the bulk point defects, the assumptions (2) and (3) are generally valid. However, the validity of assumptions (1) and (4) are questionable and worth investigation prior to the investigation of lifetime spectroscopy.

Assumption (1) assumes the investigated defect is a single-level defect. This can be easily checked by the fitting quality of the measured lifetime via the SRH equation, or the linearity of the injection dependent lifetime curve after the linearization procedure [99]. In the majority of cases, the measured lifetime cannot be well fitted with a single-level defect. In these cases, most studies assume that two single-level defects impact the measured lifetime [84], [93], [102], [103]. By adding the recombination lifetime of a secondary single-level defect, the measured lifetime can be fitted with improved quality. However, the fact that a single-level defect cannot provide satisfied fitting of the measured lifetime could also be explained by the existence of multi-level defects. In fact, a recent review paper has shown that most defects have more than one defect level [104]. Nevertheless, the possibility of multi-level defects is seldomly considered in literature [99], [105]. As discussed in the previous section, the recombination statistic of a two-level defect is different from the statistic of a single-level defect. In this thesis, a first systematic investigation of two-level defects in lifetime spectroscopy will be made. The details can be found in Chapter 4. Moreover, this analysis of two-level defects will be applied to the investigation of thermally activated defects in FZ silicon in Chapter 5.

Assumption (4) limits the application of lifetime spectroscopy to recombination-active defects. The main purpose of this thesis is the characterization of the recombination-active defects, as they have the most detrimental effect on the device performance. Nevertheless, traps are also very interesting to investigate. First, traps have been found to exist in different materials including Cz silicon [69], [106] and multi-crystalline silicon (mc-Si) [23], which are the dominant materials in the silicon photovoltaic industry. Second, even if the studied defect is not a trap, the presence of traps in the sample can impact the investigation of the interested defect [23]. This is especially important when the

investigation is done using PC-based system as traps are known to cause artifact in this type of lifetime measurements. One way to mitigate this artifact is to measure the lifetime with PL [107]. In Chapter 3 of this thesis, a customized lifetime which allows PL based lifetime measurement will be presented. Finally, although traps are not as detrimental as the recombination active defects, recent studies have revealed that traps can also decrease the carrier lifetime [108], [109]. As the quality of silicon improves and recombination-active defects are eliminated, it is possible that traps will have a stronger impact on the device performance in the future. Chapter 6 provides a more detailed review of previous works regarding traps. A thorough investigation of the properties of traps will be made and the new insights regarding traps will be highlighted.

### 2.3.1.3 Other important factors for IDLS

Apart from the consideration of the assumptions mentioned above, an accountable IDLS analysis also strongly depends on the accuracy of the extracted extrinsic recombination lifetime. This relies on two factors: the accuracy of the measured effective lifetime; and the dominance of the extrinsic recombination lifetime from the interested defect. As mentioned previously, the accuracy of measured lifetime can be impacted by traps if PC-based techniques are used. Moreover, depletion region modulation (DRM) [110] can also lead to similar artifacts as traps. PL based lifetime measurements are not impacted by these artifacts, but the calibration of PL is more complicated as PL is impacted by the optical properties of samples whereas the calibration of PC is only impacted by the detection system. In Chapter 3, a detailed description of the calibration procedures for PC and PL in the customized lifetime tester used in this thesis will be given. Meanwhile, most of the lifetime testers, including the one used in this thesis, measures the lifetime over a circular sensor area. [83] Therefore, if defects have non-uniform distribution over this sensor area, the accuracy of measured lifetime will be impacted. In the majority of this thesis, we investigate defects with uniform distributions over the measured sensor area. In Chapter 7, an approach to improve the accuracy of lifetime measurements on spatially non-uniform distributed defects will be presented.

It should also be noted that the measured lifetime is the effective lifetime involving all the recombination processes. For IDLS analysis, the recombination lifetime of the interested defect needs to be extracted from the measured effective lifetime. The intrinsic lifetime can be calculated using previous models and then subtracted from the effective

lifetime. Another way is to subtract the effective lifetime of a control sample without the interested defect, but with the same doping concentration. The intrinsic lifetime component is then removed since the intrinsic lifetime of the control sample and the interested sample is identical. The modelling of intrinsic lifetime is unnecessary in this case. This approach can also remove the component of surface defect lifetime if the control wafer and the interested wafer are passivated with identical dielectric layer and have the same thickness. Moreover, if it can be further assumed that the only difference between the interested wafer and the control wafer is with or without the interested defect, this subtraction also removes the lifetime associated to any other bulk defects existing in both wafers. As can be seen from Eq. (2.5), the effective lifetime is the harmonic sum of all the lifetime components. Obviously the dominant (lowest) lifetime component can be extracted with the least uncertainty. Therefore, it is beneficial to make sure that the recombination lifetime of the interested defect dominants the effective lifetime. As mentioned in the previous section, Auger recombination can become significant in very high injection. This could impede a reliable extraction of defect lifetime at high injection. Fortunately, it is not always necessary to reach very high injection for IDLS analysis. Usually an injection level of ten times higher than the background doping concentration is sufficient for IDLS analysis [99]. Surface recombination can be suppressed by applying high quality surface passivation techniques. Various surface passivation layers deposited by different techniques with very low surface recombination rate have been developed [85], [111]. Recombination of the other non-interested bulk defects can also impact the extraction of recombination lifetime of the interested defect. To minimize this impact, it is beneficial to choose silicon material with high bulk lifetime prior to the contamination or generation of the interested defect. Application of gettering to remove recombination active metal impurities can also be an effective way [112]. Otherwise, to increase the concentration of the interested defect can also help ensure its dominance in the effective lifetime, although lower lifetime also reduced the signal to noise ratio of the lifetime measurements and the highest achievable injection level.

### *2.3.2 Other characterization techniques*

### 2.3.2.1 Deep level transient spectroscopy

#### *(1) Principle of DLTS*

DLTS is one of the most sensitive and powerful characterization techniques for defects with deep states [113]. DLTS was first introduced in the 1970s [20] and soon gained popularity in the characterization of defects in semiconductors [52], [114]. In DLTS measurements, a Schottky diode or a *p-n* junction is made and reverse biased to create a depletion region. Within this depletion region, the majority carriers in defect states located in the majority carrier bandgap half are also depleted. If a voltage pulse of zero volt or even forward bias is applied, the majority carriers are populated in the depleted region and can be captured by those depleted defect states. When the pulse finishes and the diode is reverse biased again, those captured majority carriers are emitted back to the majority carrier band and fast depleted by the applied electric field. This changes the charge density in the depletion region; therefore, leading to a change of the capacitance of the diode. The capacitance change follows the emission of majority carriers from the defect, which is an exponential decay process with a time constant equal to the inverse of the majority carrier emission rate [20]:

$$\tau_{decay} = E_n^{-1} = 1/\sigma_n v_n n_1 \text{ for } n\text{-type material, or} \tag{2.15.1}$$

$$\tau_{decay} = E_p^{-1} = 1/\sigma_p v_p p_1 \text{ for } p\text{-type material.} \tag{2.15.2}$$

$n_1$ and $p_1$ are function of the $E_t$ and $T$ defined in Eq. (2.10). Therefore, from the decay time constant of the capacitance, information of the defect energy level can be extracted.
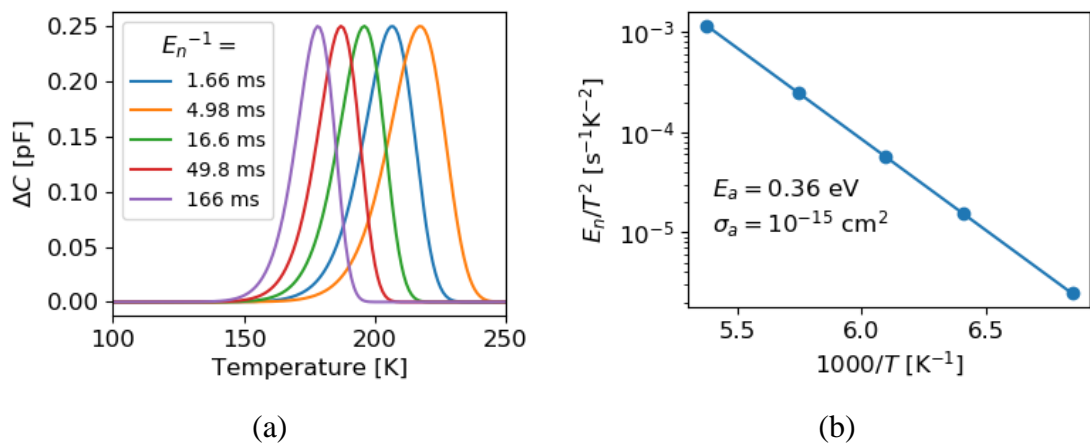


**Fig. 2.1** Plots of simulated DLTS results: (a) Temperature scans of $\Delta C$ with different rate windows; (b) Arrhenius plot for the extraction of $E_a$ and $\sigma_a$.

39

In conventional DLTS, the procedure of extracting the decay time constant from the exponential decay is simplified by the "rate window" method [20]. Instead of recording the whole exponential decay, only two points along the decay are measured. When the decay time constant equals to the reference time defined by the rate window, the measured capacitance difference ($\Delta C$) between these two points is maximized. By recording $\Delta C$ while scanning the measurement temperature, a peak of $\Delta C$ will appear at the temperature where the decay time constant equals the reference time. The height of the peak can be used to determine $N_t$ of the defect. By repeating the temperature scan while changing the rate window, an activation energy $E_a$ related to $E_t$ and an *apparent* majority carrier capture cross section $\sigma_a$ can be extracted using an Arrhenius plot [20]. A set of simulated DLTS temperature scans of $\Delta C$ with different rate windows is shown in Fig. 2.1(a). The corresponded Arrhenius plot is shown in Fig. 2.1(b). The division of $E_n$ by $T^2$ is to account for the temperature dependency of thermal velocity and density of band states.

DLTS has been used to characterize numerous defects in different materials and $E_a$ and $\sigma_a$ of these defects have been extracted and sometimes are used as the characteristics of a defect [115], [116]. However, the usage of these two parameters has a few drawbacks. First, is has been shown that many different defects can have very similar $E_a$ and $\sigma_a$ [114]. Therefore, just from the measured $E_a$ and $\sigma_a$, it is not possible to differentiate between defects. Second, $E_a$ and $\sigma_a$ only characterize the defect's emission of majority carriers, and not the overall recombination characteristics of the defect [114]. Therefore, just from the measured $E_a$ and $\sigma_a$, it is not possible to determine if a defect is recombination active or not. Finally, the measured $E_a$ and $\sigma_a$ can be different from the defect's *actual $E_t$* and *actual* majority carrier capture cross section. As $E_a$ and $\sigma_a$ are extracted from a temperature scan, the temperature dependency of $E_t$ and capture cross section can affect the extracted values [114]. Fortunately, techniques of measuring the capture characteristic of defects via DLTS have been proposed. The actual majority carrier capture cross section, as well as its temperature dependence, can be determined by doing a variation of the filling pulse length [114]. With this information, the actual $E_t$ of the defect can also be determined.

The DLTS is limited to the defects in the majority carrier bandgap half, as the voltage change is not able to modulate the occupancy of the defect states in the minority carrier bandgap half [20]. Variations of DLTS have been developed to measure the defects in the minority carrier bandgap half [114]. The filling of minority carriers in the defect states

can be achieved by using a forward biased *p-n* junction (junction DLTS) [20], or optical excitation using sub-bandgap illumination (ODLTS) [117], or generation electron-hole pairs from the back of the sample via optical electrical excitation (MCTS) [118]–[120]. Compared with DLTS for majority carrier emissions, these techniques for minority carrier emission are less straightforward as the filling of minority carriers can be incomplete [114].

In DLTS spectra, defects with very different emission rates can be easily separated. However, it is possible that defects with a similar energy level, and thus a similar emission rate coexist in the measured sample. In these cases, peaks of these defects can be amalgamated into a broad peak in the measured DLTS spectrum [121]. In order to increase the energy level resolution of DLTS, Laplace-DLTS was developed which involves a Laplacian operation of the measured exponential decay to separate different decay components [113], [121], [122]. Therefore, Laplace-DLTS can have a good resolution of defect energy levels.

*(2) Comparison of IDLS with DLTS*

Compared with DLTS, the main advantage of IDLS is its high sensitivity. Defects with concentration lower than the detection limit of DLTS can still have a significant impact on the sample lifetime, and thus can be detected by lifetime spectroscopy [21]. Meanwhile, lifetime spectroscopy directly measures the defect's recombination activity, whereas it is not trivial to quantify the recombination activity of the defect from DLTS. Although, it is possible to measure the actual $E_t$ and capture cross sections, this process involves more complicated measurements and analysis (especially for measuring the minority carrier capture cross section). Finally, DLTS relies on the depletion region formed by the Schottky diode or *p-n* junction, and thus it only measures a few micrometers deep into the wafer surface. This makes DLTS sensitive to the sample preparation. It was found that hydrogen accumulated near the surface of *p*-type silicon can impede the successful detection of defects via DLTS [123], [124]. IDLS, on the contrary, can measure the defects deep into the bulk of the silicon wafer.

However, DLTS also has a few advantages over IDLS. First, different defects can be more easily separated via DLTS, especially with the development of Laplace-DLTS. For IDLS, the separation of different lifetime components can be difficult, especially if multiple defect levels with similar recombination activity coexist in the sample. Second,

the absolute value of $N_t$ and the capture cross sections can be determined in DLTS, whereas in lifetime spectroscopy only the product of $N_t$ and the capture cross sections can be determined. Third, the electrical configuration of defects can be more easily determined via DLTS, whereas it can be difficult to determine whether there are multiple single level defects or a multi-level defect from IDLS. Finally, although DLTS only measures defects within a few millimeters from the surface of the sample, this also makes DLTS capable to measure the distribution of defect across the wafer thickness.

From the comparisons above, it can be seen that these two techniques complement each other in certain ways. For example, DLTS can be used to resolve different defect levels in the sample, whereas lifetime spectroscopy can be used to extract the recombination activity of the dominant defect. In Chapter 5 of this thesis, the electrical properties of thermally activated defects in $n$-type FZ silicon are investigated using a combination of TIDLS and DLTS in order to enable a more reliable parameterization.

### 2.3.2.2 Photoluminescence imaging

Luminescence imaging is a powerful and widely used spatially resolved characterization technique for silicon material, as well as solar cells [72], [125]–[127]. Electroluminescence (EL) imaging was developed to be a fast technique to obtain spatially resolved information regarding the solar cell quality [128]. PL imaging was then proposed as a contactless approach [72]. In PL imaging, the sample is optically excited and the emitted PL from the sample is captured by an infrared camera. As can be seen from Eq. (2.1), the radiative recombination rate is positively correlated to the excess carrier concentration. Therefore, regions with higher counts in PL image have higher excess carrier concentration. Given that the illumination light intensity is uniform, regions with higher excess carrier concentration have a higher lifetime. Therefore, PL image directly reveals the electrical quality at each location of the measured sample.

The spatially resolution of typical PL imaging tools is around 50 to 200 µm [129]. This might not be as high as other spatially resolved techniques, such as electron beam induced current [130], laser beam induced current [131], or micro-PL mapping [132]. However, compared with these scanning-based techniques, PL imaging has a huge advantage in the measurement time, which enables PL imaging to be incorporated into the production line of solar cells [133].

The characteristics of PL imaging makes it an ideal technique for defects with non-uniform spatial distribution, or non-uniform materials such as mc-Si. Due to the relatively large sensor area, conventional QSSPC lifetime measurements usually has low spatial resolution. The accuracy of measured lifetime is reduced when non-uniformity of sample exists in the sensor area [134]. PL imaging can be a good solution for this problem. Procedures to calibrate PL image to carrier lifetime image has been proposed [134]–[136]. Nevertheless, accurate quantitative analysis based on PL imaging is still challenging due to the lateral carrier flow [134]. Since in conventional PL image, different locations have different carrier concentration, carriers can flow laterally from a high concentration area to a low concentration area via diffusion and drifting (if a junction exists). With the relatively high diffusion coefficient of silicon, the lateral carrier flow can occur in a distance longer than the spatial resolution of the camera [137]. This results in a reduced spatial resolution of obtained PL image [137], [138]. Moreover, this lateral carrier flow is difficult to be quantified, which makes the conversion of PL image to lifetime image inaccurate.

Although in this thesis, the defects investigated have a uniform distribution within the sensor area of the used lifetime tester, PL imaging based spatially resolved defect characterization is investigated. In order to solve the problem of lateral carrier flow in conventional PL imaging, a new approach of using non-uniform illumination to achieve PL imaging at uniform excess carrier density is proposed. The principle and some proof of concept experiments will be described in Chapter 7.

## 2.4 Chapter summary

In this chapter, the basic concepts of recombination and lifetime have been reviewed. In particular, the defect related recombination statistics were presented, which build up the base for IDLS, the main characterization technique investigated in this thesis. Previous development of IDLS has been reviewed. The important factors for reliable IDLS analysis have been discussed. Several limitations of previous IDLS analysis have been pointed out. In this thesis, improvements of IDLS techniques on two of the limitations will be made. First, the limitation of analysis of single-level defects will be extended to two-level defects. The details can be found in Chapter 4. Second, not only recombination active defects, but also trap-like defects will be investigated. The details can be found in Chapter 6.

Moreover, other defect characterization techniques used in this thesis, including DLTS and PL imaging have been reviewed. A comparison of DLTS and IDLS have been made. It seems that these two techniques are complementary of each other. Combining these two techniques can be beneficial for the characterization of defects. In Chapter 5, a concrete example of combining these two techniques will be demonstrated.

At the end, the obstacle of using PL imaging for spatially resolved quantitative defect analysis has been pointed out. A potential approach to overcome this obstacle was proposed. The details of this approach will be presented in Chapter 7.

# Chapter 3
# Injection Dependent Lifetime Measurement System

Lifetime spectroscopy is the primary characterization technique that has been developed and applied in this thesis. In the previous chapter, the principles of lifetime spectroscopy were reviewed. In this chapter, a measurement system for lifetime spectroscopy, which has been partially developed during this thesis, will be described in detail.

This chapter begins with a brief introduction of the principles of injection dependent carrier lifetime measurement. A description of the measurement system that was developed and utilized in this thesis is then provided, with a focus on the primary features of the system (in particular, the simultaneous measurement of carrier concentration from photoconductance, PC and photoluminescence, PL). Details on the calibration methods of PC and PL will also be discussed.

## 3.1 Measurement principle

Assuming a uniform distribution of carriers, the excess carrier concentration (otherwise described as excess electron concentration, $\Delta n$) in a silicon wafer follows the continuity equation below [49]:

$$\frac{d\Delta n}{dt} = G - \frac{\Delta n}{\tau(\Delta n)} \tag{3.1}$$

which we have seen in Chapter 2 [Eq. (2.8)]. The above equation can subsequently be written in the following form:

$$\tau(\Delta n) = \frac{\Delta n}{G - \dfrac{d\Delta n}{dt}} \tag{3.2}$$

Therefore, the excess carrier lifetime can be obtained by measuring the time dependent $\Delta n$ and the generation rate in the sample. In common lifetime measurements of silicon wafers, the generation of excess carriers is achieved by illumination with the light of a photon energy higher than the silicon bandgap. Since Eq. (3.2) assumes uniform excess

carrier distribution, it is also preferable to use longer wavelength photons that are absorbed in the bulk silicon material rather than at the surface (as would be the case for short wavelength photons).

For a given illumination spectrum, the generation rate of excess carriers in silicon should be proportional to the photon flux of the light source. Therefore, $G$ can be obtained by measuring the intensity of the excitation light. The calibration of $G$ from the measured excitation light intensity will be discussed in more details in Section 3.3.

The measurement of $\Delta n$ can be achieved by measuring the PC or PL of the sample. The calibration of $\Delta n$ from the measured PC and PL will be discussed in more detail in Section 3.4.

If an excitation light with constant illumination intensity is used, $\Delta n$ will also reach a constant value after a certain period of time. In this case, Eq. (3.2) simplifies to:

$$\tau(\Delta n) = \frac{\Delta n}{G} \tag{3.3}$$

This measurement condition is referred to as the steady-state (SS) condition.

When a non-steady-state excitation light decays with a rate such that $G$ is much larger than the $d\Delta n/dt$ term, Eq. (3.3) is also valid. This measurement condition is referred to as the quasi-steady-state (QSS) condition. QSS condition requires the carrier lifetime to be much smaller than the decay time constant of the excitation light. In practice, the more generalized Eq. (3.2) is always used when a slowly decaying excitation light is used to ensure a correct calculation of lifetime.

If the excitation light on the sample is switched off abruptly such that $G = 0$ during the decay of $\Delta n$, Eq. (3.2) can be simplified to:

$$\tau(\Delta n) = \frac{\Delta n}{-\dfrac{d\Delta n}{dt}} \tag{3.4}$$

Practically, it is difficult to switch off the excitation light intensity perfectly abruptly. Nevertheless, as long as the excitation light decays at a sufficient fast rate such that $G$ is negligible compared with the $d\Delta n/dt$ term, Eq. (3.4) is valid. This measurement condition is called transient condition.

In most cases, it is not preferable to measure the lifetime in the SS condition, since steady state illumination can heat up the sample. Furthermore, one measurement can only obtain the lifetime at one injection level. However, for lifetime spectroscopy (as well as many other characterization techniques based on lifetime), it is important to measure the lifetime at various injection levels. Therefore, the transient and QSS conditions are more favorable for lifetime characterization. In the most widely used commercial lifetime tester in the silicon PV community (Sinton Instruments WCT-120 [139]), a xenon photograph flash is used as the excitation light source. By measuring $\Delta n$ as well as the light intensity during the decay of the flash, the lifetime of the sample at a range of injection levels can be obtained conveniently. The short illumination time of the flash also reduces the risk of heating up the sample during the measurement.

Compared to the QSS conditions, transient conditions are even more favorable as there is no need to measure the generation rate. This reduces the uncertainty in the measured lifetime [140]. The obstacle to transient measurements mainly comes from practical issues when measuring low lifetime samples. In the transient condition, the decay rate of $\Delta n$ is faster for samples with lower lifetimes; therefore, an excitation light source with a faster decay is required to fulfill the assumption of Eq. (3.4) when measuring this type of samples. Furthermore, the faster decay of $\Delta n$ also requires faster response and acquisition of data by the measurement system. As a result, for samples with higher lifetimes (above 200 µs in practice), it is preferable to use the transient measurement condition, whereas for samples with lower lifetimes, QSS measurements are used.

## 3.2 System description

The measurement of excess carrier lifetime in silicon can be dated back to the 1950s [73], [141], [142]. However, it was the development of the flash-based lifetime tester by Sinton Instruments [139] that simplified the measurement process to make it a routine characterization tool for silicon lifetime analysis. As mentioned previously, the WCT-120 lifetime tester of Sinton Instruments uses a xenon photograph flash as the excitation light source [143]. The decay rate of the flash can be adjusted so both transient and QSS conditions can be achieved. A long pass filter is used to reduce the high energy part of the xenon flash spectra. This creates a more uniform generation profile in the measured sample, and thus satisfying the requirements of Eq. (3.1). A shunted concentrating solar

cell is used to measure the photon flux of the flash. The system extracts $\Delta n$ by measuring the PC of the sample using an inductively-coupled coil [83].

In this thesis, a modified lifetime tester based on the WCT-120 is used. A schematic of the measurement system is shown in Fig. 3.1 below. The four main modifications are: (1) the inclusion of a cryostat to control the sample temperature; (2) the addition of a photodiode to measure $\Delta n$ from the PL of the sample; (3) the incorporation of an 808 nm laser and an 810 nm light emitting diode (LED) as two alternative excitation light sources in addition to the original xenon flash; and (4) a homemade software which enables more freedom to control the system and adoption of more recent semiconductor models for the lifetime calculation.
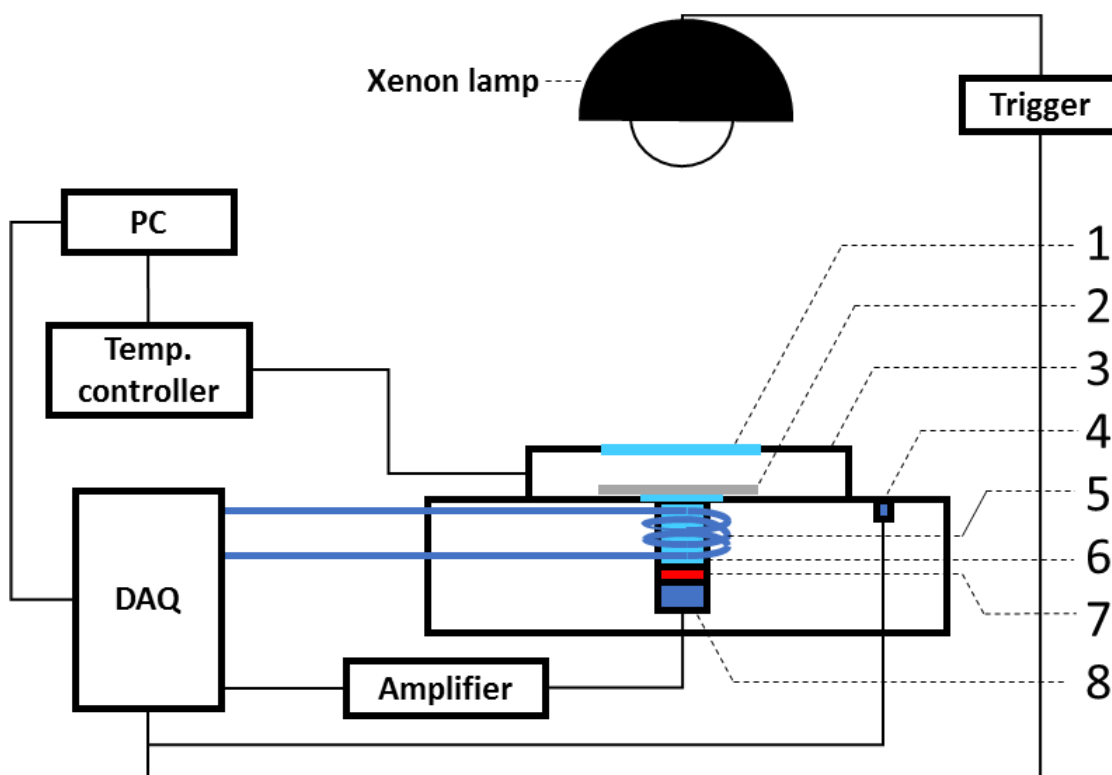


**Fig. 3.1** Schematic of the modified lifetime tester with: 1. quartz window; 2. sample; 3. cryostat; 4. reference solar cell for measuring photon flux; 5. inductively-coupled coil for PC measurements; 6. quartz tube; 7. long pass filter; and 8. silicon photodiode for PL measurements. The sketch of the alternative light sources (laser and LED) is shown in Fig. 3.4, but omitted from this figure for clearance.

### *(1) Temperature dependent measurements*

The sample sits in a temperature controlled cryostat (Instec customized unit [144]) with a transparent quartz top window which allows external optical excitation. The

temperature range of the cryostat is 80 K to 673 K. The cryostat is designed to have a spatial temperature non-uniformity within 0.1 K.

Due to the thermal resistance between the sample and the stage, there is a deviation between the actual sample temperature and the stage set temperature. Therefore, for temperature-dependent lifetime measurements, it is necessary to calibrate the actual sample temperature to the stage set temperature. For calibration, two to three K-type bare wire thermocouples (OMEGA chal-005) are attached to a calibration sample that has the same thickness and surface texture to that of the measured sample. The stage temperature is then set to various values and the sample temperatures are measured with the thermocouples after stabilization.
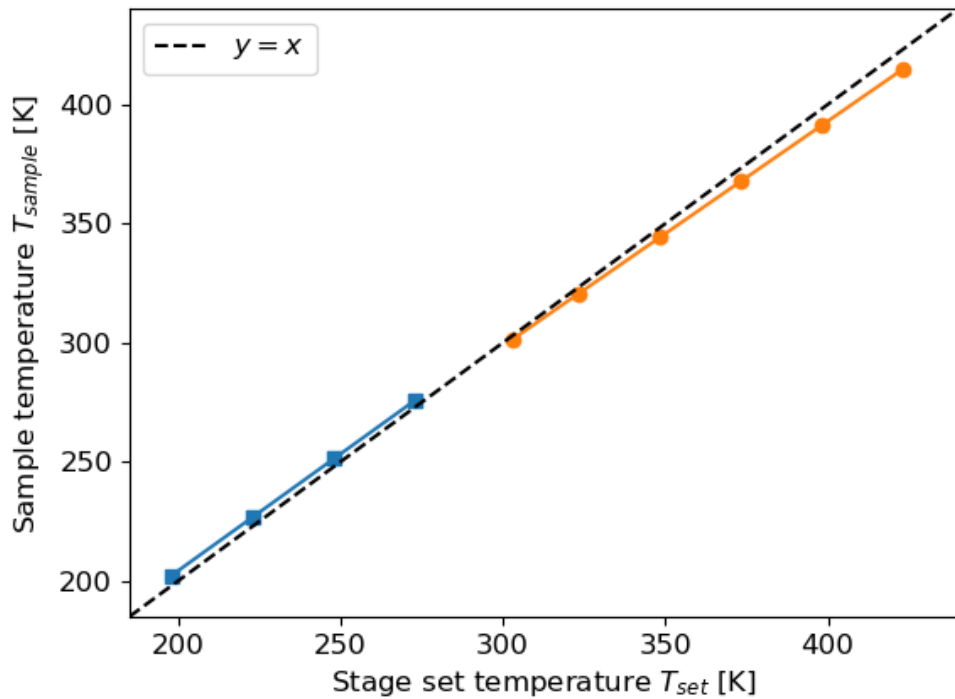


**Fig. 3.2** The actual sample temperature $T_{sample}$ as a function of $T_{set}$ for a 190 µm thick, double side polished silicon wafer. $T_{sample}$ is measured with two K-type thermocouples attached to the sample (average value). The blue and orange solid lines indicate a linear fit to the data at temperature ranges above and below room temperature, respectively.

The temperature calibration graph for a typical silicon wafer (190 µm thickness, double side polished surface) is shown in Fig. 3.2. Whilst the actual sample temperature follows a linear relationship with the stage set temperature, the deviation between the sample temperature and the set temperature increases as the temperature departs from room temperature (in both directions; low and high temperatures). Using this temperature

calibration graph, the actual sample temperature for a given stage set temperature can be determined. In most of the lifetime spectroscopy studies presented in this thesis, the temperature range for measurements is between 223 K and 423 K. From the calibration data shown in Fig. 3.2, in this temperature range there is a maximum 9 K deviation between the stage set temperature and actual sample temperature. In the analysis of temperature-dependent lifetime measurement data, the calibrated sample temperature is always used and not the stage set temperature. It should be noted that the temperature measured by the thermocouple can also deviate from the actual sample temperature, however, this deviation is expected to be less significant compared to the deviation of the stage set temperature from the actual sample temperature.

*(2) PL based lifetime measurements*

In addition to using the PC coil to measure $\Delta n$, this modified system also measures the $\Delta n$ using the PL intensity emitted by the sample. As can be seen in Fig. 3.1, a quartz rear window is placed in the cryostat and beneath this rear window the PC coil is wound around a transparent quartz tube. The PL emission is directed by the quartz tube to a silicon photodiode located at the base of the tube. A transimpedance preamplifier (Femto DLPCA-200) converts the photodiode current into a voltage signal which is recorded by a data acquisition card (DAQ, National Instrument NI 6356). A long pass filter is placed in front of the photodiode to block the illumination light. It should be noted that when measuring PL with the xenon flash, the long pass filter normally positioned beneath the flash, is replaced with a short pass filter so that the long wavelength light from the flash is not detected by the photodiode. However, when a short pass filter is used with the flash, more excess carriers will be generated closer to the front surface of the sample, which can lead to a non-uniform excess carrier profile if the sample has a low effective lifetime. Since both the PC coil and the PL photodiode measure an average carrier concentration over the sample thickness, this non-uniform excess carrier profile can lead to errors in the measured excess carrier concentration as well as the measured lifetime [145], [146]. In this thesis, when the flash with short pass filter is used for PL lifetime measurements, a PC based lifetime measurement with the flash and the long pass filter will also be made and compared to the lifetime measured by PL. In this way, the impact of the non-uniform carrier profile on the lifetime measurements can be evaluated.

*(3) Additional light sources*

Apart from the conventional xenon flash, the modified system also incorporates an 808 nm laser (Lumics LUD0808D320-D70AP) and 810 nm LED (Roithner LaserTechnik LED810-66-60) as alternative light sources. In Fig. 3.3, the spectra of the LED and the laser are overlaid with the spectra of the xenon flash and the typical PL emission spectrum of a silicon wafer. The laser and LED have much narrower spectra, and thus can be more effectively filtered out than the xenon flash light.
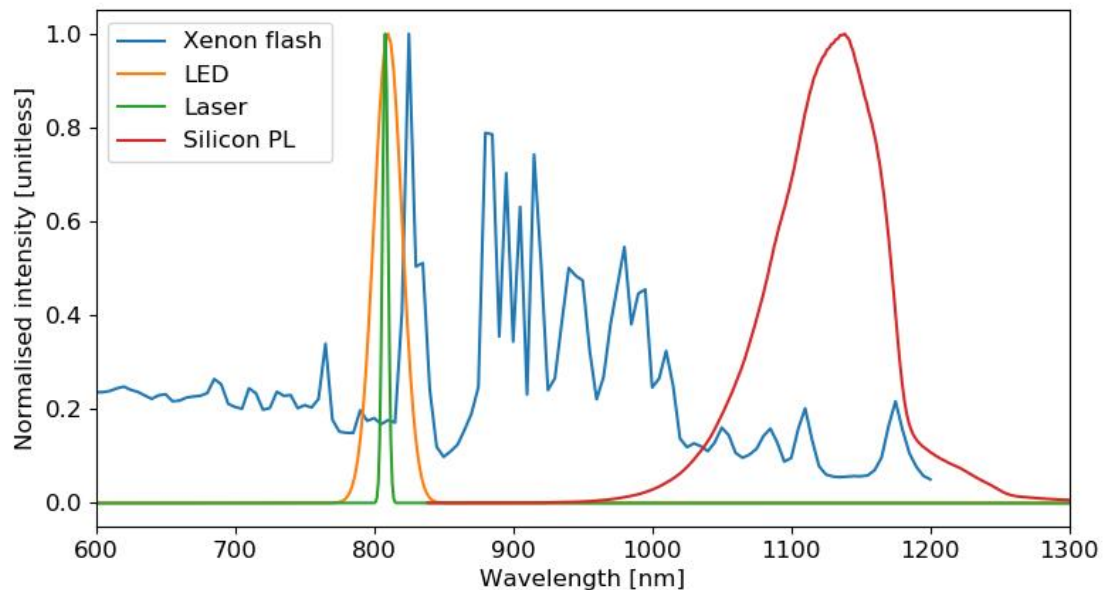


**Fig. 3.3** Spectra of the xenon flash (data from [147]), LED and laser used in the measurement system, as well as the PL emitted from a typical silicon wafer.

Compared to the xenon flash, the laser and LED allow higher flexibility to modulate the generation rate as a function of time. The xenon flash is usually used only in two modes: a relatively slow decay mode (1/1 mode, with a decay time constant of around 2.3 ms) and a faster decay mode (1/64, with a decay time constant of around 50 µs). The 1/1 mode is usually used for measuring samples with a lifetime lower than 200 µs in QSS conditions. The 1/64 mode is usually used for measuring samples with a lifetime higher than 200 µs in transient conditions. For the LED and laser, arbitrary waveform for measurements can be chosen. For example, a square wave with sharp cutoff can be used for transient measurements. One can also use a sine wave and adjust the period of the sine wave for QSS measurements. This capability is also beneficial for the calibration of PL, which is discussed in more detail in Section 3.4.2. Furthermore, the xenon flash takes a relatively long time to be charged after a measurement (6 s for 1/1 mode and 0.3 s for

1/64 mode); therefore, it is more convenient to repeat measurements using the laser or LED. Repeated measurements help to increase the signal to noise ratio, and consequently can improve the quality of lifetime measurements at low injections. Since the highest achievable light intensity of the laser and LED is around 10 suns, whereas, the highest light intensity of the flash is approximately 50 suns, the xenon flash has been kept in this modified system for high injection measurements.

A sketch of the optics for LED is shown in Fig. 3.4. The optics for the laser is similar. For the LED and laser, a separate silicon photodiode is used to measure the generation photon flux instead of the reference solar cell. A beam splitter guides a small fraction of the LED or laser light to the silicon photodiode, while the rest of the illumination light is directed at the sample being measured. The output current of the photodiode is then converted to a voltage signal by a transimpedance preamplifier and recorded by the DAQ.
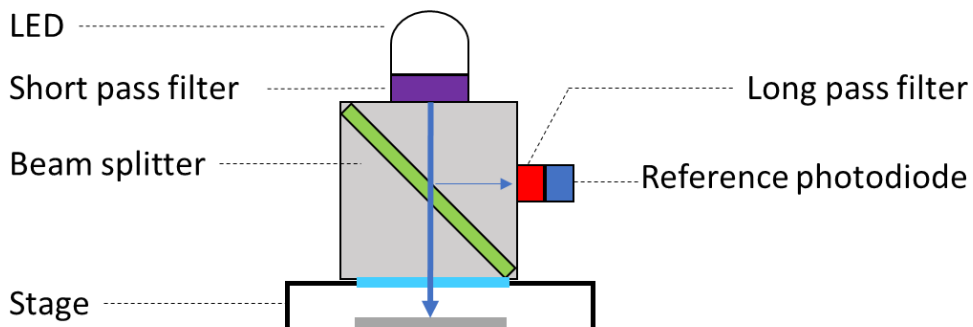


**Fig. 3.4** Sketch of the optical path of the LED. The other parts of the system are shown in Fig. 3.1 and omitted from this figure for clearance. The optical path for the laser is similar to the LED.

*(4) Customized software*

The system is controlled by a customized software which allows more freedom to adjust the measurement parameters compared to the standard WCT-120 lifetime tester. The sampling rate and acquisition time can be adjusted with more flexibility, which is essential for the PC measurements of traps in Chapter 6. Meanwhile, compared with the standard WCT-120 lifetime tester, the customized software also adopted more recent semiconductor models (such as mobility models, intrinsic carrier concentration models) for the calculation of lifetime.

## 3.3 Calibration of generation rate

To calculate the lifetime from Eq. (3.2), it is important to know $G$ accurately. The output of the reference solar cell (for xenon flash) or the output of the reference silicon photodiode (for LED and laser) is measured directly, however, these outputs need to be converted to the generation rate within the studied sample.

The reference solar cell for the flash is a shunted concentrated solar cell [143]. Its output voltage is linear with the photon flux of the flash. For the LED and laser, a reference silicon photodiode is connected to a transimpedance pre-amplifier such that it operates under short circuit condition. The system is designed such that even at the highest intensity of LED/laser, the short circuit current of the reference photodiode is linearly correlated with the photon flux. Therefore, the output voltage of the preamplifier also has a linear relationship with the photon flux of the illumination source. For the flash, LED and laser, the relationship between the illumination photon flux at the sample surface, $\Phi$, and the output voltage of the reference cell/photodiode, $V_{ref}$, can be written as:

$$\Phi = C_{sys} \cdot V_{ref} \tag{3.5}$$

where $C_{sys}$ is a calibration factor that depends on the optical path and the detection system.

Within the sample, $G$ should also be proportional to the illumination photon flux. Thus, it can be calculated according to Eq. (3.6):

$$G = C_{samp} \cdot \Phi = C_{samp} \cdot C_{sys} \cdot V_{ref} \tag{3.6}$$

where $C_{samp}$ is another calibration factor that depends on the light source as well as the optical properties of the sample being measured.

### (1) Determination of $C_{sys}$

For the xenon flash, the system-dependent calibration factor $C_{sys}$ is calibrated and provided by Sinton Instruments. For the LED and laser, $C_{sys}$ is obtained in a separate calibration measurement by directly measuring the photon flux in the sample plane with another photodiode with known external quantum efficiency:

$$\Phi = \frac{V_{cali}}{Gain \cdot q \cdot A \cdot EQE(\lambda)} \tag{3.7}$$

where $V_{cali}$ is the output voltage of the preamplifier connected to the calibration photodiode, $Gain$ is the amplification factor of the preamplifier, $q$ is the elementary charge, $A$ is the effective area of the calibration photodiode and $EQE(\lambda)$ is the external quantum efficiency of the photodiode at wavelength $\lambda$ (808 nm for the laser and 810 nm for the LED).

By changing the LED/laser light intensity and measuring $V_{ref}$ and $V_{cali}$ simultaneously, a linear plot is obtained, as shown in Fig. 3.5. It should be noted that for the calibration, the LED light intensity is set low enough so that the short circuit current of the calibration photodiode is in its linear response regime. The system-dependent calibration factor $C_{sys}$ for the LED could then be easily extracted from the slope of a linear fit of the data in Fig. 3.5. The calibration factor $C_{sys}$ of the laser is obtained in a similar method and thus is not repeated here.
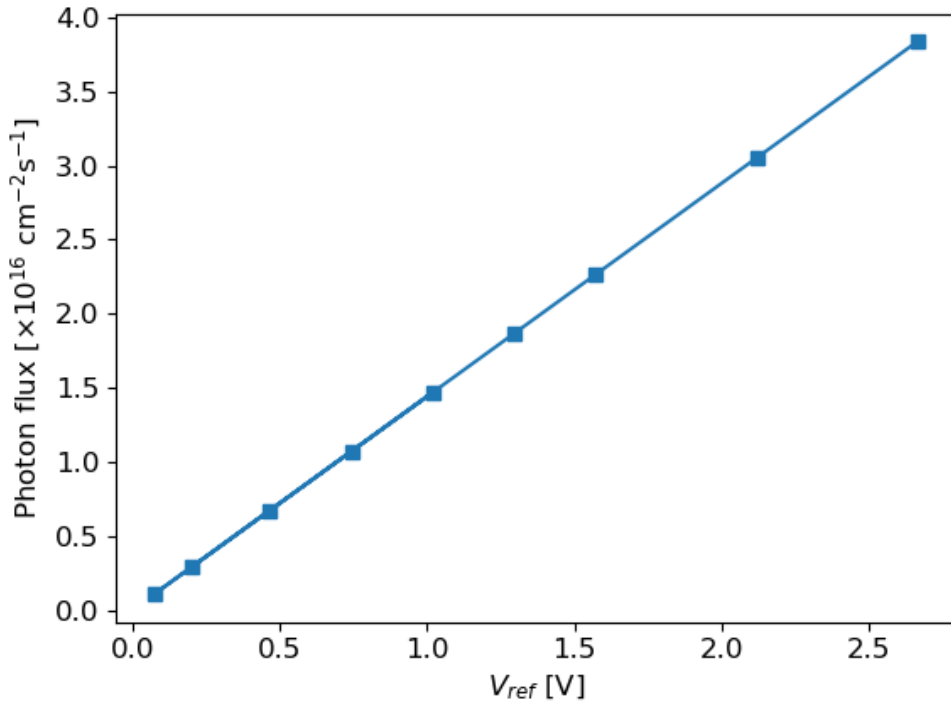


**Fig. 3.5** The measured photon flux at the sample plane vs the $V_{ref}$ for the LED in our measurement system. The solid line indicates the linear fit of the data. The photon flux is calculated from $V_{cali}$ using Eq. (3.7).

## (2) Determination of $C_{samp}$

For the flash light, the sample-dependent calibration factor $C_{samp}$ can be obtained by simulating the generation rate in the sample under the flash illumination intensity [83].

Alternatively, $C_{samp}$ for silicon samples with various bulk and dielectric coating layer thicknesses and various coating layer refractive indices have been provided by Sinton Instruments in lookup tables [143].

For the LED and laser which have narrower spectrum compared to the flash, the determination of $C_{samp}$ is easier. The absorption depth of 810 nm wavelength light in silicon is 13 µm. For typical silicon wafers with a thickness around 170 µm, most of the 810 nm light will either be reflected or absorbed (transmission is negligible). Since the LED and laser have very narrow spectra, $C_{samp}$ is equivalent to $[1 - R(\lambda)]/W$ where $R(\lambda)$ is the reflectance of the sample at $\lambda$ (808 nm for the laser and 810 nm for the LED), and $W$ is the thickness of the sample. Therefore, $C_{samp}$ can be determined from the reflectance measurement of the sample at a single wavelength.

The determination of $C_{samp}$ for the flash based measurements can suffer from more uncertainties compared to the LED/laser based measurements, as it requires knowledge of the spectrum of the flash light and the absorption of the sample over a wide wavelength range.

In this thesis, an alternative calibration method is used for the flash-based measurements. The method is based on matching the lifetime measured under transient and QSS conditions [148]–[150]. As can be seen from Eqs. (3.4) and (3.2), the lifetime measured under transient conditions is independent of $G$, whereas the lifetime measured under QSS conditions requires knowledge of $G$. Therefore, by adjusting $C_{samp}$ until the QSS lifetime curve matches the transient lifetime curve, the correct $C_{samp}$ can be determined. In this method, there is no need to measure the spectrum of the flash nor the reflectance of the sample.

Another advantage of this method is that it suppresses the uncertainty in the determination of $C_{sys}$. Essentially, this method determines the product $C_{samp} \cdot C_{sys}$ in Eq. (3.6) directly. Even if $C_{sys}$ is not accurately determined, the $C_{samp}$ obtained by this method can compensate the error in $C_{sys}$.

However, as the transient measurement is usually only possible for relatively high lifetime samples, for samples with lower lifetimes a control wafer with the same optical properties (same thickness, same surface texture, same coated dielectric layer) but higher effective lifetime is required. It should also be noticed that this approach of calibration

relies on the assumption that the lifetime measured in transient condition equals to the lifetime measured in QSS condition. This assumption might not be valid if the photo-generated carrier has a non-uniform profile across the sample thickness due to, for example, strong surface recombination and the usage of short wavelength excitation light [151]. In this case, the lifetime measured at QSS condition is closer to the bulk minority carrier lifetime than the lifetime measured at transient condition [151]. In this thesis, when using this method for calibration, the transient lifetime is matched with QSS lifetime for all the measured injection range instead of a single injection level. If the transient lifetime curve cannot be well matched to the QSS lifetime, QSS lifetime is used. The calibration for the flash in this case is done by matching the lifetime curve with the one measured with LED/laser in QSS condition[1].

## 3.4 Calibration of excess carrier concentration

In order to extract injection-dependent lifetime, it is essential to know the exact excess carrier concentration. As mentioned previously, $\Delta n$ in this modified lifetime system is measured by either a PC coil or a PL photodiode connected to a current preamplifier. Since the output from the PC coil and the current preamplifier is a voltage signal, it is essential to calibrate them to the $\Delta n$.

### *3.4.1 Calibration of Photoconductance*

The excess carrier concentration can be determined by measuring the conductance of the silicon wafer using the following relationship:

$$\Delta S = qW(\mu_n \Delta n + \mu_p \Delta p) \tag{3.8}$$

where $\Delta S$ is the PC of the sample, defined as the deviation of sample conductance under illumination from the sample's dark conductance $S_{dark}$, $q$ is the elementary charge, $\mu_n$ and $\mu_p$ are the mobility for electrons and holes, respectively, and $\Delta n$ and $\Delta p$ are the excess electron concentration and excess hole concentration, respectively.

Assuming $\Delta n = \Delta p$, then the excess carrier concentration can be calculated as:

---

[1] The deviation of the QSS lifetime and transient lifetime can also be caused by other reasons. For example, inaccurate doping or mobility model [283], or minority carrier traps[70] for the PC based measurements. Therefore, when a mismatch of QSS lifetime and transient lifetime is observed, the reason for this deviation will be firstly investigated and proper solutions will then be adopted.

$$\Delta n = \Delta p = \frac{\Delta S}{qW(\mu_n + \mu_p)} \qquad\qquad (3.9)$$

The sample thickness can be measured directly and the term $(\mu_n + \mu_p)$ can be calculated using existing mobility models in literature. Thus, $\Delta n$ can be calculated from the measured photoconductance. It is noted that the mobility is also a function of $\Delta n$, and thus an iterative procedure is required for the calculation [143]. Throughout this work, the mobility models developed by Klaassen *et al.* [152], [153] for non-compensated silicon and Schindler *et al.* [154] for compensated silicon are used. Both models are the latest available mobility models, taking the temperature dependency into consideration.

The assumption of $\Delta n = \Delta p$ is valid when the excess carrier concentration in the conduction and valence bands is dominant compared to the excess carrier concentration in any defect levels. In most cases for silicon, this assumption is valid. However, when minority carrier traps are present in the sample, this assumption can become invalid. In this case, the apparent carrier concentration calculated using Eq. (3.9) will be higher than the true minority carrier concentration and the calculated apparent lifetime will be higher than the true minority carrier lifetime. This artefact is a disadvantage of PC-based lifetime measurements. However, this also makes PC a good technique for the investigation of such traps, which will be discussed in more detail in Chapter 5.

PC-based lifetime measurements can suffer from another artefact caused by the so-called "depletion region modulation" phenomenon [110]. DRM occurs in silicon wafers with a *p-n* junction or an inversion layer induced by the stored charge within a surface dielectric layer. During illumination, excess carrier concentration can build up at the edge of the depletion region, causing a reduction of the depletion region width (this is the origin of the name DRM). Since the PC coil measures the thickness-averaged conductance of the sample, this additional excess carrier concentration at the depletion region edge can lead to artificially high apparent excess carrier concentrations at low injection levels. Therefore, similar to minority carrier traps, DRM can also cause artificially high lifetime in PC-based measurements. To avoid DRM, it is preferable to avoid measuring samples with a *p-n* junction (if not investigating the quality of the junction) or inversion layer. The latter can be done by choosing suitable surface passivation layers according to the sample type (for example, using dielectric layer with positive fixed charge for *n*-type silicon).

Equation (3.9) shows that excess carrier concentration can be calculated from photoconductance. The physical principles of photoconductance measurements and calibration procedures are now discussed. As shown in Fig. 3.6, a radio frequency (RF) alternating current (AC) through the coil beneath the silicon wafer generates a magnetic field. This magnetic field induces eddy currents in the silicon wafer which create an opposing magnetic field that increases the impedance of the PC coil. The directly measured PC coil voltage is proportional to the real part of the coil impedance, which is correlated with the sample conductance. Further details on the PC coil measurement can be found in Refs. [155], [156].
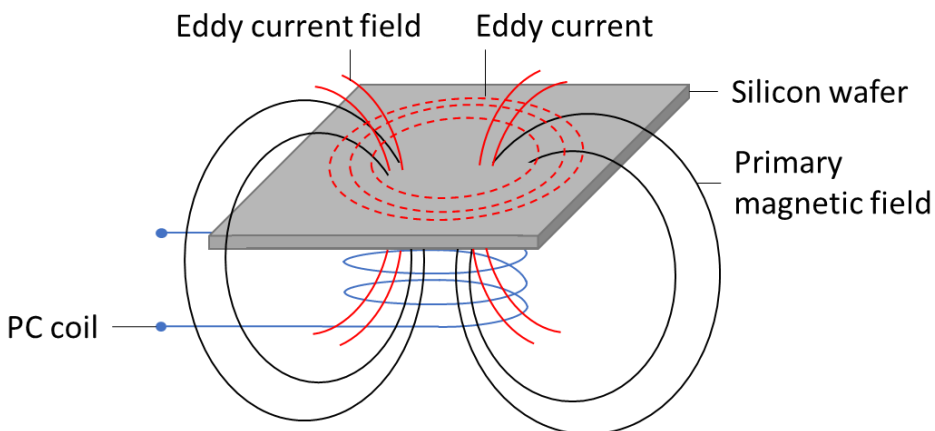


**Fig. 3.6** A schematic of the PC coil working principle. The eddy currents and magnetic fields in the sketch is not exact and for demonstration only. As the PC coil is stimulated with RF AC, the direction of the magnetic fields and eddy currents are omitted.

In order to measure the PC of the sample, a correlation between the sample conductance and PC coil output voltage must be established. This is achieved by measuring the PC coil output voltage for a set of calibration samples with known dark conductance $S_{dark}$, which are measured with four-point probe (4PP). For the modified system used in this thesis, a set of five calibration wafers with the same thickness and various resistivities are used to provide a range of conductance values. The total conductance $S$, which equals the sum of the sample conductance $S_{sample}$ and air conductance $S_{air}$, follows a quadratic relationship with the output voltage of the PC coil $V_{PC}$ [157]:

$$S = aV_{PC}^2 + bV_{PC} + c \tag{3.10}$$

where $a$, $b$ and $c$ are calibration constants. $S_{sample}$ equals the sum of $S_{dark}$ and $\Delta S$. Assuming $S_{air}$ does not change during the measurement, the PC can be obtained from the

measured PC coil voltage under illumination $V_{PC,light}$ and the measured PC coil voltage in the dark $V_{PC,dark}$:

$$\Delta S = S_{sample} - S_{dark} = a(V_{PC,light}^2 - V_{PC,dark}^2) + b(V_{PC,light} - V_{PC,dark}) \quad (3.11)$$

Generally, $V_{PC,dark}$ is measured directly before the excitation light is switched on. As the typical measurement time is a few milliseconds, $S_{air}$ can be assumed constant during the measurement time. Therefore, only $a$ and $b$ are required in order to calculate the PC. Similarly, when measuring the calibration wafers in the dark, the dark conductance of the calibration wafer and the measured PC coil voltage should follow:

$$S_{dark} = S - S_{air} = a(V_{PC,cali}^2 - V_{PC,air}^2) + b(V_{PC,cali} - V_{PC,air}) \quad (3.12)$$

where $V_{PC,cali}$ is the coil voltage when measuring the calibration wafer in the dark and $V_{PC,air}$ is the coil voltage when measuring only the air (no sample above the coil). Theoretically, only $V_{PC,cali}$ needs to be measured for the set of calibration wafers and the calibration constants $a$ and $b$ can then be extracted from a quadratic fit (as the constant $c$ is not required for calculating $\Delta S$):

$$S_{dark} = aV_{PC,cali}^2 + bV_{PC,cali} + c' \quad (3.13)$$

Note that in this quadratic fit, the obtained constant term $c' = (-aV_{PC,air}^2 - bV_{PC,air})$ is different from the calibration constant $c$ in Eq. (3.10). Although neither $c$ or $c'$ is needed for calculating $\Delta S$, the air voltage $V_{PC,air}$ is still measured as part of the calibration procedure used in this work. A comparison of the calculated $c'$ with the fitted $c'$ is utilized as an additional confirmation of the correctness of the calibration procedure.

Measurements of the calibration samples in the modified lifetime system at 303 K is shown in Fig. 3.7. $V_{PC,cali}$ is measured and averaged over 10 mins after the stage temperature stabilizes. The linear nature of the quadratic fit indicates that the linear constant $b$ has a larger impact on the voltage to conductance conversion than the quadratic constant $a$. The air voltage $V_{PC,air}$ was also measured to be 2.03 V at 30 °C. As a result, the calculated $c' = (-aV_{PC,air}^2 - bV_{PC,air})$ was determined to be 0.124, a 5.5% relative deviation from the fitted $c'$ (0.132).
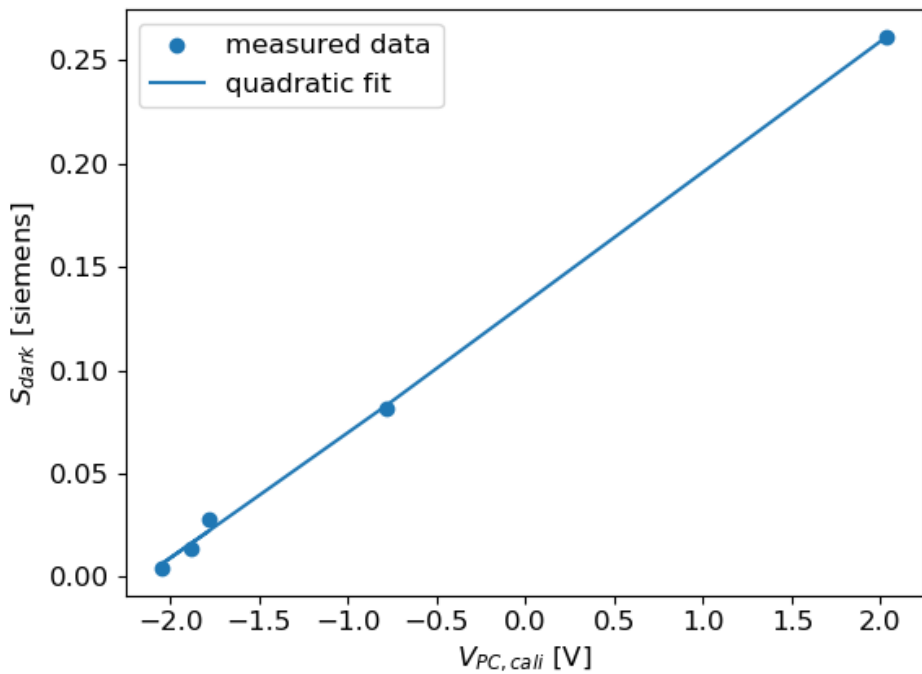
**Fig. 3.7** Measured $V_{PC,cali}$ from the PC coil plotted against known $S_{dark}$ for the five calibration wafers. The measurement was performed on the modified lifetime system at 303 K. The solid line indicates a quadratic fit of the measured data.
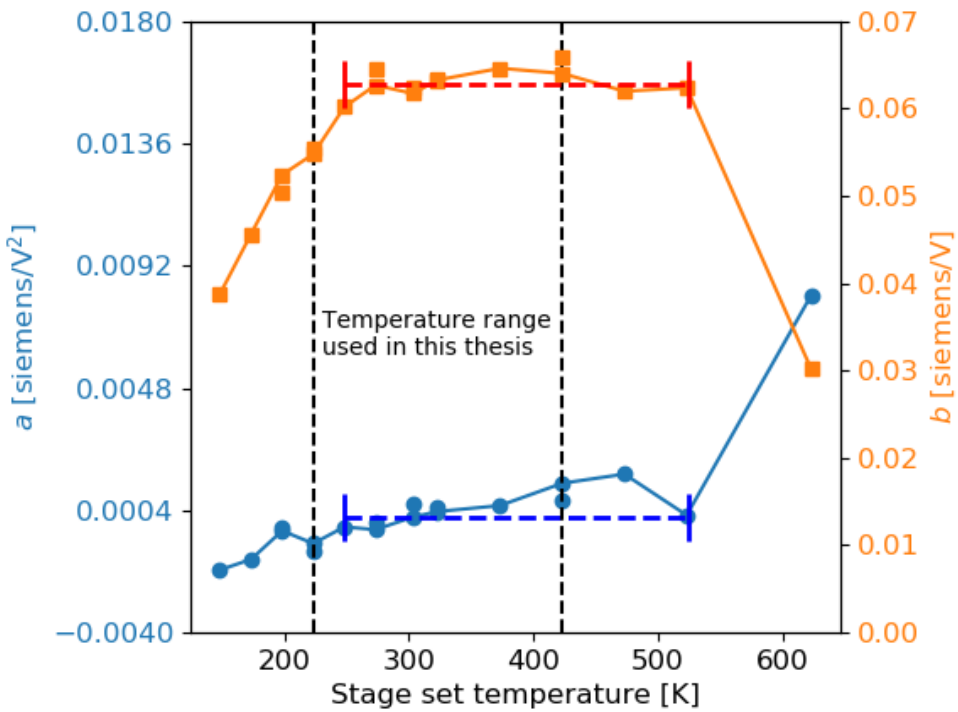


**Fig. 3.8** Calculated $a$ (left) and $b$ (right) over a stage temperature range from 148 K to 623 K. The temperature range used in this thesis has also been identified. The $a$ and $b$ are extracted using all the calibration data from 248 K to 525 K via Fig. 3.9 are indicated by the blue and red dashed lines respectively.

The same calibration procedure is then applied over the temperature range from 148 K to 623 K. The actual sample temperature is corrected using the procedure described in Section 3.2. The calibration factors $a$ and $b$ are obtained at each temperature, as shown in Fig. 3.8.

As can be seen, $a$ and $b$ are relatively stable from 248 K to 525 K. Outside this temperature range, they have a strong temperature dependence. This change in the calibration constants could be the result of: (a) the impact of stage temperature on the temperature of the PC coil, and thus the sensitivity of the coil changes, and (b) invalidity of the mobility or dopant ionization models for the calculation of the conductance of the calibration wafers at these temperatures. The used mobility model (Klaassen *et al.* [153]) is parameterized from 200 K to 500 K and the used dopant ionization model (Altermatt *et al.* [158]) is parameterized from 30 K to 300 K. Therefore, the calculated conductance of the calibration wafers might not be accurate above 500 K or below 200 K. In most of the lifetime spectroscopy measurements in this thesis, the temperature range is between 223 K and 423 K. Therefore, this uncertainty is minimized.
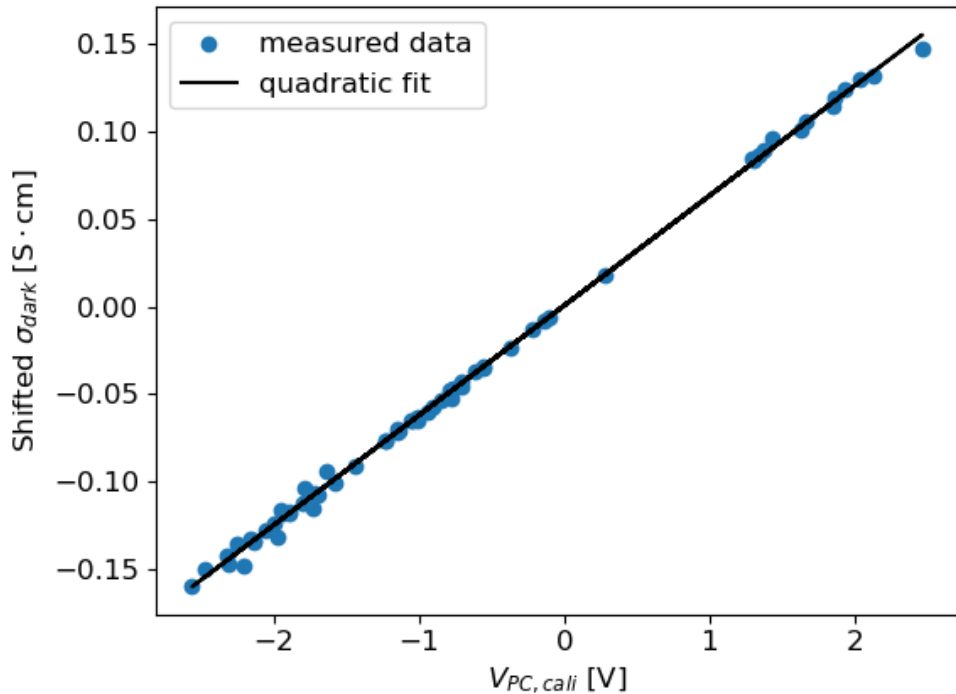


**Fig. 3.9** Measured $V_{PC,cali}$ from the PC coil plotted against shifted $S_{dark}$ for the five calibration wafers measured in the temperature range 248 K to 525 K. $S_{dark}$ is shifted by the fitted $c'$ at each temperature. The solid line indicates a quadratic fit of the measured data.

Given the apparent stability of $a$ and $b$ in the temperature range 248 K to 525 K, the accuracy of $a$ and $b$ can potentially be improved by performing the quadratic fit on measured data from all temperatures (within this range) at the same time. The measured data for all calibration samples in this temperature range are plotted in Fig. 3.9. Because $V_{PC,air}$ at each temperature is different, $c'$ is also different. Therefore, in Fig. 3.9, $S_{dark}$ is shifted by the fitted $c'$ at each temperature. This does not impact $a$ or $b$. A pair of unified $a$ and $b$ can then be obtained by fitting all the data together. The extracted $a$ and $b$ are also plotted in Fig. 3.8. When comparing the unified calibration constants with the calibration constants obtained at each temperature, it was found that the difference in the calculated excess carrier density is less than 6%. Therefore, in this temperature range (248 K to 525 K), the unified calibration constants could be used for the voltage to conductance conversion.

It is important to note that the PC coil sensor measures the conductance in the sample plane over a certain area. For a standard Sinton WCT-120 system, the sensor area is a circle of 40 mm diameter and for the modified system used in this work, the sensor area is a circle of 28 mm diameter. Within this sensor area, the coil has a different sensitivity in the radial direction. The calibration described above applies to samples larger than the sensor area. For samples with an area smaller than the sensor area, additional calibration of the coil's radial sensitivity is required. Methods for such calibration can be found in Refs. [135], [136], [159]. The Cz wafers used for the investigation of traps in Chapter 6 are circular with diameters of around 25 mm. During the lifetime measurement of these samples, additional consideration of the radial sensitivity of the coil is required. The details of the calibration process and measurement results of the coil radial sensitivity can be found in Appendix A.

For samples larger than the coil sensor area, the measured photoconductance is an average value over the sensor area weighted by the radial sensitivity of the coil. If the sample has non-uniformity such that there is non-uniform distribution of $\Delta n$ within the sensor area, the measured lifetime might be different to the actual lifetime of a smaller region within the sensor area. In the majority parts if this thesis, the measured samples are found to be uniform via PL imaging, and consequently this non-uniformity issue does not impact the PC-based lifetime measurements.

### *3.4.2 Calibration of Photoluminescence*

The excess carrier concentration can also be measured by measuring the PL emitted by the silicon wafer using the following relationship [47]:

$$\Phi_{PL} = F_{samp}B(np - n_i^2) = F_{samp}B[(n_0 + \Delta n)(p_0 + \Delta p) - n_i^2] \qquad (3.14)$$

where $\Phi_{PL}$ is the emitted PL photon flux, $F_{samp}$ is a sample dependent factor describing the probability that a PL photon can escape the sample. Since the doping concentration in most typical silicon samples is three to four orders of magnitude higher than any defect concentration, the excess carrier concentration in the defect levels is considered negligible compared to the majority carrier concentration. For *p*-type silicon, Eq. (3.14) can be safely rewrite as:

$$\Phi_{PL} = F_{samp}B[(n_0 + \Delta n)(p_0 + \Delta n) - n_i^2] \qquad (3.15)$$

As a result, PL is hardly impacted by minority carrier trapping [23], [107]. This is one of the advantages of PL-based lifetime measurements compared to PC. It has also been demonstrated that PL is not impacted by DRM as it essentially directly measures the quasi-fermi level splitting in the sample [107]. Since $n_0 \ll p_0$ in *p*-type silicon, and according to the mass of law $n_0 p_0 = n_i^2$, Eq. (3.15) can be further simplified to:

$$\Phi_{PL} = F_{samp}B(p_0 + \Delta n)\Delta n \qquad (3.16)$$

A similar calculation can be done for *n*-type silicon or compensated silicon:

$$\Phi_{PL} = F_{samp}B(N_{maj,0} + \Delta N_{minor})\Delta N_{minor} \qquad (3.17)$$

where $N_{maj,0}$ is the majority carrier concentration in thermal equilibrium and $\Delta N_{minor}$ is the excess minority carrier concentration. The simplification of Eq. (3.15) to Eq. (3.16) is valid for most silicon wafers used for PV applications.

The voltage output of the current pre-amplifier connected to the PL photodiode $V_{PL}$ is proportional to $\Phi_{PL}$ thus:

$$V_{PL} = F_{sys}\Phi_{PL} = F_{sys}F_{samp}B(N_{maj,0} + \Delta N_{minor})\Delta N_{minor} \qquad (3.18)$$

where $F_{sys}$ is a factor that depends on the PL detection system. For PL-based measurements, usually the product of $F_{sys}$ and $F_{samp}$ is used, defined as a single calibration factor $F_{PL}$. Since it is both sample-dependent and system-dependent, it needs

to be determined for each measurement separately. Once $F_{PL}$ is obtained, Eq. (3.18) can be used to calculate the excess minority carrier concentration. $B$ is a function of $\Delta n$ so an iterative procedure is needed for the conversion of $V_{PL}$ to $\Delta N_{minor}$ similar to that used for PC measurements to determine mobility [47].

Two methods are often used to obtain the calibration factor $F_{PL}$. The first method is simply to match the PL measured lifetime curve to the PC measured lifetime curve at an injection level where the PC lifetime is not impacted by minority carrier traps or DRM. The correct carrier lifetime at low injection can then be obtained from the calibrated PL lifetime.
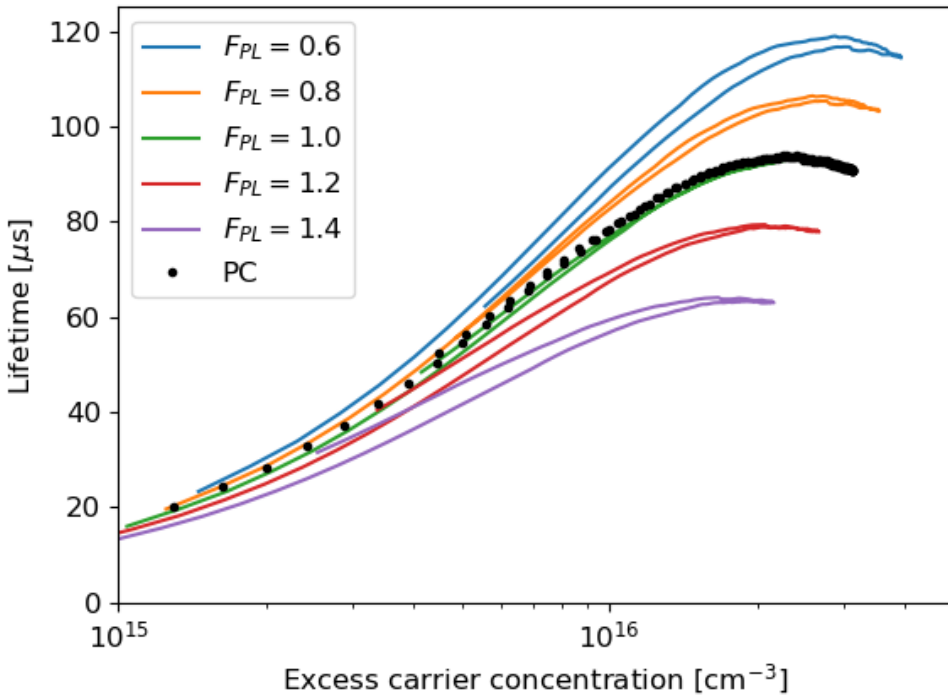


**Fig. 3.10** The PL measured lifetime curves of a silicon wafer with different $F_{PL}$ values. The PC measured lifetime of the same sample is also overlaid (black dots).

When a PC measurement is not possible, or when accurate high injection lifetime is not obtainable (due to low sample lifetime, or strong minority carrier trapping), an alternative approach to calibrate PL, the self-consistent calibration method, can be used. The method was first proposed by Trupke *et al.* [160]. In this approach, a symmetric waveform (sinusoid wave for example) of illumination is used. This can be achieved by using the LED or the laser in the modified lifetime system. The lifetime of the <u>sample</u> can be calculated from the raw PL signal for an arbitrary $F_{PL}$ value. However, only when the

correct value of $F_{PL}$ is used, the lifetime curves from the two halves of the generation waveform match each other. Incorrect $F_{PL}$ values result in hysteresis in the lifetime curve [160]. In Fig. 3.10, an example of the application of the self-consistent method for PL lifetime curves of a silicon wafer is shown. As can be seen, only when $F_{PL} = 1.0$, the two halves of the lifetime curve agree with each other. In Fig. 3.10, a PC-based lifetime measurement is also shown, and it agrees well with the correctly calibrated PL lifetime at $F_{PL} = 1.0$.

It should be noted that the self-consistent method relies on the time derivative term ($d\Delta n/dt$) in Eq. (3.2). As a result, the period of the generation waveform should be short enough, and thus the $d\Delta n/dt$ term is significant, otherwise the two halves of the lifetime curve will always match each other no matter what $F_{PL}$ is used. Meanwhile, the self-consistent method also requires the carrier lifetime to remain constant during the measurement. Therefore, if metastable defects, such as iron-boron pair (FeB), dominants the lifetime of the sample, the self-consistent method cannot be applied.

A more sophisticated calibration procedure for PL has been proposed by Giesecke *et al.* [161], [162]. Unlike other methods, this calibration procedure does not require knowledge of the sample doping concentration. However, due to the simplicity of the self-consistent method, this is the calibration method of choice for all PL calibration performed in this work.

While PL-based lifetime measurements are not impacted by minority carrier trapping or DRM, they have several disadvantages compared to PC-based measurements when measuring low lifetime samples (below 10 µs). These disadvantages mainly derive from system limitations [163]. First, in the modified system in this thesis, PL is detected by a silicon photodiode. Detecting PL spectrum of silicon with a silicon photodiode usually leads to a delay of the response of the photodiode in the range of a few microseconds [163]. This delay of response can be reduced by using an Indium gallium arsenide (InGaAs) photodiode to detect PL [163], which is planned in the future upgrade of the system. Meanwhile, the amplification process via the pre-amplifier can also induce delay of the signal in the range of a few microseconds [163]. When the lifetime of the sample is comparable with these delays, then the lifetime calculated with Eq. (3.2) can be strongly impacted. Therefore, to accurately measure PL lifetime for low lifetime samples, these delay times needs to be quantified and a correction of the measured signal is required

[163]. Second, lower lifetime samples also have a weaker PL signal, which requires a higher amplification gain. Usually, the bandwidth of a current amplifier decreases as the amplification gain increases. In the customized system used in this thesis, the bandwidth of the amplifier decreases dramatically when the gain is above $10^7$ and this leads to strong distortion of the measured signal. Therefore, in all PL measurements in this thesis, the amplification gain is kept at $10^7$ or below. This can be improved by using an amplifier with better gain-bandwidth performance. However, there is usually a tradeoff between the gain-bandwidth performance and the signal delay.

Similar to the PC coil sensor, the PL photodiode measures the PL of the sample over a certain sensor area (a square of 1 cm$^2$ diameter for this system). Therefore, the lifetime measured by PL is also impacted by the non-uniformity of the sample. This can impede an accurate injection dependent lifetime spectroscopy analysis if defects have non-uniform distribution within the sensor area. The defects and traps investigated in this thesis are uniformly distributed in the sensor area of the measurement system. For future investigation of non-uniformly distributed defects, a method to accurately measure spatially resolved lifetime for non-uniform samples is presented in Chapter 7.

## 3.5 Chapter summary

In this chapter, the principles of lifetime measurements for silicon were described. A customized temperature and injection-dependent lifetime measurement system that has been developed as part of this thesis was also introduced. The main advantages of this system are: (1) its flexibility in the choice of excitation light (xenon flash, LED and laser); (2) the wide temperature range (80-623 K); (3) the combination of PC and PL for lifetime measurements; and (4) a customized software which enables more freedom for adjusting the measurement settings.

The necessary calibration methods and results for accurate lifetime measurements used in this thesis have been presented and discussed, and includes:

1.  Calibration of the actual sample temperatures at various cryostat temperatures;

2.  Calibration of the generation rate from the measured reference signal;

3.  Converting PC coil output voltage to excess carrier density; and

4.  Converting PL signal to excess carrier density.

The developed temperature and injection dependent lifetime measurement system will be used in Chapter 5 for the investigation of newly discovered defects in FZ silicon, and in Chapter 6 for the investigation of traps in Cz silicon. In Chapter 4, methods to extract the electrical properties of defects from measured temperature and injection dependent lifetime data will be presented.

# Chapter 4
# Analysis Methods for Injection Dependent Lifetime Spectroscopy[1]

Injection dependent lifetime spectroscopy is the main characterization technique used for defect investigation in this thesis. In the previous chapter, the experimental setup for measuring IDLS data has been described. In this chapter, the method to extract electrical properties of the dominant defect from IDLS will be discussed.

First, in Section 4.1, methods for analyzing a single-level defect based on IDLS measurements will be outlined. The conventional defect parameter solution surface method [103], which is the most well developed and widely used method will be presented. Then, an alternative method developed in this thesis, will be described. In Section 4.2, a new method to analyze a two-level defect in lifetime spectroscopy, which is important but rarely considered in previous studies will be presented. In Section 4.3, important issues that can impact lifetime spectroscopy analysis will be discussed.

## 4.1 Lifetime spectroscopy analysis for single-level defect

### 4.1.1 Conventional DPSS method

The DPSS method was first proposed by Rein *et al.* [21], [103], [164] and soon became the most commonly used method for analyzing lifetime spectroscopy data. The principle of DPSS method will be described here. More details regarding the DPSS method can be found in Ref. [21]. The SRH lifetime equation, which was described in Chapter 2 is as follows:

---

[1] This Chapter is partially based on:

**Y. Zhu**, Q. T. Le Gia, M. K. Juhl, G. Coletti, and Z. Hameiri, "Application of the Newton–Raphson method to lifetime spectroscopy for extraction of defect parameters," *IEEE J. Photovoltaics*, vol. 7, no. 4, pp. 1092–1097, 2017.

**Y. Zhu**, G. Coletti, and Z. Hameiri, "Injection dependent lifetime spectroscopy for two level defects in silicon", in *IEEE 46th Photovoltaic Specialist Conference (PVSC)*, 2019.

$$\tau_{SRH} = \frac{\tau_{n0}(p_0 + p_1 + \Delta n) + \tau_{p0}(n_0 + n_1 + \Delta n)}{p_0 + n_0 + \Delta n} \qquad (4.1)$$

where $\tau_{n0}$, $\tau_{p0}$, $n_1$ and $p_1$ are defined in Chapter 2 as well [Eqs. (2.10) and (2.12)].

The aim of IDLS analysis is to extract the dominant defect's electrical properties: $E_t$, $\sigma_n$ and $\sigma_p$. However, as can be seen in the definition of $\tau_{n0}$ and $\tau_{p0}$; $\sigma_n$ and $\sigma_p$ are always multiplied by $N_t$; therefore, the absolute values of $\sigma_n$ and $\sigma_p$ cannot be extracted from IDLS. Instead, the ratio of capture cross sections $k \equiv \sigma_n/\sigma_p$ is often used as a parameter to characterize the defect [21], as it changes the shape of the injection dependent lifetime curve, whereas, $N_t$ only changes the magnitude of the curve. The SRH equation can then be rewritten as:

$$\begin{aligned} &\tau_{SRH}(E_t, \tau_{n0}, k) \\ &= \frac{\tau_{n0}(p_0 + p_1(E_t) + \Delta n) + \tau_{n0}(n_0 + n_1(E_t) + \Delta n) \times k \times (v_n/v_p)}{p_0 + n_0 + \Delta n}, \text{or} \end{aligned} \qquad (4.2.1)$$

$$\begin{aligned} &\tau_{SRH}(E_t, \tau_{p0}, k) \\ &= \frac{\tau_{p0}(p_0 + p_1(E_t) + \Delta n)/k \times (v_p/v_n) + \tau_{p0}(n_0 + n_1(E_t) + \Delta n)}{p_0 + n_0 + \Delta n} \end{aligned} \qquad (4.2.2)$$

If the SRH equation is used to fit the measured defect recombination lifetime, it can be easily shown that the fitting results are ambiguous, *i.e.*, different sets of $(E_t, \tau_{n0}, k)$ or $(E_t, \tau_{p0}, k)$ can fit the measured data with equal fitting quality [84]. DPSS is a method to visualize all of the possible defect parameters that can fit the measured data [21], [103], [164].

To demonstrate the principle of the DPSS method, the recombination lifetime of a *n*-type wafers (doping of $10^{16}$ cm$^{-3}$) with a defect located at $E_t - E_i$ of $-0.33$ eV with $\sigma_n$ of $2.4 \times 10^{-14}$ cm$^2$, $\sigma_p$ of $0.8 \times 10^{-14}$ cm$^2$ and $N_t$ of $10^{12}$ cm$^{-3}$ is simulated using Eq. (4.1). A maximum 1% random noise is added to the data. The simulated lifetime is shown in Fig. 4.1(a) and the DPSS results of this set of simulated data is shown in Fig. 4.1(b). Assuming a value of $E_t$ within the bandgap, the simulated lifetime is then fitted using $k$ and $\tau_{p0}$ as free fitting parameters [Eq. (4.2.2)]. By sweeping $E_t$ across the bandgap and plotting the fitted $k$, $\tau_{p0}$ and fitting residual as a function of the assumed $E_t$, the DPSS curves are obtained. In this thesis, the fitting residual to minimize is defined as $\sqrt{\Sigma \left( \frac{F(x)-M(x)}{M(x)} \right)^2 / N_M}$

where $F$ is the function of the fitting, it being Eq. (4.2), $M$ is the measured data (lifetime values here), $x$ is the independent variable of the function (excess carrier density here), and $N_M$ is the number $x$. The $M(x)$ in the denominator avoids increased fitting weight for larger data points. The DPSS contains three curves as a function of the assumed $E_t$: a fitting residual curve, a solution curve for $\tau_{p0}$ ($\tau_{n0}$ can be used as well) and a solution curve for $k$. These three curves are plotted at the top, middle and bottom subfigures of Fig. 4.1(b).



(a)                    (b)
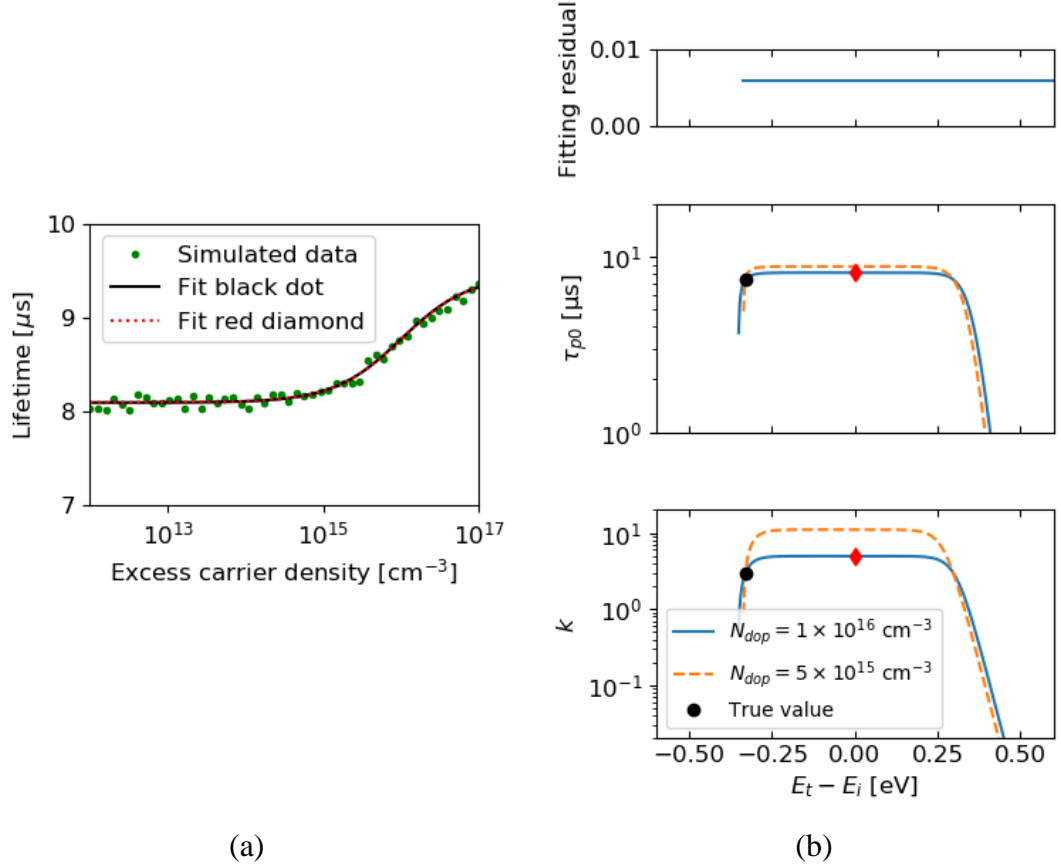
**Fig. 4.1** (a) Simulated lifetime (green dots) of a $n$-type wafers (doping of $10^{16}$ cm$^{-3}$) with a defect located at $E_t - E_i$ of $-0.33$ eV with $\sigma_n$ of $2.4\times10^{-14}$ cm$^2$, $\sigma_p$ of $0.8\times10^{-14}$ cm$^2$ and $N_t$ of $10^{12}$ cm$^{-3}$. The black line and red dotted line are the fitted lifetime curves corresponding to parameters indicated by the black dot and red diamond in (b). (b) DPSS curves for the simulated IDLS data (blue curves). The orange dashed curves indicate the DPSS curves for another set of simulated IDLS data whose simulation parameters are the same except the doping level ($5\times10^{-15}$ cm$^{-3}$). The true combination of the defect parameters is indicated by the black dots.

A few observations can be made based on the DPSS curves of Fig. 4.1(b). First, there is a range of $E_t$ where there exist a pair of $k$ and $\tau_{p0}$ that can fit the simulated injection dependent lifetime data. Moreover, within this range of $E_t$, the fitting residual is exactly the same. In Fig. 4.1(a), the fitted lifetime curves from the parameters, indicated by the black dot and red diamond in Fig. 4.1(b), are also presented. As can be seen, these two

curves coincide with each other. Outside of the solution range of $E_t$, no values of $k$ and $\tau_{p0}$ can fit the IDLS measurements. Therefore, from these DPSS curves, all the possible combinations of parameters ($E_t$, $k$ and $\tau_{p0}$) that can fit the measured lifetime curve can be easily identified. However, the exact value of defect parameters cannot be determined from a single IDLS measurement. In order to pinpoint the exact combination of $E_t$ and $k$, IDLS measurements at different temperature (TIDLS) or of samples with various doping concentration ($N_{dop}$-IDLS) are required. By plotting together the DPSS curves measured at different temperatures, the correct combination of defect parameters should be found by the intersections of the different DPSS curves if they are temperature independent. Since the term $v_p(v_n)$ in $\tau_{p0}(\tau_{n0})$ [Eq. (2.12)] is temperature dependent (its temperature dependency can be modelled by models described in Ref. [165]), and usually the DPSS curves for $\tau_{p0}$ or $\tau_{n0}$ are converted to room temperature values using the simple calculation:

$$\tau_{p0\_300K} = 1/(\sigma_p v_{p\_300K} N_t) = \tau_{p0} v_p / v_{p\_300K} \qquad (4.3.1)$$

$$\tau_{n0\_300K} = 1/(\sigma_n v_{n\_300K} N_t) = \tau_{n0} v_n / v_{n\_300K} \qquad (4.3.2)$$

Similarly, for $N_{dop}$-IDLS, assuming the dominant defect in all the samples with various doping concentrations is the same, $E_t$ and $k$ can be found at the intersections of different DPSS curves for $k$. Since in samples with various doping concentration, $N_t$ might be different, the DPSS curves for $\tau_{p0}$ or $\tau_{n0}$ might not intersect at the correct $E_t$. In Fig. 4.1, the DPSS curves for a set of simulated IDLS data of a different doping level ($5\times10^{15}$ cm$^{-3}$) are also shown as orange dashed lines (the other simulation parameters are unchanged). As can be seen, the DPSS curves from two doping levels intersect at two points. One of them agrees with the true defect parameters (black dots). The other intersection, in the opposite half of bandgap, is wrong. It results from the symmetricity of the SRH equation regarding $E_t$. Therefore, for $N_{dop}$-IDLS, there are always two possible solutions for $E_t$. However, the $k$ values at these two $E_t$ is identical [21]. For TIDLS, it might be possible to determine the true $E_t$ if $k$ is temperature independent and away from unity, as the intersection at the wrong solution is more diffuse than the correct solution [21]. In practice, considering the measurement uncertainties and the temperature dependencies of the capture cross sections, it is usually difficult to determine which of the intersections is the correct one. Nevertheless, by $N_{dop}$-IDLS or TIDLS, the number of possible solutions of defect parameters is significantly reduced from infinity to two.

Although the fitting of the SRH lifetime is not very complicated thanks to the computing power of today, it can be inconvenient to sweep $E_t$ across the whole bandgap and repeat the fitting for each $E_t$. A method to linearize the SRH lifetime was proposed by Murphy *et al.* [99] and adopted by Morishige, Jensen *et al.* [93] to obtained DPSS curves in a more convenient way.

Following the method by Murphy *et al.* [99], by introducing a new parameter $X$, the SRH lifetime in Eq. (4.1) for *p*-type wafers can be linearized:

$$\tau_{SRH} = \left[\tau_{n0} + \frac{\tau_{p0}n_1}{p_0} + \frac{\tau_{n0}p_1}{p_0} + X\left(\tau_{p0} - \frac{\tau_{p0}n_1}{p_0} - \frac{\tau_{n0}p_1}{p_0}\right)\right] \tag{4.4}$$

where $X$ is defined as the ratio between the total electron and the total hole concentrations $X = n/p = (n_0 + \Delta n) / (p_0 + \Delta n)$. A similar expression can be found for *n*-type wafers.

With this change of variable, the SRH lifetime changes to a linear form with the slope $m$ and intercept $h$, both are functions of the defect parameters:

$$\begin{cases} m = \tau_{p0}(\sigma_p) - \dfrac{\tau_{p0}(\sigma_p)n_1(E_t)}{p_0} - \dfrac{\tau_{n0}(\sigma_n)p_1(E_t)}{p_0} \\ h = \tau_{n0}(\sigma_n) + \dfrac{\tau_{p0}(\sigma_p)n_1(E_t)}{p_0} + \dfrac{\tau_{n0}(\sigma_n)p_1(E_t)}{p_0} \end{cases} \tag{4.5}$$

Hence, a simple linear fit can be used to determine $\tau_{n0}$, $\tau_{p0}$ (and thus, $k$) as a function of $E_t$ from the fitted $m$ and $h$:

$$\begin{cases} \tau_{p0} = \dfrac{[1 + \dfrac{p_1(E_t)}{p_0}]m + \dfrac{p_1(E_t)}{p_0}h}{1 - \dfrac{n_1(E_t)}{p_0} + \dfrac{p_1(E_t)}{p_0}} \\ \tau_{n0} = m + h - \tau_{p0} \\ k = (\tau_{p0}v_p)/(\tau_{n0}v_p) \end{cases} \tag{4.6}$$

By using this approach, the relatively complicated fitting of the SRH lifetime equation is simplified to a linear fit. Moreover, the linear fit needs to be done only once and all the DPSS curves can be easily calculated. This method of Morishige, Jensen *et al.* [93] greatly simplifies the DPSS method.

Equation (4.5) also explains why the fitting results of a single IDLS measurement is ambiguous. Although the lifetime is measured at many different injection levels, only two

parameters can be extracted from a single IDLS measurement: the slope and intercept. Nevertheless, in the SRH equation there are three unknown parameters: $E_t$, $\tau_{n0}$ and $\tau_{p0}$ (or $E_t$, $k$ and either $\tau_{n0}$ or $\tau_{p0}$). Therefore, it is an underdetermined system, and infinite number of solutions can be expected.

### 4.1.2 Newton-Raphson method for defect parameterization

Based on Eq. (4.5) from the previous section, an alternative method for defect parameterization is developed in this section. As mentioned before, for a single IDLS, the number of unknown parameters exceeds the number of equations. If two IDLS measurements are done ($N_{dop}$-IDLS or TIDLS), there will be four equations and three unknown parameters, so the system become solvable. This unknown defect parameters can be easily solved by the Newton–Raphson method [166].

The Newton–Raphson method is an efficient method to determine the roots of a function. The root of a function $f(x) = 0$, can be found by starting from an initial guess of the root $x_0$; an improved approximation of the root ($x_1$) can be then calculated by $x_1 = x_0 - f(x_0)/f'(x_0)$. By repeating this process as:

$$x_{n+1} = x_n - f(x_n)/f'(x_n) \tag{4.7}$$

An accurate result of the root can be obtained very quickly due to the quadratic convergence of this method. Let $x$ in Eq. (4.7) be the vector of the three unknown defect parameters of Eq. (4.5):

$$x = \begin{pmatrix} \sigma_n \\ \sigma_p \\ E_t \end{pmatrix} \tag{4.8}$$

Let $f(x)$ be the functional form of Eq. (4.5):

$$f(x) = \begin{pmatrix} f_m^1 \\ f_h^1 \\ f_m^2 \\ f_h^2 \end{pmatrix} = \begin{pmatrix} m^1 - (\tau_{p0}{}^1 - \dfrac{\tau_{p0}{}^1 n_1{}^1}{p_0{}^1} - \dfrac{\tau_{n0}{}^1 p_1{}^1}{p_0{}^1}) \\ h^1 - (\tau_{n0}{}^1 + \dfrac{\tau_{p0}{}^1 n_1{}^1}{p_0{}^1} + \dfrac{\tau_{n0}{}^1 p_1{}^1}{p_0{}^1}) \\ m^2 - (\tau_{p0}{}^2 - \dfrac{\tau_{p0}{}^2 n_1{}^2}{p_0{}^2} - \dfrac{\tau_{n0}{}^2 p_1{}^2}{p_0{}^2}) \\ h^2 - (\tau_{n0}{}^2 + \dfrac{\tau_{p0}{}^2 n_1{}^2}{p_0{}^2} + \dfrac{\tau_{n0}{}^2 p_1{}^2}{p_0{}^2}) \end{pmatrix} \tag{4.9}$$

where the superscripts '1' and '2' indicate measurements at different temperatures or doping levels. The $f'(x)$ of such a multiple variable problem can be replaced by a Jacobian matrix defined as:

$$J(\sigma_n, \sigma_p, E_t) = \begin{pmatrix} \dfrac{\partial f_m^1}{\partial \sigma_n} & \dfrac{\partial f_m^1}{\partial \sigma_p} & \dfrac{\partial f_m^1}{\partial E_t} \\[2mm] \dfrac{\partial f_h^1}{\partial \sigma_n} & \dfrac{\partial f_h^1}{\partial \sigma_p} & \dfrac{\partial f_h^1}{\partial E_t} \\[2mm] \dfrac{\partial f_m^2}{\partial \sigma_n} & \dfrac{\partial f_m^2}{\partial \sigma_p} & \dfrac{\partial f_m^2}{\partial E_t} \\[2mm] \dfrac{\partial f_h^2}{\partial \sigma_n} & \dfrac{\partial f_h^2}{\partial \sigma_p} & \dfrac{\partial f_h^2}{\partial E_t} \end{pmatrix} \tag{4.10}$$

while the inverse of the Jacobean matrix can be calculated as $(J^T J)^{-1} J^T$.

The Newton-Raphson method requires an initial guess of the solution. If the initial guess is not well chosen, several practical problems may arise: (1) When the rank of the Jacobian decreases below the number of variables (here being three), the iteration stops and fails to converge. To ensure this does not plague the result, the rank of the Jacobean is checked in the routine and if it is below three the program restarts with a new randomly chosen initial guess. (2) Another possible issue with this method is that it can converge at an energy level outside the bandgap of the material. To avoid this situation, constraints on the three defect parameters are set according to their physical range. A check has been placed in the routine to assign a random value (within the set physical range) when the parameter departs from the set range, then the iteration can continue and it quickly converges to the correct solution.

The application of a physical range on the defect parameters is also used to determine the possible energy level of the defect in the upper or lower half of the bandgap. As mentioned in the previous section, the DPSS often results in two possible defect energy levels, one in the upper half of the bandgap and the other in the lower half of the bandgap [21]. Similarly, the proposed Newton-Raphson method can also converge to two possible solutions depending on the initial guess. By restricting the range of the defect energy level ($E_t - E_i > 0$ or $E_t - E_i < 0$), the method provides the possible solution in the upper half or lower half of the bandgap. Although it cannot provide additional information regarding which half of the bandgap the defect is located in, the method does ensure that no possible solution is missed. Whether the defect is in the upper or lower half of the

bandgap can then be determined by other measurement techniques, such as DLTS. The approaches discussed above free the users from the requirement of choosing the initial guess. The method will automatically find the two possible solutions in the two bandgap halves.

In order to test the reliability of the proposed method, it is firstly compared to the conventional DPSS method for several sets of simulated data. The method is then applied to a set of experimental data from Sun *et al.* [167] and the results from both methods are compared. In this chapter, the model Altermatt *et al.* [158], [168] is used for dopant ionization. The intrinsic carrier concentration is calculated according to the models from Couderc *et al.* [169]. The bandgap and bandgap narrowing models are, respectively, from Passler [170] and Yan *et al.* [171]. The thermal velocity is calculated from models by Green [165].

To demonstrate its accuracy, the Newton–Raphson method and conventional DPSS method are applied to ideal $N_{dop}$–IDLS as well as TIDLS data modelled according to Eq. (4.1) without any simulated noise. The defect parameters used in these simulations are $E_t - E_i = -0.33$ eV, $\sigma_n = 2.4 \times 10^{-14}$ cm$^2$, $\sigma_p = 0.8 \times 10^{-14}$ cm$^2$ ($k = 3$), and $N_t = 1 \times 10^{12}$ cm$^{-3}$. In order to apply these two methods, at least two sets of IDLS data measured at different conditions are needed. Note that more sets of data will increase the reliability of the result. To simplify the demonstration, in the first simulation, only two data sets are analyzed. It is also assumed that the defect is in the lower half of the bandgap, and thus only one solution instead of two for the Newton–Raphson method is presented.

Two sets of $N_{dop}$–IDLS data with different doping ranges were modelled: The first set contains two *n*-type wafers with doping concentrations of $1\times10^{15}$ cm$^{-3}$ and $1\times10^{16}$ cm$^{-3}$; whereas the second set contains two wafers with closer doping levels of $8.5\times10^{15}$ cm$^{-3}$ and $1\times10^{16}$ cm$^{-3}$. As presented in Fig. 4.2, the chosen bulk doping levels of the first set leads to a "split" DPSS-*k* curve (blue solid line) and a "continuous" DPSS curve (orange dashed line), whereas the doping levels of the second set lead to two "continuous" DPSS curves that are close to each other. The true $E_t$ and $k$ are indicated by the black dashed-dotted lines. In both cases, one of the intersections pinpoints the true defect parameter. However, identification of the intersection points in the second set of simulated data is more difficult as the two DPSS curves are too close due to the small doping range. The results obtained by the Newton–Raphson method are presented using green dots. As can

be seen, the Newton–Raphson method accurately determines the true defect parameter values (in the range of $< 0.1\%$), indifferent of the range of doping levels. Since the defect parameter values are directly obtained, there is no need for an intersection identification step. This is one of the main advantages of the proposed method.



(a)  (b)
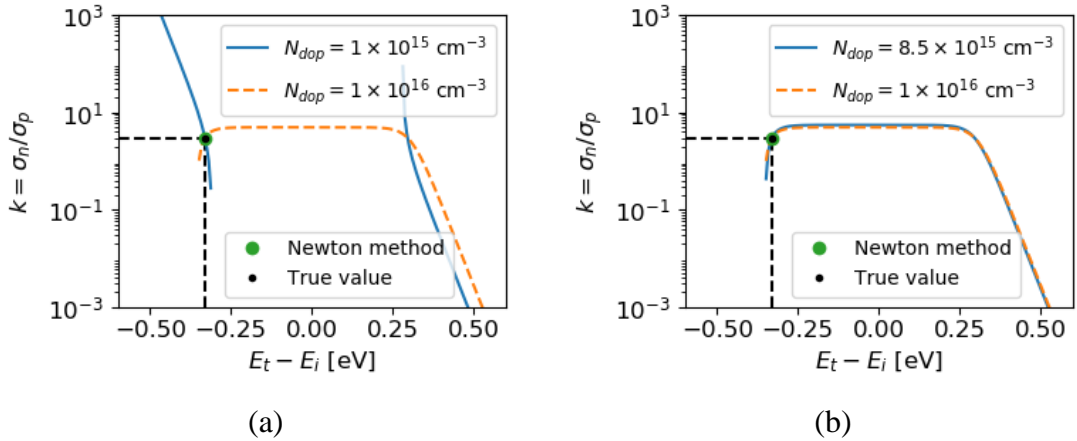
**Fig. 4.2** Comparison of results from the DPSS and Newton–Raphson methods for simulated $N_{dop}$–IDLS of $n$-type wafer at 300 K with two doping levels of (a) $1\times10^{15}$ cm$^{-3}$ and $1\times10^{16}$ cm$^{-3}$; and (b) $8.5\times10^{15}$ cm$^{-3}$ and $1\times10^{16}$ cm$^{-3}$.

The computing time of the two methods was also investigated. It was found that the computing time of the Newton–Raphson method is at least 30% faster than the conventional DPSS method, not including the additional time for the identification of intersections. The slight difference between the true defect values and the ones obtained by the Newton–Raphson method (0.1%) originates from the fact that the linear fitting of Eq. (4.4) neglects the impact of $\Delta n$ on the ionization level [158]. For a typical measurement within an injection level below $1\times10^{17}$ cm$^{-3}$, this impact can be considered negligible.

Similar results are observed for the two sets of simulated TIDLS data with two different temperature ranges, and these results are presented in Fig. 4.3. The proposed method provides an accurate result of the defect parameters regardless of the temperature range of TIDLS, whereas, the intersection points of the conventional DPSS are more difficult to identify when the temperature range is narrow, as shown in Fig. 4.3(b). Nevertheless, in this simulation the capture cross sections were assumed to be temperature independent. For the case of temperature dependent capture cross sections, the Newton–Raphson method might not be able to find the accurate solution of defect parameters as the number of unknown parameters increases. However, this difficulty also applies to the conventional DPSS method.

(a)                      (b)
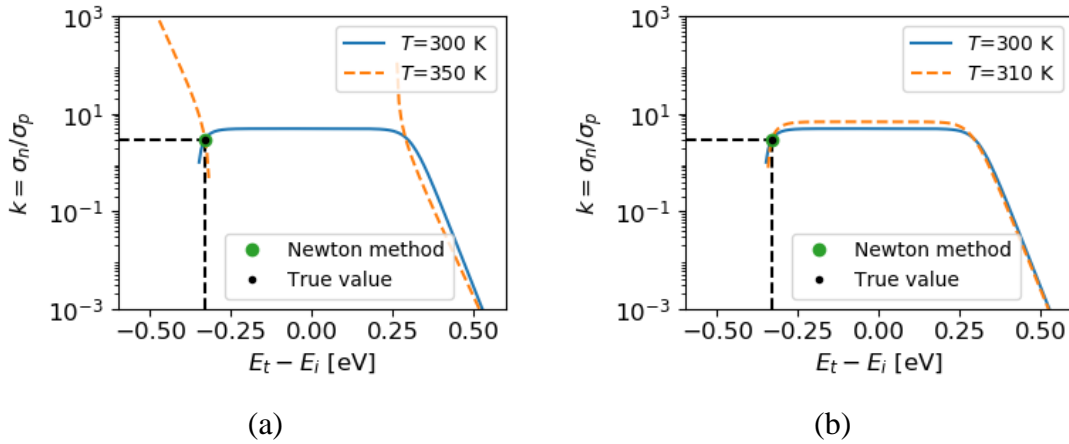
**Fig. 4.3** Comparison of results from the DPSS and Newton–Raphson methods for simulated TIDLS for of an *n*-type wafer with doping concentration of $1\times10^{16}$ cm$^{-3}$ at (a) 300 K and 350 K; and (b) 300K and 310K.



(a)                      (b)
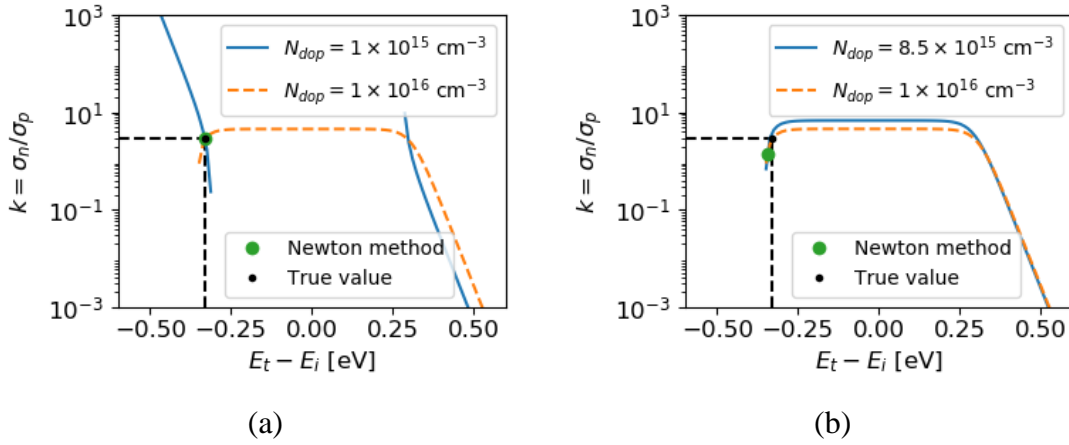
**Fig. 4.4** Comparison of results from the DPSS and Newton–Raphson methods for the same set of simulation as Fig. 4.2 but with 10% random noise in the lifetime data.

To analyze the sensitivity of the Newton–Raphson method to noise, the same sets of $N_{dop}$-IDLS measurements as Fig. 4.2 were modelled. This time, random noise (10%) was added to the simulated lifetime data. The results are displayed in Fig. 4.4. For the data with a wider doping range, the Newton-Raphson method and DPSS technique provide results close to the input true parameters; the relative errors of both methods are within 3%. For the simulations presented in Fig. 4.4(b), which have a narrower doping range, the values determined by the Newton-Raphson method are in good agreement with the intersection point of DPSS, but the calculated $E_t$ and $k$ from both methods are further from the true defect parameters (4% error in $E_t$ and 52% error in $k$). The simulations indicate that the Newton–Raphson method has similar sensitivity to measurement uncertainty as conventional DPSS curves. This is not surprising as it originates from a rearrangement of the DPSS method.

The proposed Newton–Raphson method is applied to the $N_{dop}$–IDLS data of Sun *et al.* [167]. The data set consists of five IDLS measurements on intentionally chromium (Cr) contaminated *n*-type wafers, with doping concentrations between $9.1 \times 10^{15}$ cm$^{-3}$ and $1.5 \times 10^{16}$ cm$^{-3}$. Sun *et al.* [167] simultaneously fit the five sets of data and found two possible $E_t$ of interstitial chromium (Cr$_i$) that provide similar fitting residuals. The one in the upper bandgap half with a value of $E_i + 0.322$ eV was found to be close to previously reported values in the literature. Assuming an 11% uncertainty in the lifetime measurements, $k$ was initially estimated to be between 0.7 and 12.8. By analyzing the monotonically increasing trend of the measured injection-dependent lifetime curves for all the samples, they further reduced the upper limit of $k$ to 3.2. The proposed Newton–Raphson method as well as the conventional DPSS method are applied to this set of data and the result is presented in Fig. 4.5. Here it is assumed that the bandgap half information of Cr$_i$ is known from the literature. Due to the small range of the doping levels, it is challenging to identify the intersections of the DPSS curves. This also explains the relatively wide uncertainty range of the reported capture cross section ratio by Sun *et al.* [167]. The green diamond and associated error bar in Fig. 4.5 indicates the value range determined by Sun *et al.* [167], whereas the circles indicate $E_t$ and $k$ is determined by the Newton–Raphson method. The black dots are the results of analyzing two different IDLS measurements (five sets of measurements; total of ten combinations), whereas the red dot is the result of using all five IDLS measurements. The distribution of the black dots provides a good indication of the measurement uncertainty as they should overlap with the red dot if the measured data is not impacted by noise and measurement-related uncertainties. Therefore, the Newton–Raphson method determined the defect parameter and uncertainty range as $E_t - E_i = 0.33 \pm 0.01$ eV and $k = 2.4 \pm 0.8$. These values are in good agreement with the values of Sun *et al.* [167]: within the reported range of $k$ and within 2.5% deviation of the reported $E_t$ (note that the uncertainty range of $E_t$ was not given in Ref. [167]). A possible reason for the deviation could be the use of different models for parameters, such as the thermal velocity.
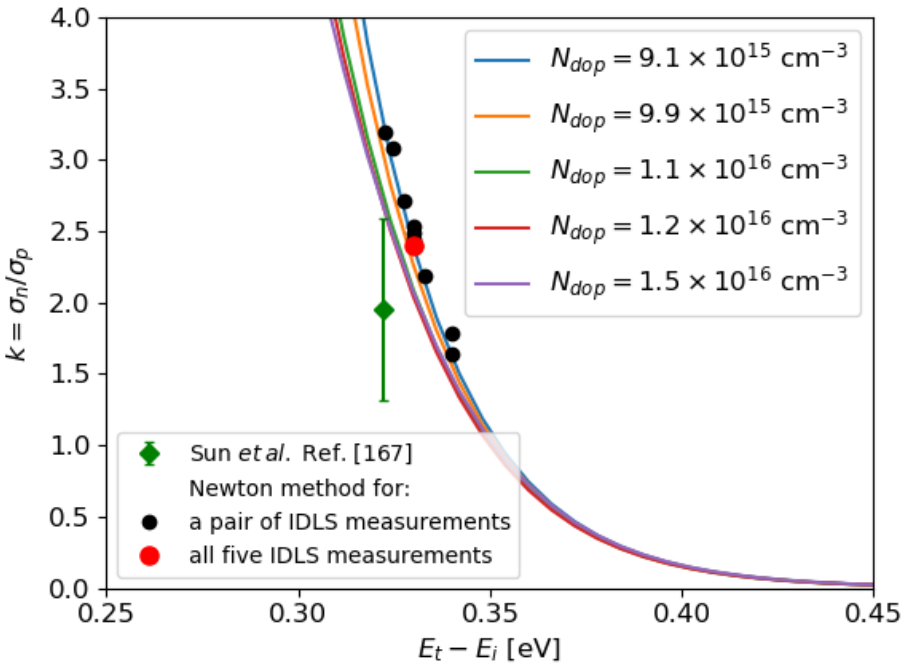
**Fig. 4.5** Comparison of DPSS and the Newton–Raphson method applied to a set of $N_{dop}$–IDLS data from Sun *et al*. [167]. The black dots indicate the results of Newton–Raphson method applied to pairs of IDLS measurements and the red dot indicates the results of Newton–Raphson method applied to all five IDLS measurements. The green diamond indicates the results from Sun *et al*. [167].

As mentioned before, the modified method used by Sun *et al*. [167] determined a relatively large range for $k$ at first. An additional step involving human inspection of the data is required to reduce this range, and this additional step might not be applicable for a different set of data. However, without any human interaction, the proposed Newton-Raphson method extracted the defect parameters, as well as their uncertainty range, in good agreement with the results of Sun *et al*. [167].

To sum up this section, a new method to extract defect parameters from $N_{dop}$–IDLS or TIDLS measurements was presented. The technique is based on the Newton–Raphson method and has the advantages of short computing time and directly providing the two possible values of defect parameters, without a need for user interaction, although, additional analysis to determine bandgap half is still required. The reliability of this method was demonstrated through simulations, as well as through analysis of previously published data. The proposed method provides the same accuracy and sensitivity to measurement noise as conventional DPSS method, and thus can be a good alternative for defect parameterization.

## 4.2 Two-level defect in lifetime spectroscopy

In the previous section, the conventional DPSS method, as well as the Newton-Raphson method proposed in this study, were described. Both methods are based on the assumption that the defect has one single energy level within the bandgap. Therefore, these two methods cannot be used to analyze defects with more than one energy levels in the bandgap. Very often the measured lifetime cannot be modelled by the presence of a single-level defect [21], [86], [88], [93], [99], [105], [172]. In this case, in order to improve the fitting quality, it is often assumed that there are two single-level defects. However, the fact that the injection dependent lifetime cannot be fitted with a single-level defect could also be explained by the presence of a two-level defect [104]. This possibility has been considered only by a very few studies [99], [105]. Actually, the majority of defects that have been investigated have multiple energy levels (*i.e.* more than two charge states) [104]. As multi-level defects and single-level defects have different recombination statistics, interpreting a multi-level defect as multiple single-level defects might cause error in the defect parameterization.

In this section, the possible consequences of misinterpreting a two-level defect as two single level defects will be evaluated in Section 4.2.1. Subsequently, a procedure for parameterization of two-level defect via IDLS will be developed in Section 4.2.2.

### *4.2.1 Impact of a two-level defect in lifetime spectroscopy*

To evaluate the possible consequences of misinterpreting a two-level defect as two single-level defects, the following simulation procedure is used. First, the injection dependent lifetimes resulting from two-level defects are simulated. The simulated lifetimes are then analyzed assuming there are two independent single-level defects and the corresponding defect parameters are extracted using the conventional DPSS method. The obtained results are then compared with the true defect parameters of the simulated two-level defect to demonstrate the consequences of such misinterpretation.

As described in Chapter 2, the injection dependent lifetime of a two-level defect is calculated using Sah-Shockley statistics [61]:

$$\tau = \frac{1 + \left(\frac{\sigma_{n1}v_n n_1 + \sigma_{p1}v_p p}{\sigma_{p1}v_p p_1 + \sigma_{n1}v_n n}\right) + \left(\frac{\sigma_{p2}v_p p_2 + \sigma_{n2}v_n n}{\sigma_{n2}v_n n_2 + \sigma_{p2}v_p p}\right)}{N_t(n_0 + p_0 + \Delta n)[\left(\frac{\sigma_{n1}\sigma_{p1}v_n v_p}{\sigma_{p1}v_p p_1 + \sigma_{n1}v_n n}\right) + \left(\frac{\sigma_{n2}\sigma_{p2}v_n v_p}{\sigma_{n2}v_n n_2 + \sigma_{p2}v_p p}\right)]} \tag{4.11}$$

In this thesis, the 2$^{nd}$ energy level refers to the transition energy between the most negatively charged state and the middle charge state, whereas the 1$^{st}$ energy level refers to the transition energy between the most positively charged state and the middle charge state. For example, for a donor-acceptor type two-level defect, the 2$^{nd}$ energy level is the transition energy between the negative charge state and the neutral charge state, whereas the 1$^{st}$ energy level is the transition energy between the most positive charge state and the middle neutral state.

The lifetime calculated from Eq. (4.11) is then analyzed using the DPSS method described in the previous section. Note that by using the Newton-Raphson method, the same results will be obtained. The DPSS method is used here as it provides a better visualization of all the possible solutions and the comparison of results is therefore easier. The calculated $\tau$ is firstly plotted as a function of $X$, instead of $\Delta n$. If the linearized lifetime $\tau(X)$ shows good linearity, the lifetime is likely to be dominated by a single defect level. Otherwise, the lifetime is impacted by more than one defect level. As two single-level defects are assumed, the linearized lifetime is fitted with the harmonic sum of two straight lines:

$$\frac{1}{\tau(X)} = \frac{1}{\tau_{defect\,1}(X)} + \frac{1}{\tau_{defect\,2}(X)} = \frac{1}{m_1 X + h_1} = \frac{1}{m_2 X + h_2} \qquad (4.12)$$

Each straight line can be then analyzed separately as a single-level defect and a DPSS for each of the two defects can be obtained. The obtained defect parameters are then compared with the parameters of the simulated two-level defects to check if the correct defect parameters are extracted. As $N_t$ cannot be determined from lifetime spectroscopy, here only the DPSS-$k$ curve is used for comparison.

**Table 4.1** Defect parameters of the two-level defects simulated in each case

|  | $E_{t1} - E_i$ [eV] | $\sigma_{n1}$ [cm$^2$] | $\sigma_{p1}$ [cm$^2$] | $E_{t2} - E_i$ [eV] | $\sigma_{n2}$ [cm$^2$] | $\sigma_{p2}$ [cm$^2$] |
|---|---|---|---|---|---|---|
| Case 1 | 0.1 | 10$^{-15}$ | 10$^{-15}$ | −0.1 | 10$^{-14}$ | 10$^{-14}$ |
| Case 2 | −0.3 | 10$^{-14}$ | 10$^{-15}$ | 0.1 | 10$^{-15}$ | 10$^{-14}$ |
| Case 3 | −0.1 | 2×10$^{-13}$ | 10$^{-14}$ | −0.5 | 4×10$^{-14}$ | 10$^{-13}$ |

From the simulation of two-level defects with a wide range of defect parameters, it was found that two-level defects can lead to three very different cases in lifetime spectroscopy, depending on the defect parameter and the sample parameters. In the

following, three examples are used to illustrate these three different cases. In the three examples, the sample parameters are kept the same: a *p*-type silicon wafer with doping of $10^{16}$ cm$^{-3}$ at 300 K, whereas the defect parameters are varied. The defect parameters of the two-level defects in each case are summarized in Table 4.1. In all case, $N_t$ is set arbitrarily to be $10^{12}$ cm$^{-3}$.

### *Case 1: Lifetime cannot be fitted as two single-level defects*

The resulting lifetimes from the two-level defect simulated in Case 1 is shown in Fig. 4.6. In Fig. 4.6 (a), the lifetime is plotted as a function of excess carrier density. In Fig. 4.6(b), the lifetime is plotted as a function of $X$. As can be seen in Fig. 4.6(b), the $\tau(X)$ curve shows a curvature, indicating that the lifetime is impacted by more than one defect level. However, the curvature of $\tau(X)$ is concave. As a concave curve cannot be fitted as a harmonic sum of two straight lines, the lifetime cannot be fitted as the presence of two single-level defects. If a lifetime of this shape is measured, and if it is certain that this shape is not the result of any measurement artifact (such as minority carrier trapping), then one can be sure that the measured lifetime is dominated by a multi-level defect instead of multiple single-level defects. Therefore, Case 1 is a relatively "safe" scenario, as the misinterpretation of the defect properties can be avoided.



|        (a)        |        (b)        |
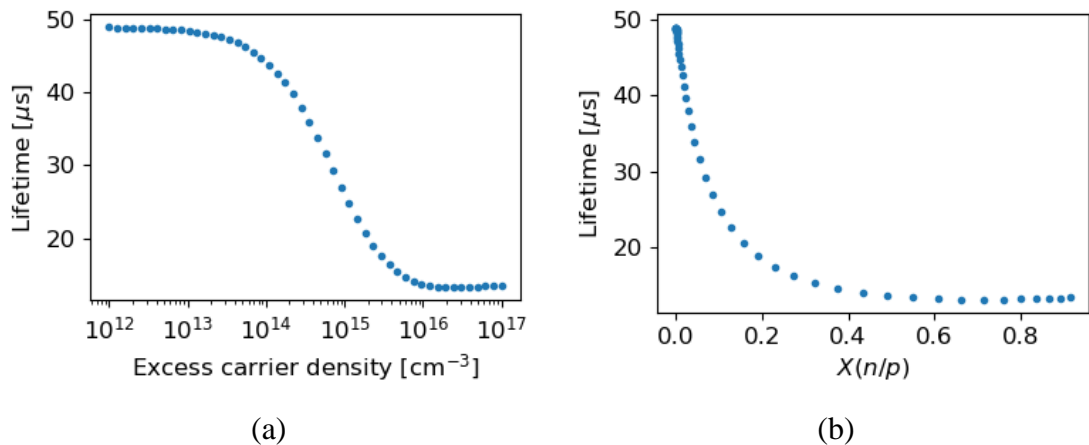
**Fig. 4.6** Simulated lifetime of the two-level defect in Case 1 as a function of: (a) excess carrier density; and (b) the ratio of total electron and hole concentrations.

### *Case 2: Correct parameterization even with misinterpretation*

The lifetime of the two-level defect simulated in Case 2 is plotted as a function of $X$ in Fig. 4.7(a). Unlike Case 1, the lifetime of the two-level defect in Case 2 shows a convex shape. Hence, when a lifetime curve of this shape is measured, one might conceive that

the curvature is a result of two single-level defects. In this case, the simulated lifetime can be well fitted by the harmonic sum of the recombination lifetimes of two single-level defects, as shown in Fig. 4.7(a). The defect parameters of these two single-level defects are then analyzed using the DPSS method described in Section 4.1.1 and the results are shown in Fig. 4.7(b). The DPSS-$k$ curves are shown as orange solid lines for the first single-level defect in the top subfigure and the 2nd single-level defect in the bottom subfigure. As can be seen, for both defects, the DPSS-$k$ curves passes through the correct defect parameters. Doping variations are then added into the simulation. The process is repeated while changing the doping concentration of the simulated sample to $5\times10^{15}$ cm$^{-3}$ and $2\times10^{16}$ cm$^{-3}$. The resulted DPSS-k curves are shown as blue dotted-dashed lines and green dashed lines respectively. As can be seen, for both defects, the DPSS-$k$ curves at different doping concentrations all pass the correct defect parameters. This indicates that correct defect parameters are obtained in this case, even though the two-level defect is misinterpreted as two single-level defects. This case is also a "safe" scenario as the misinterpretation does not lead to the wrong results.



(a)  (b)
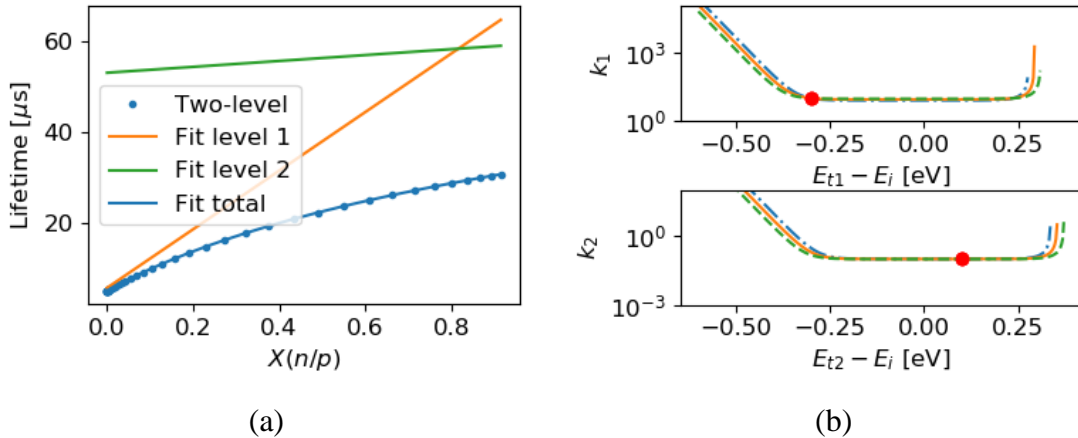
**Fig. 4.7** (a) Simulated lifetime of the two-level defect in Case 2 as a function of the ratio of total electron and hole concentrations. Fitting of the lifetime as two single-level defects are also plotted (b) The DPSS-$k$ curves of the two single-level defects used to fit the simulated lifetime. The orange solid lines indicate simulation in a sample with doping concentration of $10^{16}$ cm$^{-3}$, the blue dotted-dashed lines indicate simulation in a sample with doping concentration of $5\times10^{15}$ cm$^{-3}$, the green dashed lines indicate simulation in a sample with doping concentration of $2\times10^{16}$ cm$^{-3}$. The red dots indicate the parameters of the two-level defect used in the simulation.

### Case 3: Wrong parameterization with misinterpretation

The lifetime of the two-level defect simulated in Case 3 is plotted as a function of $X$ in Fig. 4.8(a). Similar to Case 2, the lifetime of the two-level defect in Case 3 shows a convex shape and can be well fitted by the harmonic sum of the recombination lifetimes

of two single-level defects, as shown in Fig. 4.8(a). The result of the DPSS analysis for these two single-level defects are shown in Fig. 4.8(b). As can be seen, for both defects, the DPSS-$k$ curves deviate the correct defect parameters indicated by the red dots. Doping variations are then added into the simulation. As can be seen, for both defects, the DPSS-$k$ curves at different doping concentrations all deviate from the correct defect parameters. This indicates that correct defect parameters are not obtained in this case. This case can be dangerous as the misinterpretation of a two-level defect as two single-level defects can lead to wrong results of the defect parameter. Note that it is impossible to determine from the fitting of lifetime if there is a two-level defect or two single-level defects.



(a)           (b)
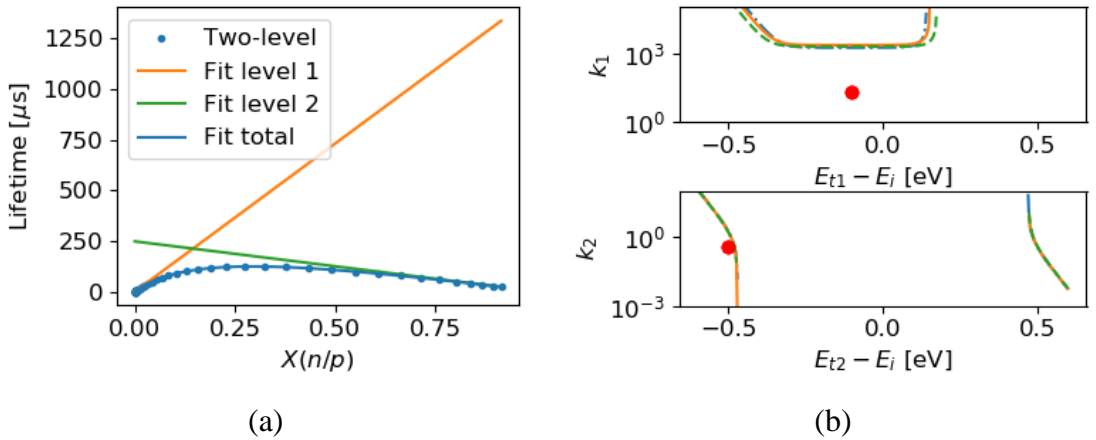
**Fig. 4.8** (a) Simulated lifetime of the two-level defect in Case 3 as a function of the ratio of total electron and hole concentrations. Fitting of the lifetime as two single-level defects are also plotted (b) The DPSS-$k$ curves of the two single-level defects used to fit the simulated lifetime. The orange solid lines indicate simulation in a sample with doping concentration of $10^{16}$ cm$^{-3}$, the blue dotted-dashed lines indicate simulation in a sample with doping concentration of $5\times10^{15}$ cm$^{-3}$, the green dashed lines indicate simulation in a sample with doping concentration of $2\times10^{16}$ cm$^{-3}$. The red dots indicate the parameters of the two-level defect used in the simulation.

To sum up, a two-level defect in IDLS can lead to three different cases: (1) the injection dependent lifetime curve cannot be fitted as two single-level defects; (2) the injection dependent lifetime curve can be fitted as two single-level defects and analyzing the lifetime as two single-level defects leads to the correct defect parameters; and (3) the injection dependent lifetime curve can be fitted as two single-level defects but analyzing the lifetime as two single-level defects leads to wrong defect parameters. Obviously, Case 3 is more dangerous than the other two cases.

Knowing these three different cases, two-level defects with the full parameterization, as obtained from the literature, are tested to identify their case. The defect parameters of titanium (Ti) [173], substitutional gold (Au$_s$) [52], [174], substitutional platinum (Pt$_s$) [52],

cobalt (Co) [175] and the boron-oxygen (BO) related defect [105] are used with the same procedure as before. As the sample parameters also impacts the results, the defects are simulated in both *n*-type and *p*-type silicon with typical doping concentration at 300 K and 400 K. The results are summarized in Table 4.2.

**Table 4.2** Category of actual two-level defects in typical *n*-type and *p*-type silicon

| | Ti | Au$_s$ | Pt$_s$ | Co | BO related |
|---|---|---|---|---|---|
| *p*-type $N_{dop} = 10^{16}$ cm$^{-3}$ $T = 300$ K | **Case 2** | **Case 2** | **Case 2** | **Case 2** | **Case 2** |
| *n*-type $N_{dop} = 2\times10^{15}$ cm$^{-3}$ $T = 300$ K | **Case 2** | **Case 2** | **Case 2** | **Case 1** | **Case 1** |
| *p*-type $N_{dop} = 10^{16}$ cm$^{-3}$ $T = 400$ K | **Case 2** | **Case 2** | **Case 2** | **Case 2** | **Case 3** |
| *n*-type $N_{dop} = 2\times10^{15}$ cm$^{-3}$ $T = 400$ K | **Case 2** | **Case 2** | **Case 2** | **Case 3** | **Case 1** |

As can be seen from Table 4.2, for Ti, Au$_s$ and Pt$_s$, all the simulated scenarios indicate the relatively safe Case 2. For Co and BO related defect, the simulated scenarios at 300 K are either Case 1 or Case 2, both of which are relatively safe. However, if measured at a higher temperature (400 K), the IDLS analysis of Co and BO related defect may result in the relatively dangerous Case 3 and a wrong defect parameterization can occur. For example, if TIDLS is used to extract defect parameters of the BO related defect in *p*-type silicon with $N_{dop} = 10^{16}$ cm$^{-3}$ and measurements involved temperature around 400 K, the resulted defect parameters will be wrong, even though at 300 K the BO related defect fall into the "safe" Case 2. The results here have a few indications: (1) in order to ensure a correct parameterization of a defect, it is recommended to consider the possibility of two-level defects if a single-level defect cannot provide satisfied fitting of the measured lifetime; and (2) it is beneficial to perform measurements with a wide doping range and temperature range, as it might be able to determine if the defect is a multi-level defect.

### *4.2.2 Defect parameterization for a two-level defect*

In the previous section, the impact of a two-level defect in IDLS analysis has been discussed. The importance of considering the possibility of a two-level defect has been

highlighted. In this section, a procedure to extract defect parameters for two-level defects in IDLS will be developed.

For a two-level defect, the defect parameters cannot be extracted using the conventional DPSS method or the proposed Newton-Raphson method. With six fitting parameters ($E_{t1}$, $E_{t2}$, $N_t\sigma_{n1}$, $N_t\sigma_{p1}$, $N_t\sigma_{n2}$ and $N_t\sigma_{p2}$), it is also much more difficult to present the solution space of the fitting. A procedure to solve these difficulties is proposed as follows.

The number of fitting parameters can be reduced from six to four by fixing the value of $E_{t1}$ and $E_{t2}$. For a given pair of $E_{t1}$ and $E_{t2}$, the values of the other four fitting parameters can be then obtained from a least-square fitting to minimize the fitting residual. In order to further improve the robustness of the least-square fitting, for a given pair of $E_{t1}$ and $E_{t2}$, the fitting can be repeated 100 times with random initial values of the other four parameters. Further increase of the repeating number seems to have no further improvement of the fitting robustness. Meanwhile, it is also found that for a given pair of $E_{t1}$ and $E_{t2}$, there is only one optimal fitting, which means the solution of the other four parameters is unique for a given pair of $E_{t1}$ and $E_{t2}$.

$E_{t1}$ and $E_{t2}$ can be swept across the silicon bandgap and the above fitting procedure can be repeated for all combinations of $E_{t1}$ and $E_{t2}$. For each combination of $E_{t1}$ and $E_{t2}$, the residual of the fitting, as well as the fitted values for the other four parameters are obtained. These values can then be illustrated by 2D maps with $E_{t1}$ and $E_{t2}$ as the two axes. From the map of the fitting residual, the possible solution space of the two energy levels can be easily identified and the other parameters can be obtained from their corresponding maps.

To illustrate the proposed procedure, a set of simulated data are used. A two-level defect with $N_t$ of $1\times10^{12}$ cm$^{-3}$ in a *p*-type silicon with doping concentration of $10^{16}$ cm$^{-3}$ is simulated. The defect parameters are identical to the one used in Case 3 of Table 4.1. At first, a single injection dependent lifetime curve calculated at 300 K is used. The procedure descried above was used to analyze the simulated data and the resulted map of fitting residual is shown in Fig. 4.9.

As can be seen, in the resulted fitting residual map, there are two large regions with low fitting residual values. These regions of low fitting residual can be considered as the

solution space of this IDLS analysis. All the pairs of $E_{t1}$ and $E_{t2}$ in these regions provide good fitting quality of the simulated data. This indicates that the fitting of a signal IDLS measurement is ambiguous. This is similar to the case of single-level defect.
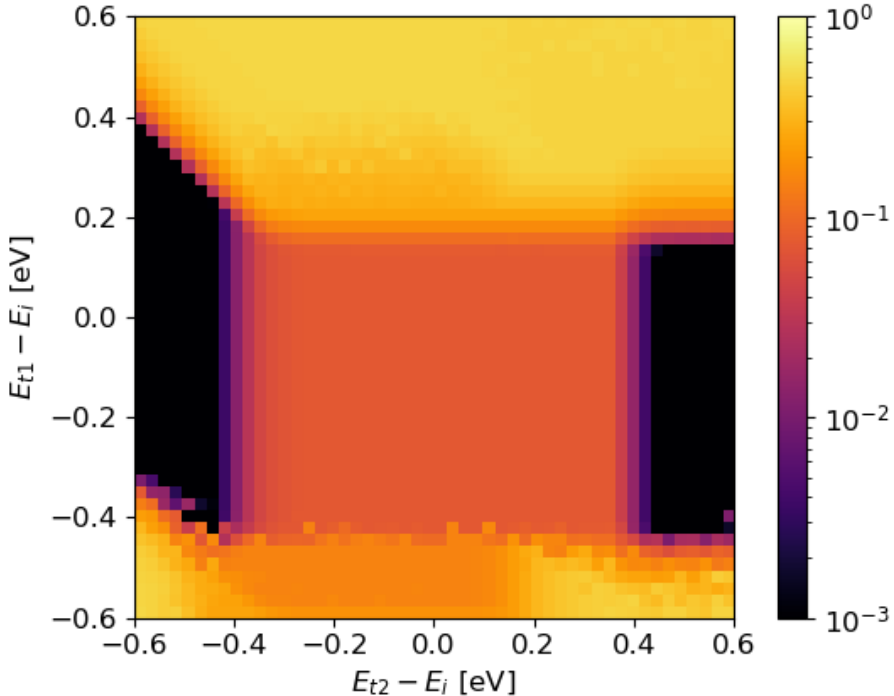


**Fig. 4.9** Fitting residual map obtained by fitting a simulated IDLS data of a two-level defect. The darker color indicates lower fitting residual.

In order to get a unique solution of the defect parameters, TIDLS data are simulated from 173 K to 373 K with an interval of 50 K. At this stage, for simplicity, it is assumed that the four capture cross sections of the two-level defect are temperature independent. The injection dependent lifetime at each temperature can be fitted separately and a fit residual map like Fig. 4.9 can be obtained for each temperature (not shown here). As the solution spaces of the obtained fitting residual maps overlap, simply adding up the fitting residual maps from each temperature will not determine the solution of the defect parameters.

However, if the lifetime data from all five temperatures are simultaneously fitted, the resulted fitting residual map has only two localized points with low fitting residual, as shown in Fig. 4.10. This indicates that by simultaneously fitting the lifetime curves at all temperatures, the number of possible solutions is reduced to two. The correct combination of energy levels is indicated by the green circle in Fig. 4.10. As can be seen, one of the localized minimal points agrees well with the correct defect parameters. This is again

very similar to the case of TIDLS or $N_{dop}$-IDLS for single level defect. By adding temperature or doping variation, the number of solutions for defect parameters reduces from infinity to two.
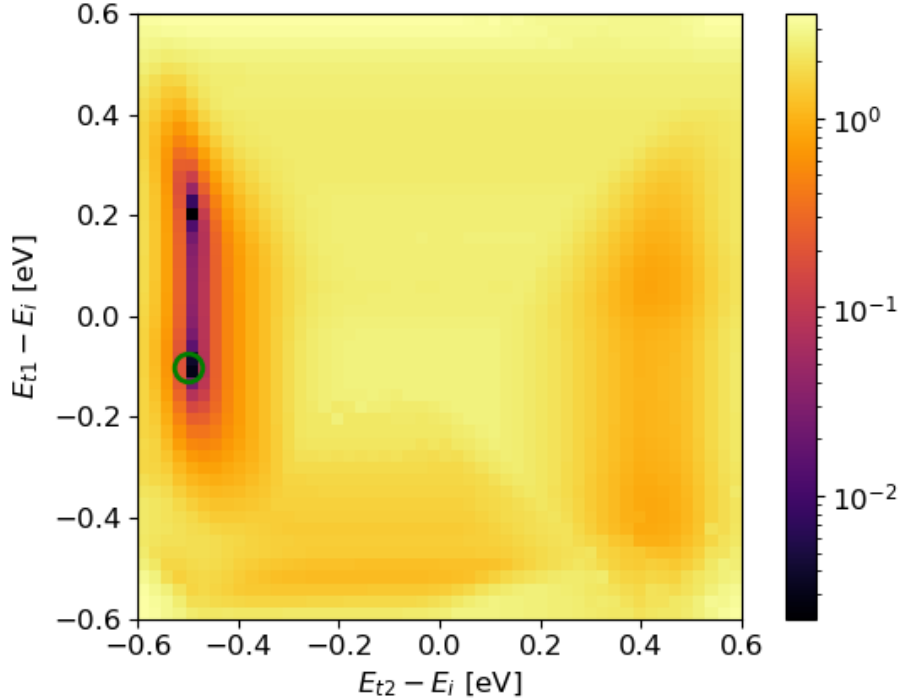


**Fig. 4.10** Fitting residual map obtained by simultaneously fitting a set simulated TIDLS data of a two-level defect. The darker color indicates lower fitting residual.

Therefore, by using the procedure described above, the solutions of the defect parameters for a two-level defect in TIDLS or $N_{dop}$-IDLS can be reliably extracted. The whole solution space can be easily visualized. Meanwhile, it appears that TIDLS or $N_{dop}$-IDLS for two-level defects also suffers from the problem of a wrong solution in the opposite half of the bandgap. Other techniques such as DLTS will be useful to rule out the possibility of the wrong solution.

The procedure above is demonstrated for a relatively simple scenario: TIDLS with temperature independent capture cross sections. If the capture cross sections are temperature dependent, then the TIDLS data at different temperature cannot be fitted simultaneously. For $N_{dop}$-IDLS, if the defect concentration in samples with different doping concentrations is different, the $N_{dop}$-IDLS data at different doping concentrations cannot be fitted simultaneously either. In this case, the IDLS data at each measurement condition needs to be fitted separately. In order to determine the defect parameters, the maps of the fitted $N_t\sigma_{n1}$, $N_t\sigma_{p1}$, $N_t\sigma_{n2}$ and $N_t\sigma_{p2}$ need to be investigated. An example

of this detailed analysis will be presented in Chapter 5 during the investigation of the thermally activated defects in *n*-type FZ silicon.

## 4.3 Other important issues for lifetime spectroscopy analysis

Previously, the issue of two-level defects in lifetime spectroscopy analysis has been discussed. The importance of analyzing two-level defects in the correct way has been highlighted. In this section, a few other important issues for lifetime spectroscopy will be discussed. The issues discussed here have not been properly solved in the literature, but all of them are important for an accountable lifetime spectroscopy analysis.

The first issue discussed here is related to TIDLS only. As mentioned in previous sections, by adding the temperature variation to IDLS, the actual location of the defect parameters can be extracted. However, this requires an assumption regarding the temperature dependency of the defect parameters. In the conventional DPSS method, it is almost always assumed that $E_t - E_V$ or $E_C - E_t$ of the defect is temperature independent [21], [93], [103], [164], [167]. In a few cases, it is assumed that $E_t - E_i$ is temperature independent [95]. This assumption is the base that enables the determination of the $E_t$ from measurements at different temperatures. Indeed, in most literature reporting defect parameters, $E_t$ is usually reported as a single value without temperature dependency data. Nevertheless, in DLTS study of Au in silicon, where the temperature dependency of defect energy level was properly measured [176], it has been found that $E_C - E_t$ decreases with increasing temperature (by 0.015 eV from 200 K to 230 K). If the $E_C - E_t$ data in Ref. [176] are converted to $E_t - E_i$, it also show temperature dependency, although, the temperature dependency is weaker (increase by 0.01 eV from 200 K to 230 K). Therefore, the assumption of temperature independent $E_C - E_t$ or $E_t - E_i$ is not always valid. It seems that the DLTS community is aware of this temperature dependency of $E_C - E_t$ as it causes a deviation between the activation energy extracted from DLTS and the actual defect energy level [114]. However, the lifetime spectroscopy community seems to be less aware of this issue. Surprisingly, in most studies where TIDLS results were compared to DLTS results [21], [167], [175], [177], good agreements regarding $E_t$ have been be achieved. One explanation for this observation is that for most defects, the temperature dependency of $E_C - E_t$ is probably weak. In the case of Au in Ref. [176], $E_C - E_t$ was found to decrease by 0.015 eV from 200 K to 230 K. If this temperature dependency is consistent across all the temperatures, this leads to a deviation of around

0.05 eV for $E_C - E_t$ in TIDLS measurements that cover a temperature range of 100 K. Therefore, for a moderate temperature range, the impact of the temperature dependency of $E_C - E_t$ on TILDS seems to be relatively small. However, it should be kept in mind that if a wide temperature range is used, the temperature dependency of $E_C - E_t$ can cause large uncertainty in TIDLS analysis. In this thesis, a temperature independent $E_t - E_i$ is assumed for most cases, except in Chapter 5 where TIDLS data are compared to DLTS data, whereby $E_C - E_t$ instead of $E_t - E_i$ is assumed to be temperature independent.

Another important issue regarding TIDLS is the temperature dependency of the capture cross sections. The capture cross sections are well known to be temperature dependent, and their temperature dependency depends on the capture mechanism [21], [104]. In the work of Rein [21], it was assumed that $\sigma_n$ and $\sigma_p$ have the same temperature dependency; therefore, $k$ can be considered as temperature independent. This is why the defect parameters can be found in the intersections of the DPSS-$k$ curves from different temperatures. This assumption was also used for most of the following TIDLS studies [86], [88], [95]. However, there is no strong support for this assumption. As a defect can capture electrons and holes with different capture mechanism, there is no reason why $\sigma_n$ and $\sigma_p$ cannot have different temperature dependencies. For defects whose $\sigma_n(T)$ and $\sigma_p(T)$ were properly measured, different temperature dependencies have been found [173], [178]. Therefore, the assumption of temperature independent $k$ is generally invalid. If $\sigma_n$ and $\sigma_p$ have very different temperature dependencies, temperature dependency of $k$ can be very significant. Therefore, the assumption of temperature independent $k$ can lead to a large error in the TIDLS analysis. In this thesis, the assumption of temperature independent $k$ is only used in simulated data for demonstration of methods. In the analysis of real measured data, this assumption is removed and a detailed consideration of $\sigma_n(T)$ and $\sigma_p(T)$ is made.

The last issue that will be discussed in this section, is not only related to TIDLS but to all the IDLS-based techniques. As mentioned in Section 4.2, in many IDLS measurements, a single-level defect cannot provide good fitting quality of the measured lifetime curve [21], [86], [88], [93], [99], [105], [172]. In most of the previous studies, two single-level defects were usually considered. In this thesis, the possibility of a two-level defect is also considered. However, more complicated scenarios are also possible, and the analysis then becomes too difficult. It is quite easy to determine if there is more than one dominant

defect level or not by using the lifetime linearization method of Murphy *et al.*[99]. However, if there are more than one defect levels impacting the measured lifetime, currently, there is no established method to determine the exact number of the defect levels. Even for the case of two single-level defects, a systematic study on the reliability of decoupling the two single-level defects from the measured lifetime is missing. This issue has not been solved in this thesis. However, a few remarks can be made on this issue: (1) a wider injection range of measured lifetime is beneficial for decoupling of multiple defects. Therefore, in the customized lifetime tester developed in Chapter 3, different excitation light sources are used to cover a wider injection range. A PL detector is used to avoid the artifacts of the low injection lifetime measurement due to minority carrier trapping or DRM. (2) If one of the defect levels is dominating the measured lifetime for most of the injection range, the uncertainty of the extracted parameters for this defect tends to be small. On the contrary, if a defect level only impacts the measured lifetime weakly, the uncertainty of the extracted parameters for this defect can be significant, as a small uncertainty in the measured lifetime can be amplified during the lifetime fitting. (3) It is important to take special care when selecting the samples, as well as for the sample preparation for lifetime spectroscopy. Ideally, it would be good if only the investigated defect exists in the bulk of the sample. Using a relatively defect-lean FZ silicon and well controlled induction of defects (for example, by ion implantation) can be a good method to avoid other unwanted defects. However, if this is impossible, one needs to at least make sure that the interested defect is dominating the effective lifetime of the sample. A control wafer to monitor the other recombination channels in the sample is essential. By using the approaches described above, the impact of this issue can be reduced, although, a more systematic study of this issue is still very beneficial for a proper implementation of lifetime spectroscopy analysis.

## 4.4 Chapter summary

In this chapter, the methods of analyzing IDLS, the main characterization technique used in this thesis, has been described. First, the most widely used DPSS method for analyzing single-level defect in lifetime spectroscopy was discussed. A new method based on a mathematic approach was then proposed. This newly proposed method was found to be a reliable alternative of the DPSS method and provides an instructive view on the useful information implied in an IDLS measurement.

The conventional IDLS analysis was then extended from single-level defects to two-level defects. The consequences of misinterpreting a two-level defect as two single-level defects were demonstrated. A procedure to extract defect parameters for a two-level defect in lifetime spectroscopy was then developed. At the end of the chapter, a few important issues which can impact the accuracy of lifetime spectroscopy analysis were discussed. The potential approaches to reduce the impact of these issues were also presented.

Note that the accuracy of measured lifetime is critical for accurate defect parameterization in lifetime spectroscopy. In this thesis, great efforts are made to improve the accuracy of the measured lifetime. In Chapter 3, detailed calibration processes of the developed injection dependent lifetime tester were presented. In Chapter 6, the properties of traps, which can lead to artefacts in the low injection of PC-based lifetime measurements, will be investigated thoroughly. In Chapter 7, a PL imaging-based technique, which can be used to provide accurate spatially resolved lifetime imaging of samples with spatially non-uniform distributed defects, will be presented.

Although IDLS is a very sensitive technique with which to investigate the electrical properties of defects in silicon, it should be noted that it still has some deficiencies. In order to overcome these deficiencies and ensure a more comprehensive characterization of the defects, it is beneficial to combine lifetime spectroscopy with other techniques such, as DLTS. This point will be highlighted in Chapter 5 during our investigation of the thermally activated defects in *n*-type FZ silicon.

# Chapter 5
# Characterization of Defects in *n*-type Float-Zone Silicon[1]

Float-zone silicon was conventionally conceived as bulk defect lean material. Nevertheless, recent research has revealed that very detrimental bulk defects can be thermally activated in FZ silicon. The exact origin of these defects is still unknown. In this chapter, the technique of lifetime spectroscopy described in Chapter 4 is applied to characterize these thermally activated defects in *n*-type FZ silicon. Furthermore, DLTS is also incorporated into the investigation, and the advantages of combining lifetime spectroscopy with DLTS techniques will be demonstrated.

In Section 5.1, major findings from previous studies regarding thermally activated defects in FZ silicon are summarized. Section 5.2 describes the measurement details for the investigation of these defects. The conclusions regarding the electrical characteristics of the defects will be summarized and discussed in Section 5.3.

## 5.1 Thermally activated defects in float-zone silicon

The Czochralski process is used for the growth of single crystal silicon for the majority of the terrestrial PV market [12]. However, Cz silicon usually contains relatively high oxygen content which can form recombination active centers during silicon solar cell processing, or form complex structures with other impurities in silicon, which leads to degradation of the device [57], [179], [180]. Meanwhile, contamination from the crucibles used for the Cz process is in general unavoidable [181]. Therefore, for laboratory purposes where high purity is required, FZ silicon is usually the preferred option [182]. In FZ growth no crucible is used; an RF heating coil is used to create a localized molten zone along a polycrystalline silicon rod. As the RF coil moves along the

---

[1] This chapter is partially based on:

**Y. Zhu**, F. E. Rougieux, N. Grant, J. Mullins, J. Ann De Guzman, J. Murphy, V. Markevich, G. Coletti, A. Peaker, and Z. Hameiri, in 9th International Conference on Silicon Photovoltaics, 2019.

rod (so does the molten zone), the impurities tend to segregate in the molten area instead of the solidified silicon. Therefore, most of the impurities will be driven to the tail of the rod and very pure silicon is obtained. In the silicon PV research community, FZ silicon is widely used for the fabrication of laboratories high efficiency solar cells [183]–[185]. Conceived as stable and defect lean material, it is also often used as control wafers in various experiments or to monitor surface passivation quality and film coating properties [186]–[188].

Recently, it has been found that FZ silicon might not be as defect-lean or as stable as we thought. Grant *et al*. revealed a lifetime degradation of more than one order of magnitude for FZ silicon after isochronal annealing between 450 °C to 700 °C [22]. This indicates that detrimental defects have been activated during the annealing at those temperatures. With a further annealing at temperatures higher than 1000 °C for half an hour, the lifetime can recover to the original level, indicating a deactivation of the defects. Moreover, the deactivation appears to be stable, which means re-annealing the FZ wafers at temperatures between 450 °C to 700 °C will not lead to further degradation of lifetime [189]. Therefore, only after this high temperature annealing process the FZ silicon can be considered as stable and bulk defect free material. It was also found that these thermally activated defects can be partially passivated by hydrogenation [96].

From PL imaging of the degraded samples, it was found that the activated defects were non-uniformly distributed across the wafers: the degradation occurs mostly at the center circular area of the wafers, whereas the periphery of the wafers suffers much less degradation [22]. This spatial distribution indicates the defects might be related to vacancies. During the FZ silicon growth, nitrogen is usually incorporated to avoid the formation of detrimental voids and to improve the mechanical strength of ingot [190]–[193]. The incorporation of nitrogen can result in a higher concentration of vacancies in the center of the wafer than the edge of the wafer [191], [194]–[196]. Grant *et al*. also found the degradation behavior of the nitrogen doped samples was different from samples grown without nitrogen incorporation [189].

If there was no awareness of these thermally activated defects, experiments based on the assumption of defect free (or at least stable) FZ silicon can suffer from large errors.

DLTS has been used in several studies to characterize the electrical properties of the thermally activated defects [22], [189]. Several majority carrier emission signals can be

detected by DLTS measured at the center of the degraded samples [22], [189]. This emission signals cannot be detected in the non-annealed samples or samples annealed at temperature above 1000 °C. These emission signals are not detected even at the periphery of the degraded samples. These results indicate that several defect levels are activated during the degradation annealing process and at least one of these defect levels is responsible for the reduction of lifetime. However, DLTS analysis in Refs. [22], [189] did not reveal which of the levels is dominant in recombination of charge carriers.

Later, a study by Mullins *et al*. conducted more detailed DLTS analysis on these defects in *n*-type FZ silicon [197]. It has been suggested that nitrogen doping during the FZ silicon growth plays a significant role in the defect formation. It was suspected that the un-clustered vacancies might act as defect precursors and form recombination active defects with other impurities or intrinsic defects upon the degradation annealing. However, the definite composition of the defects remains unclear. It was also demonstrated by Mullins *et al*. that the defects distribute uniformly across the wafer thickness, and thus confirm that the activated defects are bulk defects [197]. The ambient atmosphere for the annealing was also found to be irrelevant for the activation of defects [197]. The DLTS results by Mullins *et al*. identified electron and hole emission signals quite different from previous studies [197]. This suggests that the thermally activated defects depend also on the growth condition of the material. This no doubt complicates the investigation of these defects.

Since the thermally activated defects can lead to a lifetime reduction of more than one order of magnitude, they can easily be the dominant recombination sources in FZ silicon. This makes lifetime spectroscopy very suitable for the investigation of these defects. In previous studies, injection dependent lifetime spectroscopy has been used for the parameterization of these defects. However, due to the ambiguity nature of IDLS, as discussed in Chapter 4, the energy level and capture cross section ratio of the defects could not be determined.

The following sections will investigate these thermally activated defects in FZ silicon. By combining TIDLS and DLTS, the electrical properties of the defects are extracted. Additionally, PL spectroscopy is used to investigate the potential radiative transition from these defect levels. It should be noted at this stage, only *n*-type FZ silicon is used in this study. The investigation of these defects in *p*-type material is included in the future plan.

## 5.2 Experimental methods

In this study, a set of phosphorus doped *n*-type FZ silicon wafers grown in nitrogen ambient from the same manufacturer (Siltronic) packed in the same box are used. The wafers are four inch, 190 μm thick, with resistivity of 1 Ω·cm. The wafers were divided into three groups. The first group of the wafers were non-annealed. The second group of wafers were annealed at 500 °C under nitrogen ambient for 30 mins (labelled as the "degraded group"). The third group of wafers were annealed at 1000 °C under nitrogen ambient for 30 mins and are referred to as the "Stable group". From previous studies it is known that this high temperature annealing process is able to stabilize the FZ silicon and prevent further formation of the defects, no matter if the wafers have been degraded or not [189]. Since the wafers might not be neighboring wafers from the same ingot, each group contains three to four wafers to strength the statistics of results.
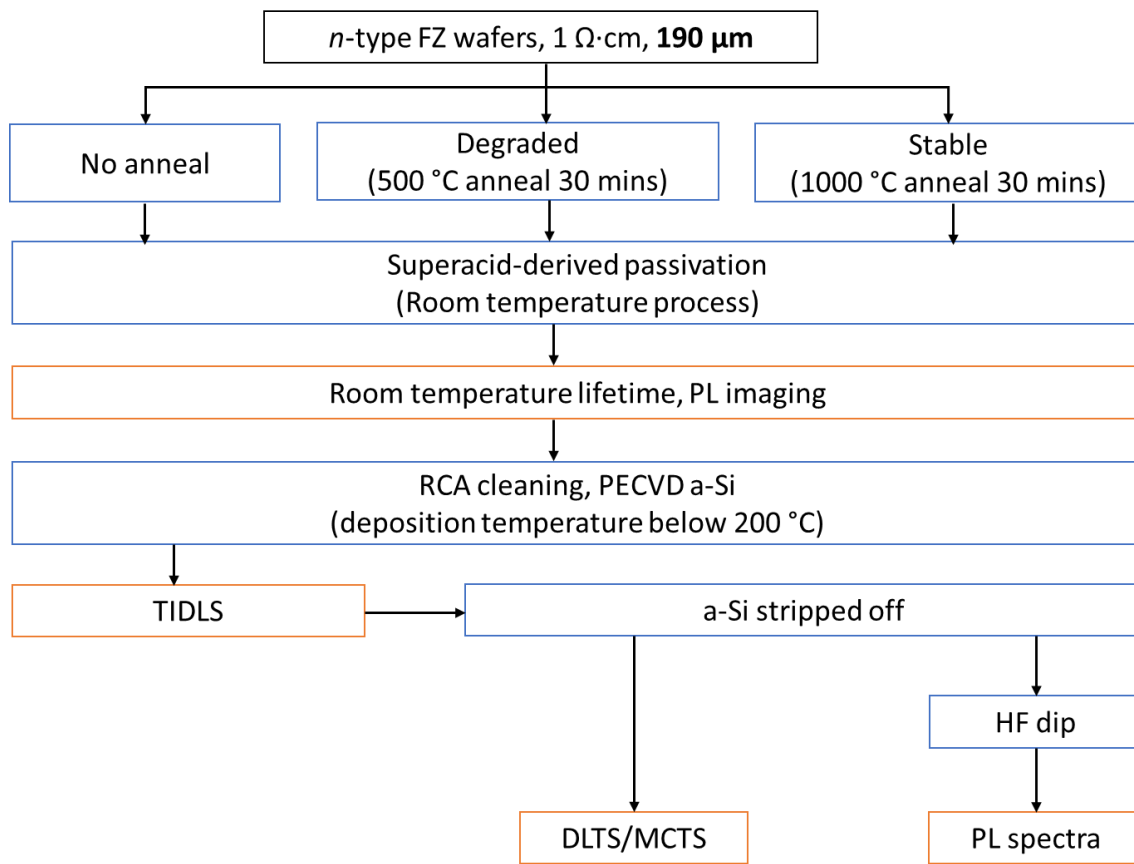


**Fig. 5.1** Flowchart of the experimental design for the investigation of the thermally activated defects in *n*-type FZ silicon.

The process and characterization for each group of wafers is shown in the flowchart of Fig. 5.1. After the corresponding annealing process, all the wafers first went through a

superacid-derived passivation [bis(trifluoromethane)sulfonimide (TFSI) in 1, 2-dichloroethane (DCE)] [198], [199]. This superacid-derived passivation was conducted at room temperature; therefore, no thermal budget was added to the wafers. Superacid-derived passivation provides excellent passivation quality with surface recombination velocity (SRV) around 1 cm/s for wafers with similar resistivity [199]. It is also stable for a time duration long enough for lifetime (at room temperature) and PL imaging measurements; therefore, the activation of defects during the annealing process can be monitored.

Unfortunately, the superacid-derived passivation is not stable enough for TIDLS measurements, and therefore all wafers were then RCA (Radio Corporation of America) cleaned and passivated again by an amorphous silicon (a-Si) layer via PECVD [200]. The deposition temperatures were kept below 200 °C to minimize the thermal budget on the samples and to avoid potential hydrogen induced passivation of the defects. The passivation quality and stability of the a-Si layer were tested with a separate set of FZ wafers. It was found that the a-Si passivation achieves an SRV below 10 cm/s and remain stable up to 200 °C. TIDLS measurements of the samples from -50 °C to 150 °C were performed with the temperature dependent lifetime tester described in Chapter 3. After the lifetime measurements at elevated temperatures, the carrier lifetimes of the samples were measured again at room temperature to check if the TIDLS measurements had an impact on the defects.

For DLTS and MCTS measurements, the a-Si layer was stripped off from the samples with a mixture of 49% hydrofluoric (HF) acid and 69% nitric acid (ratio of 1:10) for two minutes followed by rinsing in deionized water. Schottky barrier diodes (SBDs) and ohmic contacts were formed by thermal evaporation of metal layers onto the sample surfaces subjected to cleaning and dipping in diluted HF prior to the evaporation. For the SBDs, gold was evaporated through a shadow mask while an aluminum layer was deposited at the back surface to serve as an ohmic contact. For MCTS measurements, an open area at the back side of the samples was left for optical excitation using a 940 nm light emitting diode.

PL spectroscopy was applied to investigate the potential radiative transition from the activated defect levels. To avoid the impact of PL emission from the a-Si layer on the measured PL spectra, the a-Si layers were stripped off. The samples were dipped in HF (49%) for one minute to achieve a temporal surface passivation. For PL spectra

measurements, a LED with wavelength of 660 nm is used for excitation, while the emitted PL spectra is monitored with an InGaAs spectrometer with a detection range from 900 nm to 1700 nm. The samples are cryostat cooled by liquid nitrogen so that the PL spectra can be measured down to 80 K.

## 5.3 Electrical characterization of the defects

### 5.3.1 Thermal activation of the defects

The activation of defects in *n*-type FZ silicon wafers is monitored by room temperature lifetime and PL image measurements with superacid-derived passivation after annealing of the wafers. The PL images are calibrated into carrier lifetime images by a QSSPC lifetime measurement. The calibrated PL images of one wafer from each group is shown in Fig. 5.2. As can be seen, the wafer annealed at 500 °C shows a much lower lifetime in the center than the periphery of the wafer. The wafer annealed at 1000 °C and the non-annealed wafer, on the contrary, shows uniformly high carrier lifetime.
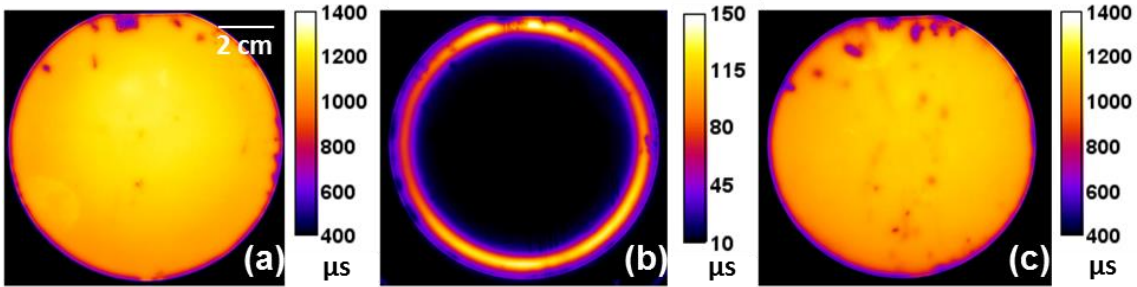


**Fig. 5.2** Calibrated carrier lifetime images for one wafer from each group after the superacid derived passivation: (a) non-annealed wafer, (b) wafer annealed at 500 °C and (c) wafer annealed at 1000 °C.

The observed lifetime and PL image results are in agreement with previous studies [22], [96], [189], [197]. The annealing at 500 °C activated very detrimental defects which are distributed with much higher concentration in the center of the wafer than the periphery. Annealing at 1000 °C, on the contrary, did not activate these defects. Although the stability of the wafers annealed at 1000 °C has not been tested with a further annealing at 500 °C, previous studies indicates that this high temperature annealing process permanently annihilates the thermally activated defects and makes FZ silicon truly stable [189]. In this work, the wafers annealed at 1000 °C are mainly used as control wafers of the surface passivation quality in order to investigate those thermally activated bulk defects.

### 5.3.2 DLTS: defect levels in the majority carrier bandgap half

Although the TIDLS measurements were performed before the DLTS and MCTS measurements, the DLTS results will be introduced first for a clear analysis of the electrical properties of the defects. The DLTS spectra for one sample from each group are shown in Fig. 5.3. For each sample, DLTS measurements are performed at two locations: one at the center of the wafer and the other near the edge of the wafer. As can be seen, no clear electron emission signals are detected in the spectra of the non-annealed sample or the stable sample. In the DLTS spectrum measured at the center of the degraded sample, four distinguished peaks can be observed. In the DLTS spectrum measured near the edge of the degraded wafer, the broad peak at around 180 K can be detected but the amplitude is much smaller than the one measured at the center of the wafer. Using a Laplace-DLTS analysis [113], [122], it was found that the peak at around 180 K consists of contributions from two electron emission signals. These five electron emission signals are labelled with $E_1$ to $E_5$, respectively.
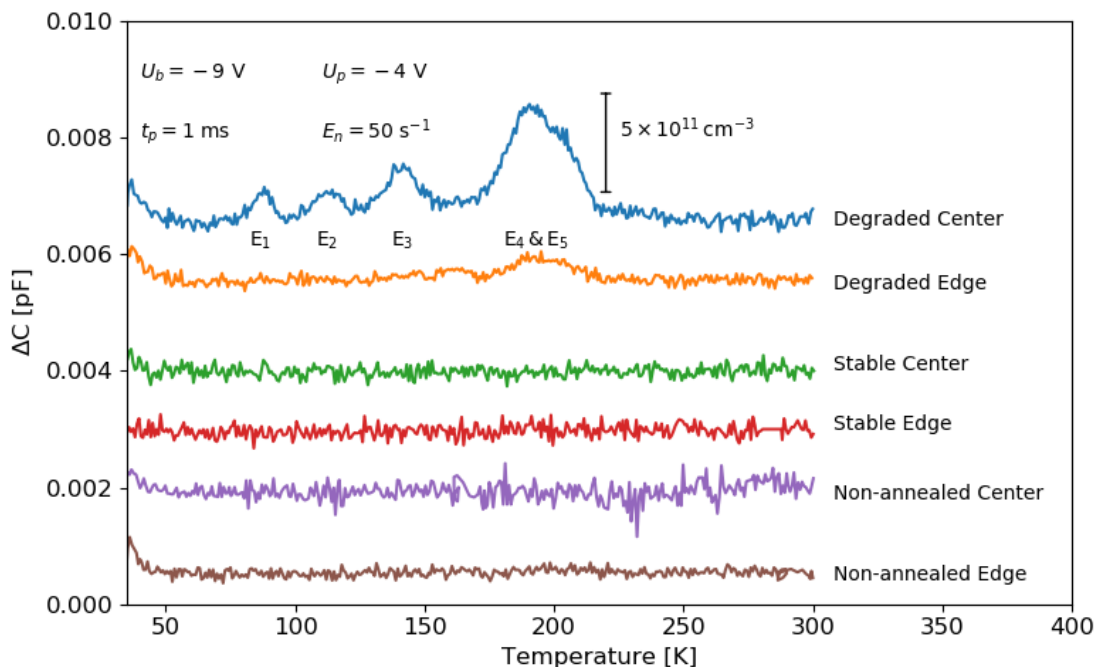


**Fig. 5.3** The DLTS spectra measured on a degraded wafer, a non-annealed wafer and a stable wafer. On each wafer, the measurements were taken at two locations: one in the center and one near the edge. The spectra are shifted for clarity. The measurement settings are shown in the graph. $U_b$ and $U_p$ are the reverse bias voltage and filling pulse voltage respectively, and $t_p$ is the filling pulse length.

By measuring the electron emission signals at various temperatures, their activation energies $E_{na}$ can be determined by an Arrhenius plot, as shown in Fig. 5.4. The extracted

$E_{na}$ and *apparent* electron capture cross sections $\sigma_{na}$ for $E_1$ to $E_5$ are listed in Table 5.1. These detected defect levels are similar to the ones identified by Grant *et al.* [22], yet different from the ones of Mullins *et al.* [197] The possible reason for that could be the different manufacturer of FZ silicon, as suggested by Mullins *et al.* [197] In the degraded samples studied by Grant *et al.* [22], $E_3$ center has the highest concentration among all the traps, whereas, according to this study $E_4$ and $E_5$ traps have higher concentrations. In either case, it is unclear which level is responsible for the dramatic decrease of lifetime.
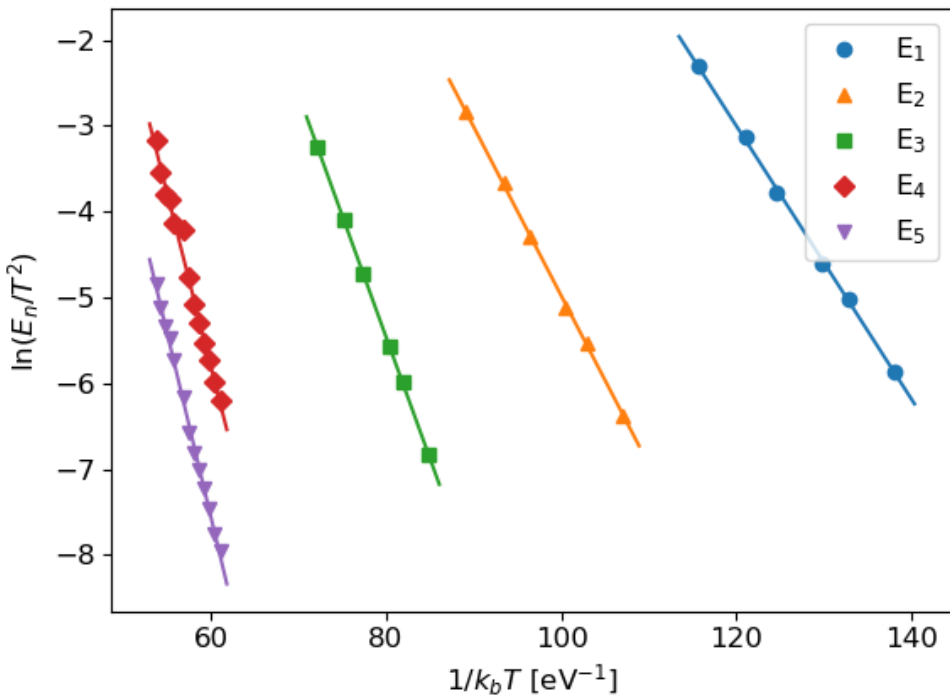


**Fig. 5.4** The Arrhenius plots for the five electron emission signals detected at the center of the degraded wafers labelled from $E_1$ to $E_5$. The solid lines indicate the linear fits of the data.

**Table 5.1** The $E_{na}$ and $\sigma_{na}$ for $E_1$ to $E_5$ detected in the degraded wafers

|  | $E_1$ | $E_2$ | $E_3$ | $E_4$ | $E_5$ |
|---|---|---|---|---|---|
| $E_{na}$ [eV] | 0.16±0.005 | 0.20±0.005 | 0.28±0.005 | 0.405±0.01 | 0.43±0.01 |
| $\sigma_{na}$ [cm$^2$] | $1.15\times10^{-15}$ | $3.71\times10^{-16}$ | $4.18\times10^{-15}$ | $1.54\times10^{-14}$ | $1.17\times10^{-14}$ |

It should be noted that $\sigma_{na}$ extracted from the Arrhenius plot is not the *actual* electron capture cross section of a defect level. To further investigate the capture characteristics of these activated defects, the DLTS spectra are measured with various filling pulse length $t_p$. In Fig. 5.5, the DLTS spectra measured with $t_p$ of 1 μs and 1 ms are shown. As can be seen, the change of the amplitudes of peaks from $E_1$, $E_2$ and $E_3$ are small upon the

change of the $t_p$. The amplitude of the E4 peak changes by around 50%. However, this change is still small compared to the change of $t_p$ (three orders of magnitude). On the contrary, the E5 peak seems to disappear completely in the DLTS spectra measured with $t_p$ of 1 µs. These results indicate that the $\sigma_n$ for E1, E2, E3 and E4 are relatively large and likely to be temperature independent and the $\sigma_n$ for E5 is likely to be small.
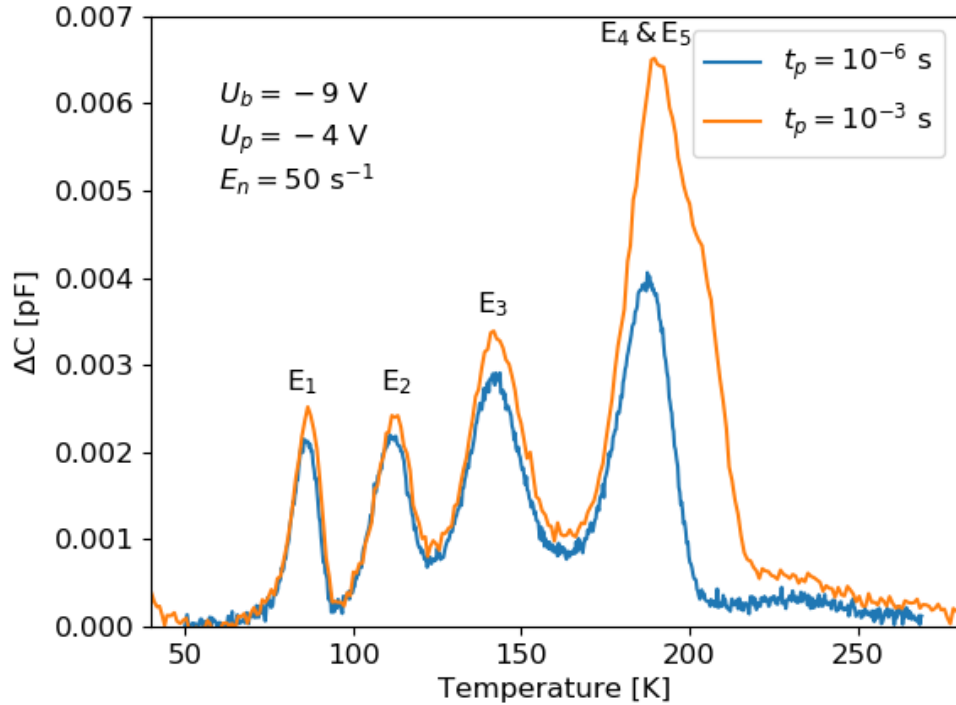


**Fig. 5.5** DLTS spectra measured at the center of the degraded wafer with two different filling pulse lengths $t_p$. The measurement settings are indicated in the Figure.

The $\sigma_n$ for E5 and its temperature dependency was measured. Unfortunately, due to the relatively high background doping concentration and the limitation of the used DLTS system, it is impossible to accurately measure the $\sigma_n$ for E1, E2, E3 and E4. The change of amplitude for the E5 peak as a function of $t_p$ is shown in Fig. 5.6. The change of the peak amplitude can be fit with the following equations:

$$\Delta C = C_1 + C_2 \left[ 1 - \exp\left( -\frac{t_p}{\sigma_n v_n n_0} \right) \right] \tag{5.1}$$

where $C_1$ and $C_2$ are parameters related to the properties of the capacitance. Since $\sigma_n v_n n_0$ can be fitted from the measured curves in Fig. 5.6 (a) and $v_n$ and $n_0$ are known parameters, $\sigma_n$ can be easily calculated. The calculated $\sigma_n$ at four different temperatures are plotted in Fig. 5.6 (b). As can be seen, $\sigma_n$ follows an exponential temperature dependency: $\sigma_n =$

$\sigma_\infty \exp\left(\frac{-E_\infty}{k_bT}\right)$ with $\sigma_\infty = 6.9 \times 10^{-16}$ cm$^2$ and $E_\infty = 0.19$ eV . This temperature dependency indicates that the most likely electron capture mechanism is multi-phonon emission capture [201].
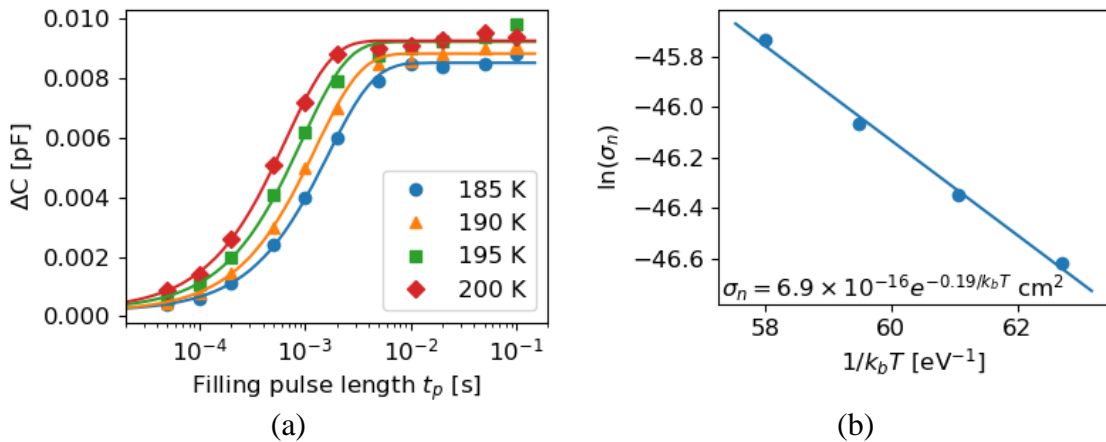


**Fig. 5.6** The electron capture characteristics for the electron emission signal $E_5$ measured at the center of the degraded sample. (a) the DLTS peak amplitude as a function of the filling pulse length measured at four temperatures. (b) the extracted $\sigma_n$ as a function of temperature. The solid line indicates a linear fit of the Arrhenius plot.

### 5.3.3 MCTS: defect levels in the minority carrier bandgap half

Since DLTS detects the emission signal of majority carriers, it usually only measures the defect level in the majority carrier bandgap half (the upper half of the bandgap for *n*-type material). In order to investigate the possibility of defect in the lower half of the bandgap, minority carrier transient spectroscopy measurements were concluded. In MCTS measurements, minority carriers were generated (in this study, by light excitation), and thus the minority carrier emission signal can be detected [118].

In Fig. 5.7, the MCTS spectra measured on one wafer from each group are shown. The MCTS measurements were conducted at the center of the wafers. As can be seen, in the MCTS spectrum measured on the degraded sample, a peak from hole emission is detected (labelled as $H_1$). On the MCTS spectra measured at the non-annealed wafer and stable wafer, no hole emission signal can be detected. This result indicates that at least one defect level in the lower half of the bandgap is activated during the thermal annealing at 500 °C.
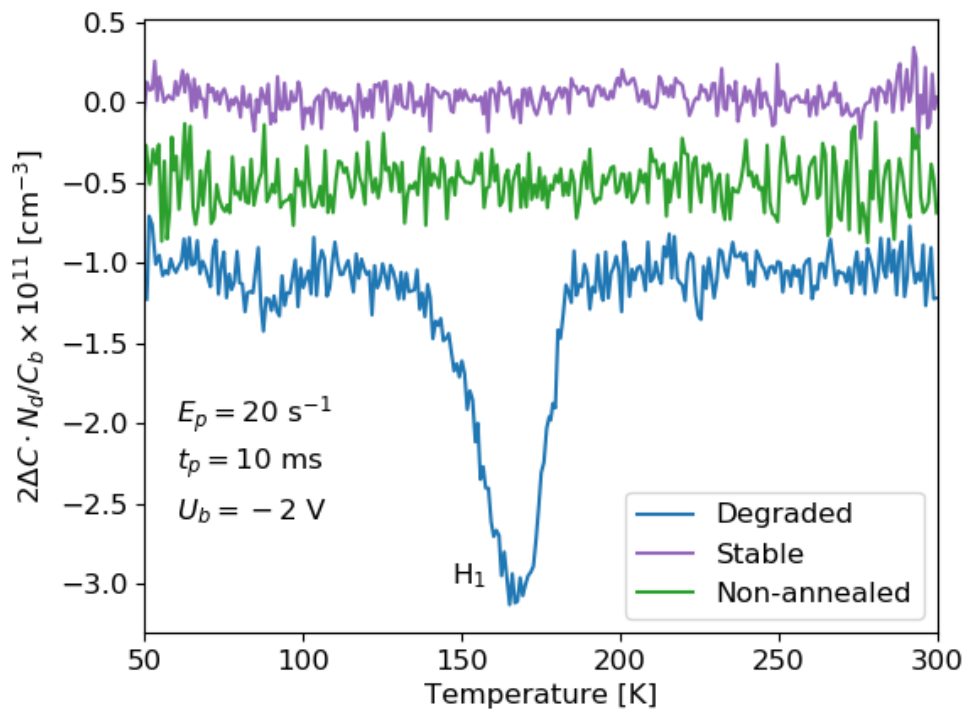
**Fig. 5.7** The MCTS spectra measured on the center a degraded wafer, a non-annealed wafer and a stable wafer. The spectra are shifted for clarity. The measurement settings are shown in the graph. The $y$ axis is converted to an estimation of defect density. $N_d$ is the donor concentration and $C_b$ is the base capacitance.
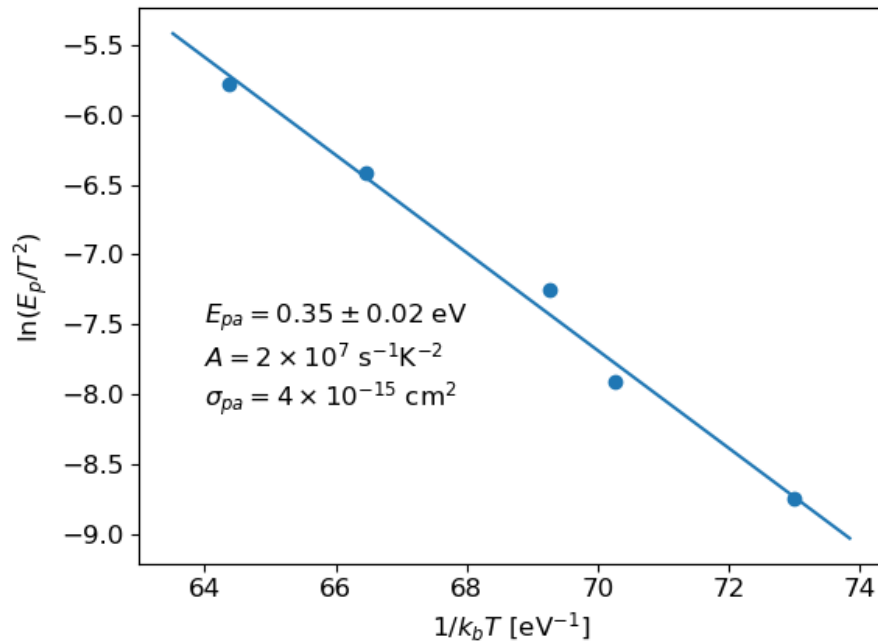


**Fig. 5.8** The Arrhenius plots for the hole emission signal $H_1$ detected at the center of the degraded wafer. The solid lines indicate the linear fit in the Arrhenius plot.

Similar to DLTS measurements, the activation energy $E_{pa}$ and the apparent hole capture cross section $\sigma_{pa}$ of the activated defect level can be determined by measuring the hole emission signal at various temperatures as shown in Fig. 5.8. From the Arrhenius plot, an activation energy $E_{pa}$ of 0.35±0.02 eV and $\sigma_{pa}$ of 4×10$^{-15}$ cm$^2$ are extracted.

Unfortunately, due to the relatively low defect concentration, the capture characteristics of H$_1$ cannot be accurately measured. Therefore, the value of its actual $\sigma_p$ nor its temperature dependency cannot be determined.

## 5.3.4 TIDLS: identify the dominant defect level

As revealed by the DLTS and MCTS measurements, multiple defect levels have been activated during annealing at 500 °C. Nevertheless, due to the difficulty of measuring the capture cross sections, it is challenging to identify which levels are responsible for the dramatic reduction of the carrier lifetime after the annealing. As described in Chapter 2, lifetime spectroscopy characterizes defects from the measured carrier lifetime, and thus it is sensitive to the dominant recombination defects in the sample. Therefore, in this section TIDLS will be combined with the extracted information from the DLTS/MCTS measurements to provide a better understanding of the electrical properties of the defects.

### 5.3.4.1 Room temperature lifetime measurements

Before presenting the temperature dependent measurements, it is worthwhile to first discuss the room temperature lifetime measurements. In Fig. 5.9, the room temperature injection dependent lifetime curves of one sample from each group after the superacid-derived passivation are shown. All measurements were done at the center of the wafer by a standard Sinton WCT-120 lifetime tester [82]. The sensor area is a circular with a diameter of 40 mm; therefore, the non-uniformity in the degraded sample does not impact the measurement. As can be seen, the non-annealed sample and the stable sample both show lifetime above 1 ms whereas the degraded sample has lifetime of around 10 µs. The thermally activated defects lead to a lifetime reduction of two orders of magnitude across the measured injection range. The lifetime of the degraded sample after re-passivation by PECVD a-Si, which is also shown in Fig. 5.9. As can be seen, similar effective lifetimes are obtained by the a-Si and by the superacid derived passivation. This indicates: (a) the effective lifetime of the degraded sample is dominated by the thermally activated bulk defects; and (b) the PECVD process did not modify the activated defects. After the

temperature and injection dependent lifetime measurement, the lifetime of the degraded samples at room temperature was measured again. As can be seen, the lifetime shows no change after the temperature dependent measurements. This indicates that the thermally activated defects are not changed during TIDLS measurements. The results from these room temperature measurements are favorable for the TIDLS analysis as: (a) the fact that the defects are stable during the measurements makes the comparison of temperature dependent measurements possible; and (b) the dominance of the activated defects reduced the impact of other recombination channels on the lifetime spectroscopy analysis.
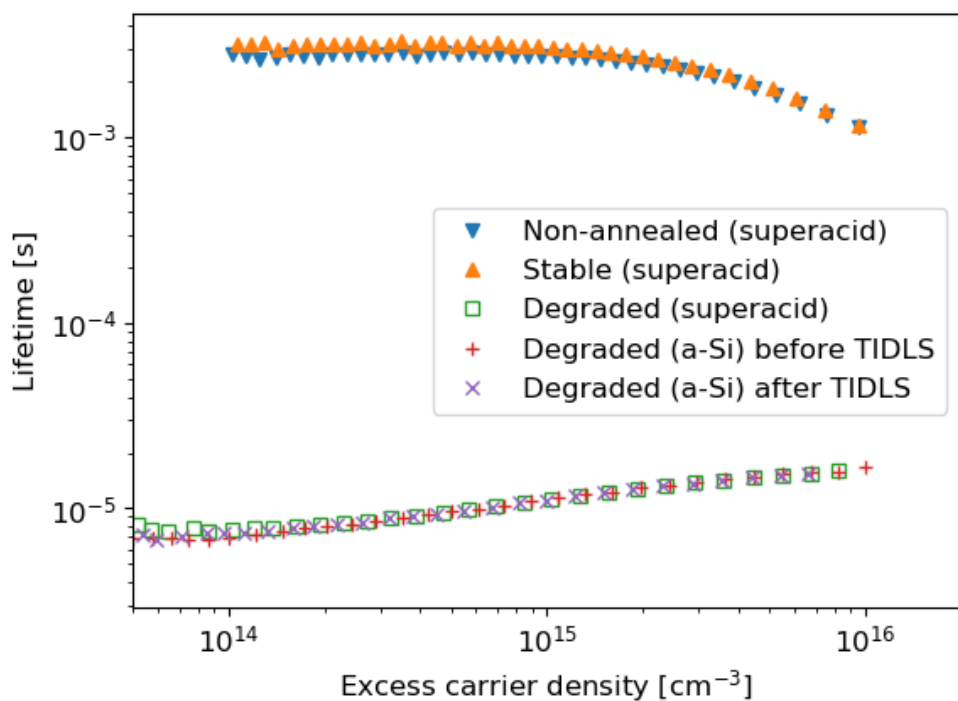


**Fig. 5.9** Room temperature injection dependent lifetime of the non-annealed wafer, degraded wafer and stable wafer with superacid-derived passivation. The room temperature lifetime curves of the degraded wafer with PECVD a-Si passivation before and after the temperature dependent measurements are also shown.

### 5.3.4.2 Temperature and injection dependent lifetime measurements

The injection dependent lifetime of the degraded wafer and the stable wafer were measured from −50 °C to 150 °C, using the developed lifetime tester described in Chapter 3. The results are shown in Fig. 5.10.
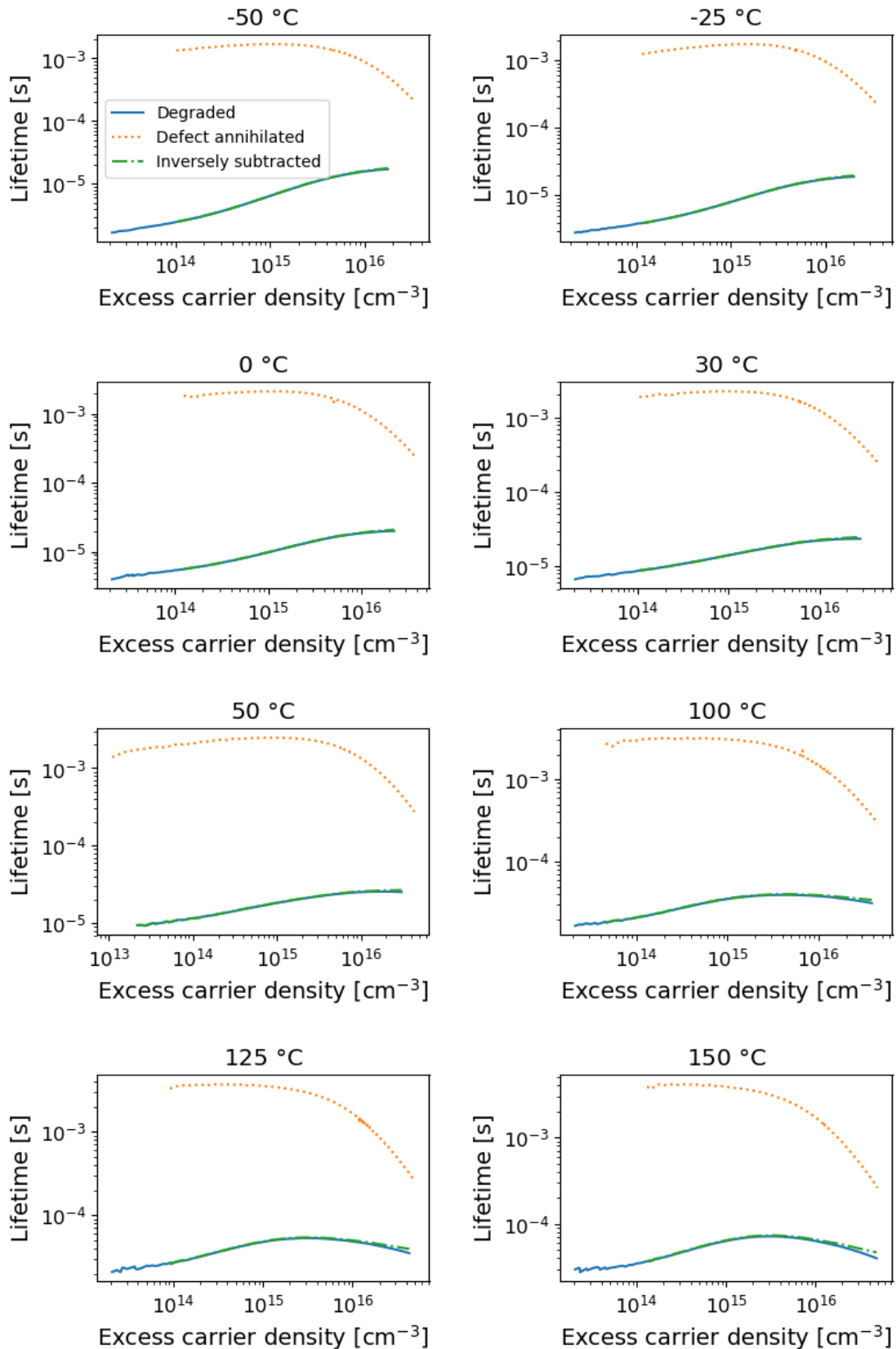
**Fig. 5.10** Injection dependent lifetime of the degraded sample (measured at the center) $\tau_{degraded}$ and of the stable sample $\tau_{stable}$ at each measured temperature. The green dash-dotted lines indicate the inversely subtracted lifetime of $\tau_{stable}$.from $\tau_{degraded}$.

In order to extract the defects related recombination lifetime from the measured effective lifetime, the lifetime of the stable sample $\tau_{stable}$ was inversely subtracted from the lifetime of the degraded wafer $\tau_{degraded}$:

$$\tau_{defects} = \cfrac{1}{\cfrac{1}{\tau_{degraded}} - \cfrac{1}{\tau_{stable}}} \tag{5.2}$$

Since the degraded wafer and the stable wafer has the same doping concentration and were passivated using the same PECVD process, this operation cancels out the intrinsic lifetime and the surface lifetime, and the resulted $\tau_{defects}$ is the recombination lifetime related to the thermally activated defects.

The inversely subtracted lifetime at each temperature is also shown in Fig. 5.10. As can be seen, for all the measured temperatures, the inversely subtracted lifetime is close to the effective lifetime of the degraded sample, indicating again that the effective lifetime of the degraded sample is dominated by the thermally activated bulk defects. For the accuracy of the TIDLS analysis, we still use the extracted $\tau_{defects}$.
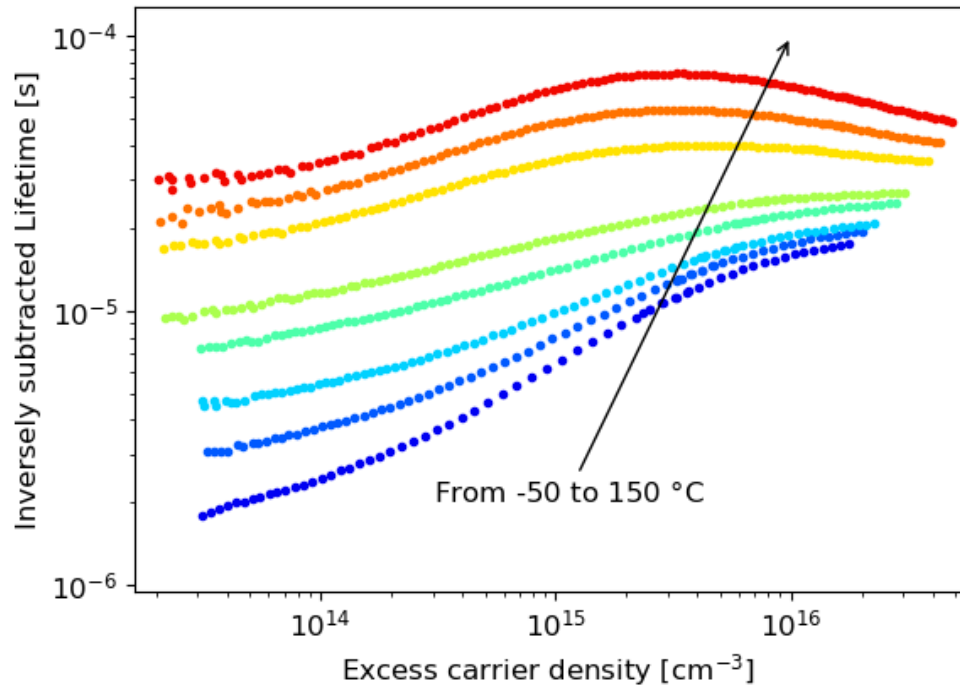


**Fig. 5.11** The inversely subtracted lifetime $1/(1 / \tau_{degraded} - 1/\tau_{stable})$ at each measured temperature of the degraded sample

For the ease of comparison, the inversely subtracted lifetime $\tau_{defects}$ curves at all measured temperature of the degraded sample are shown in Fig. 5.11. As can be seen, $\tau_{defects}$ increases as temperature increases. The temperatures indicated in Fig. 5.10 and Fig. 5.11 are the stage set temperature instead of the actual sample temperature. The actual sample temperature has been calibrated using the procedure described in Chapter 3. For the lifetime spectroscopy analysis, the calibrated actual sample temperature instead of the stage set temperature is used.

### 5.3.4.3 Defect parameterization

*(1) Linearization of SRH lifetime*

After the extraction of defects related recombination lifetime $\tau_{defects}$, the $\tau_{defects}$ was checked as to whether it is dominated by a single-level defect. This can be done by applying the linearization method [99] described in Chapter 4. Instead of plotting lifetime as a function of $\Delta n$ as shown in Fig. 5.10 and Fig. 5.11, the lifetime as a function of $X$ $(n/p)$ is each measured temperature is plotted in Fig. 5.12.

As can be seen, after the change of variable, the lifetime at all measured temperature shows a concave shape, indicating that more than one defect levels are impacting the measured lifetime. Hence, more than one defect levels were activated during annealing at 500 °C, which is in alignment with previous DLTS/MCTS results. As mentioned previously in Chapter 4, this can be resulted from either two or more single-level defect, or one or more multi-level defect, or even a combination of single-level defects and multi-level defects. However, it seems that two defect levels (two single-level defect or one two-level defect) are sufficient to fit the measured lifetime at all measured temperatures. Therefore, following Occam's razor, this study assumes only two defect levels. This section assumes two single-level defects, while the next section considers the possibility of a two-level defect.

In Fig. 5.12, the fit of the measured lifetime assuming two single-level defects is shown as a red solid line. The lifetimes of the two single-level defects are indicated by the orange dashed line and the green dahs-dotted line. As can be seen, the harmonic sum of lifetime from two single-level defects provides good fitting quality for all the measured temperatures.
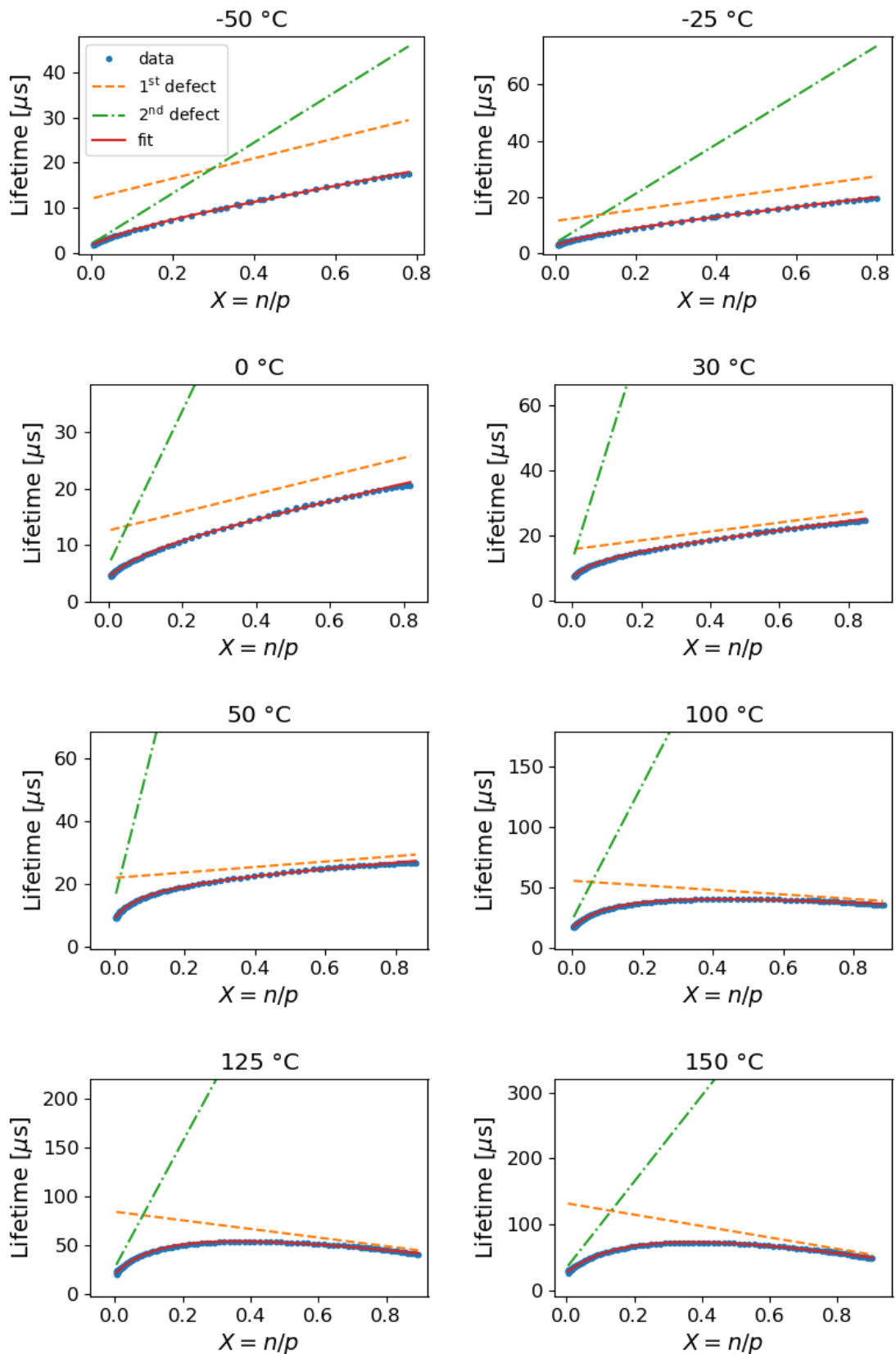
**Fig. 5.12** The defect related recombination lifetime plotted as a function of *X* at each measured temperature. In each subfigure, the green dash-dotted and orange dotted lines indicate the lifetimes of two single-level defects used to fit the measured lifetime. The red solid line indicated the harmonic sum of the lifetimes from the two single-level defects.

As can be seen from Fig. 5.12, in all the measured temperature range, the 1st single-level defect dominants most of the injection range. For temperature below 100 °C, the slope of the linearized lifetime curve for the 1st defect is positive. As the measurement temperature increases above 100 °C, the slope becomes negative. As mentioned in Chapter 4, this change of sign is beneficial for lifetime spectroscopy analysis as it reduces the uncertainty of the extracted parameters. The 2nd single-level defect only dominants very low injection levels. The linearized lifetimes for the 2nd defect at all measured temperatures are positive. These makes the parameterization of the second defect more prone to measurement uncertainties. Therefore, the following discussion focuses only on the 1st single-level defect.

*(2) Conventional DPSS method and Newton-Raphson method*

The TIDLS results for the 1st defect are presented by the DPSS curves [21] shown in Fig. 5.13. In the bottom three subfigures, the solution space curves for the product of $N_t$ and $\sigma_n$, product of $N_t$ and $\sigma_p$ and $k$ are presented. It should be noted that in lifetime spectroscopy $N_t$ cannot be separated from the capture cross sections, and thus the absolute value of the capture cross section cannot be extracted. However, as $N_t$ is independent of temperature, the DPSS curves of the product of $N_t$ and $\sigma_{n/p}$ are equivalent to the DPSS curves for $\sigma_{n/p}$.

On the top subfigure, the standard deviation (SD) of each set of DPSS curves at various temperatures is presented. The standard deviation is normalized by the average value of each set of DPSS curves to avoid the impact of the absolute values. The SD curves are only plotted in the energy range of the intersection of the domains of all DPSS curves. This range is the possible range of the energy level of the dominant defect, as for any energy level outside of this range, at least one of the measured injection dependent lifetime curve cannot be fitted. Theoretically, if $\sigma_n$ is temperature independent, then the actual defect energy level should be found in the minima of the SD curve of $\sigma_n$. Since at this stage of the analysis, the temperature dependency of the capture cross sections is unknown, the SD curves of $\sigma_n$, $\sigma_p$, and $k$ are all shown. As can be seen, in the lower half of the bandgap, the possible range of the defect energy level is quite narrow, and all the SD curves show a local minimum value at around $E_t - E_V = 0.25$ eV. In the upper half of the bandgap, the possible range of the defect energy level is in the range $E_C - E_t >$

0.3 eV. The minimum points of different SD curves are at different energy levels (see top figure).
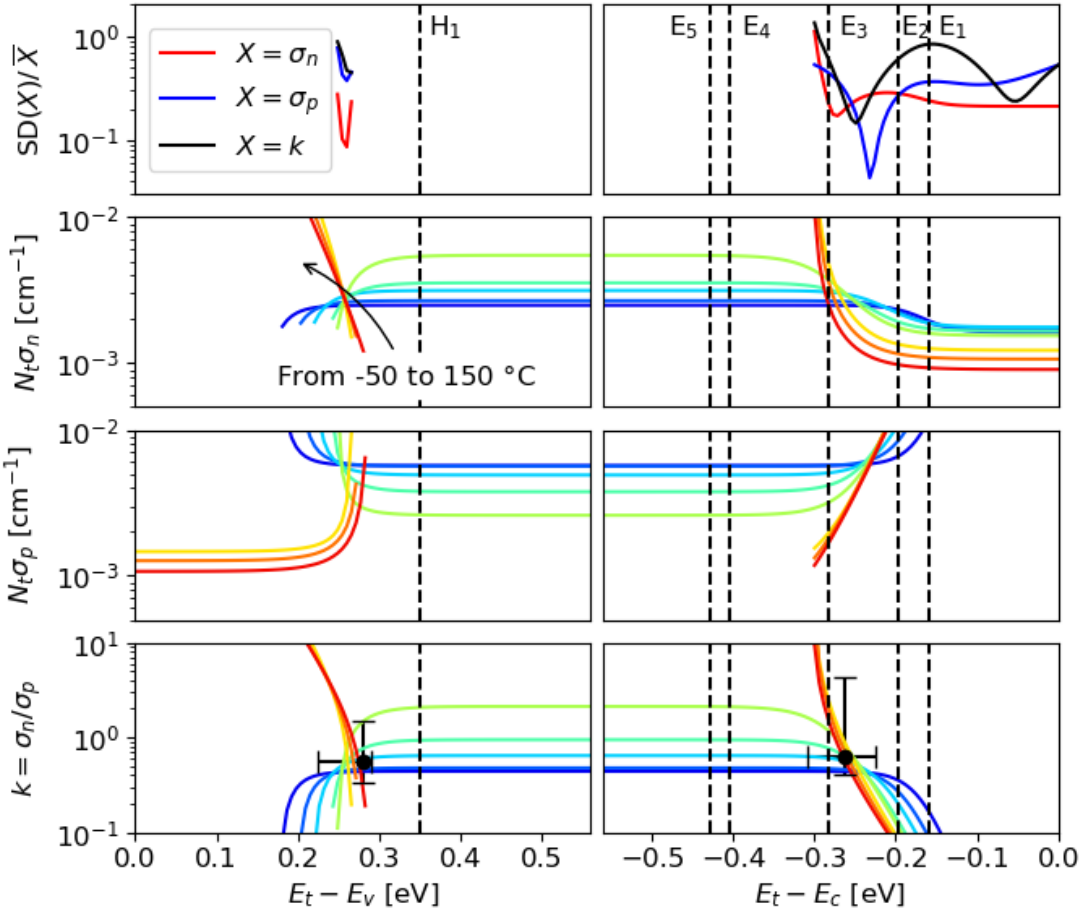


**Fig. 5.13** Defect parameter solution curves of the product of $N_t$ with $\sigma_n$, product of $N_t$ with $\sigma_p$, and $k$ of the 1st single-level defect extracted from the two defect fitting. The top subfigure shows the SD of each set of DPSS curves at various temperatures normalized by their average values. The vertical dashed lines indicate the activation energies of the emission signals detected by DLTS or MCTS. The black dots and error-bars indicate the defect parameters and their uncertainties obtained by Newton-Raphson method.

Apart from the analysis using the conventional DPSS method, the Newton-Raphson method proposed in Chapter 4 is also applied to analyze the TIDLS data. The extracted $E_t$ and $k$ values via the Newton-Raphson method are shown in the bottom subfigure of Fig. 5.13 by black dots. These extracted values are using the data from all the measured temperatures. As described in Chapter 4, data of only two different temperatures are required for the extraction of $E_t$ and $k$. By applying the Newton-Raphson method for each set of two temperatures, the uncertainty range of the extracted values can be obtained. This is indicated by the error-bars associated to the black dots in Fig. 5.13. As can be seen, the extracted values of $E_t$ via the Newton-Raphson method are quite close to the minima

of the standard deviation curve for $k$ in both bandgap halves. This highlights again the simplicity of the Newton-Raphson method and its equivalence to the conventional DPSS method. However, the challenging of relying only on the Newton-Raphson method here is that the capture cross sections need to be assumed as temperature independent. Unfortunately, the information gathered from DLTS and MCTS could not support this assumption. Therefore, the following discussion will be based on the analysis using the conventional DPSS method.

### *(3) Combining TIDLS with DLTS/MCTS*

In the other parts of this thesis, $E_t$ is usually referenced to $E_i$. In this section in order to compare the TIDLS results with previous DLTS/MCTS results, the DPSS curves for the lower half of the bandgap is plotted against $E_t - E_V$, and the DPSS curves for the upper half of the bandgap is plotted against $E_C - E_t$. The activation energies for the electron emission signals and the hole emission signal detected by DLTS/MCTS are plotted as vertical dashed lines. However, it should be noted that these activation energies extracted from the Arrhenius plots can be different from the actual defect energy levels due to the temperature dependency of capture cross sections [104], [114].

Assuming first that $\sigma_n$ is temperature independent, then $E_t$ of the defect is expected to be found in the minima of the standard deviation curve of $\sigma_n$ (red curve in the top subfigure of Fig. 5.13). Meanwhile, the defect $E_t$ should be close to the activation energy extracted by DLTS (if the temperature dependency of the $E_t$ itself is neglected). Under this circumstance, E3 is the most likely defect level, as its activation energy is very close to the local minimum of the standard deviation curve for $\sigma_n$ in the upper half of the bandgap. Although measurement of the actual $\sigma_n$ via DLTS has not been successful, it is indicated that $\sigma_n$ of E3 is relatively large and likely to be temperature independent. From the DPSS curve, the product of $N_t$ and $\sigma_n$ can be extracted at this energy level, which is in the order of $10^{-3}$ cm$^{-1}$. Using the $N_t$ estimated by DLTS and the $\sigma_{na}$ of E3 to calculate this product, a value in the order of $10^{-3}$ cm$^{-1}$ is obtained. This good agreement also supports the hypothesis of E3 as the dominant defect level.

### *(4) Considering the temperature dependency of capture cross sections*

Assuming $\sigma_n$ is temperature independent, previous analysis seems to indicate that E3 is likely to be the dominant defect level. However, as direct measurement of $\sigma_n$ as a function

of temperature has not been successful, it is important to consider the possibility of temperature dependent capture cross sections. Assuming the capture cross sections are temperature dependent, the SD curves in Fig. 5.13 cannot be used.

From literature it is known that the capture cross sections can have different temperature dependencies, depending on the capture mechanism [21], [104]. If the capture mechanism is classical Auger capture [202] or radiative capture [203], then the capture cross section is usually temperature independent. If the capture mechanism is cascade capture or excitonic-enhanced Auger capture [38], [204]–[206], then the capture cross section follows a power law temperature dependence:

$$\sigma(T) = \sigma_0 T^{-\alpha} \tag{5.3}$$

If the capture mechanism is multi-phonon emission capture [201], then the capture cross section follows an exponential temperature dependence:

$$\sigma(T) = \sigma_\infty \exp\left(\frac{-E_\infty}{k_b T}\right) \tag{5.4}$$

If the capture mechanism is two-stage cascade capture [207], then the capture cross section follows a mix of power law and exponential temperature dependence:

$$\sigma(T) = T^{-2} \exp\left(\frac{\Delta E}{k_b T}\right) \tag{5.5}$$

From the DPSS curves, the values of $N_t \sigma_n$ and $N_t \sigma_p$ can be extracted as a function of temperature at any assumed energy level. Therefore, at any assumed energy level $\sigma(T)$ can be fitted using the four possible temperature dependencies described by Eqs. (5.3) to (5.5), and $\sigma(T) = constant$. The quality of the fitting is indicated by the fitting residual defined in similar way as in Chapter 4. For $\sigma(T) = constant$, the "fitting residual" is the standard deviation normalized by the average value. In Fig. 5.14, the lowest fitting residual value among the four different fitting at each possible energy level is shown. The blue symbols indicate the lowest residual for fitting $\sigma_n(T)$, whereas, the orange symbols indicate the lowest residual for fitting $\sigma_p(T)$. The green symbols represent the sum of fitting residual of fitting $\sigma_n(T)$ and $\sigma_p(T)$. Similar to previous figures, the activation energies of the emission signals detected by DLTS or MCTS are indicated by the vertical dashed lines.

The dot symbol indicates that the optimal fitting at that energy level is achieved by the power law temperature dependency using Eq. (5.3). A square symbol indicates the optimal fitting at that energy level is achieved by the exponential law temperature dependency using Eq. (5.4). A triangle symbol indicates the optimal fitting at that energy level is achieved by the mix of power law and exponential law temperature dependency using Eq. (5.5). It is found that in all energy levels, at least one of the three temperature dependency provides smaller fitting residual than the case of $\sigma(T) = constant$. It should be noted that there are infinite possible values of $E_t$. The reason for having only finite discrete data points in Fig. 5.14 is that the fitting was done only to discrete number of $E_t$.
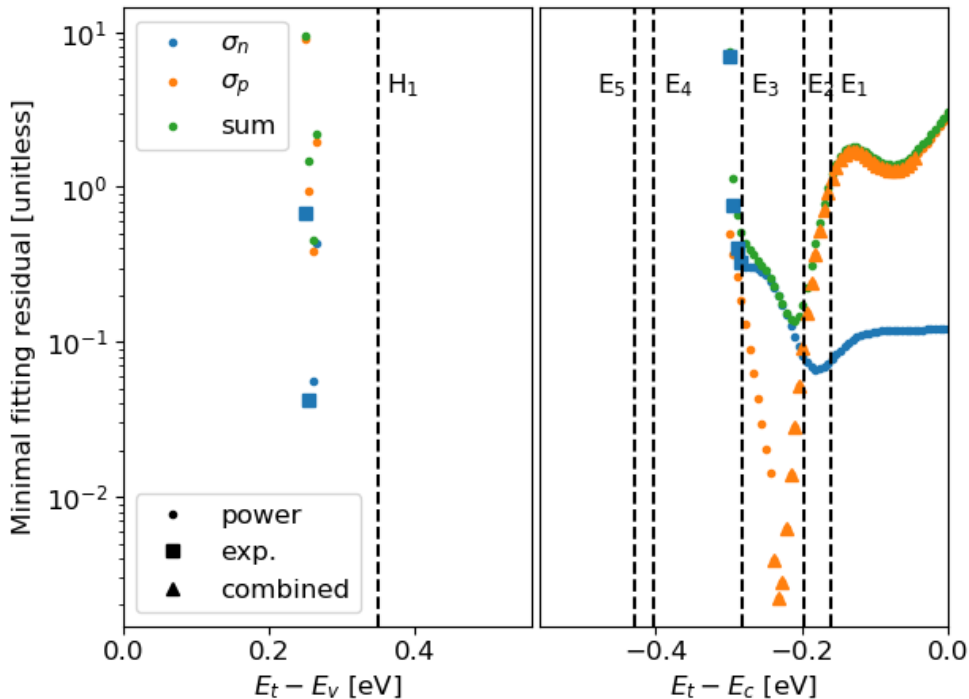


**Fig. 5.14** The lowest fitting residual values of fitting $\sigma_n(T)$ and $\sigma_p(T)$ of the dominant defect using the three possible temperature dependencies described by Eqs. (5.3) to (5.5). The different symbols indicate the temperature dependency that provides the optimal fitting. The vertical dashed lines indicate the activation energies of the emission signals detected by DLTS or MCTS.

Let us first consider the possibility of a defect in the lower half of the bandgap. We can notice that the activation energy of level H₁ is not within the possible range of energy level obtained by TIDLS. The only possibility for H₁ to be the dominant defect level is that the activation energy of H₁ is different from the defect energy level due to the temperature dependency of $\sigma_p$. From Fig. 5.14, it can be noticed that the optimal fitting of $\sigma_p(T)$ is always achieved by a power law dependency. This indicates that if $\sigma_p$ is

temperature dependent, it most likely follows the power law dependency. However, the impact of a power low dependency on the extraction of activation energy via DLTS Arrhenius plot is small, as the Arrhenius plot represents an exponential dependency, which is usually much stronger than a power law dependency. In order to illustrate this, the energy level is assumed to be at $E_t - E_V = 0.26$ eV (the point with the minimal fitting residual for $\sigma_p$ in the lower half of the bandgap). The extracted $\sigma_p$ at this energy level is shown in Fig. 5.15 (a). As can be seen, it can be fitted with relatively high fitting quality using a power law dependency: $\sigma_p(T) = \sigma_0 T^{-1.8}$. Considering this temperature dependency, the hole emission rate measurements by MCTS can be written as:

$$\frac{E_p}{T^2} = \gamma \sigma_p(T) \exp\left(-\frac{E_t - E_V}{k_b T}\right) = \gamma \sigma_0 T^{-1.8} \exp\left(-\frac{E_t - E_V}{k_b T}\right) \tag{5.6}$$

where $\gamma$ is material dependent constant independent of temperature. If an Arrhenius plot of $E_p/T^2$ (as in conventional MCTS analysis) is used to extract the value of $E_t - E_V$, the extracted value is impacted by the term $T^{-1.8}$. In order to remove this impact, the term $E_p/T^{(2-1.8)} = E_p/T^{0.2}$ instead of $E_p/T^2$ is used for the Arrhenius plot. The result is shown in Fig. 5.15 (b) and the extracted activation energy is 0.376 eV, only 0.026 eV different from the original activation energy (0.35 eV). This new activation energy is still outside the possible range of the energy levels as defined by the TIDLS analysis in the lower half of the bandgap. Therefore, it can be concluded that the defect level $H_1$ identified by MCTS cannot be the dominant defect level responsible for the dramatic lifetime degradation.



(a)                            (b)
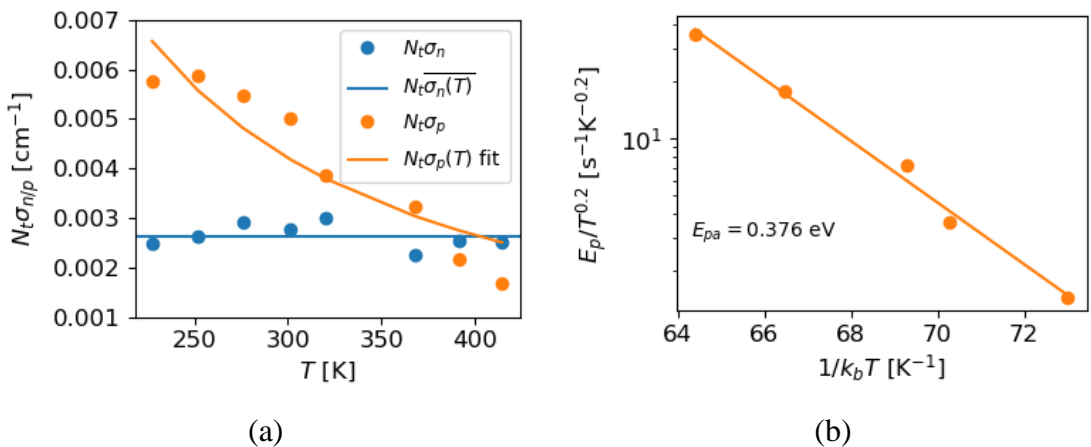
**Fig. 5.15** (a) $N_t \sigma_n(T)$ and $N_t \sigma_p(T)$ extracted at $E_t - E_V = 0.26$ eV for the dominant defect in TIDLS analysis. The blue line indicates the average value of $N_t \sigma_n$. The orange line indicates a power law fit of $N_t \sigma_p(T)$. (b) MCTS Arrhenius plot assuming a power law temperature dependent $\sigma_p$. The solid line indicates the linear fit of the Arrhenius plot.

Let us now consider the possibility of a defect in the upper half of the bandgap. First, it is noticed that the activation energies of E4 and E5 are not within the possible energy range confined by TIDLS analysis. For E5, the actual $\sigma_n(T)$ has been measured to be $\sigma_n = \sigma_\infty \exp\left(\frac{-E_\infty}{k_b T}\right)$ with $\sigma_\infty = 6.9 \times 10^{-16}$ cm$^2$ and $E_\infty = 0.19$ eV . Taking this temperature dependency into consideration, a corrected energy level for E5 can be determined as 0.24 eV below $E_C$ instead of the original 0.43 eV. However, at this corrected energy level, $\sigma_n(T)$ can be best fitted by a power law dependency (see Fig. 5.14). An exponential fit cannot be used to fit $\sigma_n(T)$ at this energy level as $\sigma_n$ decreases with temperature. This conflicts with the properties of E5 identified by DLTS; therefore, E5 cannot be the dominant defect. The possibility of E4 can be ruled out with similar reason for ruling out H1. Even considering the temperature dependency of $\sigma_n(T)$, the deviation between the activation energy of E4 and the possible energy range defined by TIDLS is still too large.
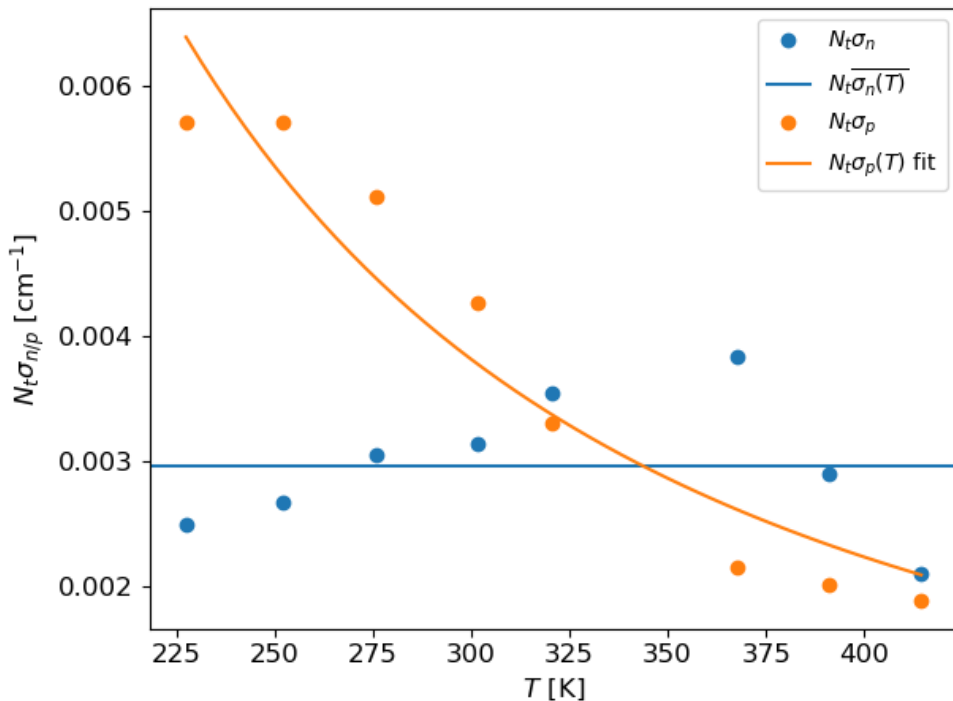


**Fig. 5.16** $N_t\sigma_n(T)$ and $N_t\sigma_p(T)$ extracted at the activation energy of E3 for the dominant defect in TIDLS analysis. The blue line indicates the average value of $N_t\sigma_n$. The orange line indicates a power law fit of $N_t\sigma_p(T)$.

As discussed previously, E3 is likely to be the defect level of this dominant defect if $\sigma_n$ is temperature independent. At the activation energy of E3, $\sigma_p(T)$ can be fitted with a power law dependency with good fitting quality. The $N_t\sigma_n(T)$ and $N_t\sigma_p(T)$ extracted at

the activation energy of $E_3$ are shown in Fig. 5.16. $\sigma_n$ seems to remain relatively constant across the measured temperature range. From the fitting $\sigma_p(T) = \sigma_0 T^{-\alpha}$ with $\alpha = 1.86$ can be found. Therefore, $E_3$ remains to be a possible candidate of the dominant defect level.
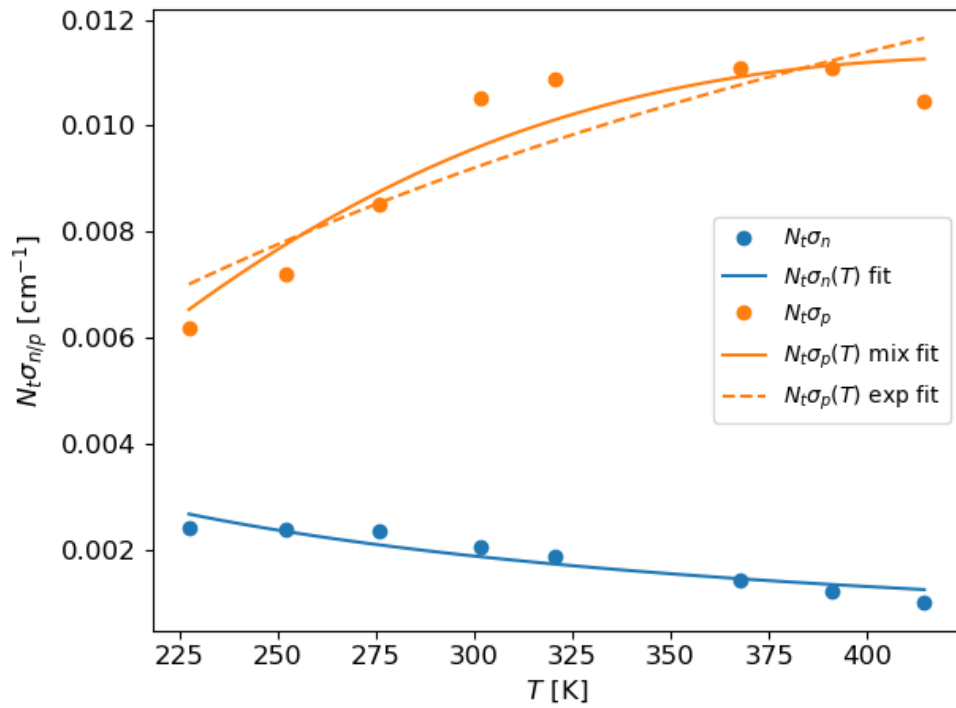


**Fig. 5.17** $N_t \sigma_n(T)$ and $N_t \sigma_p(T)$ extracted at the activation energy of $E_2$ for the dominant defect in TIDLS analysis. The blue line indicates a power law fit of $N_t \sigma_n$. The orange solid line indicates the fit by a mix of power law and exponential temperature dependence of $N_t \sigma_p(T)$. The orange dashed line indicates the fit by an exponential temperature dependence of $N_t \sigma_p(T)$.

Considering the temperature dependency of $\sigma_n$, the activation energies of $E_1$ and $E_2$ are also within the possible energy range. At the activation energy of $E_1$, the fitting residual for $\sigma_p(T)$ is much higher than the case of $E_2$. Therefore, between $E_1$ and $E_2$, it seems like $E_2$ is more likely to be the dominant defect level. The $N_t \sigma_n(T)$ and $N_t \sigma_p(T)$ extracted at the activation energy of $E_2$ are shown in Fig. 5.17. From the fitting $\sigma_n(T) = \sigma_0 T^{-\alpha}$ with $\alpha = 1.27$ can be determined. The impact of this power law dependency on the DLTS Arrhenius plot is evaluated to be only 0.01 eV change of the activation energy. From Fig. 5.14 it seems that at the activation energy of $E_2$, $\sigma_p(T)$ is best fitted with a mix of power law and exponential temperature dependence $\sigma_p(T) = T^{-2} \exp\left(\frac{\Delta E}{k_b T}\right)$. This fitting is shown in Fig. 5.17 as the orange solid line and indicates $\Delta E$ to be $-0.08$ eV.

Nevertheless, $\sigma_p(T)$ can also be fitted by an exponential law $\sigma(T) = \sigma_\infty \exp\left(\frac{-E_\infty}{k_b T}\right)$ with good fitting quality and extracted $E_\infty$ of 0.02 eV (orange dashed line).

From the previous analysis, combining TIDLS results and DLTS/MCTS results, we can conclude that the most likely defect level for the dominant defect is either the E₃ or E₂ identified by DLTS based on the information we have now. The parameters of these two possible candidates of the dominant defect level are summarized in Table 5.2. It was mentioned previously that the product $N_t \sigma_n$ for E₃ extracted from TIDLS is in the same order of magnitude as $N_t \sigma_{na}$ extracted by DLTS. For E₂, it was found that $N_t \sigma_n$ extracted from TIDLS is one order of magnitude higher than $N_t \sigma_{na}$ extracted by DLTS. However, it should be noted that the actual capture cross section $\sigma_n$ can be different from the apparent capture cross section $\sigma_{na}$ obtained from the DLTS Arrhenius plot [114]. Meanwhile, the defect concentration $N_t$ estimated by DLTS could also suffer from some uncertainties. Therefore, it cannot be determined whether E₂ or E₃ is the dominant defect level based on the comparison of $N_t \sigma_n$ and $N_t \sigma_{na}$. It should also be noted that it was also assumed that the dominant defect level can be detected by DLTS and MCTS. It is possible that the most recombination active defect cannot be detected by DLTS/MCTS, as for example in the case of BO related defect [124].

**Table 5.2** The possible parameters of the dominant defect assuming two single-level defects

| | E₃ | E₂ |
|---|---|---|
| $E_C - E_t$ | 0.28±0.005 eV | 0.21±0.01 eV |
| $\sigma_n(T)$ | $\sigma_n(T) = constant$ | $\sigma_n(T) = \sigma_0 T^{-\alpha}$<br>$\alpha = 1.27$ |
| $\sigma_p(T)$ | $\sigma_p(T) = \sigma_0 T^{-\alpha}$<br>$\alpha = 1.86$ | $\sigma_p(T) = T^{-2} \exp\left(\frac{\Delta E}{k_b T}\right)$<br>$\Delta E = -0.08$ eV<br><br>$\sigma_p(T) = \sigma_\infty \exp\left(\frac{-E_\infty}{k_b T}\right)$<br>$E_\infty = 0.02$ eV |

In order to have a more decisive conclusion on the dominant defect level, in the future it is worthwhile to measure the lifetime of samples with various doping concentration, as well as *p*-type material so that $N_{dop}$-IDLS can be performed. In this case, the analysis will not be impacted by the temperature dependency of the capture cross section. Furthermore, as done by most of the previous TIDLS analysis, a hidden assumption in this work is that the temperature dependency of defect level is negligible [21]. By performing $N_{dop}$-IDLS

this assumption can be removed. The only issue with $N_{dop}$-IDLS is the assumption that the thermally activated defects in samples with different doping concentrations is the same.

A similar analysis process is also conducted for the 2nd single-level defect used to fit the TIDLS data. As mentioned previously, lifetime spectroscopy results for the 2nd single-level defect suffer from much larger uncertainty than in the case of the 1st defect. Therefore, the conclusions for the 2nd defect cannot be made at this stage.

### 5.3.4.4 Possibility of two-level defect

As mentioned in Chapter 4, when the defect related recombination lifetime cannot be fitted with just one single-level defect, the possibility of a multi-level defect should also be considered. Therefore, in this section the TIDLS are reanalyzed assuming the dominant defect is a two-level defect using the procedure developed in Chapter 4. This procedure assumes that $\sigma_n$ has the same temperature dependency as the $\sigma_p$ (so the capture cross section ratio is temperature independent). However, at this stage there is not enough evidence to support this assumption. Therefore, in the following analysis, an extension of this procedure will be used, *i.e.*, the TIDLS measurements will be analyzed assuming $\sigma_n$ and $\sigma_p$ have different temperature dependencies.
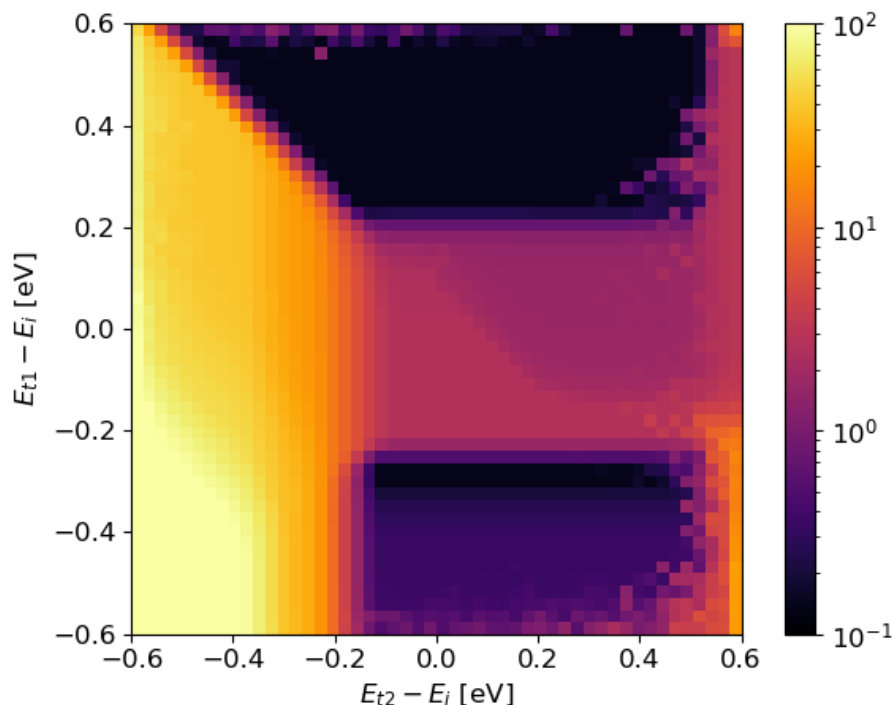


**Fig. 5.18** Map of the sum of fitting residuals for fitting lifetime at each measured temperature with a two-level defect. The two axes indicate the energy level of a two-level defects.

Following the procedure described in Chapter 4, the injection dependent lifetime is fitted at each temperature separately assuming the lifetime is dominated by a two-level defect. The map of the sum of fitting residuals is shown in Fig. 5.18. As can be seen, there are large regions of low fitting residual (below 0.1) in this map. Any combinations of energy levels within these regions can provide good fitting quality of the measured lifetime. Therefore, just from this map, one can only determine the constraints of the two energy levels instead of their actual values.
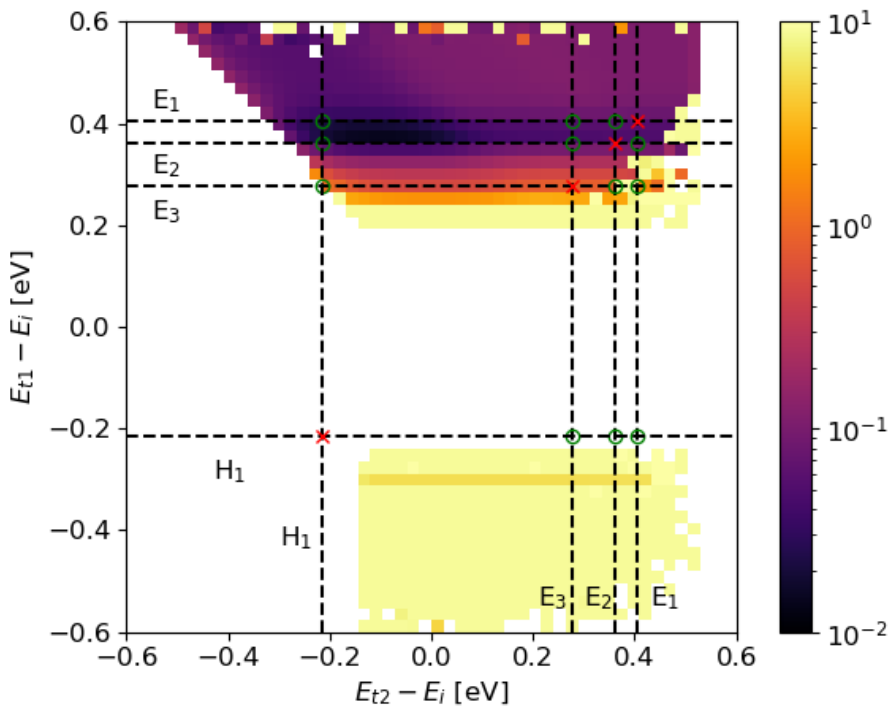


**Fig. 5.19** The map of the minimal of fitting residuals for fitting $\sigma_{n1}(T)$ with the four possible temperature dependencies. The dashed lines indicate the activation energies of $E_1$, $E_2$, $E_3$ and $H_1$ identified by DLST/MCTS.

In order to pinpoint the location of the two energy levels, the maps of the fitted capture cross sections are now examined. A similar strategy as the previous section is used. For each combination of energy levels, the extracted four $\sigma(T)$ are fitted using the four temperature dependencies. The minimal value of the four fitting residuals are then used as a metric for the fitting quality of $\sigma(T)$. For example, in Fig. 5.19, the map of fitting quality for $\sigma_{n1}(T)$ is shown. For simplicity, the regions where the measured lifetime cannot be well fitted (regions in Fig. 5.18 with fitting residual above 1) are removed. As can be seen, in this map, there is still a relatively large region with low fitting residual (below 0.1). Only for combinations of energy levels within this region, the extracted $\sigma_{n1}(T)$ achieves good fitting quality within existing temperature dependencies. The

horizontal dashed lines and vertical dashed lines are used to indicate the activation energies of $E_1$, $E_2$, $E_3$ and $H_1$ identified by DLTS/MCTS. In the DLTS/MCTS measurement, the emission signals from the two levels of a two-level defect usually have the same peak amplitude. $E_1$, $E_2$, $E_3$ and $H_1$ have similar peak amplitude whereas the peak amplitudes of $E_4$ and $E_5$ are quite different. Therefore, if there is really a two-level defect, the possible energy levels should come from $E_1$, $E_2$, $E_3$ and $H_1$. If this is the case, the location of the two energy levels should appear in one of the intersections (marked as green circles) of the dashed lines (except the ones with two same energy levels which are marked with a red cross). As can be seen, there are a few intersections of dashed lines in the region with minimal fitting residual below 0.1. Nevertheless, the minimal fitting residual map of $\sigma_{p1}(T)$, $\sigma_{n2}(T)$, and $\sigma_{p2}(T)$ suggests that the intersections of ($E_1$, $H_1$) and ($E_2$, $H_1$) provides a relatively satisfied fitting for all four $\sigma(T)$.

The electrical properties of the two possible cases of a two-level defect are listed in Table 5.3. Since $\sigma_{n1}(T)$ and $\sigma_{p2}(T)$ both have a power law temperature dependency, their impact on the activation energies in DLTS/MCTS measurements are found to be small. Again, it should be emphasized that the assumption is that both energy levels are detected by DLTS/MCTS. In reality, it is possible that the most recombination active defect is not detected by DLTS/MCTS.

**Table 5.3** The possible electrical properties of the dominant defect assuming a two-level defect

|  | Possibility 1 | Possibility 2 |
|---|---|---|
| $E_C - E_{t1}$ | 0.16±0.01 eV | 0.21±0.02 eV |
| $\sigma_{n1}(T)$ | $\sigma_{n1}(T) = \sigma_0 T^{-\alpha}$ <br> $\alpha = 1.78$ | $\sigma_{n1}(T) = \sigma_0 T^{-\alpha}$ <br> $\alpha = 1.99$ |
| $\sigma_{p1}(T)$ | $\sigma_{p1}(T) = T^{-2} \exp\left(\dfrac{\Delta E}{k_b T}\right)$ <br><br> $\Delta E = -0.11$ eV | $\sigma_{p1}(T) = \sigma_\infty \exp\left(\dfrac{-E_\infty}{k_b T}\right)$ <br> $E_\infty = 0.03$ eV <br> $\sigma_{p1}(T) = T^{-2} \exp\left(\dfrac{\Delta E}{k_b T}\right)$ <br> $\Delta E = -0.09$ eV |
| $E_{t2} - E_V$ | 0.35±0.02 eV | 0.35±0.02 eV |
| $\sigma_{n2}(T)$ | $\sigma_{n2}(T) = \sigma_\infty \exp\left(\dfrac{-E_\infty}{k_b T}\right)$ <br> $E_\infty = 0.13$ eV | $\sigma_{n2}(T) = \sigma_\infty \exp\left(\dfrac{-E_\infty}{k_b T}\right)$ <br> $E_\infty = 0.12$ eV |
| $\sigma_{p2}(T)$ | $\sigma_{p2}(T) = \sigma_0 T^{-\alpha}$ <br> $\alpha = 5.41$ | $\sigma_{p2}(T) = \sigma_0 T^{-\alpha}$ <br> $\alpha = 5.16$ |

Based on the information at this stage, it is also difficult to determine whether there are two single-level defects or one two-level defect. In order to have a better determination of the defects' electrical structure, it is useful to measure the lifetime of samples with different doping concentrations, or to measure the capture characteristics by DLTS/MCTS using samples with higher resistivities.

### 5.3.5 PL spectra measurements

To detect possible radiative transitions from the thermally activated defects in FZ silicon, the PL emission spectra at 80 K are recorded at two locations across the samples from each group (center and edge). The normalized spectra are shown in Fig. 5.20. The spectra are intentionally shifted for a clear display. The peaks between 0.95 eV and 1.2 eV are the band-band emission peaks with various phonon absorption and emission processes [208].
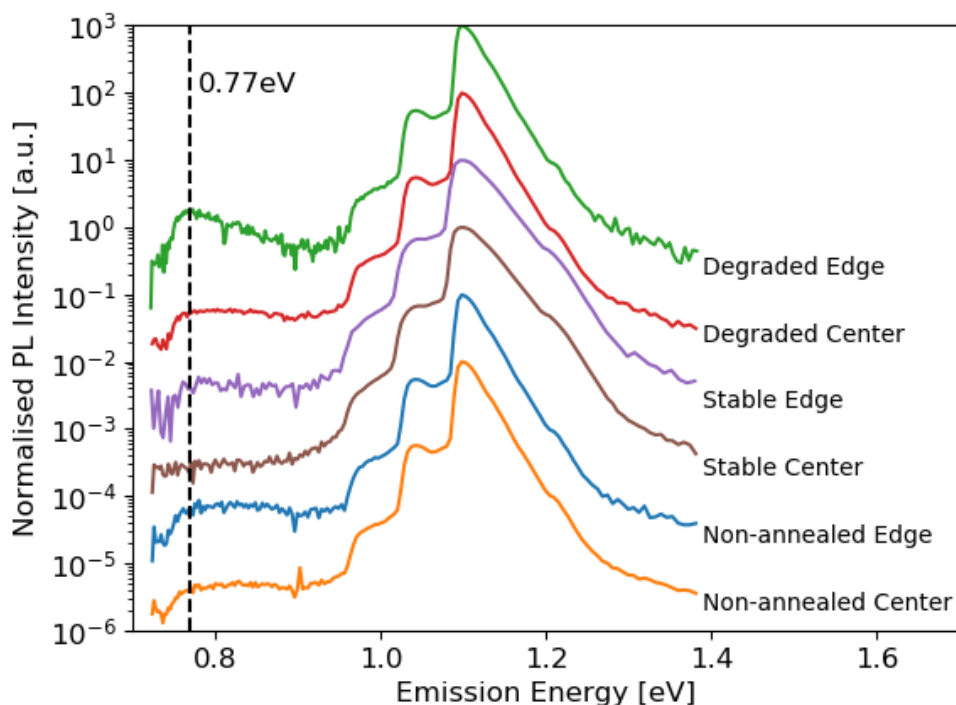


**Fig. 5.20** The 80 K PL spectra measured on a degraded wafer, a non-annealed wafer and a stable wafer. On each wafer, the measurements were taken at two locations: one in the center and one near the edge. The spectra are shifted for clarity.

At 0.77 eV, an apparent sub-bandgap PL band can be observed in the spectrum measured at the center of the degraded wafer. This PL band is either much less obvious or completely undistinguishable in the other spectra, indicating that this PL band might come from the activated defects. If this PL band originates from the interaction of a single

defect level with the conduction or valence band, its peak energy corresponds to a defect level of 0.4 eV from one of the band edges. Interestingly, this coincides with the E$_4$ found by DLTS. Further investigations are to be done for a confirmation of the origin of this sub-bandgap PL emission. Nevertheless, it can serve as a signature for at least one of these thermally activated defects.

## 5.4 Chapter summary

In this chapter, thermally activated defects in *n*-type FZ silicon were investigated by combining lifetime spectroscopy, and the conventional DLTS and MCTS techniques. A detailed analysis has been done to extract the defects' electrical properties by comparing TIDLS results and DLTS/MCTS results. In this analysis, the advantages of combining lifetime spectroscopy and DLTS for defect characterization are highlighted. The conventional DLTS/MCTS measurements are powerful to extract defect energy levels. Lifetime spectroscopy is sensitive to the more recombination active defect level and the information of capture cross section ratio can be extracted. Therefore, these two techniques are good complements in defect parameterization.

A few possibilities of the thermally activated defects' energy levels and temperature dependencies of capture cross sections have been identified. A decisive determination among these possibilities are planned in future investigations including: using $N_{dop}$-IDLS to reduce the complicity induced by temperature dependency of capture cross sections; and measuring *p*-type samples for a better determination of the bandgap halves of the defect.

At the end, a very interesting sub-bandgap luminescence was identified by low temperature PL spectra measurements only on the samples with the defect. This sub-bandgap luminescence can be used as a signature of these thermally activated defects.

# Chapter 6
# Characterization of Traps in Czochralski Silicon[1]

The previous chapter focuses on the investigation of defects which are very recombination active and detrimental for the device performance. Apart from these type of recombination active defects, there is another type of defect which are usually referred to as "traps" [23], [106], [209]. For clarity, in this thesis the term "defect" is defined as any imperfection in the silicon lattice presenting electron states within the silicon bandgap. The term "trap" is defined as a defect from which the captured carriers are "released" with a rate much slower than the recombination rate of the carriers in the sample. If the traps capture minority carriers upon excitation, they are referred to as minority carrier traps, vice versa for majority carrier traps.

Although traps are less recombination active, they can have significant impact on PC based lifetime measurements, and thus impede an accurate analysis of lifetime spectroscopy. Meanwhile, as silicon quality continues to improve, the carrier recombination via traps could start to impact the solar cell performance in the future. Therefore, this chapter focuses on the investigation of traps, in particular the traps in Cz silicon. First, the impact of traps in PC measurements will be illustrated and a brief review of previous studies on traps will be reviewed in Section 6.1. In Section 6.2, an approach to investigate traps via simulation and experimentation will be described. In Sections 6.3 and 6.4, minority carrier traps and majority carrier traps in Cz silicon will be investigated.

## 6.1 Traps in photoconductance measurements

PC based measurements such as QSSPC [82] and microwave PC decay (μ-PCD) [210], [211] are widely used in the PV community for measuring the lifetime of silicon wafers.

---

Frequently, artificially high lifetime is observed at low to medium injection in PC based lifetime measurements [110]. This artefact hinders a correct judgement of the minority carrier lifetime. One source for this artificially high lifetime is the presence of minority carrier traps within the sample [23], [82]

Trap activities in QSSPC measurement have been investigated intensively. Based on the simplified trap model of Hornbeck and Haynes (HH) [73]. Macdonald *et al*. [23] explained the mechanism of trap-associated artificially high lifetime as a result of charge neutrality, whereby the trapped minority carriers lead to extra charges in the majority carrier band. Due to the assumption of $\Delta n = \Delta p$ that is commonly used in PC based lifetime measurements, these extra charges are misinterpreted as excess minority carriers, and thus artificially high apparent excess carrier density and artificially high lifetime are observed. Based on this explanation, a correction method (the "bias-light" method) was later proposed [212] to estimate the true effective lifetime from the measured artificially high lifetime (apparent lifetime). Macdonald *et al*. [23] also extracted the energy level of the trap in mc-Si and found a correlation between the trap density and the dislocation density. With a similar approach, Schmidt *et al*. [106] investigated traps in *p*-type Cz silicon and found a correlation between the trap density and the oxygen content within the sample.

These studies greatly deepen the understanding of trap-associated high apparent lifetime. All of these studies focus on PC measurements under steady-state conditions. Nevertheless, this is not always the case. An example is the traps in *n*-type Cz silicon. Hu *et al*. [69] suggested that these traps are actually in a transient condition based on their extremely long PC decay time constant (in the range of two minutes), even though the measurement was conducted under typical QSS measurement settings. Similar to the study of Macdonald *et al.* [23], Hu *et al.* [69] adopted the simplified HH model for the trap analysis.

The simplified HH model adopted by these studies assumes that there is no interaction between the trap level and the majority carrier band, which means: (a) the recombination of electrons and holes in the trap level; and (b) the emission of majority carriers from the trap level are neglected. It was demonstrated both in the original study of HH [73], as well as more recently [108], [109], [213] that recombination via the trap level can have an impact on PC measurements. For such a case the simplified HH trap model fails. In

the original work of HH, a modified model was also proposed in order to take the recombination in the traps into consideration. Nevertheless, the emission of majority carriers from the trap level is still assumed to be negligible.

In the work of HH and other aforementioned works based on it, the trap associated PC measurements were analyzed with analytical solutions (closed-form expressions) of carrier continuity equations derived under certain assumptions. Apart from these works, traps have also been investigated by numerically solving the carrier continuity equations in both steady state [68], [108], [109] and transient [214], [215] conditions. The benefit of the numerical solutions is that no assumptions are made about the carrier capture or emission processes. Therefore, these numerical approaches should have a wider validity compared with those works using analytical solutions. Nevertheless, when one wants to extract trap parameters from measured PC data, the numerical approaches are more complicated than using the analytical solutions.

Apart from the difference in using numerical approaches or analytical solutions, the aforementioned works also differ in the analysis of traps in either SS or transient conditions. Compared to SS conditions, transient conditions do not require calibration of the generation rate. Nevertheless, SS measurements provide information that cannot be extracted from transient measurements. What is important (and will be demonstrated in Section 6.3) is that traps impact the transient PC measurement differently from SS PC measurement. It is therefore important to analyze traps according to the actual measurement condition.

In the next section, the methods used to numerically simulate traps and experimentally measure traps using PC will be described. The numerical simulation will then be used in later sections to verify the analytical solutions derived in this study under certain assumptions. In Section 6.3, the minority carrier traps in Cz silicon will be investigated, highlighting the difference of measuring traps in SS condition and transient condition. Meanwhile, the approach of trap parameterization proposed in this work will be compared with the methods applied from previous works. In Section 6.4, the majority carrier traps in Cz silicon will be investigated and a very interesting negative photoconductance (NPC) phenomenon that can be associated with these traps will be presented.

## 6.2 Simulation and PC based measurement of traps

This section mainly describes the numerical simulation approach as well as the measurement procedure for the investigation of both minority and majority carrier traps. Apart from numerical simulations, analytical solutions have also been used in this study. They will be discussed in more detail in Sections 6.3and 6.4.

### *6.2.1 Numerical simulation of traps*

Whether a defect is a recombination active defect or a trap, it can have four processes: capture an electron; capture a hole; emit a captured electron back to conduction band; and emit a captured hole back to the valence band. These four processes are illustrated in the sketch shown in Fig. 6.1.
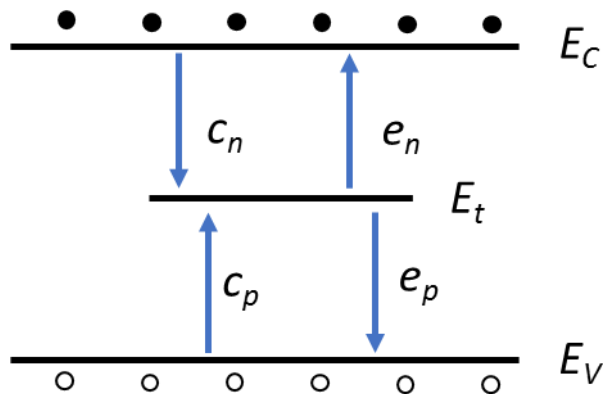


**Fig. 6.1** Illustration of the four carrier exchange processes associated with a defect level and the silicon energy bands. $c_n$, $c_p$, $e_n$ and $e_p$ are respectively, the rates of electron capture, hole capture, electron emission and hole emission of the defect level.

Therefore, the carrier concentrations impacted by a defect are governed by the following rate equations:

$$\frac{dn}{dt} = G + e_n - c_n \tag{6.1.1}$$

$$\frac{dp}{dt} = G + e_p - c_p \tag{6.1.2}$$

$$\frac{dn_t}{dt} = c_n - e_n - c_p + e_p \tag{6.1.3}$$

$$\frac{dp_t}{dt} = c_p - e_p - c_n + e_n \tag{6.1.4}$$

where $n_t$ is the density of occupied trap states, *i.e.*, density of capture electrons in the trap states, and $p_t$ is the density of unoccupied trap states, *i.e.*, density of hole captured in the trap states (the sum of $n_t$ and $p_t$ equals to the total trap density $N_t$). $e_n$ and $e_p$ are respectively the emission rate of electrons and holes from the defect per volume. $c_n$ and $c_p$ are respectively the capture rate of electrons and holes by the defect per volume. The thermal generation and other recombination sources, such as intrinsic recombination and surface recombination, are omitted as they play a negligible role here. If multiple defects exist, the rates from each defect can be added up in each rate equation. From a detailed balance, the four rates can be calculated as [59], [60]:

$$e_n = n_t \sigma_n v_n n_1 \tag{6.2.1}$$

$$c_n = n(N_t - n_t)\,\sigma_n v_n \tag{6.2.2}$$

$$e_p = (N_t - n_t)\sigma_p v_p p_1 \tag{6.2.3}$$

$$c_p = p n_t \sigma_p v_p \tag{6.2.4}$$

There is no general solution for the set of rate equations. However, for a given initial condition and $G(t)$, the rate equations can be numerically solved easily thanks to today's computing power. Under SS condition, the set of rate equations becomes linear dependent. The solving under this condition requires an additional equation from the charge neutrality:

$$n - n_0 + n_t - n_{t0} = p - p_0 \tag{6.3}$$

The carrier concentration in thermal equilibrium with the presence of defects can be calculated using an iteration procedure proposed in Ref. [68].

After solving the rate equations, the PC ($\Delta S$) of a sample can be calculated as:

$$\Delta S = qW(\mu_n \Delta n + \mu_p \Delta p) = qW(\mu_n + \mu_p)\Delta n + qW\mu_p \Delta n_t \tag{6.4}$$

where $\Delta$ denotes the deviation of the concentration from the thermal equilibrium condition.

For *p*-type silicon, the apparent excess minority carrier density $\Delta n_{app}$ and apparent lifetime $\tau_{app}$ can then be calculated as:

$$\Delta n_{app} = \Delta n + \frac{\mu_p}{\mu_n + \mu_p}\Delta n_t \tag{6.5.1}$$

$$\tau_{app} = \frac{\Delta n_{app}}{G - \frac{d\Delta n_{app}}{dt}} \tag{6.5.2}$$

Analogue equations can be obtained for *n*-type silicon.

In this chapter, the carrier mobility is calculated using the model of Klaassen *et al*. [152], [153]. The ionization model is calculated using the model of Altermatt *et al.* [158], [168]. The intrinsic carrier density is calculated using the model of Couderc *et al*. [169]. The thermal velocity is calculated using the model of Green [165].

The rate equations here are valid for any defect, whether it is a recombination active defect or a trap. For recombination active defect, $\Delta n = \Delta p$ is usually valid; therefore, carrier concentrations can be solved analytically under this assumption. In fact, the SRH equation discussed in Chapter 2 is derived in this way. Nevertheless, the assumption of $\Delta n = \Delta p$ is by definition not valid for traps. Therefore, numerically solving the rate equations is required, unless further assumptions are used.

It should also be noted that the analysis in this study mainly focuses on the trap with a single energy level. The analysis of multi-level trap is much more complicated and requires further works. Results of some of the preliminary investigations of two-level minority carrier traps in PC measurements are included in the Appendix B.

### 6.2.2 PC based measurement of traps

The PC measurements are carried out using the customized lifetime tester described in Chapter 3. The PC and excitation light intensity are recorded simultaneously. Two different light sources are used. The first light source is the xenon flash with a decay time constant $\tau_G$ of 2.3 ms, as typically used in QSSPC measurements by standard Sinton Instruments WCT-120 lifetime testers. For silicon wafers with effective lifetime values of below 200 µs, this flash renders the measurements to be in a QSS condition. Apart from the xenon flash, the LED with a wavelength of 810 nm in the customized lifetime tester is also used as an illumination source which can provide SS excitation of various intensities on the sample. The system is placed in a light-tight box to remove the impact of environmental light on the trap level occupancy. In this study, the samples are kept in

the dark for at least ten minutes before each measurement to ensure that the trap occupancy is at the thermal equilibrium level.

## 6.3 Minority carrier traps

We start with the investigation of minority carrier traps. The samples used in this study are three 430 µm thick, *n*-type Cz silicon wafers with doping levels of $8.1\times10^{15}$ cm$^{-3}$, $9.6\times10^{15}$ cm$^{-3}$ and $1.4\times10^{16}$ cm$^{-3}$. The wafers are circular with diameters of around 25 mm, which is smaller than the sensor area of the customized lifetime tester. Therefore, adjustment has been made to the PC coil calibration factors when measuring the lifetime of the wafers. The details of this adjustment can be found in the Appendix A. These wafers are from different positions along the same ingot. The ingot was intentionally contaminated with Cr during the ingot growth. From the mass of Cr added into the ingot, the Cr concentration in the wafers is estimated to be at the level of $10^{12}$ cm$^{-3}$. It is well known that Cr exists as Cr$_i$ in *n*-type silicon that is highly recombination-active [167], [177], [216], [217]. The Cr$_i$ dominates the minority carrier lifetime of the sample to allow a correct evaluation of the SS PC measurements (this point will be further explained in Section 6.3.2). The oxygen content in the samples was estimated to be around $6\times10^{17}$ cm$^{-3}$ by Fourier transform infrared (FTIR) spectroscopy [218]. Both surfaces of the samples were passivated by PECVD SiN$_x$. The effective lifetimes of the samples with SiN$_x$ passivation are between 10 to 20 µs at the injection level of $10^{15}$ cm$^{-3}$. After corresponding PC measurements, the SiN$_x$ layers on the sample with doping level of $1.4\times10^{16}$ cm$^{-3}$ were stripped off. The effective lifetime of this sample dropped to around 1 µs at the injection level of $10^{15}$ cm$^{-3}$. This sample was then measured again to evaluate the impact of minority carrier lifetime on the measured trap time constant. The purpose of doing so will be further explained in Section 6.3.2. It should also be noted that the traps in the samples are unrelated to Cr$_i$. PC measurements have also been performed on wafers from a control ingot grown under the same condition but without Cr contamination. The trap-associated PC behaviors appear to be similar for the wafers with and without Cr.

### 6.3.1 Minority carrier traps in steady state PC measurement

As mentioned previously in Section 6.1, several previous studies investigated the behavior of minority carrier traps measured under SS conditions. Most of these studies were based on the work of Macdonald *et al.* [23], which proposed a simplified analytical

equation that correlates the measured apparent carrier density and apparent lifetime with trap's electrical parameters:

$$\Delta n_{app,simplified} = \Delta n[1 + \frac{\mu_p}{\mu_n + \mu_p}\frac{N_t}{(\Delta n + n_1)}] \qquad (6.6.1)$$

$$\tau_{app,simplified} = \tau_r + \tau_r\frac{\mu_p}{\mu_n + \mu_p}\frac{N_t}{(\Delta n + n_1)} \qquad (6.6.2)$$

where $\tau_r$ is the recombination lifetime of minority carriers, *i.e.*, the true minority carrier lifetime. The above equations are derived for electron traps in *p*-type silicon. For hole traps in *n*-type silicon, analogue equations can be obtained.

Using Eq. (6.6), the energy level and trap concentration can be extracted from the measured injection dependent apparent lifetime curve.

However, apart from the assumption of being in SS condition, the analytical equations from Macdonald *et al.* [23] are based on the simplified HH trap model, which assumes that there is no interaction of traps with the majority carrier band [73]. For electron traps in *p*-type silicon, this indicates the rates $c_p$ and $e_p$ are both negligible compared to $c_n$ and $e_n$. However, as can be seen from Eqs. (6.2.1) to (6.2.4), these four rates are function of trap parameters. For example, $e_n$ increased exponentially whereas $e_p$ decreases exponentially with the increase of $E_t - E_i$. If $E_t$ of the trap is closer to the valence band, $e_p$ can be significant and non-negligible. Without the knowledge of trap parameters, the assumptions of the simplified HH model cannot be verified and the use of Eq. (6.6) might be invalid. To illustrate this point, the numerical approach described in Section 6.2.1 is used to check the validity of Eq. (6.6) with different trap parameters. As mentioned previously, the numerical simulation considered all the four rates thus no further simplification of the rates equation is made. Therefore, the lifetime obtained from the numerical simulation should be valid for any single-level trap following the rate equations of carrier concentrations.

In Fig. 6.2, the simulated apparent lifetime and true minority carrier lifetime as a function of apparent minority carrier density are plotted. The sample parameters and trap parameters used in this simulation are provided in the figure caption. The apparent lifetime calculated analytically using Eq. (6.6) is also plotted. As can be seen, in this case it agrees well with the simulated lifetime. This indicates the assumptions made in this

simplified apparent lifetime equation are valid. The trap simulated in this case has a $\sigma_p$ five orders of magnitude smaller than $\sigma_n$. Therefore, the rates $c_p$ and $e_p$ are indeed negligible compared to $c_n$ and $e_n$.
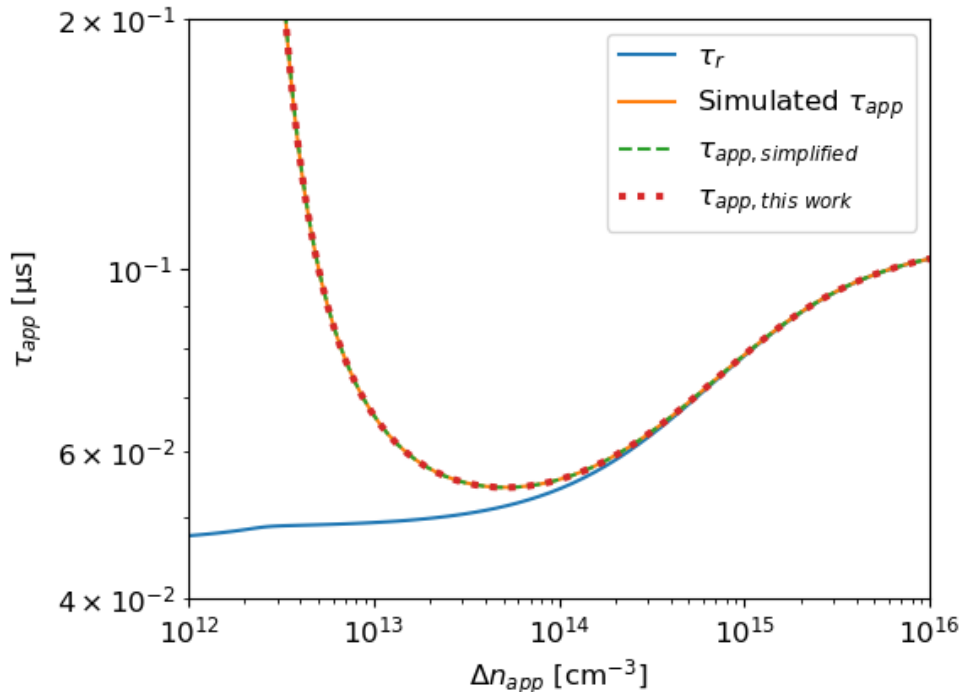


**Fig. 6.2** The simulated SS apparent lifetime of a $p$-type silicon wafer with doping concentration of $10^{15}$ cm$^{-3}$. The sample contains a trap with $N_t$ of $10^{13}$ cm$^{-3}$, $E_t - E_i$ of 0 eV, $\sigma_n$ of $10^{-14}$ cm$^2$, $\sigma_p$ of $10^{-19}$ cm$^2$. The orange solid line indicates the apparent lifetime obtained from numerical simulations. The green dashed line indicates the apparent lifetime calculated using the analytical Eqs. (6.6.1) and (6.6.2). The red dotted line indicates the apparent lifetime calculated using the analytical Eqs. (6.16.1) and (6.16.2). The blue solid line indicated the true minority carrier lifetime.

However, if $\sigma_p$ of the trap is increased to be two orders of magnitude smaller than $\sigma_n$, the apparent lifetime calculated analytically using Eq. (6.6) starts to deviate from the simulated apparent lifetime. This result is shown in Fig. 6.3. The reason for this deviation is that the assumptions used to derive Eq. (6.6) are no longer valid. In this case, if the simplified equations are used to analyze traps, the trap parameterization can suffer from large errors.

The two examples above highlights the importance of verifying the assumptions when using the simplified equations to analyze traps. However, as mentioned previously, the validity of those assumptions depends on the trap parameters which is unknown a priori. One way to avoid those assumptions is to use the numerical solution to fit the measured lifetime. However, the fitting process can be complicated with four fitting parameters (three trap parameters $E_t - E_i$, $\sigma_n$ and $\sigma_p$, and the trap concentration $N_t$). In the following

part, an alternative analytical solution will be derived. It has a wider validity than the simplified equations from previous works, whereas the simplicity of using a close-form expression for trap parameterization can be kept.
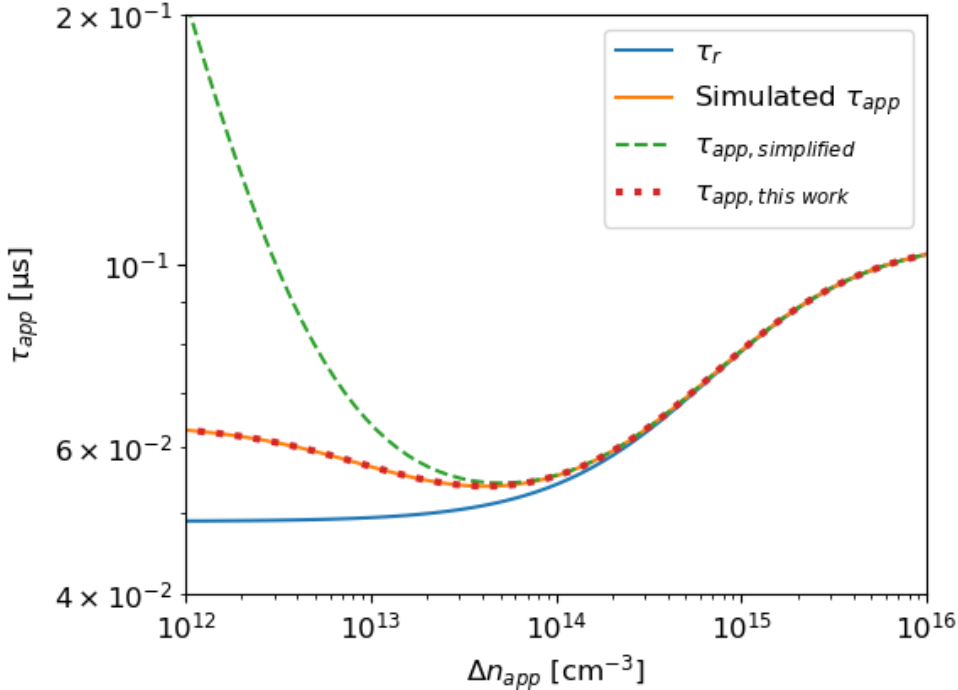


**Fig. 6.3** The simulated SS apparent lifetime of a $p$-type silicon wafer with doping concentration of $10^{15}$ cm$^{-3}$. The sample contains a trap with $N_t$ of $10^{13}$ cm$^{-3}$, $E_t - E_i$ of 0 eV, $\sigma_n$ of $10^{-17}$ cm$^2$, $\sigma_p$ of $10^{-19}$ cm$^2$. The orange solid line indicates the apparent lifetime obtained from numerical simulations. The green dashed line indicates the apparent lifetime calculated using the analytical Eqs. (6.6.1) and (6.6.2). The red dotted line indicates the apparent lifetime calculated using the analytical Eqs. (6.16.1) and (6.16.2). The blue solid line indicated the true minority carrier lifetime.

For the rate equations under SS condition. the time derivation term becomes 0 and Eq. (6.1.3) changes to:

$$c_n - e_n = c_p - e_p \tag{6.7}$$

Replacing the terms using Eqs. (6.2.1) to (6.2.4), the above equation changes to:

$$\sigma_n v_n n p_t - \sigma_n v_n n_1 n_t = \sigma_p v_p p n_t - \sigma_p v_p p_1 p_t \tag{6.8}$$

Expanding the terms to the deviation from thermal equilibrium, above equation changes to:

$$\sigma_n v_n (n_0 + \Delta n)(p_{t0} + \Delta p_t) - \sigma_n v_n n_1 (n_{t0} + \Delta n_t)$$
$$= \sigma_p v_p (p_0 + \Delta p)(n_{t0} + \Delta n_t) - \sigma_p v_p p_1 (p_{t0} + \Delta p_t) \tag{6.9}$$

Meanwhile, in thermal equilibrium, Eq. (6.8) becomes:

$$\sigma_n v_n n_0 p_{t0} - \sigma_n v_n n_1 n_{t0} = \sigma_p v_p p_0 n_{t0} - \sigma_p v_p p_1 p_{t0} \tag{6.10}$$

Subtracting Eq. (6.10) from Eq. (6.8) leads to:

$$
\begin{aligned}
\sigma_n v_n (n_0 \Delta p_t + \Delta n p_{t0} + \Delta n \Delta p_t) - \sigma_n v_n n_1 \Delta n_t \\
= \sigma_p v_p (p_0 \Delta n_t + \Delta p n_{t0} + \Delta p \Delta n_t) - \sigma_p v_p p_1 \Delta p_t
\end{aligned}
\tag{6.11}
$$

For $p$-type silicon at low injection, it is reasonable to assume:

$$p_0 \gg \Delta p = \Delta n + \Delta n_t \gg n_0 \tag{6.12}$$

Using this assumption, Eq. (6.11) can be simplified to:

$$\sigma_n v_n \Delta n (p_{t0} + \Delta p_t) - \sigma_n v_n n_1 \Delta n_t = \sigma_p v_p p_0 \Delta n_t - \sigma_p v_p p_1 \Delta p_t \tag{6.13}$$

At thermal equilibrium, $p_{t0}$ can be calculated via the equilibrium Fermi distribution:

$$p_{t0} = \frac{p_0}{p_0 + p_1} N_t \tag{6.14}$$

With $\Delta n_t = -\Delta p_t$ and Eq. (6.14), Eq. (6.13) can be rewrite to:

$$\Delta n_t = \frac{\sigma_n v_n \dfrac{p_0}{p_0 + p_1} N_t}{\sigma_n v_n (\Delta n + n_1) + \sigma_p v_p (p_0 + p_1)} \tag{6.15}$$

With this, the apparent carrier density and apparent lifetime can be calculated using:

$$\Delta n_{app} = \Delta n + \Delta n \frac{\mu_p}{\mu_n + \mu_p} \frac{\sigma_n v_n N_t \dfrac{p_0}{p_0 + p_1}}{\sigma_n v_n (\Delta n + n_1) + \sigma_p v_p (p_0 + p_1)} \tag{6.16.1}$$

$$\tau_{app} = \tau_r + \tau_r \frac{\mu_p}{\mu_n + \mu_p} \frac{\sigma_n v_n N_t \dfrac{p_0}{p_0 + p_1}}{\sigma_n v_n (\Delta n + n_1) + \sigma_p v_p (p_0 + p_1)} \tag{6.16.2}$$

Analogue expressions can be obtained for $n$-type silicon.

Therefore, new analytical equations which correlate the measured apparent lifetime with trap parameters are derived. They are more complicated than the simplified Eqs. (6.6.1) and (6.6.2) used in previous studies. However, the equations derived here does not require assumptions regarding any of the four rates related to traps. It is not difficult to see that if the terms related to capture and emission of holes become negligible, Eqs. (6.16.1) and (6.16.2) simplified to Eqs. (6.6.1) and (6.6.2). The assumption required here

[Eq. (6.12)] is in general fulfilled for most PV silicon materials. An implied assumption from Eq. (6.12) is that the trap concentration $N_t$ needs to be much smaller than the base doping concentration $p_0$.

The validity of Eqs. (6.16.1) and (6.16.2) have been checked with the numerical simulations. For the traps simulated in Fig. 6.2 and Fig. 6.3, the apparent lifetimes calculated by Eqs. (6.16.1) and (6.16.2) are also presented in respected figures. As can be seen, in both cases, the apparent lifetime analytically calculated agrees well with the numerically simulated lifetime. Apart from the two cases in Fig. 6.2 and Fig. 6.3, other cases a wide range of trap parameters have been checked and Eqs. (6.16.1) and (6.16.2) are found to be accurate.

In order to illustrate the relevance of the more complicated equations derived in this work, a simplification error is defined as the difference between the simplified equation and the equation derived in this work:

$$Simplification\ error = \frac{\left|\tau_{app,this\ work} - \tau_{app,simplified}\right|}{\tau_{app,this\ work}} \times 100\% \qquad (6.17)$$
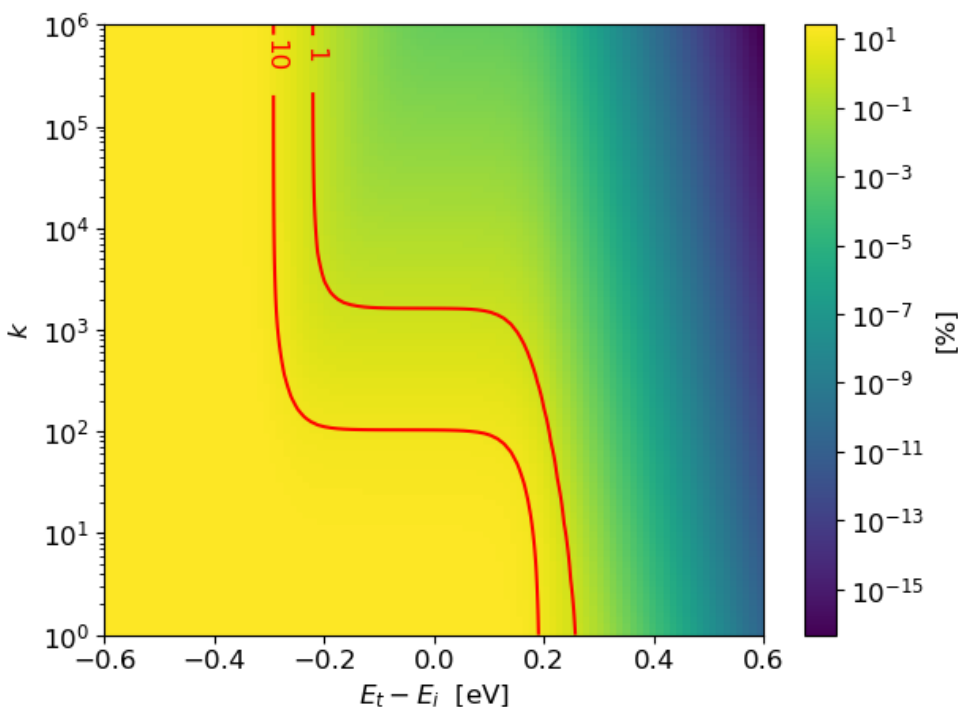


**Fig. 6.4** Map of simplification error [Eq. (6.17)] as a function of $E_t$ and $k$. It is calculated on a $p$-type silicon wafer with doping concentration of $10^{15}$ cm$^{-3}$ with a minority carrier trap concentration of $10^{13}$ cm$^{-3}$ at 300 K. The calculation is at an injection level of $10^{13}$ cm$^{-3}$. The red solid lines indicate the contours with simplification errors of 1% and 10% respectively.

This equation represents the error occurred if the simplified equations (6.6.1) and (6.6.2) are used to calculate the apparent lifetime. It is not the absolute error in trap parameterization when using Eqs. (6.6.1) and (6.6.2). However, it provides a good indication for that error. The simplification error defined here is a function of the trap parameters ($E_t$ and $k$), trap concentration $N_t$, sample doping concentration, temperature and injection level.

Using Eq. (6.17) the map of simplification error is calculated for a $p$-type silicon wafer with doping concentration of $10^{15}$ cm$^{-3}$ at 300 K and a minority carrier trap concentration of $10^{13}$ cm$^{-3}$ at an injection level of $10^{13}$ cm$^{-3}$. The result is shown in Fig. 6.4. As can be seen, for a certain $k$ value, the error of using the simplified equation becomes larger when the trap energy level is closer to the valence band in this $p$-type scenario. This is easy to understand as the rate $e_p$ increases exponentially as $E_t$ approached the valence band and the assumption used in the simplified equation breaks down.

Therefore from Fig. 6.4, the error resulted from using the simplified equation can be easily evaluated for a given combination of $E_t$ and $k$. Nevertheless, it should be noted that not all combinations of $E_t$ and $k$ can lead to a minority carrier trap, which causes the artificially high apparent lifetime. The extent of the impact of minority carrier traps on the PC based lifetime also depends on trap parameters ($E_t$ and $k$), trap concentration $N_t$, sample doping concentration, temperature and injection level. In a similar way to Eq. (6.17), the "Trapping extent" can be defined as:

$$Trapping\ extent = \frac{\tau_{app} - \tau_r}{\tau_r} \times 100\% \qquad (6.18)$$

This equation represents the difference between the apparent lifetime measured by PC based techniques and the true minority carrier lifetime. The map of trapping extent calculated with the same parameters as the simplification error map is shown in Fig. 6.4. The absolute number in this map looks relatively small as the calculation is done at the injection level equal to the trap concentration. At a lower injection level, the deviation of $\tau_{app}$ from $\tau_r$ is much more significant.

As can be seen, for a certain capture cross section ratio $k$, traps with energy level near the mid-gap actually have stronger "trapping effect" ($\tau_{app}$ higher than $\tau_r$). This is a bit counterintuitive as people usually think traps have energy levels close to the band edges. However as can be seen from Fig. 6.4, traps that have energy levels close to the band

edges usually does not lead to apparently high lifetime in PC based measurement. Similar results have been previously found by Mcintosh *et al.* [68].
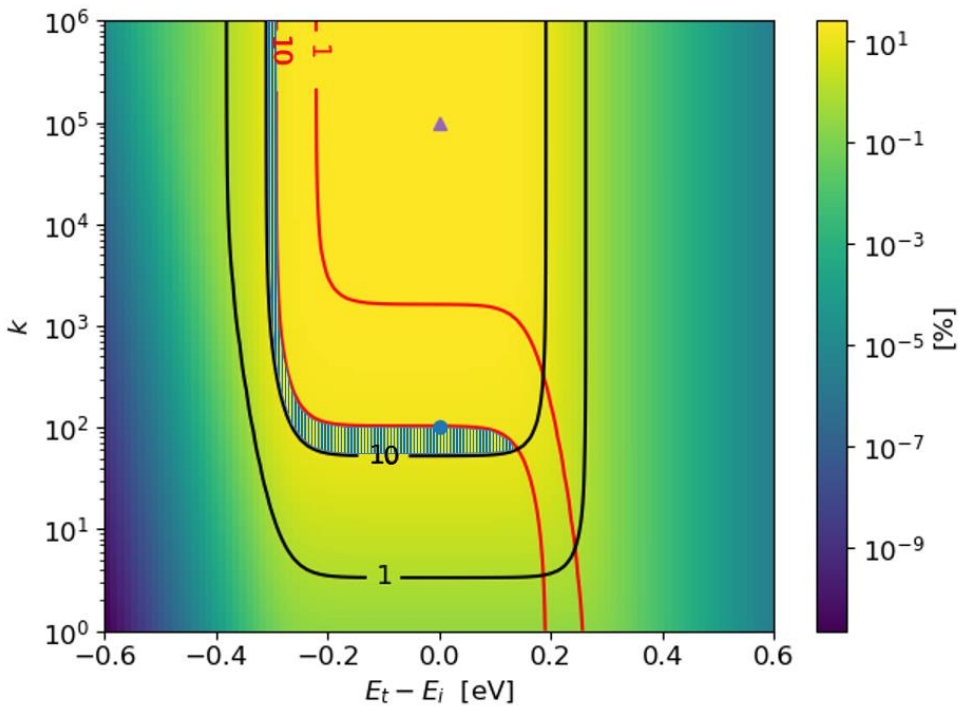


**Fig. 6.5** Map of Trapping extent [Eq. (6.18)] as a function of $E_t$ and $k$. It is calculated on a *p*-type silicon wafer with doping concentration of $10^{15}$ cm$^{-3}$ with a minority carrier trap concentration of $10^{13}$ cm$^{-3}$ at 300 K. The calculation is at an injection level of $10^{13}$ cm$^{-3}$. The black solid lines indicate the contours with trapping extent of 1% and 10% respectively. The red solid lines indicate the contours with simplification error of 1% and 10% respectively. The location of trap parameters used in Fig. 6.3 is indicated by the blue circular. The location of trap parameters used in Fig. 6.2 is indicated by the purple triangle.

The relevance of the analytical equations proposed in this work can be illustrated by combining the trap extent map and simplification error map. The contours with trapping extent of 1% and 10% are also plotted on the map. The patterned area in Fig. 6.5 indicates the region where the trap parameters leads to strong trapping effect and the usage of the simplified equation leads to significant error. The trap simulated in Fig. 6.3 is indicated by the blue circular. As can be seen, it is in that patterned region and as can be seen from Fig. 6.3, there is indeed strong tapping effect and large error in the $\tau_{app,simplified}$. There is a region where the trapping effect is strong but the usage of the simplified equation leads to smaller error. The trap simulated in Fig. 6.2 is indicated by the purple triangle and it belongs to this region. Similarly, the region where the usage of the simplified equation leads to a significant error but the trapping effect is weak can be easily identified.

Therefore, from Fig. 6.5 it can be easily identified how much a minority carrier trap impacts the PC based lifetime measurement and how relevant it is to use the more complicated equations proposed in this work instead of the simplified equations. However, as mentioned previously, the two maps in Fig. 6.4 and Fig. 6.5 also depend on the doping and temperature of the sample. Therefore, for different scenario they should be re-calculated. The absolute values in the two maps are also functions of trap concentration. Nevertheless, trap concentration is just a scaling factor and does not change the shape of the two maps.

### 6.3.2 Minority carrier traps in transient PC measurement

In the previous section, minority carrier traps in SS PC measurements were investigated. Analytical equations correlate the measured apparent lifetime with trap parameters were derived. However, as mentioned previously, traps can be in a transient condition even though the measurement was conducted under typical QSS measurement settings.

In this section, firstly it will be demonstrated experimentally that traps may not be in a SS regime even under typical QSS measurement settings. The difference between the trap-associated artificially high lifetimes measured under transient and SS conditions will also be shown and discussed. Next, analysis of traps under transient conditions will be made and a new method to extract trap parameters from transient PC decay measurements will be developed. A comparison of the proposed method and the analytical solutions from previous studies is made. Finally, the developed method will be demonstrated by extracting the electrical parameters of traps in $n$-type Cz silicon.

The PC based lifetime of an $n$-type Cz wafer with doping concentration of $1.4 \times 10^{16}$ cm$^{-3}$ is shown in Fig. 6.6. The orange crosses indicate the lifetime measured with LED in SS conditions at six different light intensities, while the blue circles indicate the lifetime measured with the xenon flash. The higher injection part of the blue circles is obtained from a single flash measurement with an acquisition time of around 20 ms. Still with the xenon flash, the low injection part is obtained by extending the acquisition time to one minute and taking 200 repeat measurements to increase the signal to noise ratio of the data. The plateau of lifetime at low injection corresponds to a single exponential decay of the PC.
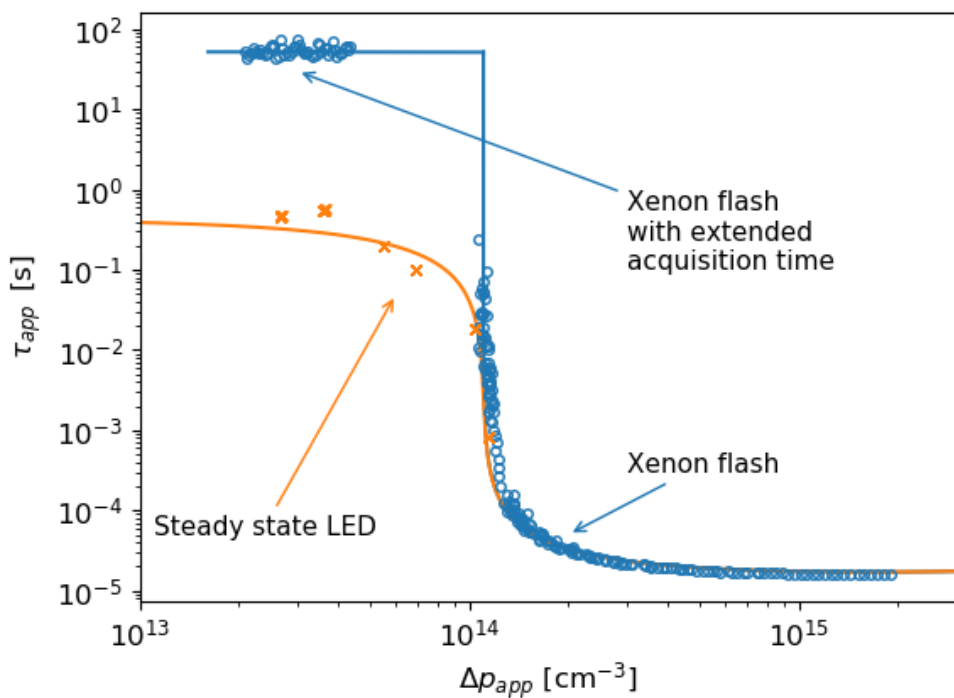
**Fig. 6.6** Apparent lifetime of an *n*-type Cz wafer with doping level of $1.4 \times 10^{16}$ cm$^{-3}$ measured with PC. The blue circles are lifetime measured with a xenon flash and the orange crosses are SS lifetime measurements using an LED for excitation. The blue solid line and orange dashed line indicate the optimal fitting of the apparent lifetime from full numerical simulation.
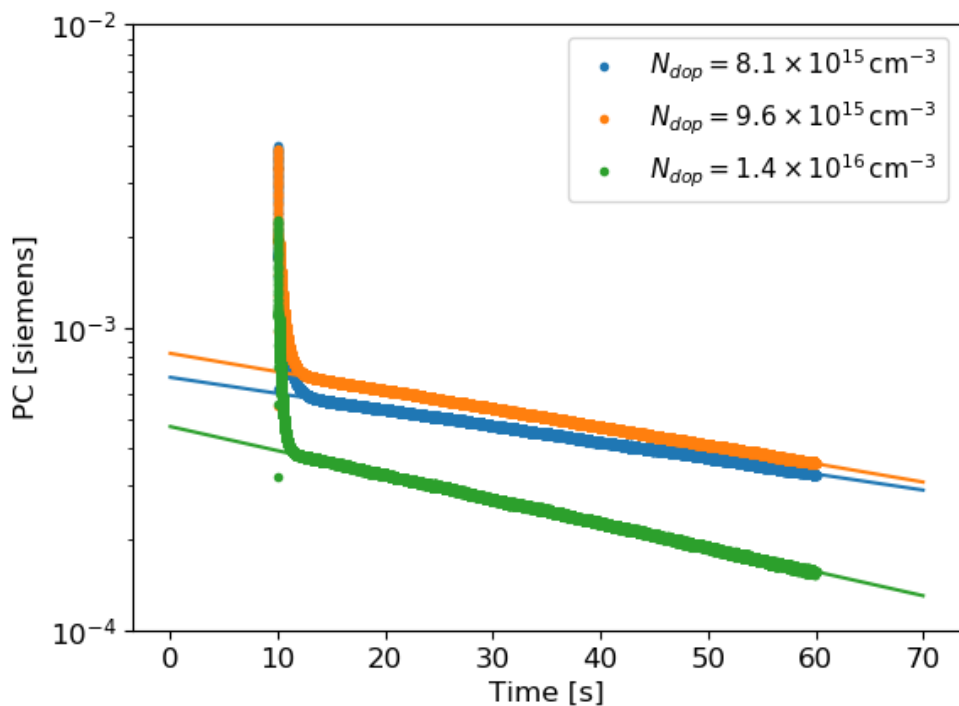


**Fig. 6.7** Measurement results of PC decay of three *n*-type Cz silicon wafers of various doping levels. The straight lines indicate a single exponential fit of the decay.

The PC of the three *n*-type Cz silicon wafers measured with the xenon flash and an acquisition time of one minute is presented in Fig. 6.7. The xenon flash is trigged at time $t = 10$ s. As can be seen, for all three samples, the PC shows an initial fast decay followed by a much slower single exponential decay. The initial fast decay is due to the presence of $Cr_i$ in the sample, which acts as a fast recombination channel of excess charge carriers [92], [177], [216], [217]. The much slower decay could be explained the "de-trapping" of minority carriers from the trap level. Here, the "de-trapping" of minority carriers indicates the overall decrease of $p_t$ for *n*-type material (decrease of $n_t$ for *p*-type material), which is not only the emission of minority carriers from the trap level, but also includes the capture and emission of majority carriers. The PC decay time constants of all three samples (in the range of 54 to 82 seconds) are more than four orders of magnitude longer than the decay time constant $\tau_G$ of the xenon flash (2.3 ms) used in the measurements. Therefore, there is no doubt that this long PC decay is a *transient* measurement (no external generation) instead of *quasi-steady-state* process, even though a flash for typical QSSPC measurements has been used. The fast decay part is still under QSS conditions, as the recombination lifetime is still much shorter than $\tau_G$.

Similar to Hu *et al.* [69], the trap-associated carrier dynamics in this study are also found to be in a transient regime, even if the measurement is conducted using typical QSSPC settings. Furthermore, as can be seen in Fig. 6.6, the lifetime measured by the xenon flash deviates significantly from the true SS lifetime measured by LED. This indicates that the trap-associated apparent lifetime under SS conditions is different from the one measured under transient conditions.

The reason for the difference between traps in SS condition and traps in transient condition can be explained as follows. According to Eqs. (6.5.1) and (6.5.2), in PC based measurement, the fundamental reason for the artificially high lifetime is $\Delta p_t$ becomes comparable with $\Delta p$ for *n*-type silicon ($\Delta n_t$ becomes comparable with $\Delta n$ for *p*-type silicon). In SS condition, the ratio of $\Delta n_t$ and $\Delta n$ depends only on the trap parameters $E_t$ and $k$ for a given $N_t$ in a sample with given doping concentration and temperature. This dependence is reflected by the trap extent map in Fig. 6.5. However, in transient conditions, the ratio of $\Delta n_t$ and $\Delta n$ can also be impacted by the other recombination channels in the sample. If $\Delta n_t$ decays much slower than $\Delta n$ in a transient measurement, the ratio of $\Delta n_t$ and $\Delta n$ can also increase as a function time. In an extreme example, a defect which is normally not considered as a trap in SS condition can lead to an artificially

high lifetime if measured in transient condition. This happens if the other recombination channel in the sample leads to a $\tau_r$ much shorter than the decay time constant of excess captured minority carriers in that defect.
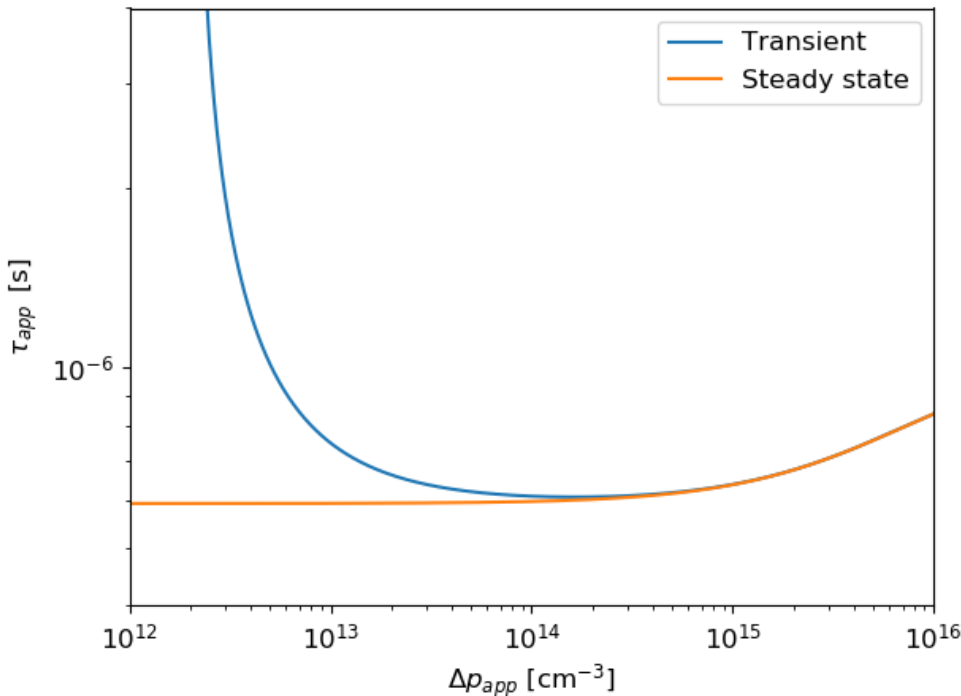


**Fig. 6.8** Simulated apparent lifetime in SS condition and transient condition for an *n*-type silicon wafer with doping of $10^{16}$ cm$^{-3}$ at 300 K with $\tau_r$ of around 0.6 μs, and a defect with $E_t - E_i$ of $-0.3$ eV, $\sigma_n$ of $10^{-20}$ cm$^2$, $\sigma_n$ of $10^{-20}$ cm$^2$ and $N_t$ of $10^{13}$ cm$^{-3}$.

A numerical simulation has been done to illustrate this example. In Fig. 6.8, the simulated apparent lifetime of a *n*-type silicon wafer in SS condition and transient condition are shown. The simulated sample has a $\tau_r$ of around 0.6 μs and a defect with $N_t$ of $10^{13}$ cm$^{-3}$. The parameters of the defect are listed in the figure caption. As can be seen, in SS, the apparent lifetime does not show any "trapping effect". In this sense, the simulated defect should not be considered as a trap. However, a very strong trapping effect is shown in the transient apparent lifetime. The reason is because the very low $\tau_r$ of the sample leads to the decay of $\Delta p$ much faster than the decay of $\Delta p_t$ from the defect.

The simulation results above highlight again the difference between traps in SS condition and transient condition. It is therefore important to analyze traps with respect to the correct regime they are in; otherwise misinterpretation of the trap behavior might occur. This section focuses on the analysis of traps in transient PC decay.

Firstly, a brief review of previous studies on traps in transient condition will be made. As mentioned previously, the simplified HH trap model was adopted to analyze the SS PC lifetime impacted by minority carrier traps [23], [106], [212]. The original work of HH [73] actually focused on traps in transient condition and an analytical form of the transient PC lifetime impacted by traps was also derived as (for *n*-type silicon)[2]:

$$\tau_{decay} = 1/\sigma_p v_p p_1 + n_t \tau_r / p_1 \tag{6.19}$$

This equation has been adopted and extended for the studies of traps by several other authors [141], [219]–[221]. The equation above is derived under the assumption that there is only a negligible interaction between the trap level and the majority conduction band. For *n*-type silicon, this means (a) the trap level does not capture electrons from the conduction band (negligible $c_n$), *i.e.* the trapped holes are unlikely to recombine with electrons and will only be re-emitted back to the valence band; (b) the trap level does not emit any electron to the conduction band (negligible $e_n$).

Regarding the first part of the assumption, since $c_n$ is proportional to the electron concentration in the conduction band, it may not be negligible for samples with relatively high doping levels. Actually, in the original work of HH, a model taking $c_n$ into consideration was also proposed and an analytical equation for the transient PC decay time constant (for *n*-type silicon) was derived:

$$\frac{1}{\tau_{decay}} = \sigma_n v_n n_0 + \frac{1}{1/\sigma_p v_p p_1 + n_t \tau_r / p_1} \tag{6.20}$$

The term $\sigma_n v_n n_0$ in Eq. (6.20) accounts for the capture of electrons into the trap level. As can be seen, Eq. (6.20) is equivalent to Eq. (6.19) when $\sigma_n v_n n_0$ is negligible compared with the other terms. However, the overall decay time constant can also be dominated by $\sigma_n v_n n_0$ when the doping concentration is high enough. Since Eq. (6.20) is based on less strict assumptions than Eq. (6.19), it is referred to as the HH trap model and Eq. (6.19) is referred to as the simplified HH trap model. It should be noted that for the HH trap model, the emission of majority carriers from the trap level ($e_n$ for *n*-type silicon) is still assumed to be negligible. Nevertheless, $e_n$ is a function of trap energy level and can be significant if the trap energy level is close to the majority carrier band. Without prior knowledge of

---

[2] From this point, the discussions are based on *n*-type silicon, but analogue analysis for *p*-type silicon can be easily made.

the trap parameters, the assumption regarding negligible $e_n$ (as well as for negligible $c_n$) is difficult to verify. Therefore, special care is required before using Eq. (6.19) or Eq. (6.20) to analyze the traps in transient PC decay.

Now a new analytical solution for traps in transient conditions based on different assumptions as HH model will be derived. This new analytical solution assumes that the capture of minority carriers by the trap ($c_p$ for $n$-type silicon) is negligible. Since $c_p$ is proportional to the hole concentration in the valence band, this assumption is valid if the holes are depleted quickly via other recombination channels in the sample, such as other recombination active defects in the bulk or surface of the sample. For PC decay measurements, this assumption is valid when the minority carrier lifetime is much shorter than the minority capture time constant of the trap.

The rate equation of the density of occupied trap states [Eq. (6.1.3)] can be rewritten into form of excess carriers:

$$\frac{d\Delta n_t}{dt} = \sigma_n v_n (n_0 + \Delta n)(p_{t0} + \Delta p_t) - \sigma_n v_n n_1 (n_{t0} + \Delta n_t)$$
$$- \sigma_p v_p (p_0 + \Delta p)(n_{t0} + \Delta n_t) + \sigma_p v_p p_1 (p_{t0} + \Delta p_t) \tag{6.21}$$

Subtracting the thermal equilibrium terms [Eq. (6.9)] from Eq. (6.21) leads to:

$$\frac{d\Delta n_t}{dt} = \sigma_n v_n (n_0 \Delta p_t + \Delta n p_{t0} + \Delta n \Delta p_t) - \sigma_n v_n n_1 \Delta n_t$$
$$- \sigma_p v_p (p_0 \Delta n_t + \Delta p n_{t0} + \Delta p \Delta n_t) + \sigma_p v_p p_1 \Delta p_t \tag{6.22}$$

As mentioned before, $\Delta p$ is assumed to be fast depleted by other recombination channels so that $c_p$ is negligible, and for $n$-type is it reasonable to assume at low injection:

$$n_0 \gg \Delta n = \Delta p + \Delta p_t \approx \Delta p_t \gg p_0 \tag{6.23}$$

With this, Eq. (6.22) can be simplified to:

$$\frac{d\Delta p_t}{dt} = -\frac{d\Delta n_t}{dt} = -\sigma_n v_n n_0 \Delta p_t - \sigma_n v_n n_1 \Delta p_t - \sigma_p v_p p_1 \Delta p_t \tag{6.24}$$

which indicates a single exponential decay of $\Delta p_t$ with a decay time constant $\tau_{decay}$:

$$1/\tau_{decay} = (\sigma_n v_n n_0 + \sigma_n v_n n_1 + \sigma_p v_p p_1). \tag{6.25}$$

Since $\Delta p$ is depleted, the overall PC decay is dominated by the much slower decay of $\Delta p_t$ after a long enough time during the decay. A similar equation for this decay time constant was also derived by Blood and Orton under similar assumptions [114].

A comparison of this new analytical solution with the one from HH trap model will now be made. First, numerical simulations are used to check the validity of Eq. (6.20) from HH and Eq. (6.25) proposed in this work. Note again that in the numerical simulation all the four processes in Fig. 6.1 are considered and none of them are assumed to be negligible. Two cases are simulated here. Each case contains a trap, with its density and defect parameters listed in Table 6.1. The $\tau_r$ of each case is listed as well. Case 2 has a higher $\tau_r$ and higher trap energy level compared to Case 1. Compared to Case 1, Case 2 has a reduced probability of minority carrier recapture and an increased probability of majority carrier emission.

**Table 6.1** Parameters used for simulation of Fig. 6.9

|  | Case 1 | Case 2 |
|---|---|---|
| $\tau_r$ [s] | $8\times10^{-6}$ | $6\times10^{-8}$ |
| $N_t$ [cm$^{-3}$] | $1\times10^{14}$ | $1\times10^{14}$ |
| $\sigma_n$ [cm$^2$] | $3\times10^{-18}$ | $3\times10^{-18}$ |
| $\sigma_p$ [cm$^2$] | $5\times10^{-14}$ | $5\times10^{-14}$ |
| $E_t - E_i$ [eV] | $-0.15$ | $0.35$ |

The numerically simulated transient PC decay lifetime of the two cases in an *n*-type wafer with a doping level of $2\times10^{15}$ cm$^{-3}$ is shown in Fig. 6.9 as blue curves. The low injection lifetime (single exponential decay time constant) calculated using the HH model with Eq. (6.20), and Eq. (6.25) derived in this study are also plotted as black and red dashed lines, respectively. As can be seen, for Case 1 [Fig. 6.9 (a)], the simulated lifetime agrees well with the lifetime predicted by Eq. (6.20) of the HH model yet deviates from the one predicted by Eq. (6.25) derived in this study. The calculated lifetime from Eq. (6.19) of the simplified HH model also deviates from the simulated lifetime. On the contrary, for Case 2 [Fig. 6.9 (b)] the simulated low injection lifetime agrees well with the decay time constant calculated by the equation proposed in this study yet deviates from the one predicted by the HH model.

The results here can be explained as follows. For Case 1, the trap has an energy level in the lower half of the bandgap. Therefore, the term $e_n$ becomes negligible and the

assumption of the HH model is fulfilled. However, for the doping level of the sample used in this simulation, the term $c_n$ is not negligible; therefore; Eq. (6.19) from the simplified HH model does not agree with the simulation. Meanwhile, since the hole recombination lifetime of the sample is not significantly lower than the hole capture time constant of the trap, the assumption required for Eq. (6.25) derived in this study in this study ($c_p$ is negligible) is not fulfilled in this case. Therefore Eq. (6.25) fails to predict the low injection carrier decay time constant.



(a) Case 1                                    (b) Case 2
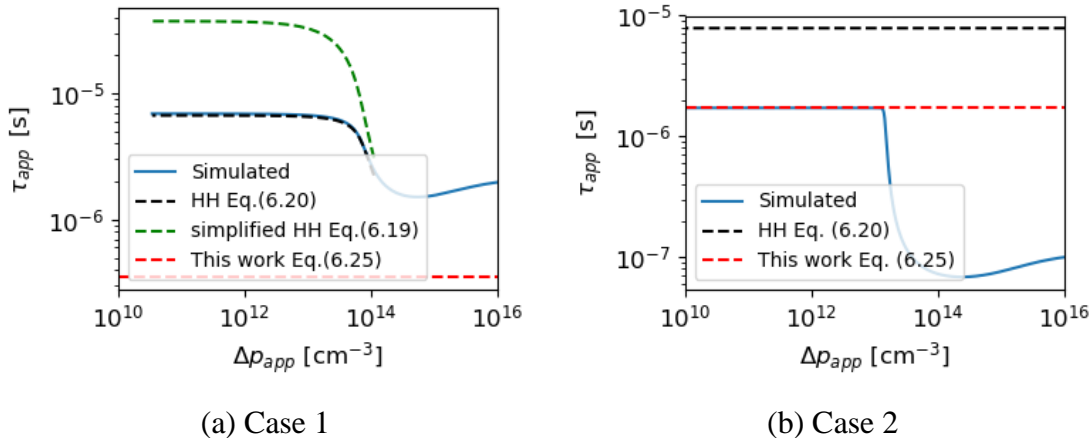
**Fig. 6.9** Comparison of full numerical simulations and analytically solutions of transient PC lifetime for an *n*-type silicon wafer containing the defects listed in Table 6.1. The blue solid line indicates the apparent lifetime simulated by numerically solving carrier continuity equations. The black, green and red dashed lines indicate analytically calculated lifetime using Eq. (6.20), Eq. (6.19) and Eq. (6.25) respectively. Figures (a) and (b) correspond to Case 1 and Case 2, respectively.

For Case 2, the minority carrier lifetime has a lower value. During the transient decay, the depletion of minority carriers becomes much faster than the "de-trapping" process. Therefore, the assumption regarding $c_p$ made in Eq. (6.25) is valid. However, the trap has an energy level close to the conduction band. Since $e_n$ increases exponentially with the energy level, the assumption made in the HH trap model ($e_n$ is negligible) is not valid. Therefore, it is not surprising that Eq. (6.25) agrees with the simulation, whereas the HH model deviates from the simulation in this case.

As can be seen from the simulations above, the HH trap model and the analytical equation derived in this study are complementary to each other. The HH trap model is more suitable for the case where the recapture of the minority carriers in the trap level is significant (but the majority carrier emission is negligible). The equation in this work is more suitable for the case where the majority carrier emission is not negligible (but the minority carrier recapture is negligible). For ease of comparison, Table 6.2 lists the

commonly used analytical solutions of traps (as well as the ones from this work) and their assumptions.

**Table 6.2** Analytical solutions for traps in PC based measurements from literature and this work

| Analytical solution | Condition | Assumptions (for *n*-type Si) |
|---|---|---|
| HH simplified Eq. (6.19) [73] | Transient | $c_n, e_n \ll c_p, e_p$ |
| McDonald *et al.* Eq. (6.6) [23] (Adopted from HH) | Steady state | |
| Hu *et al.* [69] (Adopted from HH) | Transient | |
| HH full Eq. (6.20) [73] | Transient | $e_n \ll c_p, e_p$ |
| This work Eq. (6.16) | Steady state | $n_0 \gg \Delta n = \Delta p + \Delta p_t \gg p_0$ |
| This work Eq. (6.25) | Transient | $1/\tau_r \gg \sigma_p v_p N_t$ ($c_p$ is negligible) $n_0 \gg \Delta n = \Delta p + \Delta p_t \approx \Delta p_t \gg p_0$ |

Compared to the HH trap model, the usage of equation proposed in this work has several advantages. First, the assumption in equation of this work can be confirmed with the same sample. In the HH model, the assumption is that the majority carrier emission is negligible. However, the majority carrier emission only depends on the unknown trap's electrical parameters. Changing the sample preparation or the measurement conditions will not allow a check of the validity of this assumption. For the equation in this work, the assumption is that minority carrier recapture is negligible. This depends on both the trap parameters and the minority carrier lifetime of the sample. Again the trap's parameters cannot be altered, but it is possible to change $\tau_r$ of the sample, *e.g.* via removing the sample surface passivation. That is, the assumption can be confirmed by simply reducing the lifetime of the sample and confirming that the trapping time constant remains unchanged. Second, the decay time constant in the equation of this study is only a function of the trap parameters, and not impacted by trap density. This makes direct comparison of samples with various doping and trap concentrations much easier.

The proposed equation can be used to extract trap parameters. Based on Eq. (6.25), if $1/\tau_{decay}$ is plotted as a function of $v_n n_0$ for multiple samples with the same trap but various doping levels, a linear plot should be obtained. Therefore, the transient decay time

constants of samples with various doping concentrations provide two independent measurements: from the slope of the linear fit, $\sigma_n$ can be extracted; The intercept of the linear fit is $\sigma_n v_n n_1 + \sigma_p v_p p_1$. Since $n_1$ increases exponentially with the trap energy level, whereas $p_1$ decreases exponentially with trap energy level, as long as there is no extreme difference in the magnitude of $\sigma_n$ and $\sigma_p$, the intercept should be either dominated by $\sigma_n v_n n_1$ or $\sigma_p v_p p_1$, depending on the trap energy level. Thus, the majority carrier capture cross section can be determined; $\sigma_p$ and $E_t$ cannot be determined uniquely but their values can be constrained.

The method proposed above is then applied to parameterize the minority carrier traps in the three measured samples in this work. Before that, the validity of the assumption made in the proposed method (the recapture of minority carriers is negligible) needs to be checked. First evidence of the validity of this assumption is the single exponential decay of the PC (Fig. 6.7). If this assumption is not fulfilled, the transient PC decay will not be exponential as indicated by HH [73]. Another way to check the validity of this assumption is to check if the transient PC decay time constant changes after changing $\tau_r$ of the sample. If the original $\tau_r$ of the sample is not low enough for this assumption to be valid, the transient PC decay time constant is expected to change as $\tau_r$ decreases. This is the motivation to measure the sample with doping level of $1.4 \times 10^{16}$ cm$^{-3}$ twice, once with SiN$_x$ passivation and once with SiN$_x$ stripped off. The $\tau_r$ of the sample decreased by one order of magnitude after the SiN$_x$ removal. However, negligible change of the PC decay time constant was observed (from 54.4 s to 53.1 s). The fact that the PC decay time constant remains almost unchanged indicates that the $\tau_r$ of the sample with SiN$_x$ is already low enough for the assumption to be valid.

A plot of $1/\tau_{decay}$ as a function of $v_n n_0$ for the three samples of this work is presented in Fig. 6.10. As can be seen, a good linear fit is obtained. From the slope of the linear fit, the $\sigma_n$ of the trap is extracted as $(5.05 \pm 1.95) \times 10^{-26}$ cm$^2$. From the intercept of the linear plot $\sigma_n v_n n_1 + \sigma_p v_p p_1$ is found to be $(3.93 \pm 4.31) \times 10^{-3}$ s$^{-1}$.

Since the long PC decay time constant in *n*-type Cz silicon was also reported by HH [74] and Hu *et al*. [69], data points from these two studies are also included in Fig. 6.10. Both data points are in a reasonably good agreement with the measured data (24% relative deviation for Haynes and Hornbeck and 27% for Hu *et al*.). Since the exact doping of the sample is not reported in Hu *et al*. [69], the $v_n n_0$ of that point is estimated from the

reported ingot resistivity. This might explain the relatively large deviation of this point from the fitted line. However, if the two data points from literature are fit together with the three data points measured in this work, an R-squared value of 0.979 is obtained, indicating a good linear fitting quality. This provides a strong support for the validity of Eq. (6.25) derived in the study. It also indicates that the origin of the traps in the samples of this study may be the same as that of the samples used in the other two studies.
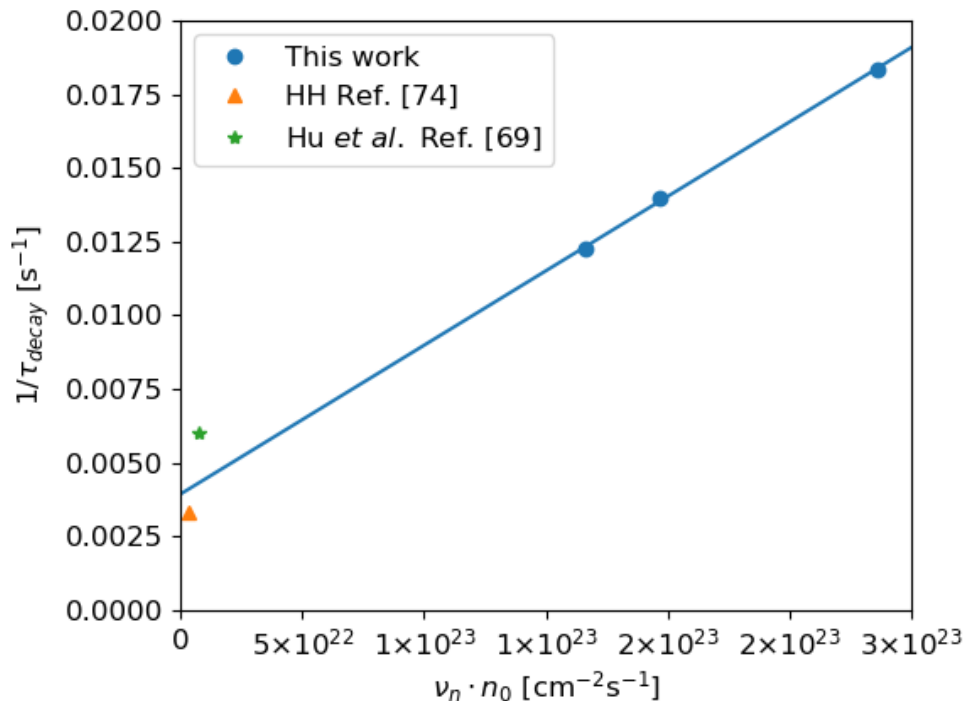


**Fig. 6.10** Plot of the inverse PC decay time constant as a function of the product of thermal velocity and equilibrium electron concentration for the three *n*-type wafers of this study. Two data points from literature (HH [74] and Hu *et al.* [69]) are also plotted.

Using the method described above, the value of $\sigma_n$, as well as a constraint for $\sigma_p$ and $E_t$ of the trap have been extracted. As the true SS PC lifetime of the sample with doping level of $1.4 \times 10^{16}$ cm$^{-3}$ was also measured, this information is used to further determine the value of $\sigma_p$ and $E_t$. With the extracted value of $\sigma_n$ and the constraint for $\sigma_p$ and $E_t$ as input parameters, Eq. (6.16) is used to fit the SS and PC lifetime of the sample. It is found that the best fit is achieved with $\sigma_p = (3.30 \pm 0.66) \times 10^{-19}$ cm$^2$. With $\sigma_p$ found there are still two possible solutions for the trap energy level and trap density: either $E_t - E_i = 0.09 \pm 0.04$ eV and $N_t = 1.6 \times 10^{14}$ cm$^{-3}$ or $E_t - E_i = 0.31 \pm 0.04$ eV and $N_t = 1.9 \times 10^{14}$ cm$^{-3}$. Both solutions provide a reasonably good fit of both the SS and transient lifetimes. In the first solution, the intercept is dominated by the hole's emission

$(\sigma_p v_p p_1)$ whereas in the second solution the intercept is dominated by the electron's emission $(\sigma_n v_n n_1)$. In Fig. 6.6, the numerically calculated lifetimes with the second solution is plotted as well (orange dash line for SS and blue solid line for transient). The fitting with the first solution looks similar and therefore is not presented here. It should be noted that $\sigma_p$ extracted here is impacted by the true minority carrier lifetime of the sample at low injection. In the fitting of the SS lifetime $\tau_r$ is required. An estimate for $\tau_r$ was taken as the minority carrier lifetime is dominated by the SRH lifetime of $Cr_i$. Based on the defect parameters of $Cr_i$ from Ref. [167], the minority carrier lifetime in the samples should have a very weak injection dependence below injection level of $10^{15}$ cm$^{-3}$. It should also be noted that without the information from the previous linear fit, the numerical fitting can be very ambiguous.

Table 6.3 summarizes the results of the extracted parameters. It should be noted that the main aim here is to demonstrate the method developed in this study, instead of trying to get accurate parameters of the trap. For the latter objective, a set of samples with a wider range of doping is more favorable. Simultaneously fitting the SS and transient PC data for all samples would also help to determine the trap's electronic parameters.

**Table 6.3** Parameters Extracted for the traps in the *n*-type Cz wafers

| Parameters | $\sigma_n$ [cm$^2$] | $\sigma_p$ [cm$^2$] | $E_t - E_i$ [eV] |
|---|---|---|---|
| Values | $(5.05\pm1.95)\times10^{-26}$ | $(3.30\pm0.66)\times10^{-19}$ | $0.09\pm0.04$ |
| | | | $0.31\pm0.04$ |

If the HH trap model is applied to analyze the measured data in this study, then Eq. (6.20) will be simplified to $1/\tau_{decay} = \sigma_n v_n n_0 + \sigma_p v_p p_1$ as $\tau_r$ is small enough. Therefore, only the solution with $E_t - E_i = 0.09 \pm 0.04$ eV can be obtained and the possibility of $E_t - E_i = 0.31 \pm 0.04$ eV will be missed.

Hu *et al.* found that this trap in *n*-type Cz silicon is related to the oxygen content and thermal donors in the sample [69]. As after thermal donor removal (rapid thermal annealing at 1000 °C for 10 s [222]), the samples in this study are no longer impacted by traps, this result seem to support the conclusions of Hu *et al.* [69]. However, further investigations are required for the examination of the nature of this trap.

## 6.4 Majority carrier traps and negative photoconductance

The previous sections focus on the investigation of minority carrier traps, which can lead to artificially high apparent lifetime in PC based measurement. In this section majority carrier traps will be investigated and the interesting NPC which can be attributed to the majority carrier traps will be discussed.

First, the experimental observation of NPC will be presented and a brief literature review on NPC will be made in Section 6.4.1. A model using majority carrier traps to explain the NPC phenomenon will then be proposed and numerical simulation will be used to reproduce NPC. Conditions for NPC to occur will then be derived analytically. In the end, a method to extract trap parameters from the measured NPC will be proposed.

### 6.4.1 Experimental observation of negative photoconductance

In this work, an *n*-type silicon wafer with doping concentration of $1.1\times10^{16}$ cm$^{-3}$ is used. The wafer used here came from the same ingot as the wafers used in the minority carrier trap investigation. The PC of the samples was measured using the customized lifetime tester described in Chapter 3.
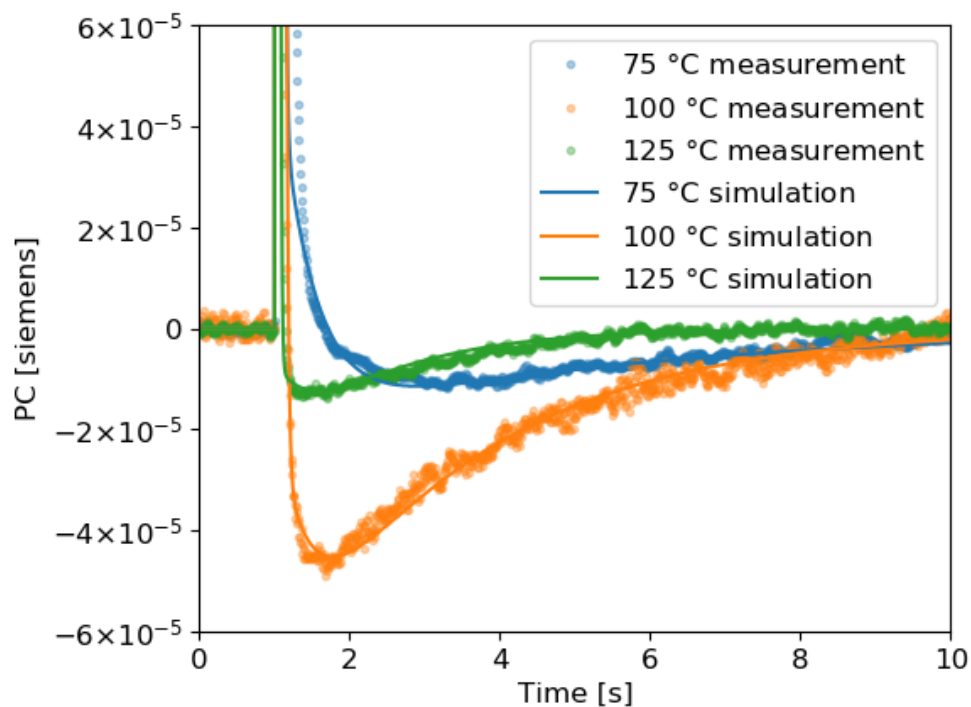


**Fig. 6.11** Measurement of transient NPC in an *n*-type silicon wafer at three different temperatures. The solid lines indicate fitting of the measured data using numerical approach. In this fitting, $E_t - E_i = 0.12$ eV is used, $\sigma_n^T$ of $9.5\times10^{-25}$ cm$^2$, $1.8\times10^{-24}$ cm$^2$, $2.6\times10^{-24}$ cm$^2$ are used for 75 °C, 100 °C and 125 °C respectively.

The transient NPC was observed when the wafers were measured at 75 °C, 100 °C, 125 °C and 150 °C, as shown in Fig. 6.11. For clarity, the 150 °C data is omitted from the plot. In order to increase the signal to noise ratio, 200 measurements were taken at each temperature and the data in Fig. 6.11 shows the average of these measurements. In order to ensure that the sample was at thermal equilibrium at the beginning of the subsequent measurement, a delay of 20 minutes after each measurement was imposed.

In Fig. 6.11, the sample remains in the dark until an excitation by a Xenon flash lamp with a decay time constant of 2.3 ms. The PC of the sample increases, as expected, during illumination. The peak PC is 0.5 siemens at 75°C (not shown in the Figure). At the end of illumination, there is an initial fast decay of the PC due to the recombination of the excess carriers. Atypically, this fast decay does not stop at zero, but decreases below zero to a negative value. Therefore, a negative PC was observed. After a minimum value is reached, the PC slowly increases back to the thermal equilibrium value. Since the sheet resistance of the sample is 10.9 $\Omega$/sq, the observed NPC cannot be explained by the non-linear conductance -voltage response of the coil [223].

NPC is an interesting phenomenon since intuitively one would expect the conductance of a semiconductor to increase above its equilibrium value under illumination due to generation of electron-hole pairs. In the past, NPC has been observed in gold-doped germanium [224], gold-doped silicon [225]–[228], cobalt-doped silicon [229], and other materials [230]–[239]. However, different time scale and different temperature and wavelength dependence of the NPC were reported in these studies with different speculations regarding the cause of the NPC. For example, the NPC reported by Stöckmann is a persistent phenomenon in which the PC of the sample remains negative when the sample is illuminated [235]; whereas the NPC reported by Kurosu *et al.* is a transient phenomenon in which the PC of the sample drops to negative after illumination being switched off, before slowly increasing back to zero [226]. Kimura *et al.* found that in gold-doped silicon the NPC is the most pronounced at around 295 K [228], whereas Höpfel found the amplitude of NPC in GaAs quantum-well monotonically decreases with temperature [236]. Stöckmann, Rose and Höpfel explained the NPC effects by the presence of multiple defect levels [235]–[237]. Altukhov *el al.* attributed the NPC of a two-dimensional hole layer at silicon surface to the quantum scattering of multi-exciton complexes [238], whereas Joshi *et al.* explained the NPC observed in $Cd_xFe_{1-x}Se$ by sub-bandgap excitations [239]. In quantum-well heterostructures, NPC was explained by the

annihilation of majority carriers in the well [232]. Following the path of multiple defect levels, Kimura *et al.* developed a model to explain the transient NPC effect in gold-doped silicon [227], and later successfully reproduced experimental results using this model [228]. However, a more general and quantitative understanding of the transient NPC model has not been presented.

### 6.4.2 Model for the observed negative photoconductance

In this section, a model to explain the transient NPC observed in the measured *n*-type Cz silicon will be proposed. In order to have NPC, the majority carrier concentration or the minority carrier concentration (or both of them) need to fall below their thermal equilibrium level. For silicon wafer, with a typical doping level used for photovoltaic applications (around $10^{16}$ cm$^{-3}$), the majority carrier concentration is more than ten orders of magnitude higher than the minority carrier's thermal equilibrium concentration at room temperature. Even at 200 °C, the majority carrier concentration is still more than three orders of magnitude higher than the minority carrier concentration. This means that the dark conductance is dominated by the majority carriers. Thus, to have a noticeable reduction in conductance below the sample's dark conductance value, the majority carrier concentration has to fall below the dark carrier concentration. This can occur, for example, by the capture of majority carriers into a trap level.

With this idea, a model is proposed which involves two defects, one acting as majority carrier trap and the other as a recombination active center, to explain the occurrence of the transient NPC. This model is similar to the one proposed by Kimura *et al.* for the transient NPC in gold-doped silicon [227]. However, the model by Kimura *et al.* involves a single defect with two energy levels where the electrons can directly move from one level to the other. However, the model proposed in this study involves two distinct single level defects, this direct transition between the two defects is unlikely to happen. This section mainly describes the model in a qualitative way to facilitate the understanding of the mechanism of transient NPC from two defects. More quantitative analysis is then presented in the subsequent sections.

The two defects system is presented in Fig. 6.12 with a set of band diagrams for an *n*-type sample. Here, $E_C$ and $E_V$ are the energy level of the conduction band and valence band, respectively. Two defects are presented: a defect that acts as a strong recombination center ($E_t^R$) (the Cr in the measured sample), and a defect that behaves more like a

majority carrier trap ($E_t^T$). The superscripts "$R$" and "$T$" denote recombination active defect and majority carrier trap respectively. The black circles represent electrons, while the open circles represent holes.
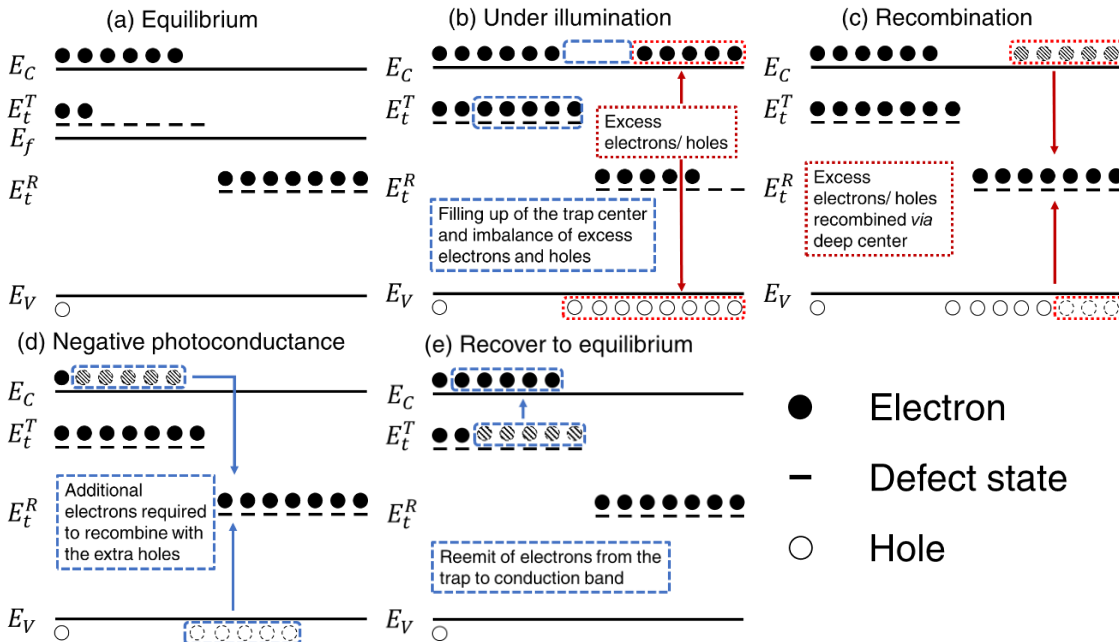


**Fig. 6.12** Two-defects model for transient NPC in $n$-type silicon. The diagram provides a qualitative representation of the carrier concentrations; the number of electrons and holes does not represent the exact quantity.

**Step (a)**: At thermal equilibrium, the occupation probability at each energy level depends only on the temperature and its distance from the Fermi level $E_f$. Here $E_t^T$ is assumed to be close to $E_f$, thus, there are a relatively high fraction of unoccupied trap states. The occupancy of the recombination active level is less critical for NPC.

**Step (b)**: When the sample is illuminated, $\Delta n$ and $\Delta p$ populate the conduction band and valence band, respectively. At the same time, the occupancy of defect states also changes. For a defect, whether its occupancy increases or decreases under illumination depends on the energy level and capture cross section ratio of the defect [240]. For the majority carrier trap level, its occupancy needs to increase under illumination, *i.e.* it fills up with electrons under illumination. For the recombination active defect, there is no requirement regarding the change of its occupancy under illumination. If the net change of occupied electrons in the defect levels is not zero, there will be an imbalance between $\Delta n$ and $\Delta p$.

**Step (c)**: When the illumination is turned off, the excess carriers recombine through the recombination active defect. The emission rate of electrons from the trap level is required to be much slower than the electron capture rate of the recombination active level.

Therefore, the occupancy of the trap level remains almost unchanged at this stage. Electrons are being stored in the trap level.

**Step (d)**: When $\Delta n$ equals zero, $\Delta p$ is still above zero since some of electrons are trapped in the trap level. Therefore, the recombination active defect level continues to capture additional electrons from the conduction band to recombine with those excess holes. As a result, $n$ falls below its thermal equilibrium level, and the PC becomes negative when $\Delta p$ approaches zero.

The above model explains the mechanism for the occurrence of the transient NPC. Now it will be simulated by numerically solving the rate equations as described in Section 6.2.1. Simulations were performed to match the experimental data as shown in Fig. 6.11. The simulated PC agrees very well with the experimental data for all three temperatures. The $\sigma_n^T$ and $E_t^T$ values used for the fitting are reported in the figure caption. The use of different $\sigma_n^T$ at different temperatures will be discussed in Section 6.4.4. It should also be noted that for each temperature, the fitted trap parameters are not unique solutions, *i.e.*, other sets of parameters can provide the same quality of fit. The fitting is less sensitive to other defect parameters such as $\sigma_p^T$, $\sigma_n^R$ $\sigma_p^R$ and $E_t^R$, and therefore their values are not provided.
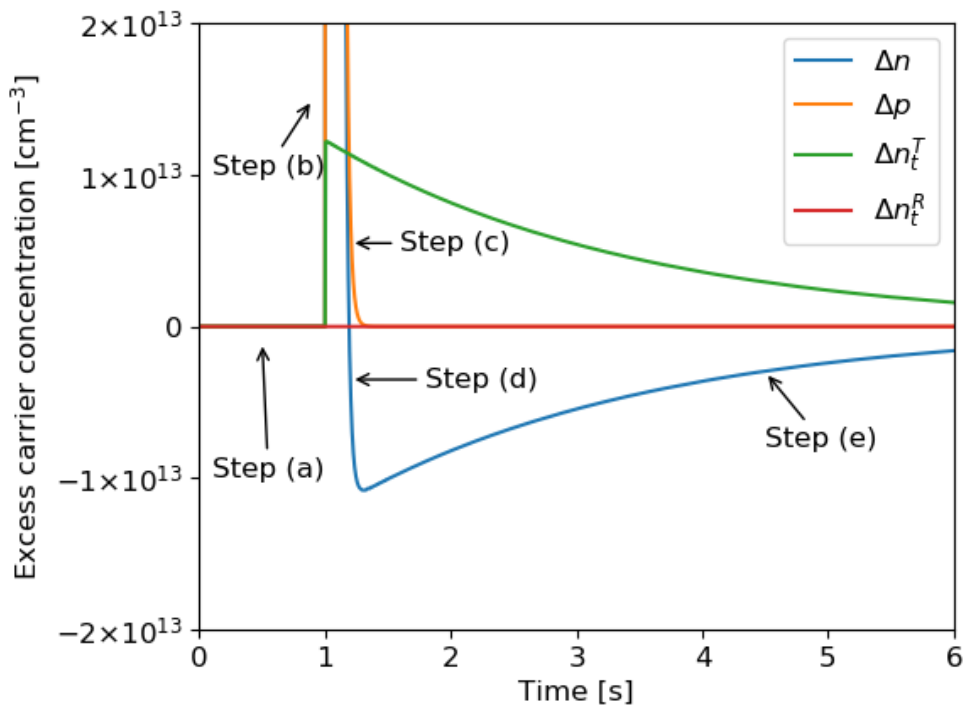


**Fig. 6.13** Excess carrier concentration as a function of time for the simulation of the 100 °C data. The corresponding steps in Fig. 6.12 are indicated.

In order to support the previous qualitative description of the transient NPC model, in Fig. 6.13 $\Delta n$, $\Delta p$, $\Delta n_t^T$ and $\Delta n_t^R$ are plotted as a function of time for the simulation of the 100 °C case. The aforementioned steps of the transient NPC are also indicated in Fig. 6.13. It can be seen that after the illumination is turned off ($t = 1$ s), there is a fast decay of both $\Delta n$ and $\Delta p$. The minority carrier concentration $\Delta p$ quickly drops to zero, whereas $\Delta n$ drops below zero due to the filled trap level ($\Delta n_t^T$). When $\Delta n_t^T$ slowly decreases due to emission of electrons, $\Delta n$ increases back to its thermal equilibrium value.

### 6.4.3 Required conditions for negative photoconductance to occur

From previous qualitative discussion of the model, three critical conditions for transient NPC to occur in *n*-type silicon can be identified. First, the trap needs to be a majority carrier trap, *i.e.* be filled up by electrons during illumination. This reduction of electrons concentration in the conduction band is the causes of the NPC. Second, during the recombination process, the emission rate of electrons from the trap needs to be slower than the electron capture rate of the recombination active level. Otherwise, the electron concentration would not drop below its equilibrium value. Finally, the hole capture rate of the trap level needs to be much smaller than the hole capture rate of the recombination active level during the recombination process. Otherwise, the trapped electrons will be directly annihilated with the excess holes in the valence band. Based on this discussion, the analytical form of these three conditions will be derived.

At thermal equilibrium electron concentration $n_0 = n_i \exp\left(-E_f/kT\right)$; the trapped electron concentration $n_{t0}^T$ can be calculated from the distance of its $E_t^T$ to $E_f$:

$$\frac{n_{t0}^T}{N_t^T} = \frac{1}{\exp\left(\dfrac{E_t^T - E_f}{kT}\right) + 1} = \frac{n_0}{n_0 + n_1^T} \tag{6.26}$$

In order to have sufficient number of states to be filled up during illumination, $n_{t0}^T/N_t^T$ should not be close to unity, which means $E_t^T$ needs to be close to $E_f$ for *n*-type material. Under SS illumination, the trapped electron concentration $n_t^T$ can be calculated by solving the rate equations in SS condition:

$$\frac{n_t^T}{N_t^T} = \frac{(n_0 + \Delta n)\sigma_n^T/\sigma_p^T + p_1^T}{(n_0 + n_1^T + \Delta n)\sigma_n^T/\sigma_p^T + p_1^T + p_0 + \Delta p} \tag{6.27}$$

For $n$-type silicon with $E_t^T$ close to $E_f$, $p_1$ and $p_0$ can be considered negligible compared to $n_0$. When the injection level is high enough that $\Delta n \gg \Delta n_t^T$ and $\Delta n_t^R$, $\Delta p$ can be considered equal to $\Delta n$. Under these conditions Eq. (6.27) can be simplified to:

$$\frac{n_t^T}{N_t^T} = \frac{(n_0) + (\Delta n)}{(n_0 + n_1^T) + (\sigma_p^T/\sigma_n^T + 1)\Delta n} \tag{6.28}$$

In order for the trap level to fill up under illumination, $n_t^T$ needs to be larger than $n_{t0}^T$. With Eqs. (6.26) and (6.28), $n_t^T > n_{t0}^T$ leads to:

$$\frac{(n_0 + \Delta n)\sigma_n^T/\sigma_p^T + p_1^T}{(n_0 + n_1^T + \Delta n)\sigma_n^T/\sigma_p^T + p_1^T + p_0 + \Delta p} > \frac{n_0}{n_0 + n_1^T} \tag{6.29}$$

which is equivalent to:

$$\frac{1}{(\sigma_p^T/\sigma_n^T + 1)} > \frac{n_0}{n_0 + n_1^T} \tag{6.30}$$

which leads to:

$$\exp\left(\frac{E_t^T - E_f}{kT}\right) > \frac{\sigma_p^T}{\sigma_n^T} \tag{6.31}$$

For the second condition, it requires $e_n^T < c_n^R$, *i.e.*:

$$\sigma_n^T v_n n_1^T n_t^T < \sigma_n^R v_n n(N_t^R - n_t^R) \tag{6.32}$$

For $n$-type silicon, immediately after the initial fast recombination, the electron concentration $n$ can be approximated as $n_0$. Since the trap level is filled up during illumination and has a slow re-emission rate, it is reasonable to approximate $n_t^T$ as $N_t^T$. The $(N_t^R - n_t^R)$ term depends on the defect parameters of the recombination center; however, its upper limit is $N_t^R$. Therefore, Eq. (6.32) can be simplified to:

$$\exp\left(\frac{E_t^T - E_f}{kT}\right) < \frac{\sigma_n^R}{\sigma_n^T}\frac{N_t^R}{N_t^T} \tag{6.33}$$

For the third condition, it requires $c_p^T < c_p^R$ during the recombination process:

$$\sigma_p^T v_p p n_t^T < \sigma_p^R v_p p n_t^R \tag{6.34}$$

Again, $n_t^T$ can be approximated as $N_t^T$, and the upper limit of $n_t^R$ is $N_t^R$. The above inequality can be simplified to:

$$\sigma_p^T N_t^T < \sigma_p^R N_t^R \tag{6.35}$$

Together with the first two conditions, the general condition for transient NPC to occur with the presence of a trap level and a recombination active level has been derived as:

$$\begin{cases} \dfrac{\sigma_p^T}{\sigma_n^T} < \exp\left(\dfrac{E_t^T - E_f}{kT}\right) < \dfrac{\sigma_n^R}{\sigma_n^T}\dfrac{N_t^R}{N_t^T} \\ \sigma_p^T N_t^T < \sigma_p^R N_t^R \end{cases} \tag{6.36}$$

Despite the few simplifications that have been made, the above set of constraints has been found to serve well as necessary conditions to observe transient NPC based on numerical simulations.

Apart from the theoretical conditions, a relatively large $\Delta n_t^T$ is beneficial for clearly observing the transient NPC in actual experiments. Therefore, a relatively large $N_t^T$ and high illumination intensity assist in observing the transient NPC.

Again, the conditions derived in this section are based on *n*-type silicon, an analogue derivation for *p*-type silicon should be found easily. Additionally, the derivation is based on the proposed model where a bulk recombination active defect is presented, since the measured wafers were known to be Cr-contaminated. However, it should be noted that this bulk recombination active defect can be replaced by any other fast recombination channel, such as surface defects, or radiative recombination in direct bandgap semiconductor. Similar transient NPC can be measured on samples from the same supplier (grown under the same conditions), but without Cr contamination, when the quality of the surface passivation is poor. In this case, the surface recombination, instead of Cr, acts as a fast recombination channel. The majority carrier trap level is the irreplaceable part for the occurrence of the transient NPC. In the situations of other fast recombination channels, the conditions for the NPC to happen will have different forms.

### 6.4.4 Trap parameterization from negative photoconductance

From the analysis in the previous section, it can be seen that the transient NPC can only be observed in samples with defect of certain electrical properties. The unique characteristics of the transient NPC could potentially provide information of the trap level.

In this section, a method to extract some of the parameters from the recovery process [Step (e)] of the transient NPC will be proposed.

From the previous analysis, it can be noticed that the emission of electrons from the trap dominates the recovery process. During this time, $\Delta n_t^R$ and $\Delta p$ are effectively zero due to the fast recombination channel [see Step (c) in Fig. 6.13]. Therefore, $\Delta n$ should equal to $-\Delta n_t^T$ according to charge neutrality (both $\Delta n$ and $\Delta n_t^T$ can be negative). For a trap (in an $n$-type sample) whose energy level is located near $E_f$, $e_p$ and $c_p$ are negligible compared to $e_n$ and $c_n$. The change rate of $n_t^T$ can be safely simplified from Eq. (6.1.3) to:

$$\frac{\mathrm{d}n_t^T}{\mathrm{d}t} = -\sigma_n^T v_n n_1^T n_t^T + \sigma_n^T v_n n (N_t^T - n_t^T) \tag{6.37}$$

Rewriting the equation in terms of excess carriers gives:

$$\frac{\mathrm{d}\Delta n_t^T}{\mathrm{d}t} = -\sigma_n^T v_n [(n_1^T + n_0)\Delta n_t^T - \Delta n (N_t^T - n_{t0}^T) + \Delta n \Delta n_t^T] \tag{6.38}$$

The term $\Delta n \Delta n_t^T$ is negligible compared to the other terms during the recovery process. Since $\Delta n$ should equal to $-\Delta n_t^T$, combined with Eq. (6.26), Eq. (6.38) can be simplified to:

$$\frac{\mathrm{d}\Delta n_t^T}{\mathrm{d}t} = \sigma_n^T v_n \left( n_1^T + n_0 + N_t^T \frac{n_1^T}{n_1^T + n_0} \right) \Delta n = -\frac{\mathrm{d}\Delta n}{\mathrm{d}t} \tag{6.39}$$

Hence, during the recovery process, $\Delta n(t)$ should have the form of $A_N \times \exp(-t/\tau_{NPC})$. $A_N$ is the amplitude depending on the defects' parameters and the measurement conditions. The time constant $\tau_{NPC}$ can be calculated as:

$$\tau_{NPC} = 1/[\sigma_n^T v_n \left( n_1^T + n_0 + N_t^T \frac{n_1^T}{n_1^T + n_0} \right)] \tag{6.40}$$

Since $\Delta p$ is zero, the change rate of photoconductance should have the same time constant as $\Delta n$. This time constant is a function of just three parameters: $\sigma_n^T$, $E_t^T$ and $N_t^T$. If the time constant is measured at three different temperatures, these three parameters can be extracted (when they are independent of temperature) by, for example, the Newton-Raphson method presented in Chapter 5. Alternatively, the parameters can be extracted by measuring the time constant of three samples with different doping levels

(although, it may be challenging for the samples to have the same trap center and for the NPC to be observed in all of them).

If $N_t^T$ is much smaller than the doping level of the sample, Eq. (6.40) can be further simplified to:

$$\tau_{NPC} = 1/[\sigma_n^T v_n (n_1^T + n_0)] \tag{6.41}$$

The simplified equation has only two unknown parameters, and thus by measuring the time constant at two temperatures or two doping levels, $E_t^T$ and $\sigma_n^T$ can be extracted. At lower temperatures, $\tau_{NPC}$ will become more sensitive to the $N_t^T$ term in Eq. (6.40), since both $n_1^T$ and $n_0$ decrease with temperature. By measuring $\tau_{NPC}$ at a lower temperature, $N_t^T$ could potentially be determined. However, at a lower temperature the transient NPC may not be observed, as the aforementioned conditions may fail to be satisfied. For example in the samples measured in this study, the NPC is less pronounced as temperature decreases, and it completely disappeared at temperatures below 50 °C.
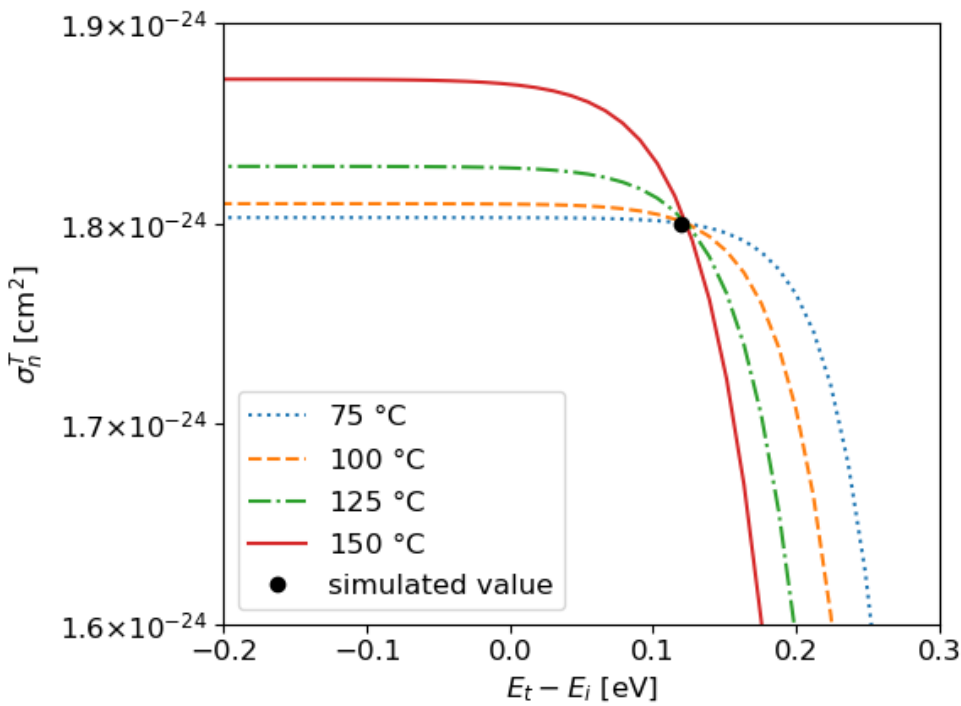


**Fig. 6.14** Solution curves of the electron capture cross section and energy level for a majority carrier trap center simulated at 75 °C, 100 °C, 125 °C and 150 °C. The black dot indicates the correct trap parameters.

The proposed method is firstly applied to a set of simulated NPC data. In the simulation, $E_t^T$ and $\sigma_n^T$ are set to 0.12 eV above intrinsic level and $1.8 \times 10^{-24}$ cm², respectively. The

time constants of the recovery process are extracted at four simulated temperatures (75 °C, 100 °C, 125 °C and 150 °C). Using Eq. (6.40), the value of $\sigma_n^T$ at any assumed $E_t^T$ can be calculated for each time constant. Similar to the DPSS methods [21] described in Chapter 4, this process provides a solution curve of the trap parameters at each temperature. The trap parameters can be extracted from the intersection of all the curves. The result of the simulated data is presented in Fig. 6.14. As can be seen, the four curves display a sharp intersection at the simulated value of $E_t^T$ and $\sigma_n^T$.

This method is then applied to the data shown in Fig. 6.11 and the result is presented in Fig. 6.15. The fitted time constants are 4.92±0.14 s, 2.48±0.05 s, 1.49±0.07 s and 1.13±0.08 s for measurements at 75 °C, 100 °C, 125 °C and 150 °C, respectively. The reported uncertainty range is the 95% confidence interval for the fitting.
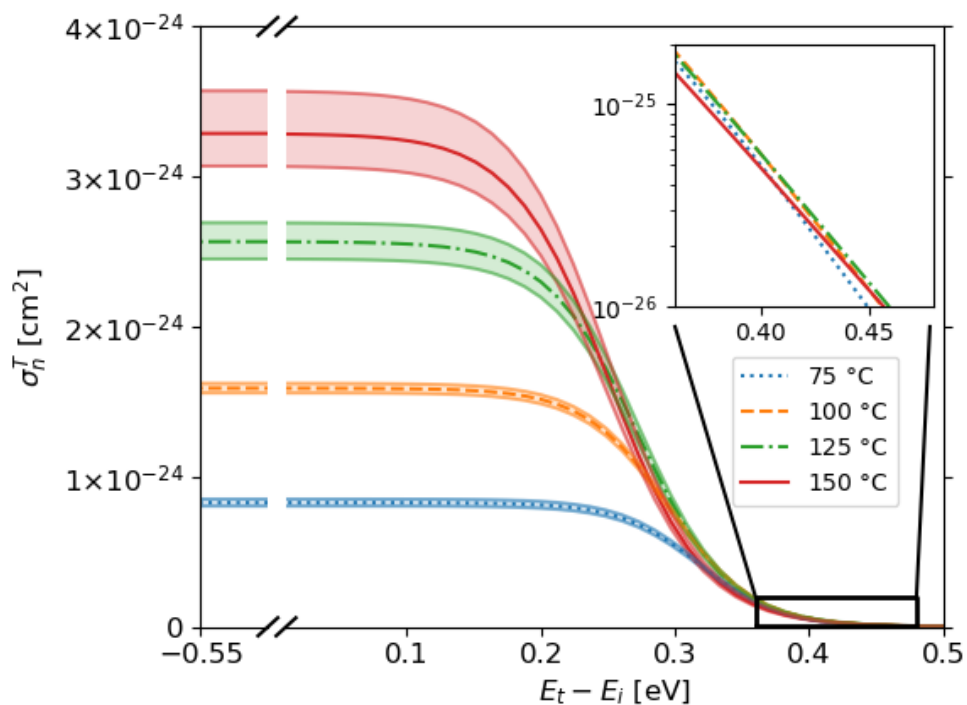


**Fig. 6.15** Solution curves of the electron capture cross section and energy level for the majority carrier trap center measured at 75 °C, 100 °C, 125 °C and 150 °C. The uncertainty range of each solution curve is also indicated.

In the linear scale plot, the four curves are quite close to each other in the range of $E_t^T > 0.3$ eV. However, no clear intersection of the four curves can be identified in this range. There are two possible reasons for that: (a) $E_t^T - E_i$ is above 0.3 eV but the uncertainty of the measurement is too large. In this energy range, the four curves are too close to each other, thus even small uncertainty in the measured time constant can leads

to large uncertainty in $E_t^T$ and $\sigma_n^T$. (b) $\sigma_n^T$ is temperature dependent and therefore no intersection can be observed.

According to Fig. 6.15, if $E_t^T - E_i$ is below 0.1 eV, $\sigma_n^T$ at each temperature equals the plateau value of each corresponding curve. Under this assumption, $\sigma_n^T$ follows an exponential temperature dependency [Eq. (5.4)]: $\sigma(T) = \sigma_\infty \exp\left(\frac{-E_\infty}{k_b T}\right)$ with $\sigma_\infty$ of $2 \times 10^{-22}$ cm$^2$ and an $E_\infty$ of 0.23 eV. If $E_t^T - E_i$ is indeed below 0.1 eV, according to Eq. (6.36), an extremely low value of $\sigma_p^T$ (in the order of $10^{-28}$ cm$^2$) is required.

One possible method to overcome the difficulty of a temperature dependent capture cross section is to measure samples with various doping levels, instead of measuring one sample at various temperatures. According to Eq. (6.41), plotting the measured $1/\tau_{NPC}$ as a function of $n_0$, allows the determination of $E_t^T$ and $\sigma_n^T$ from a simple linear fit. The measurement of sample with various doping is in the future plan of this work. At this stage, it is also not able to determine the origin and nature of these majority carrier traps in the measured $n$-type Cz silicon. Whether it has a relation with the minority carrier traps identified in Section 6.3 would also be interesting to investigate in the future.

## 6.5 Chapter summary

In this chapter, trap-like defects in silicon have been investigated. Although traps are generally not very recombination active and have relatively small impact on the device performance, they can have significant impact on the PC based lifetime measurement. For techniques like lifetime spectroscopy where accurate measurements of lifetime are required, the understanding of trap properties is essential.

First, the minority carrier traps in PC measurement are investigated. The difference of traps in SS condition and traps in transient condition is highlighted. A method to extract trap parameters from transient PC measurement has been developed. Appling this method, the electrical properties of minority carrier traps in $n$-type Cz silicon have been extracted.

The majority carrier traps which can lead to a very interesting transient NPC phenomenon are also investigated. The condition for the NPC to occur has been derived analytically. A method to extract trap parameters from the measured NPC has been proposed and applied to the majority carrier traps in $n$-type Cz silicon.

# Chapter 7
# Characterization of Defects with Non-uniform Distribution

In previous chapters, the investigation of recombination active defects or traps are based on the assumption that the defects are uniformly distributed within the sensor area of the measurement tool. However, if defects in the sample are not uniformly distributed, the measured signal is actually an averaged value over the sensor area with a certain weighting. If we want to use the measured lifetime to investigate the properties of the defect, obviously this averaged lifetime will lead to error in the lifetime spectroscopy analysis. Theoretically, one can reduce the sensor area such that the defect distribution within this smaller area can be considered as uniform. However, in practice a reduced sensor area usually indicates a smaller signal and a reduced signal to noise ratio.

Spatially non-uniform distribution of defects is not uncommon. For example, mc-Si is by nature a non-uniform material. The crystallographic defects such as grain boundaries, dislocations, as well as metal impurities, all distribute non-uniformly in mc-Si. For mono-crystalline silicon, defects can also have spatial non-uniform distribution. For example, the thermally activated defects in FZ silicon, investigated in Chapter 6, has a much higher distribution in the center of the wafer than at the edge of the wafer. Fortunately, these defects have a relatively uniform distribution in the center of the wafer which is larger than the sensor areas of our measurement systems. Therefore, our measurements were not impacted by this non-uniform distribution. In the Cz wafer, non-uniform distribution of defects also exists. The striation defects related to oxygen precipitate, oxygen induced stacking fault (OSF), and thermal donors all have non-uniform distribution in the Cz wafer. A spatially resolved characterization technique is thus beneficial for more accurate investigation of these defects in silicon.

This chapter focuses on PL imaging, the most widely used spatially resolved characterization techniques for silicon wafer and solar cells. First, the limitations of conventional PL imaging for characterizing the spatially non-uniformly distributed

defects will be outlined. Finally, a modified approach of PL imaging which could potentially overcome those limitations will be proposed.

## 7.1 Conventional PL imaging and its limitations

As a fast, powerful and contactless characterization technique, PL imaging [72] has been widely used in the photovoltaic community to obtain the spatial non-uniformity of silicon bricks, wafers, solar cells, and modules [72], [125]–[127], [241]–[243].

In a conventional PL imaging measurement, the sample is excited by a spatially uniform light source and the PL from the sample is captured by a camera. Higher PL intensity indicates a higher excess carrier density ($\Delta n$). Given that the generation rate ($G$) is uniform, locations with higher $\Delta n$ represent a higher carrier lifetime. Therefore, qualitative spatially resolved information of the sample quality can be obtained from PL images [72]. Apart from qualitative information that is obtained from the relative PL counts, PL images can be converted to quantitative carrier lifetime images for silicon wafers by calibrating the PL counts to absolute $\Delta n$ [72], [134], [135], [149]. Combined with knowledge of the Shockley-Read-Hall defect parameters, the carrier lifetime image can be further converted to images of metastable defects, such as iron [244], chromium [245] and others [246]. For solar cells, using a similar calibration processes, spatially resolved local voltage [247], [248], saturation current [249], [250], fill factor [251], temperature coefficient [252], [253], efficiency [254] and many other parameters [255], [256] can be obtained. More recently, by measuring PL imaging at various temperatures and various excitation intensities, spatially resolved TIDLS has been attempted in order to investigate the spatially resolved dominant defects' properties [257].

However, since the sample is under uniform excitation intensity in conventional PL imaging, any non-uniformity in the sample quality will lead to a gradient of the quasi-Fermi level splitting. This gradient induces a net lateral carrier flow in the sample. This lateral carrier flow leads to inaccuracies in all the aforementioned PL imaging based quantitative analysis methods [137]. For example, in the carrier lifetime imaging technique, when lateral currents are present, the lifetime is not simply the ratio of $\Delta n$ and $G$ but an additional term of the lateral current needs and this needs to be considered. For non-diffused silicon wafers, this lateral current is dominated by lateral diffusion. A method to quantify this diffusion term and de-smear the carrier lifetime image was proposed by Phang *et al.* [137], [138], However, due to the Laplacian operation in the

diffusion term, this method is quite sensitive to measurement noise. For diffused silicon wafers or completed solar cells, the lateral current flow is dominated by drift via the emitter and metal contacts, which is even harder to quantify or accurately correct for.

## 7.2 PL imaging at uniform excess carrier density

Recently, Heinz *et al.* proposed an approach to mitigate the lateral current flows in PL imaging measurements of silicon wafers by using an adaptive non-uniform excitation [258]. They proposed that by iteratively adjusting the illumination intensity at each pixel according to the PL intensity at that pixel, a uniform PL image of the measured wafer can be achieved. The information regarding the sample non-uniformity can then be obtained from the non-uniform excitation image that is used to achieve a uniform PL image. The advantage of this approach is that the non-uniformity information of the sample can be extracted at the same injection level. Moreover, the lateral balancing current in the sample can be avoided, and thus more accurate quantitative analysis is possible. The work of Heinz *et al.* [258] discussed the theory of this method and demonstrated its feasibility via simulations. In this work, the feasibility and advantages of this method will be demonstrated experimentally.

PL imaging with non-uniform excitation has been previously achieved using a digital micromirror device (DMD) for contactless series resistance imaging, emitter sheet resistance and diffusion length measurement [259], [260]. The details of these applications will be presented in Appendix C. In these applications, the non-uniform illumination is used to intentionally induce lateral carrier flow in a contactless manner. In this section, on the contrary, the non-uniform illumination is used to counterbalance the intrinsic lateral carrier flow in PL imaging due to sample non-uniformity. A DMD modulates the illumination at a frequency in the order of 10 kHz, the average light intensity determined by the duty cycle between on and off. This represents a non-steady state condition and impedes the application of the adaptive non-uniform excitation method in many practical cases. In this section, a liquid-crystal-display (LCD) based illumination setup is used which can achieve arbitrary steady state non-uniform excitation patterns [261].

### 7.2.1 Setup for PL imaging at uniform excess carrier density

A schematic diagram of the LCD-based PL imaging setup used in this study is shown in Fig. 7.1. It is similar to a conventional PL imaging setup except for modifications of

the light source. After being homogenized, the light is polarized. The polarized light then passes a controlled LCD panel and a secondary polarizer. The two polarizers have perpendicular axes. By adjusting the voltage applied to each pixel, the LCD panel can twist the polarization of the light at each pixel from 0 degree to 90 degrees. Together with the two polarizers, the LCD panel enables the light intensity at each pixel to be adjusted from 0% to 50% of its original value. The LCD panel used in this work has a spatial resolution of 1024×768 pixels, an on/off dynamic range of 4000:1 with 8-bit grey scale resolution. The actual dynamic range that can be achieved by two neighbor pixels is smaller than the nominal dynamic range. A short pass filter is used to block any illumination light that could be detected by the camera reaching the sample.

In the current setup, the light intensity of the current setup is limited to 30 mW/cm$^2$. One pixel of the LCD panel corresponds to a square area of 180×180 μm$^2$ on the sample plane. The PL emitted from the sample is captured by a silicon complementary metal–oxide–semiconductor (CMOS) camera with a spatial resolution of 2048×2048. One pixel of the captured image corresponds to a square area of 55×55 μm$^2$. The pixels of the LCD panel and the camera were carefully aligned before the measurement.
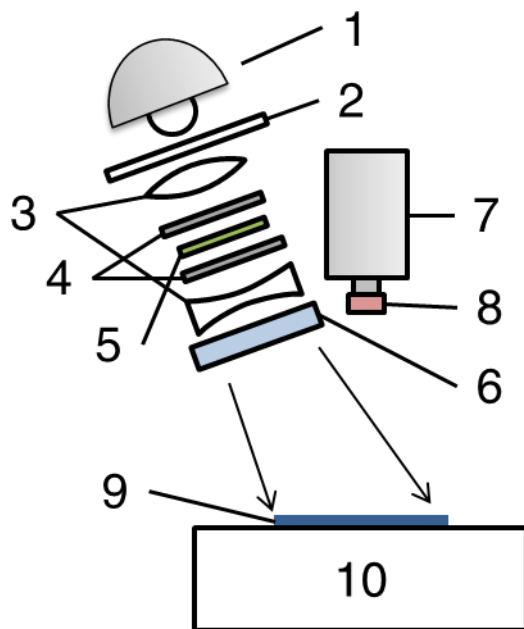


**Fig. 7.1** Sketch of the LCD-based PL imaging setup with: (1) light source and concave mirror; (2) beam homogenizer (3) lens; (4) polarizers; (5) LCD panel; (6) short pass filter; (7) silicon CMOS camera; (8) long pass filter; (9) sample; and (10) sample stage.

In order to obtain PL images at uniform $\Delta n$, an iteration procedure to adaptively adjust the excitation light intensity at each position of the sample is used. First, a PL image with

spatial uniform light intensity is taken as the starting point of the iteration. An arbitrary position is then chosen to be the position where the light intensity is kept unchanged. For any other position $(x, y)$, at the $i^{th}$ iteration, the light intensity is calculated as:

$$\Phi_{x,y}^i = \Phi_{x,y}^{i-1} \left[ \frac{PL_o^{i-1}}{PL_{x,y}^{i-1}} \varepsilon + (1 - \varepsilon) \right], \tag{7.1}$$

where $\Phi_{x,y}^i$ is the light intensity at position $(x, y)$ in the $i^{th}$ iteration and $PL_{x,y}^{i-1}$ is the PL counts at position $(x, y)$ in the $(i - 1)^{th}$ iteration. An arbitrary position "$o$" is then chosen where the light intensity remains constant during the iteration. $PL_o^{i-1}$ is the PL counts at that position in the $(i - 1)^{th}$ iteration. $\varepsilon$ is a damping factor with the value between 0 and 1. A lower damping value will lead to slower, but more stable convergence [258]. Due to the moderate injection dependence of the carrier lifetime of our samples, a damping factor of unity is used in order to obtain a fast convergence. The iteration is set to end when the relative change of light intensity compared to the previous iteration is below 5% for every pixel.

In the iteration procedure proposed by Heinz *et al.* the calibrated $\Delta n$ value is used [258], whereas in this work the measured PL intensity is directly used. This makes no difference for the iteration since our measurements are in low injection where the PL intensity is proportional to $\Delta n$.

To minimize any artifact due to the camera, the obtained PL image is flat-field corrected using the $\cos^4(\theta)$ law [262] and deconvolved using the method described in [263] during each iteration.

### 7.2.2 Proof-of concept on solar cells

As a proof of concept, the iteration procedure above was first tested on two mini solar cells. The two mini cells (20 mm×10 mm) were cleaved from a uniform 6-inch *p*-type mono-crystalline aluminum back surface field solar cell. One of the two mini cells was uniformly degraded via boron-oxygen activation using an accelerated laser degradation procedure [264]. These two mini cells (see insets of Fig. 7.2) can be connected in parallel via their terminals during measurements in order to enable carrier exchange between them. In these proof of concept measurements, these two mini cells are treated as two macro pixels and the light intensity on these two macro pixels was adaptively adjusted until these two pixels reached the same PL intensity.

At this stage the non-uniformity introduced by the fingers and busbars of the solar cells is ignored. The PL counts used for each iteration step are taken as an average of the cell area. The method is demonstrated by imaging the two cells simultaneously and using the LCD to change the light intensity across one of the cells. In each iteration step, the light intensity on the degraded cell is kept unchanged and the light intensity on the non-degraded cell is adaptively adjusted with the following simplified iteration procedure:

$$\Phi_{nd}^i = \Phi_{nd}^{i-1} \frac{PL_d^{i-1}}{PL_{nd}^{i-1}} \tag{7.2}$$

where the subscripts "$d$" and "$nd$" indicate the degraded cell and non-degraded cell, respectively. In the initial iteration, the two cells are illuminated with the same light intensity as in conventional PL imaging.
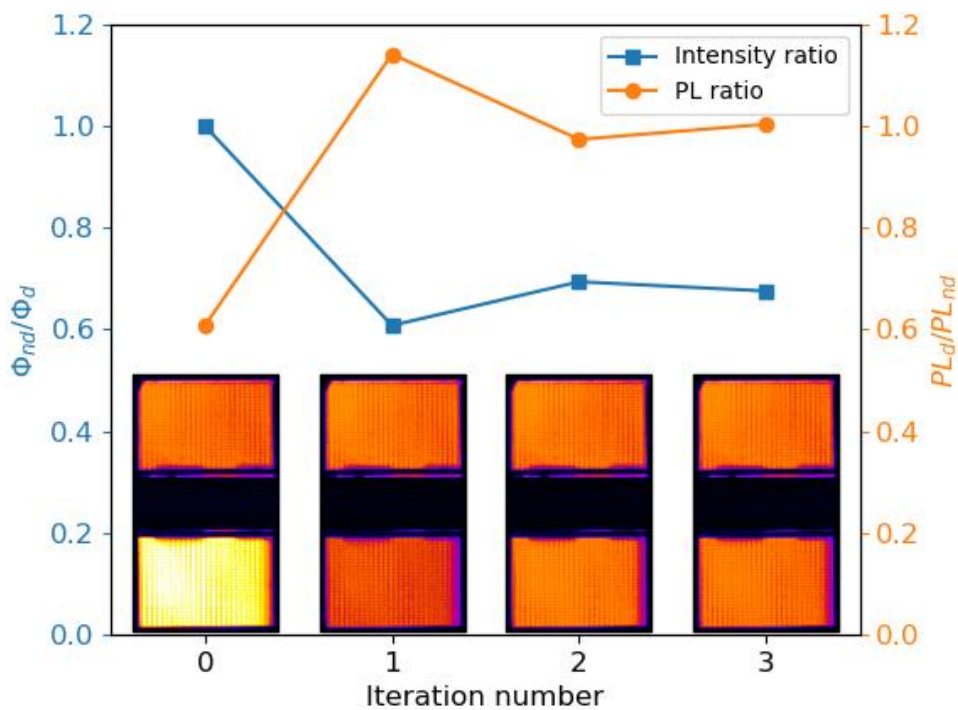


**Fig. 7.2** The excitation light intensity ratio, the PL intensity ratio and the PL images of the two mini cells during the first three iterations, with the two cells electrically disconnected from each other.

In a first step the two cells were measured while they were disconnected, in order to exhibit the simple scenario where there is no carrier exchange between them (no impact of lateral carrier flows). The ratios of the light intensity and of the PL intensity between the non-degraded and degraded cells during each iteration step are shown in Fig. 7.2. The figure also includes the PL images of the cells during the iteration. As can be seen, in this

case three iterations (after the initial one) were required to reach an identical PL intensity between the non-degraded and degraded cells, *i.e.* a unity PL intensity ratio (right hand axis of Fig. 7.2). Since the two cells are disconnected and the light intensity on the degraded cell is kept unchanged, the PL intensity of the degraded cell remains unchanged during all iterations. For the non-degraded cell, its PL intensity decreases below $PL_d$ in the first iteration, resulting in a $PL_d/PL_{nd}$ ratio exceeding unity, then exceeds $PL_d$ and finally reaches the same value as $PL_d$. The overshooting in the first iteration is due to an injection dependent carrier lifetime. The PL ratio $PL_d/PL_{nd}$ in the initial iteration is 0.61, whereas the $\Phi_{nd}/\Phi_d$ in the last iteration is 0.68. This difference is likely to a result of the injection dependency of the lifetime of the non-degraded cell.
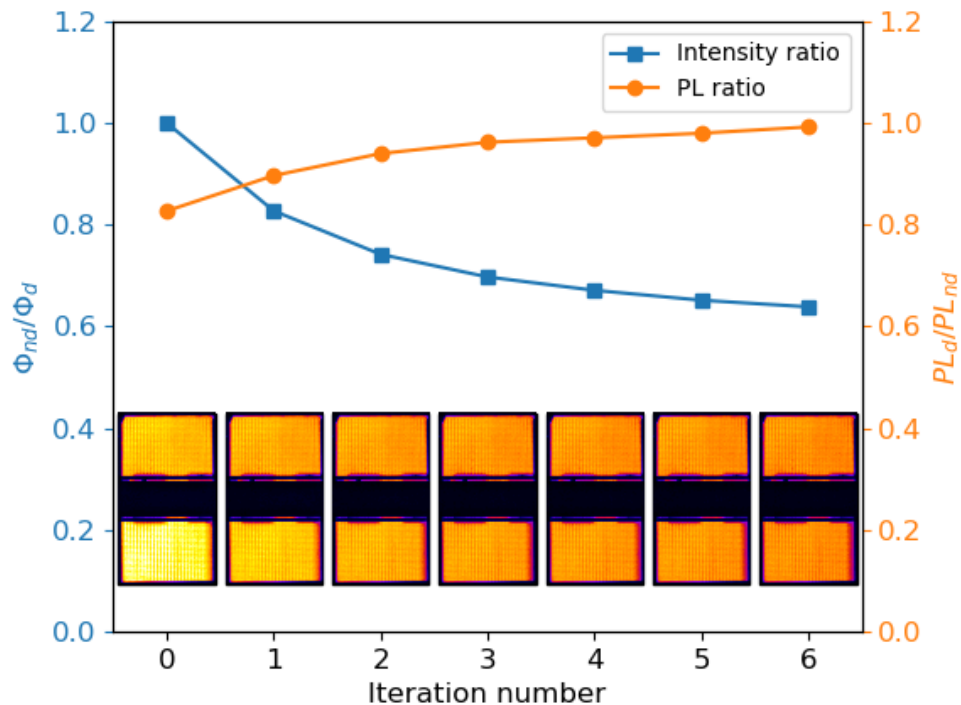


**Fig. 7.3** The excitation light intensity ratio, the PL intensity ratio and the PL images of the two mini cells during the iteration when the two cells are connected in parallel.

The same procedure is repeated in a second experiment, this time with the two mini cells electrically connected in parallel in order to represent the scenario where these two cells are two neighbor regions of a large cell that are impacted by lateral carrier flow. The result of this scenario is shown in Fig. 7.3. Compared to the simpler case of Fig. 7.2 this scenario requires more iterations (six after the initial one) to reach a PL ratio of unity between the two mini cells. As the two mini cells are connected, even though $\Phi_d$ is kept unchanged, $PL_d$ still decreases when $\Phi_{nd}$ decreases as carrier flow from the non-

degraded cell to the degraded cell is reduced. This prolongs the iteration process compared to the case where the two mini cells are disconnected.

The scenario where the two cells are disconnected reflects the true difference between the two cells' quality, as it is not impacted by the lateral carrier flow, whereas the scenario where the two cells are connected represents what would be obtained in conventional PL imaging, when the two cells are neighbor regions of a large cell. Therefore, the PL ratio $PL_d/PL_{nd}$ in the initial iteration ($\Phi_{nd}/\Phi_d = 1$) of the disconnected case (0.61, see Fig. 7.2, corresponding to an implied voltage difference of around 12.7 mV) represents the true difference between the cells under uniform $G$. The ratio in the connected scenario (0.83, corresponding to an implied voltage difference of around 4.8 mV) is smaller as it is impacted by lateral carrier flow. The difference between these two scenarios highlights the impact of lateral carrier flow on conventional PL imaging.

It is important to note that under uniform generation, the two cells are at different injection levels. The ratio $\Phi_{nd}/\Phi_d$ in the last iteration of the disconnected scenario (0.68) reflects the difference of the two cells at the same injection level as the two cells have the same PL intensity, and thus the same $\Delta n$. Ideally, $\Phi_{nd}/\Phi_d$ in the last iteration of the connected scenario should also have a value of 0.68 as it should not be impacted by the lateral carrier flow when the two cells have the same $\Delta n$. The final $\Phi_{nd}/\Phi_d$ in the connected case (Fig. 7.3) is slightly lower (0.64, 6% relative difference). Part of this difference might come from the fact that there is non-uniformity within the two mini cells. Nevertheless, the results shown here still demonstrate that the proposed method allows achieving a uniform $\Delta n$ in PL imaging measurement via adaptively adjusting the excitation light intensity, even with the impact of lateral carrier.

### 7.2.3 Application to silicon wafers

The proposed adaptive excitation method was then applied to a non-uniform silicon wafer. A rectangular (40 mm×80 mm) $p$-type Cz silicon wafer with resistivity of 1.6 $\Omega\cdot$cm was used. The silicon wafer went through double side phosphorus diffusion resulting in a sheet resistance of 50 $\Omega$/sq. It was then RCA cleaned and double side passivated with silicon nitride using an industrial plasma enhanced chemical vapor deposition system (MAiA, Meyer Burger) [265]. Half of the wafer was then degraded using the same degradation procedure as used for the mini solar cell. A mask was used to achieve a boundary between the degraded and non-degraded regions that is as sharp as possible during the laser

degradation process. A conventional PL image (measured using uniform illumination) of the wafer is shown in Fig. 7.4.
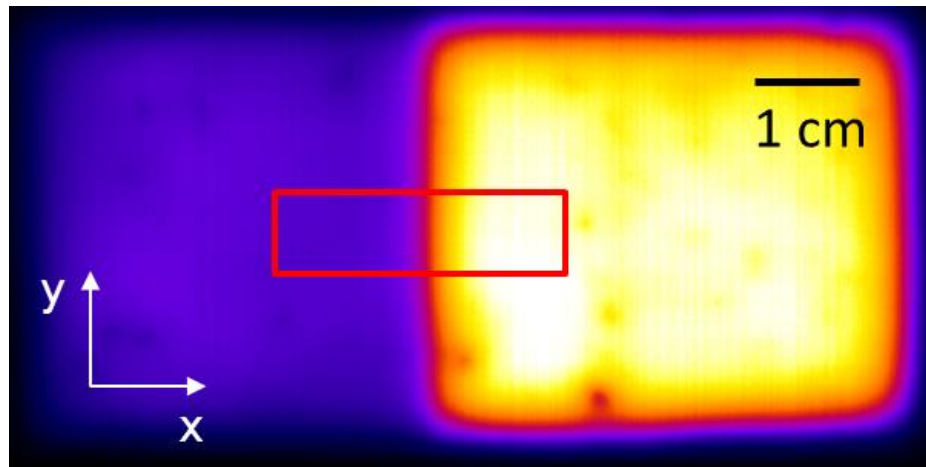


**Fig. 7.4** PL image with spatially uniform excitation intensity of a double side diffused silicon wafer, half of which was degraded by boron-oxygen activation. The area of interest is indicated by the red rectangle.

In this work we focused on the center region of the wafer, marked with a red rectangle (10 mm×20 mm) in Fig. 7.4. The aim is to achieve a uniform PL image within this area. Meanwhile, the two-dimensional problem is simplified to a one dimensional problem by assuming that the sample is uniform in the $y$ direction in this rectangular area. Therefore, the iteration procedure can be simplified to:

$$\Phi_x^i = \Phi_x^{i-1} \frac{\overline{PL_o^{i-1}}}{\overline{PL_x^{i-1}}} \tag{7.3}$$

where $\overline{PL_x^{i-1}}$ is the PL intensity averaged in the $y$ direction at position $x$ within the rectangular area in the $(i-1)^{th}$ iteration. The leftmost position of the rectangular area was chosen as the reference point (position "$o$"). Although only the center area of the sample is focused on, the illumination light is extended to the entire sample to avoid lateral carrier flow from the rectangular area to other regions of the sample.

The results of the non-uniform excitation PL imaging measurements are shown in Fig. 7.5, with four iterations required for convergence. In order to ensure an optimal contrast of each image, different color scales are used in Fig. 7.5. The horizontal profiles of PL counts and normalized light intensity are also presented in the above figure. As can be seen, the PL image of the rectangular area becomes quite uniform at the end of the process. The horizontal PL counts profile is almost flat, with a maximum ±5% relative deviation.
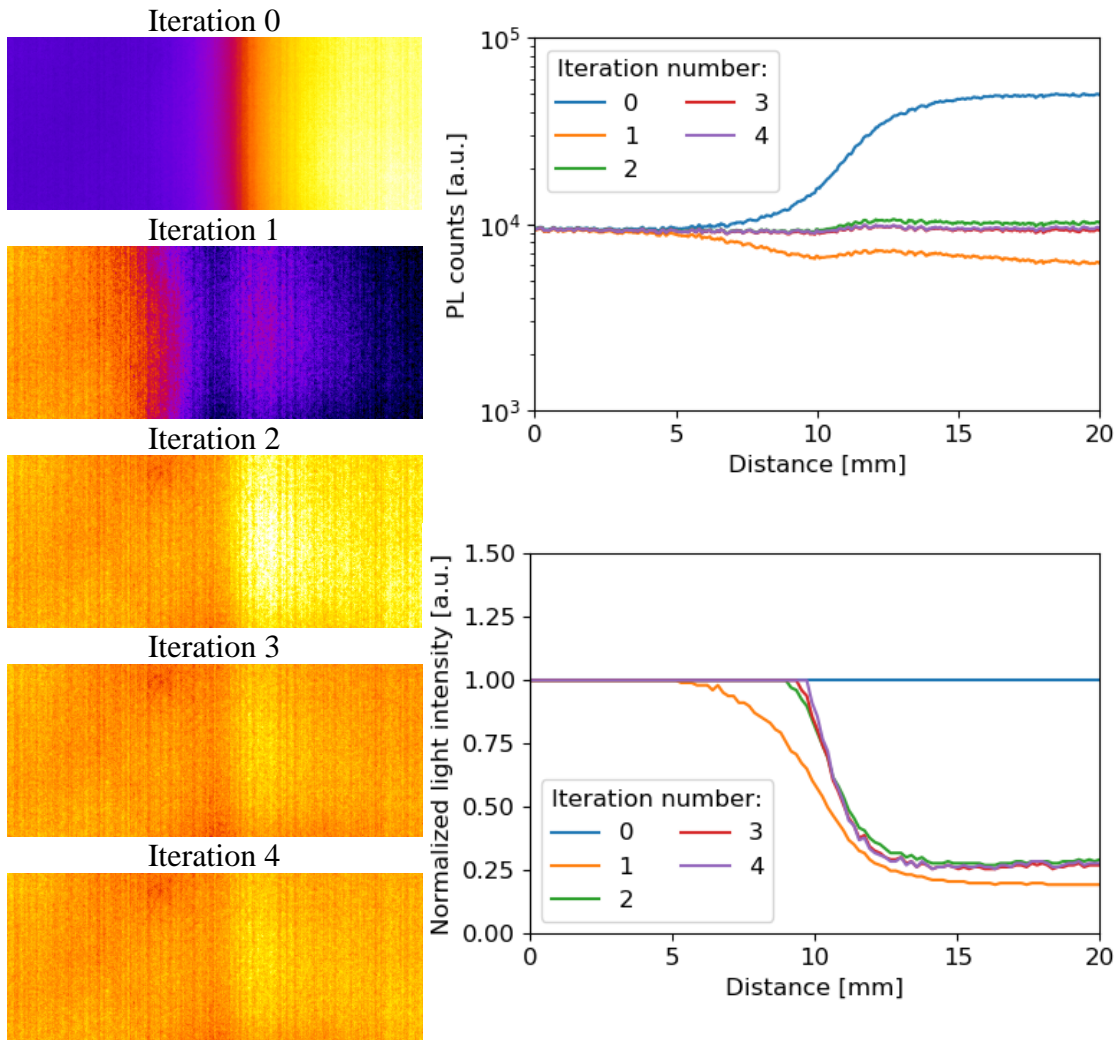
**Fig. 7.5** PL images (left column) and cross sectional profiles (averaged in the *y*-direction across the image) of the PL intensity and of the light intensity (right column) of the region of interest (red rectangle in Fig. 7.4; 20 mm wide) after each iteration step. Distance 0 is defined as the left-most edge of the sample.

The carrier lifetime images obtained from the conventional and proposed new methods are now compared. Under steady state condition, the carrier lifetime $\tau$ can be calculated as the ratio of $\Delta n$ and $G$:

$$\tau = \frac{\Delta n}{G} \qquad (7.4)$$

Under low injection conditions, the PL intensity is proportional to $\Delta n$. In conventional PL imaging, since a uniform light intensity is used ($G$ is uniform across the sample), $\tau$ is thus proportional to the PL intensity. In PL images with uniform $\Delta n$, $\tau$ is proportional to the inverse of $G$, and the latter proportional to the excitation light intensity. The normalized carrier lifetime profiles using the two approaches are presented in Fig. 7.6. The carrier lifetime profile from the conventional approach is extracted from the initial

PL image (Iteration 0), whereas the carrier lifetime profile from adaptive excitation PL imaging is extracted from the inverse of the excitation light intensity in the last iteration. Both profiles are normalized to the leftmost point, as the excitation light intensity there is kept unchanged during the iteration.
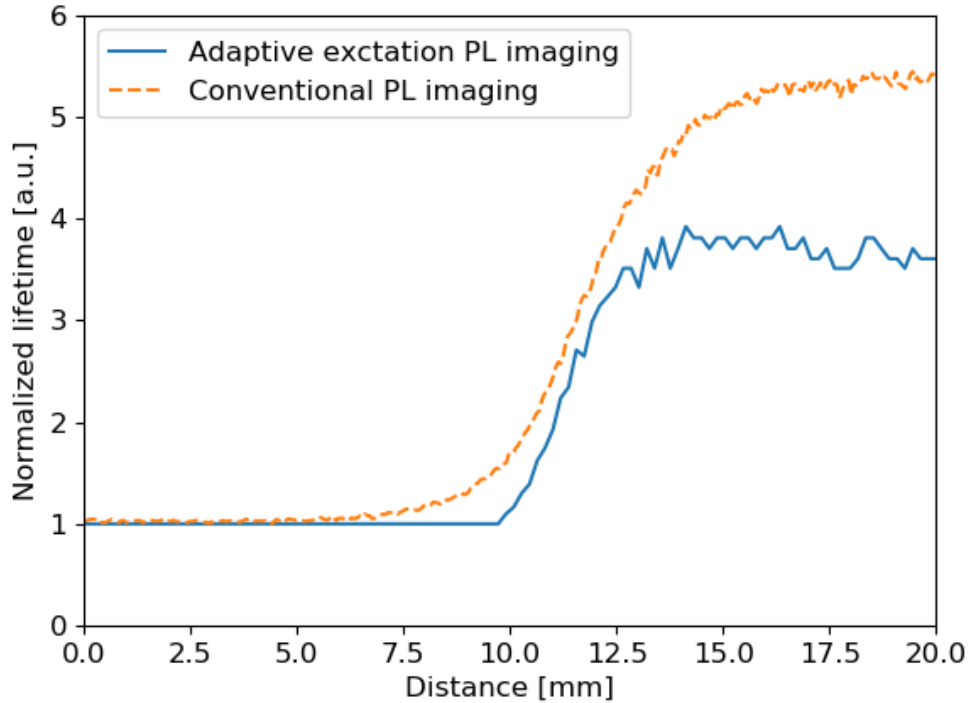


**Fig. 7.6** Horizontal profiles of carrier lifetime obtained from the conventional PL imaging approach (red, dashed line) and from the adaptive excitation PL imaging (black, solid line).

As can be seen, the $\tau$ profile from the PL image with uniform $\Delta n$ shows a sharper transition than the profile obtained from the conventional PL image. This is because in the conventional PL imaging there is a lateral carrier flow from the non-degraded region to the degraded region, which "smears out" the local recombination properties, as an additional term in the denominator of Eq. (7.4) is required to take account for the lateral carrier flow [137].

Note that for the non-degraded region, $\tau$ obtained from the new approach is lower than $\tau$ obtained from the conventional PL image, resulting in lower contrast. This is caused by the injection dependence of carrier lifetime [188]. In the conventional PL image, the injection level in the non-degraded region is more than five times higher than in the degraded region. As our test wafer is impacted by a boron-oxygen defect, a higher carrier lifetime at higher injection levels is expected [79], [105], [266]–[268]. Since in the uniform $\Delta n$ image the non-degraded region was at a lower injection compared to

conventional PL imaging, it is not surprising that a lower $\tau$ is obtained. The new approach of adaptive excitation PL imaging thus provides a unique opportunity to extract spatially resolved carrier lifetime of a sample at the same injection level, which is very beneficial for all quantitative analysis methods that are based on calibrated carrier lifetime images.

### 7.2.4 Limitations of current setup

Although PL images at uniform injection for a non-uniform silicon wafer were achieved in this study using the adaptive excitation method, it should be noted that there are several potential practical limitations that may impact the application of this method to samples with strong spatial non-uniformity, such as mc-Si wafers.

First, the resolution of the resulting carrier lifetime image is limited by the resolution of the LCD panel or the camera (the lower one). In our current setup, the resolution is limited by the LCD panel. One pixel corresponds to a size of $180\times180$ μm$^2$. By using an LCD panel with higher resolution and modifications of the optical path (*i.e.*, reducing the illumination area), the resolution can be increased by a factor of four to five. Such an improved resolution will still be insufficient to fully resolve grain boundaries or dislocations in mc-Si. However, it is not the aim of the adaptive excitation method to fully resolve grain boundaries or dislocations in mc-Si. It should be noted that the carrier smearing effect will still be strongly suppressed in adaptive excitation PL imaging. The result will thus still be much sharper than conventional PL images. For samples with defects that are non-uniformly distributed in a relatively large scale; for example, the striations in *n*-type Cz silicon [269] and the thermally activated defects in FZ silicon investigated in Chapter 5 [22]; the adaptive excitation PL image will be very beneficial to obtain more accurate lifetime images.

Second, the accuracy of the result of adaptive excitation PL images is limited by the sharpness and contrast of the non-uniform excitation. The LCD panel used in this work has a dynamic range of 4000:1 which allows the light intensity to be varied by more than three orders of magnitude. LCD panels with a higher dynamic range ($>10^4$:1) are also available. This allows the implementation of the adaptive excitation method to samples with large lifetime variations. Nevertheless, the contrast ratio of two neighboring pixels is much lower than the nominated dynamic range of the device. If the sharpness of the excitation light image is worse than the sharpness of the non-uniform features of the sample, the resulting PL image will never be perfectly uniform. For example, in our

measurement of the silicon wafer shown in Fig. 7.5, there is still ±5% relative deviation in the final PL image, and this deviation remains as the iteration continues. The reason for this residual PL non-uniformity is currently under investigation. It might be partially due to the insufficient sharpness of the excitation light images.

Third, the achievable light intensity is a challenge for the implementation of adaptive excitation PL imaging. The highest light intensity of our current setup is around 30 mW/cm$^2$, corresponding to roughly one third of one sun equivalent intensity. By using a more powerful light source and adjusting the optics, it should be possible to reach stronger light intensities (above one sun). Since the highest achievable injection level is limited by the regions with the lowest carrier lifetime, PL images at uniform $\Delta n$ for a sample with regions of very low carrier lifetime will require a very strong light intensity. For example, to achieve a uniform $\Delta n$ of $10^{15}$ cm$^{-3}$ image for a wafer with regions of 1 μs requires a local illumination intensity exceeding 4000 mW/cm$^2$ (for a light source with wavelength of 800 nm), equivalent to 40 suns, which is very challenging to realize in practice. A PL image at uniform injection level can still be obtained but at a much lower injection level. However, it should be noted that this limitation is also valid for conventional PL imaging. It is just less apparent in conventional PL imaging as the regions with high carrier lifetime can reach a higher injection level in the measurement. It is also noted that while lifetime measurements at a specific injection level (*e.g.* $\Delta n = 10^{15}$ cm$^{-3}$) are very commonplace in the PV research community, such high injection levels are not representative of either open circuit voltage or let alone maximum power point conditions in a solar cell in most practical cases, and thus the need to be able to achieve such higher injection levels in the adaptive technique discussed in this chapter is thus questionable.

## 7.3 Chapter summary

In this chapter, an LCD based PL imaging setup was built that enables the use of spatial non-uniform excitation. With this setup, the excitation light intensity was adaptively adjusted at each position of the sample to achieve a PL image at uniform excess carrier density. The lateral balance currents between two silicon solar cells with different carrier lifetime are successfully eliminated. Furthermore, a uniform PL image was obtained for a diffused silicon wafer with spatially non-uniform carrier lifetime.

This approach of adaptive excitation PL imaging is inherently free of the impact of lateral carrier flows within the sample, which impede the accurate quantitative analysis

of local recombination in conventional PL images. The new approach provides sharper images compared to conventional PL imaging. Without the impact of the lateral carrier flow, the new approach also leads to more accurate carrier lifetime images as well as other PL imaging based quantitative analysis. Finally, unlike a conventional PL image where the sample operates under uniform generation rate, the sample operates under a spatially uniform injection level in adaptive excitation PL imaging. These features make adaptive excitation PL imaging an ideal quantitative characterization technique for defects with spatially non-uniform distribution in silicon wafers or solar cells.

Currently, the adaptive excitation PL imaging method is at the proof of concept stage. Limitations of our current setup have been discussed. For further implementation of the adaptive excitation PL imaging, we plan to use LCD panels with higher resolution and higher contrast ratio, and light sources with higher light intensity.

# Chapter 8
# Summary and Future Works

The major aim of this thesis is to improve the characterization of the electrical properties of defects in silicon for photovoltaic applications. Chapter 3 presented the development of TIDLS measurement system and the procedures for calibration of the PC and PL in lifetime measurements. In Chapter 4 methods of analyzing IDLS data to extract the parameters of recombination active defects were developed. In Chapter 5, thermally activated defects in FZ silicon were investigated using the system developed in Chapter 3 and the methods developed in Chapter 4, together with other characterization techniques such as DLTS. Although less detrimental to PV device performance, traps in silicon with their unique properties, were also worth an investigation. In Chapter 6, the properties of minority and majority carrier traps were investigated via simulation as well as using the developed system. In Chapter 7, an approach based on PL imaging with non-uniform illumination for an accurate spatially resolved characterization of non-uniformly distributed defects was proposed.

One of the main conclusions from this thesis is that proper assessments of the electrical properties of defects requires significant amount of cautiousness. Many of the established methods that are commonly used for defect parametrization are based on assumptions that are difficult to be validated. One of the main outputs of this thesis is to examine the established methods and to develop alternative or improved ones. For example, in Chapter 4 the assumption of a single-level defect was tested and a new procedure to parameterize two-level defects was suggested. In Chapter 6, alternative methods for trap parameterization were proposed with assumptions that can be easily validated. Apart from examining the assumptions behind the applied methods, the importance of combining different techniques for defect characterization is highlighted in this thesis. A concrete demonstration was provided in Chapter 5, where IDLS and DLTS were combined to improve the reliability of the extracted defect parameters.

The detailed original contributions and future works of this thesis are summarized in the following sections.

## 8.1 Summary of original contributions

### 8.1.1 Theoretical original contributions

1. An alternative method for defect parameterization via IDLS techniques was proposed in this thesis. The conventional DPSS method is based on the fitting of SRH equations. The newly proposed method, on the contrary, uses Newton-Raphson method to solve the inverse problem of SRH equation to extract defects parameters.

2. The impact of two-level defects on IDLS analysis was studied. It has been demonstrated that if a two-level defect is misinterpreted as two single-level defects, the resulted defect parameters can be wrong. Previous IDLS analysis methods are only applicable to single-level defects. In this thesis, the analysis of two-level defects via IDLS was investigated systematically for the first time. A reliable method to visualize the whole solution space of IDLS for two-level defects has been proposed.

3. Previous studies of minority carrier traps in QSSPC measurements assumes that there is no interaction of the trap with the majority carrier band. In practice, this assumption is not easy to verify. In this thesis, a more general analytical equation describing the behavior of minority carrier traps in QSSPC measurement was derived. This equation has a wider validity than the one proposed in previous studies.

4. A method to extract minority carrier trap parameters from transient PC decay measurements was also developed. This method assumes negligible minority carrier recapture by the traps. Compared with the methods proposed by previous studies, the assumption of the newly proposed method can be fulfilled more easily by inducing fast recombination channel into the sample to deplete the minority carriers.

5. A model to explain the phenomenon of negative PC by majority carrier traps was developed. It has been found that the temporary capture of majority carriers by the traps can lead to a transient negative PC if the trap is coexisting with other fast recombination channels. A method to extract parameters of the majority carrier traps from the measured negative PC was also developed.

6. A spatially resolved technique is beneficial for the characterization of non-uniformly distributed defects. Accurate quantitative spatially resolved characterization is usually

impeded by the lateral carrier flow in the sample. A method based on non-uniform illumination PL imaging was developed to counterbalance the lateral carrier flow in the sample. By adaptively adjusting the illumination intensity at each location of the sample, a PL image at uniform excess carrier density can be achieved. The spatially resolved recombination information can then be extracted from the applied non-uniform illumination pattern without the impact of lateral carrier flow.

### 8.1.2 Experimental original contributions

1. A system for measuring temperature and injection dependent lifetime of silicon wafers was developed. The system incorporated a xenon flash, an LED and a diode laser as light sources, and consequently the lifetime of wide injection can be measured. Apart from a PC coil in a conventional lifetime tester, a PL detector is also used. Artifacts due to minority carrier trapping and DRM can be removed by measuring the lifetime with PL. A temperature cryostat is integrated to allow measurements from liquid nitrogen temperature to 400 °C.

2. Thermally activated defects in $n$-type FZ silicon was studied by combining TIDLS and DLTS techniques. The defects are found to reduce the carrier lifetime of FZ silicon by more than two orders of magnitude. The electrical properties of the defects have been extracted with careful analysis. The possibility of two single-level defects and one two-level defects are both considered. Furthermore, it has been demonstrated that the combination of IDLS and DLTS greatly improves the accountability of the extracted defect parameters.

3. Minority carrier traps in $n$-type Cz has been investigated via PC measurements using the newly proposed methods. These traps are found to cause a slow decay of PC with decay time constant of around one minute. Even if the samples are measured in typical QSSPC condition, the decay of PC is actually in a transient condition due to this long decay time constant. It has also been demonstrated that when minority carrier traps exist in the sample, the apparent lifetime of the sample measured in steady state condition is different from the one measured in transient condition. This highlights the importance of analyzing traps according to the actual measurement conditions. The electrical properties of the trap have been extracted from these PC measurements.

4. Majority carrier trap in *n*-type Cz has also been studied via the measured negative PC. Unfortunately, due to the relatively small signal, an accurate determination of the trap parameters has not been made at this stage.

5. An LCD based setup PL imaging with non-uniform illumination was developed to achieve PL imaging at uniform excess carrier concentration. As a proof of concept measurement, the lateral current flow between two parallel connected mini solar cells with different lifetimes has been eliminated. Furthermore, PL images at uniform excess carrier density for a non-uniform silicon wafer have been achieved. Due to the lack of lateral carrier flow, more accurate lifetime imaging can be achieved. Meanwhile, the lifetime image can be extracted at the same injection level across the wafer. Therefore, this approach can be very beneficial for the analyzing of spatially non-uniformly distributed defects.

## 8.2 Future works

In this thesis, a few improvements on IDLS have been made. Nevertheless, one important issue for IDLS has not been fully resolved yet. The capability of resolving multiple defects via IDLS has not been systematically studied. It is easy to determine if the lifetime is dominated by one single-level defect. However, if it is found that there are more than one defect levels impacting the measured lifetime (as in the majority cases), it is not easy to determine whether there are two or more single-level defects, or one two-level defect, or an even more complicated case. It is thus worthwhile to investigate: (a) the fundamental resolution capability of IDLS for the number of defect levels; and (b) the uncertainty of each extracted defect component from the IDLS.

A thorough investigation of the thermally-activated defects in FZ silicon has been made in Chapter 5. However, there remains a few uncertainties around the extracted defect parameters. For a more accurate and decisive determination of the defect parameters, it is worthwhile to use $N_{dop}$-IDLS, and thus the impact from temperature dependent parameters can be removed. It is also important to measure *p*-type FZ wafers for more reliable results from DLTS and MCTS.

The investigation of traps in Chapter 6 focus on the case of single-level traps. The case of two-level traps is also interesting to investigate. A few preliminary results for the investigation of two-level traps can be found in Appendix A. In the future, a more

thorough investigation of the trap behavior of two-level traps in PC measurements should be made.

An LCD-based setup for achieving PL image at uniform excess carrier concentration has been developed and proof of concept measurements with this setup has been presented in Chapter 7. The limitations of the current setup were also outlined. Future works involves the further improvements of the setup by increasing the intensity of illumination light source, and increasing the resolution and contrast ratio of the LCD panel. Meanwhile, application of this setup for spatially resolved IDLS study for defects with non-uniform distribution is also planned.

# Appendix A
# Radial sensitivity of photoconductance coil

As mentioned in Chapter 3, the PC coil used in the developed lifetime measurement system has a circular sensor area with a diameter of 28 mm. The standard WCT-120 lifetime testers from Sinton Instrument have a 40 mm diameter circular sensor area [82]. The PC measured by the coil is a weighted average value over the sensor area. The calibration described in Chapter 3 is for samples larger than the sensor area. In order to measure samples smaller than the sensor area (for example, the Cz wafers of Chapter 6), additional consideration of the radial sensitivity of the coil is required. This consideration is also required for calibrating the PL imaging of non-uniform samples to excess carrier concentration image using the PC-based lifetime measurements [134], [136].

In this Appendix, the method of measuring the radial sensitivity of the PC coil will be explained. Results of the radial sensitivity of the PC coil in the customized lifetime tester of Chapter 3 will also be presented.

## A.1 Radial sensitivity of the coil

The PC coil used in the common lifetime testers is circular. Assuming radial symmetry of the coil and a sensitivity $s_r$ as a function of $r$, the distance to the center of the circular, the measured conductance $S_m$ should be:

$$S_m = \int_0^\infty 2\pi r s_r(r) S(r) \, dr \tag{A.1}$$

where $S(r)$ is the actual conductance of the sample at $r$.

It has been demonstrated by several studies that the radial sensitivity of the PC coil can be approximated by a Gaussian function [135], [136], [159]:

$$s_r(r) = A_r \exp\left(-\left(\frac{r - r_0}{\sigma_s}\right)^2\right) \tag{A.2}$$

where $r_0$ and $\sigma_s$ are parameters related to the coil that defines the shape of the sensitivity function. $A_r$ is a normalization factor which can be calculated by:

$$\int_0^\infty 2\pi r s_r(A_r, r)\, dr = 1 \qquad (A.3)$$

According to Eq. (A.1), for a uniform circular sample with radius $R$ smaller than the radius of the PC coil sensor area, the measured PC $\Delta S_m$ is $\Delta S \int_0^R 2\pi r s_r(r)\, dr$. In order to obtain the correct PC, the coil calibration factors $a$ and $b$ should be divided by $\int_0^R 2\pi r s_r(r)\, dr$.

## A.2 Measurement of the radial sensitivity

The radial sensitivity of the PC coil has been measured by a few previous studies. Kiliani *et al.* [136] used a uniform circular wafer passivated by SiN$_x$. The SiN$_x$ of the wafer was circularly laser ablated and the lifetime of the wafer was measured as a function of the width of the ablation; $s_r$ of the coil can then be fitted. Giesecke *et al.* [135] adopted a different approach. A uniform wafer was used and the wafer was covered with an opaque object with a small pinhole. By measuring the lifetime of the wafer as a function of the position of the pinhole, $s_r$ was calculated. In these two approaches, $s_r$ was obtained from fitting the lifetime data. The main disadvantage of these two approaches is that the results can be impacted by the lateral carrier flow. In the method of Kiliani *et al.* [136], the carrier can flow from the high lifetime region to low lifetime region. In the method of Giesecke *et al.* [135], carrier can flow from the illuminated region to non-illuminated region.

Giesecke later proposed another method [159]. A square wafer was carefully positioned at different locations of the measurement plane and the dark conductance of the sample was measured. Fitting the measured dark conductance as a function of the location of the wafer can be then used to extract $s_r$. As the dark conductance data is fitted, this method is not impacted by the lateral carrier flow. As a square wafer is used, a geometry factor was used by Giesecke to correct the measured data. However, the square wafer could also lead to a distortion of the eddy current created by the coil, which causes a local modification of the coil sensitivity.

In this thesis, a set of circular wafers with the various radius cut from a uniform Cz wafer with resistivity of around 3 Ω·cm is used. These wafers are placed concentric to the

coil sensor area and the net dark voltage ($V_{dark} - V_{air}$) of the coil is measured. The usage of circular wafers can reduce the distortion of the eddy current.

The results of this measurement on the customized lifetime tester developed in Chapter 3 are shown in Fig. A.1. By fitting the measured data using Eq. (A.1), $r_0$ and $\sigma_s$ of the coil sensitivity function can be obtained.
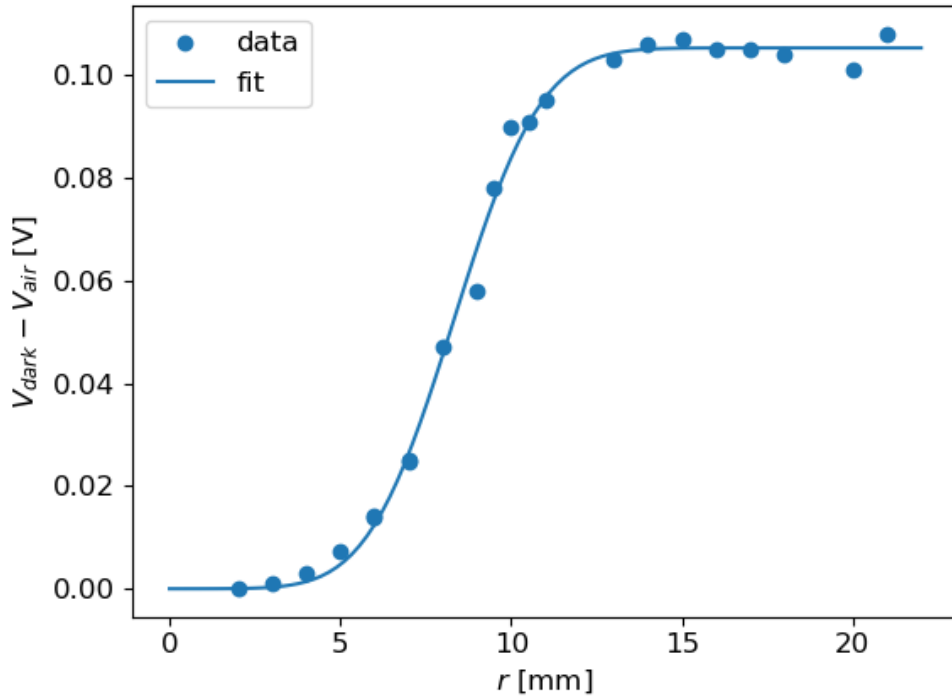


**Fig. A.1** The measured net dark voltage of a set of circular wafers with various radius. The solid line indicates a fit of the measured data.

Using the same method, the radial sensitivity function of a standard WCT-120 lifetime tester from Sinton Instruments is also measured. The extracted $r_0$ and $\sigma_s$ of the sensitivity function are summarized in Table A.1.

**Table A.1** Comparison of $r_0$ and $\sigma_s$ from this study and the literature

|  | $r_0$ | $\sigma_s$ |
|---|---|---|
| Customized system this work | 7.81 | 2.91 |
| WCT-120 this work | 9.01 | 3.51 |
| WCT-120 Kiliani *et al.* [136] | 9.3 | 3.6 |
| WCT-120 Giesecke *et al.* [135] | 8.34 | 5.44 |
| WCT-120 Giesecke [159] | 8.25 | 3.65 |

The sensitivity functions, using the parameters listed in Table A.1, are plotted in Fig. A.2 for comparison. As can be seen, the coil has the highest sensitivity at around its radius (*i.e.* just above the coil). For the customized lifetime tester developed in this thesis, the coil has a radius of around 7 mm, while for the standard WCT-120 lifetime tester, the coil has a radius of around 10 mm. Further away from the radius, the coil sensitivity drops to zero at the center of the coil and at a distance around twice of the coil radius. Therefore, the sensor area of a PC coil has a diameter of twice the coil diameter. The different peak height of the coil sensitivity is due to the difference in the $\sigma_s$ value of the sensitivity function. A smaller $\sigma_s$ value leads to larger $A_r$ according to Eq. (A.3), and is thus a higher peak of the $s_r$ function.
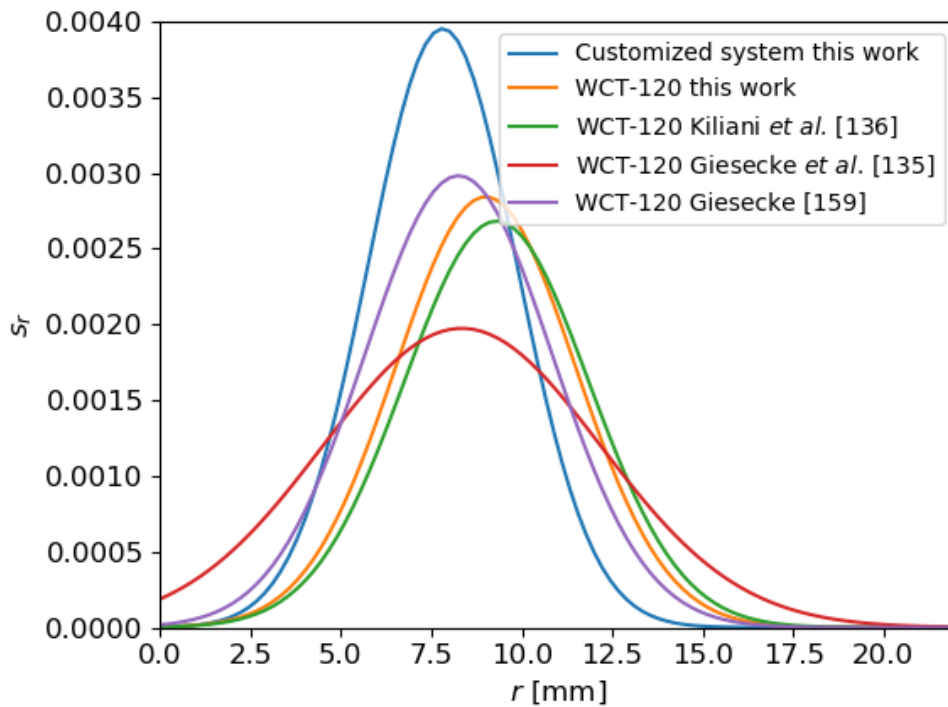


**Fig. A.2** Comparison of the coil sensitivity functions obtained from this work and the literature.

For the standard WCT-120 lifetime testers, the coil sensitivity function obtained in this study is similar to the functions obtained by Kiliani *et al.* [136] and Giesecke [159]. The small deviation might come from the system deviation, measurement uncertainty, or the disadvantages of the methods applied by previous studies.

# Appendix B
# Preliminary results on two-level minority carrier traps

In Chapter 6, the analysis of traps is focused on single-level traps. As mentioned in Chapter 4, defects can have more than one defect level. Therefore, the case of multi-level traps also requires an investigation. In this Appendix, preliminary results regarding two-level minority carrier traps will be presented. More thorough studies are planned in future works.

The investigations here mainly focus on the behavior of two-level traps in transient PC decay measurements. Similar to the approach of Chapter 6, in this section the recapture of minority carrier traps is assumed to be negligible, which can be fulfilled by inducing fast recombination channels into the sample.

## B.1 Simulation for two-level defects

The numerical simulation of two-level defects is similar to the simulation for single-level defects described in Chapter 6 with a modification to the carrier rate equations:

$$\frac{\mathrm{d}n}{\mathrm{d}t} = G + e_{n1} + e_{n2} - c_{n1} - c_{n2} \tag{B.1.1}$$

$$\frac{\mathrm{d}p}{\mathrm{d}t} = G + e_{p1} - c_{p1} + e_{p2} - c_{p2} \tag{B.1.2}$$

$$\frac{\mathrm{d}f_p}{\mathrm{d}t} N_t = c_{p1} - e_{p1} - c_{n1} + e_{n1} \tag{B.1.3}$$

$$\frac{\mathrm{d}f_n}{\mathrm{d}t} N_t = c_{n2} - e_{n2} - c_{p2} + e_{p2} \tag{B.1.4}$$

$$f_p + f_m + f_n = 1 \tag{B.1.5}$$

where the subscript "1" and "2" denote the first level and the second level of the defect. As mentioned in Chapter 4, in this thesis, the 2nd energy level is the transition energy between the most negatively charged state and the middle charge state, whereas the 1st

energy level is the transition energy between the most positively charged state and the middle charge state. $f_p$, $f_m$, and $f_n$ are, respectively, the fraction of the defect in the most positively charged, the middle, and the most negatively charged state. The capture and emission rates for electron and holes can be calculated as:

$$e_{n1} = N_t f_m \sigma_{n1} v_n n_1, \qquad e_{n2} = N_t f_n \sigma_{n2} v_n n_2 \qquad\qquad (B.2.1)$$

$$c_{n1} = N_t f_p \sigma_{n1} v_n n, \qquad c_{n2} = N_t f_m \sigma_{n2} v_n n \qquad\qquad (B.2.2)$$

$$e_{p1} = N_t f_p \sigma_{p1} v_p p_1, \qquad e_{p2} = N_t f_m \sigma_{p2} v_p p_2 \qquad\qquad (B.2.3)$$

$$c_{p1} = N_t f_m \sigma_{p1} v_p p, \qquad c_{p2} = N_t f_n \sigma_{p2} v_p p \qquad\qquad (B.2.4)$$

Using the equations above, the carrier concentration and the charge state distribution of the two-level defects can be numerically solved using similar approach described in Chapter 6.

## B.2 Decay behavior of two-level trap

The PC decay of a two-level trap is firstly compared to the decay of single level traps by the numerical simulation. The transient PC decay of an *n*-type silicon wafer with $N_{dop}$ of $10^{14}$ cm$^{-3}$ at 300 K is numerically simulated with four different cases: (a) a sample contains a two-level defect ($E_{t1} - E_i$ of 0.4 eV, $E_{t2} - E_i$ of −0.1 eV, $\sigma_{n1}$, $\sigma_{p1}$, $\sigma_{n2}$, $\sigma_{p2}$ of $10^{-18}$ cm$^2$) with $N_t$ of $10^{12}$ cm$^{-3}$; (b) a sample contains a single-level defect with the same parameters as the 1st level of the two-level defect; (c) a sample contains a single-level defect with the same parameters as the 2nd of the two-level defect; and (d) a sample contains the two single-level defects [of (b) and (c)]. In all simulations, $\tau_r$ of the sample is set to be around $10^{-6}$ s. It has been confirmed that this $\tau_r$ is low enough that the recapture of minority carrier by the traps is negligible, *i.e.*, the assumption used for the analytical equation of the PC decay time constant [Eq. (6.25)] in Chapter 6 is valid.

Instead of presenting the simulated PC decays as a function of time, the apparent lifetime curves calculated from the PC decays are presented in Fig. B.1 for a better comparison of different cases. As can be seen, the single-level defect with the same parameters as the first level (green line) of the two-level defect does not cause artificially high $\tau_{app}$, indicating that this defect level is not an effective minority carrier trap. On the contrary, the second single-level defect (orange line) leads to artificially high $\tau_{app}$, and thus is an effective minority carrier trap. The PC decay time constant calculated using Eq.

(6.25) of Chapter 6 for the second single-level defect is also plotted. As can be seen, it agrees with the plateau of the simulated $\tau_{app}$. This confirms again that the assumption for the derivation of Eq. (6.25) is valid. In the case of the coexistence of the first single-level defect and the second single-level defect in the sample, the $\tau_{app}$ is identical to the case of only the second single-level defect in the sample. This is not surprising as the overall PC decay is dominated by the second defect. The 1st defect is neither an effective minority carrier trap nor a recombination active defect in this case, and thus has a negligible impact on the PC decay and $\tau_{app}$.
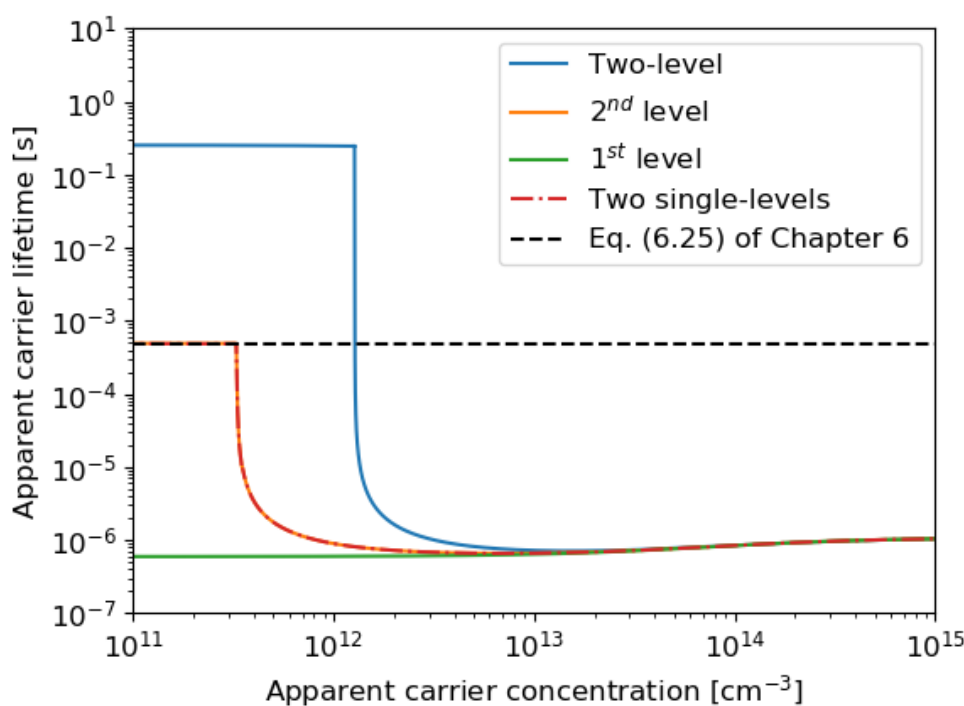


**Fig. B.1** Simulated transient apparent lifetime curves of an *n*-type silicon contains a two-level defect (blue solid line), the first level of the two-level defect (green solid line), the second level of the two-level defect (orange line), and both levels as two single-level defects (red dash-dotted line). The simulation parameters can be found in the text.

In the case of the two-level defect, $\tau_{app}$ also shows artificially high value and plateaus at a value even higher than the case of two single-level defects. This result has two implications: (1) a single exponential decay of the PC (equivalent to the plateau of the $\tau_{app}$ curve) is not sufficient to support the assumption of single-level trap. The PC decay of a sample with two-level decay can also be fitted with a single exponential. (2) the correlation between the PC decay constant and the defect parameters for two-level traps is different from the one for single-level traps. Therefore, Eq. (6.25) cannot be applied to

two-level traps. The cause of this deviation is the interaction between the two energy levels. For the two-level defect simulated above, the second level is empty of minority carriers (holes) at the initial of the decay while the first level is full with holes. Before a hole can be depopulated via the second level, the first level needs to depopulate a hole. In this case, the depopulation rate of holes from the second level is much faster than the depopulation rate of holes from the first level. Therefore, the overall hole depopulation rate, as well as the PC decay rate, is dominated by the 1st level. This is quite different from the case of two independent defect levels, where the 1st level has a negligible impact on the PC decay.



(a)                                                    (b)
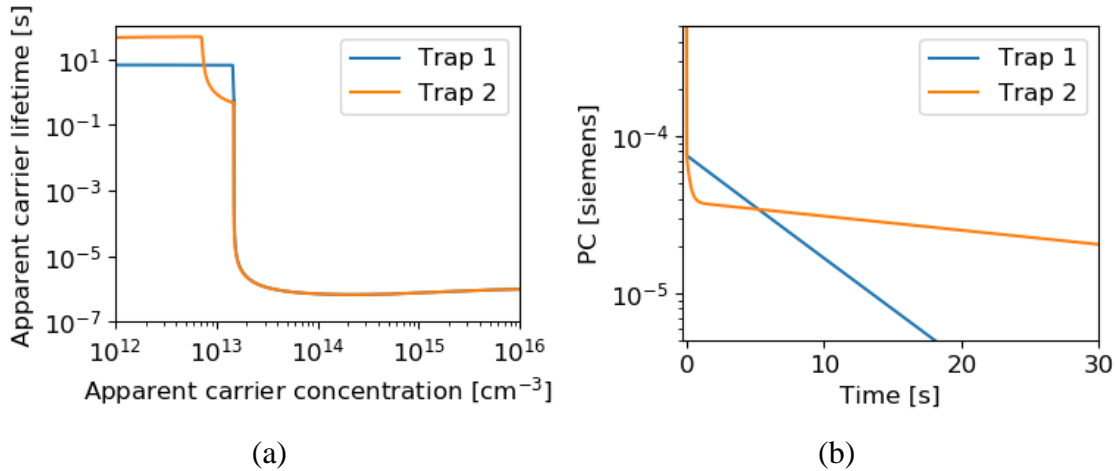
**Fig. B.2** Comparison of the simulated (a) transient apparent lifetime, (b) PC decay of two different two-level traps in an *n*-type silicon wafer. The simulation parameter can be found in the text.

In the simulation above, the depopulation of minority carriers is dominated by one level of the two-level defect. Therefore, the PC shows a single exponential decay. However, it is possible that both levels of a two-level defect impact the decay. To demonstrate this, the PC decay of an *n*-type silicon wafer with $N_{dop}$ of $10^{14}$ cm$^{-3}$ at 300 K is numerically simulated with two cases: (1) a sample contains a different two-level defect ($E_{t1} - E_i$ of 0.4 eV, $E_{t2} - E_i$ of −0.1 eV, $\sigma_{n1}$ of $10^{-22}$ cm$^2$, $\sigma_{p1}$ of $10^{-22}$ cm$^2$, $\sigma_{n2}$ of $10^{-18}$ cm$^2$, $\sigma_{p2}$ of $10^{-18}$ cm$^2$) with $N_t$ of $10^{13}$ cm$^{-3}$; and (2) a sample contains a two-level defect ($E_{t1} - E_i$ of 0 eV, $E_{t2} - E_i$ of 0.2 eV, $\sigma_{n1}$ of $10^{-22}$ cm$^2$, $\sigma_{p1}$ of $10^{-18}$ cm$^2$, $\sigma_{n2}$ of $10^{-25}$ cm$^2$, $\sigma_{p2}$ of $10^{-19}$ cm$^2$) with $N_t$ of $10^{13}$ cm$^{-3}$. Similar to previous simulations, $\tau_r$ of the sample is set to be around $10^{-6}$ s so that the recapture of minority carrier by the traps is negligible.

In Fig. B.2 the simulated transient apparent lifetime curve and PC decay of these two cases are plotted. The first trap is similar to the two-level trap in the previous simulation.

The overall minority carrier depopulation is dominated by the first level and the PC shows one single exponential decay (the initial fast decay due to recombination is not considered). However, for the case of the second trap, two distinct exponential decays can be observed. The slower decay is reflected as the plateau of the apparent lifetime curve, while the faster decay is reflected as a concave transitional curve to the plateau. For the second two-level trap, the depopulation rate of minority carriers from the second level is slower than the depopulation rate of the first level. Therefore, the final PC decay (the slower exponential decay) is dominated by the second level. The faster exponential decay is impacted by the depopulation of both levels.

Due to the interaction between the two levels, the derivation of an analytical equation describing the PC decay related to a two-level trap is challenging. It is obvious that the final PC decay time constants of the two two-level traps simulated above will have different forms, as they are impacted by different levels. A more thorough study of the PC decay time constant for two-level traps is planned as a future work.

## B.3 Doping dependency of the transient decay

From previous simulations, a single exponential PC decay can be resulted from a single-level trap or a two-level trap. The correlation between the decay constant and trap parameters for these two cases are different. Therefore, it is beneficial to be able to differentiate two-level traps and single-level traps. A potential approach is to measure samples with the same type of traps but with various doping concentrations. This will be demonstrated via numerical simulations.

In the following simulation, the two-level defect ($E_{t1} - E_i$ of 0.4 eV, $E_{t2} - E_i$ of $-0.1$ eV, $\sigma_{n1}$ of $10^{-22}$ cm$^2$, $\sigma_{p1}$ of $10^{-22}$ cm$^2$, $\sigma_{n2}$ of $10^{-18}$ cm$^2$, $\sigma_{p2}$ of $10^{-18}$ cm$^2$) and the second single-level defect ($E_t - E_i$ of $-0.1$ eV, $\sigma_n$ of $10^{-18}$ cm$^2$, $\sigma_p$ of $10^{-18}$ cm$^2$) in Fig. B.1 are simulated separately in a set of $n$-type samples with various doping concentrations. The inverse of the PC decay time constant is plotted against the doping of the sample in Fig. B.3. As can be seen, for the single-level trap, $1/\tau_{decay}$ follows a linear relationship with the sample doping concentration. This agrees with the analytical equation of $\tau_{decay}$ [Eq. (6.25)] in Chapter 6. However, for the two-level defect, the relationship between $1/\tau_{decay}$ and doping concentration seems to be quadratic instead of linear. Although an analytical correction of $\tau_{decay}$ and doping concentration for two-level traps is not yet

available, this non-linear dependence could be used as a good indication of two-level traps.
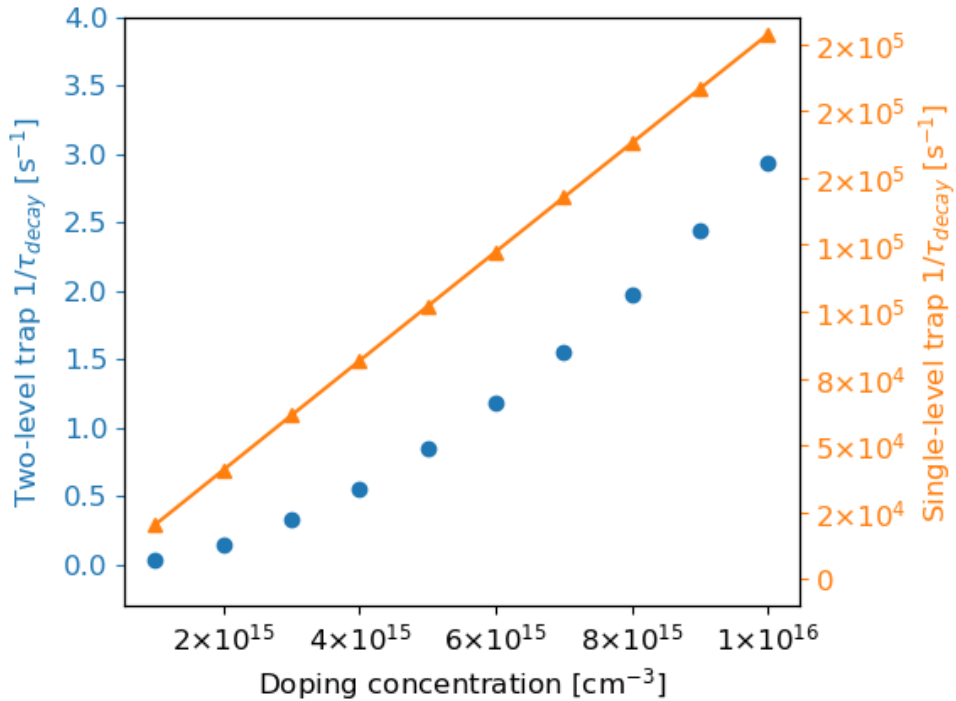


**Fig. B.3** The inverse of PC decay time constant as a function of doping concentration simulated for a *n*-type silicon wafer contains a two-level trap or a single-level trap. The parameters of simulation can be found in text.

In Chapter 6, minority carrier trap in *n*-type Cz silicon was investigated. Similarly, the PC decay of several *p*-type Cz silicon wafers were also measured. These wafers were cut from the same ingot and their doping concentrations varies from $1.11 \times 10^{16}$ cm$^{-3}$ to $1.22 \times 10^{16}$ cm$^{-3}$. Similar to the investigation of the *n*-type Cz wafers, the PC decay of these *p*-type wafers were measured with and without SiN$_x$ surface passivation. While the effective lifetime changes by one order of magnitude, the PC decay time constant barely changed. This verifies the assumption of negligible minority carrier recapture in the traps.

The $1/\tau_{decay}$ as a function of $v_p p_0$ measured for these *p*-type Cz samples are plotted in Fig. B.4. As can be seen, the measured data seem to follow a linear relationship. However, the intercept of the fitted straight line has a negative intercept, which violates the analytical equation derived in Chapter 6. Therefore, the decay behavior of the minority carrier traps in these *p*-type wafers cannot be described by that analytical equation. Furthermore, two data points from Hornbeck and Haynes [73], for minority carrier traps in *p*-type silicon are included in the figure. As can be seen, it seems these two data

together with the data measured in this study, follows a quadratic law. If the minority carrier traps in the samples measured in this study are assumed to be the same traps as in Hornbeck and Haynes [73], it is possible to explain this quadratic law dependency by the existence of two-level traps. However, the nature and parameterization of these traps in *p*-type Cz silicon requires further investigation.
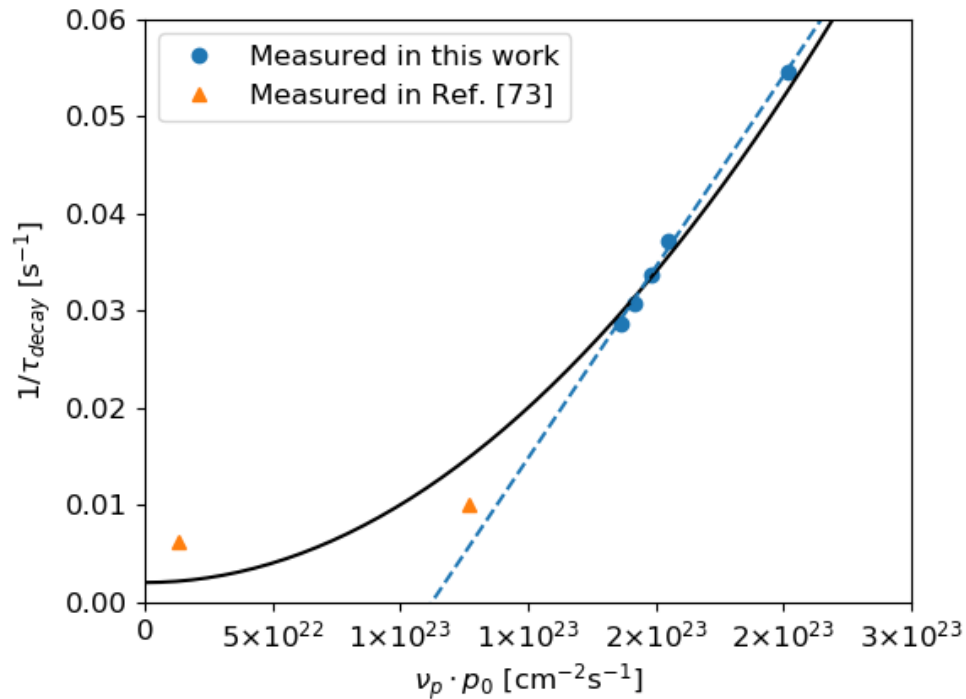


**Fig. B.4** Plot of the inverse PC decay time constant as a function of the product of thermal velocity and equilibrium hole concentration for the three *p*-type wafers of this study. Two data points from Hornbeck and Haynes [73] are also plotted. The black solid line is a quadratic function and serves as a guidance to the eye.

## B.4 Summary

The behaviors of minority carrier traps with two energy levels have been investigated mainly via numerical simulations. From the simulation results, it can be seen that:

1. A single exponential decay of PC is not sufficient to support the assumption of single-level trap, as two-level traps can be also fitted with a single exponential decay.

2. The decay time constant for two-level traps is different from the one of single-level traps; therefore, the method in Chapter 6 for trap parameterization is not applicable for two-level traps.

3. The transient PC decay with a two-level trap is impacted by the interaction of the two energy levels. The overall decay can be impacted or dominated by different processes depending on the parameters of the trap; therefore, development of a general analytical equation to describe the decay time constant can be challenging.

4. A possible method to differentiate a two-level trap from a single-level trap is to measure the PC decay time constant of samples with a wide range of doping concentration. A non-linear relationship between the inverse of the decay time constant and doping concentration is expected for two-level traps.

5. Initial measurement results of minority carrier traps in $p$-type Cz silicon indicate that the traps are likely to be two-level instead of a single-level.

In the future plan, a more systematic analysis of the transient PC decay time constant of two-level traps will be done. Moreover, the properties of the minority carrier traps in $p$-type Cz silicon, which are possible to be two-level traps, will be investigated more thoroughly.

# Appendix C
# Other applications PL imaging with non-uniform illumination[1]

In Chapter 7, an approach of using non-uniform illumination to eliminate lateral carrier flow in PL imaging was presented. The lateral carrier flow in convention PL imaging smears out the resulted images and impede an accurate determination of spatially resolved carrier lifetime images. Nevertheless, the lateral carrier flow can also be useful for certain applications. For example, lateral carrier flow can be used to obtain resistance information from luminescence imaging-based techniques. Conventionally, this is commonly done via current injection in EL [270]–[272] or via PL with current extraction (PLCE) [249], [273], [274].

Non-uniform illumination provides an alternative means for stimulating lateral carrier flow within a wafer or solar cell, without the need for electrical contacts. In this appendix, a DMD-based non-uniform illumination PL imaging technique will be presented and applied to: contactless series resistance ($R_s$) imaging of solar cells; contactless emitter sheet resistance ($\rho_{she}$) measurement of diffused wafers; and diffusion length measurement for non-diffused silicon wafers.

## C.1 Introduction

If non-uniform illumination is used, the carriers generated in areas of higher illumination flow *via* a combination of drift and diffusion to areas of lower intensity due to gradients in the quasi Fermi energy levels. For a diffused wafer or a solar cell, this lateral carrier current is impacted by a combination of the various resistances within the sample,

---

[1] This Appendix is based on:

whereas for a silicon wafer without a junction, this lateral current is impacted by the diffusion length.

Previously, by applying non-uniform illumination, Kasemann *et al.* [275] proposed a contactless technique to extract the qualitative $R_s$ image. The non-uniform illumination was realized by using a conventional uniform illumination source combined with partial shading of the solar cell using opaque baffles. Although only a qualitative $R_s$ image was obtained, the result showed good agreement with the result obtained from a contact-based quantitative $R_s$ imaging method [273]. The idea of PL imaging with non-uniform illumination was also applied by Juhl *et al.* [276] to extract the emitter $\rho_{she}$ of diffused silicon wafers. In Ref. [276], a conventional uniform illumination source was used and a circular long pass filter is placed on top of the wafer to create a local region with close to zero generation rate, while still enabling luminescence from the non-illuminated region underneath the filter to be detected. By numerical simulation as well as experimental verification, a correlation between the maximum to minimum PL counts ratio and the emitter $\rho_{she}$ was established. The $\rho_{she}$ determined by this technique showed good agreement with results obtained by other measurement techniques.

In the two methods mentioned above, non-uniform illumination was achieved by physically placing a mask or optical filter on top of the sample. In the specific case of the $R_s$ imaging method by Kasemann *et al.* [275], the mechanical baffles need to be custom designed to match the layout of the front grid, whereas the method by Juhl *et al.* [276] is limited by the size of available filters. This disadvantage can be solved by using a DMD [277] to achieve the non-uniform illumination. A DMD consists of a rectangular array of micrometer sized mirrors which can be controlled individually and at high frequency to switch between on and off states. Each micromirror is imaged onto a different location in the sample plane. When in the ON state, a single mirror reflects light onto the sample, and when in the OFF state the light is directed away from the sample. Compared with the LCD technique used in Chapter 7, DMD can generally achieve a higher contrast ratio and higher light intensity [277]. Meanwhile, in this Appendix, the micromirrors are either in fully ON state or fully OFF state, and thus the problem of non-steady state illumination of DMD does not impact this study.

The DMD technology has previously been used for the characterization of solar cells. Using two different approaches, Halls *et al.* [278] and Gupta *et al.* [279] applied a DMD

for laser beam induced current measurements in order to reduce the measurement time, while Dennis *et al.* [280] designed a new solar simulator with a DMD and a supercontinuum laser.

## C.2 DMD-based PL imaging setup

The DMD-based PL imaging setup used in this appendix is very similar to the LCD-based PL imaging setup described in Chapter 7, except that the LCD panel is changed with a DMD chip. An ultra-high-performance (UHP) lamp is used as the light source and the light is firstly guided to a DMD chip with a resolution of 1920×1200 and a contrast ratio of 20000:1. The light is then either reflected into a light sink or projected on to the sample, depending on the state of each micromirror. A short pass filter is mounted in front of the projection lens to filter out light with wavelength above 950 nm. The highest light intensity in this preliminary set-up is measured to be between 0.15 to 0.4 suns equivalent, for illuminated areas corresponding to 6 inch- and 4 inch-cells, respectively. The emitted PL is captured by a silicon charge-coupled device (CCD) camera with a 950 nm long pass filter in the front of the lens to block the excitation light.

## C.3 Contactless series resistance imaging

The DMD-based PL imaging setup is first applied to obtain the contactless $R_s$ image. The method of Kasemann *et al.* [275] was applied to a mono-crystalline aluminum back-surface-field solar cell with three busbars. Compared to physically shading the sample, using the DMD to create a non-uniform illumination is advantageous since there is no need to fabricate physical baffles with cell specific dimensions or to mechanically move the baffles above the cell. The measurement results by the DMD-based method are presented in Fig. C.1 (only half of the cell is presented in the figure). Fig. C.1(a) presents the PL image of the sample (measured with full area homogeneous illumination). A region with a lower lifetime is seen at the bottom of the image (marked by a red circle). The two partially illuminated PL images are acquired by projecting white and black illumination patterns, respectively, onto adjacent cell sections separated by the busbars, as shown in Fig. C.1(b) and Fig. C.1(c). In Fig. C.1(b), only the top part of the cell is illuminated and carriers generated in this part flow to the bottom non-illuminated region. The inverse scenario is shown in Fig. C.1(c). If a solar cell is under two different operation conditions, the difference of local voltage drop due to series resistance $\Delta V_S(x, y)$ can be related to the ratio of the PL fluxes $\Phi_{PL}$, according to [275]:

$$\Delta V_{term} + \Delta V_S(x, y) = k_b T \ln \left[ \frac{\Phi_{PL,1}(x, y)}{\Phi_{PL,2}(x, y)} \right] \tag{C.1}$$

where $\Delta V_{term}$ is the difference in the terminal voltages of the two operating points, which is independent of the position $(x, y)$.
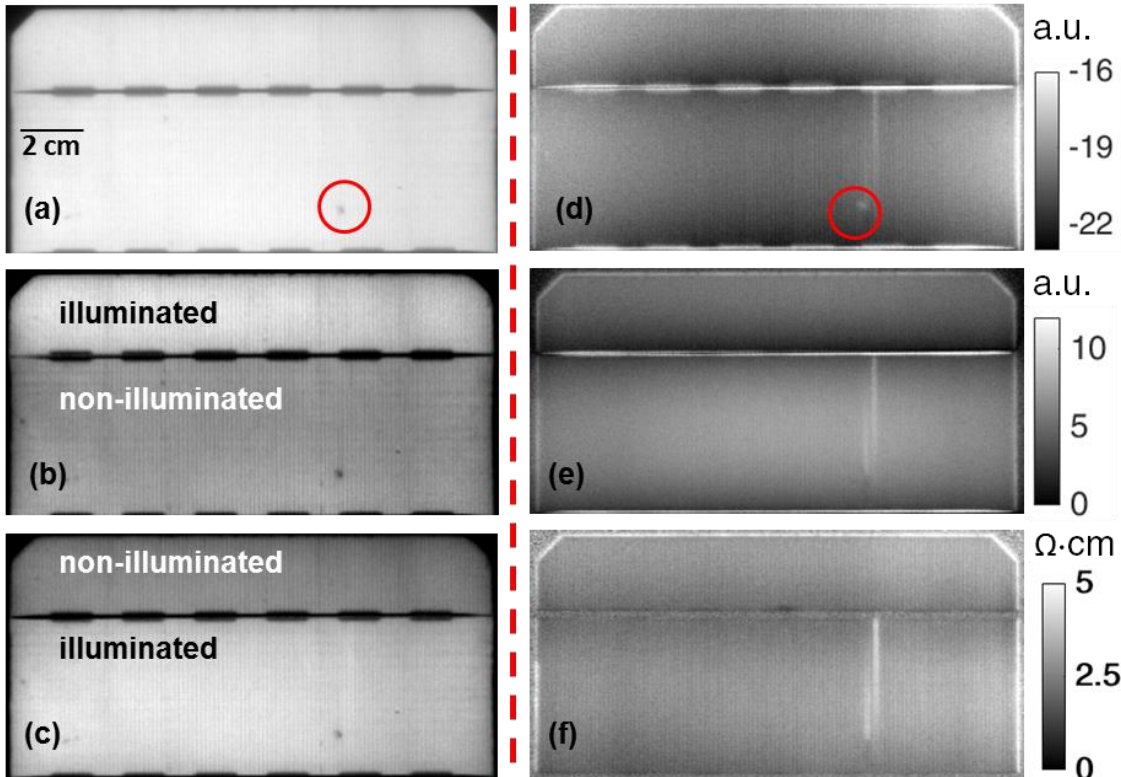


**Fig. C.1** (a) Open circuit PL image of a monocrystalline screen printed solar cell; (b) non-uniformly illuminated PL image, where only the top part of the cell is illuminated; (c) non-uniform illumination PL image where only the bottom part of the cell is illuminated; (d) the resulting qualitative contactless $R_s$ image according to the method of Kasemann *et al.* [275]; (e) the contactless $R_s$ image by the modified method (see text for details); and (f) $R_s$ image obtained by a commercial PL imaging system (LIS-R1 of BT imaging) using the method of Kampwerth *et al.* [274].

In the method of Kasemann *et al.* [275], the illuminated areas of the two partially illuminated PL images [top part of Fig. C.1(b) and bottom part of Fig. C.1(c)] are combined into one image and then divided by the full area illuminated image. The result of this procedure is shown in Fig. C.1(d). According to Eq. (C.1), this ratio image is proportional to the voltage difference of the two operating points, which is correlated to the local series resistance. However, since the illumination intensity used is relatively low, carriers can flow across the cell *via* the emitter. Therefore, a reduction of the contrast of the $R_s$ image is expected and the low lifetime region is still visible in Fig. C.1(d). This issue can be addressed by exploiting an additional advantage of using DMD-based

illumination: the PL from non-illuminated areas is captured by the camera while it is completely blocked if an opaque shading mask is used. For the illuminated area, the captured image represents a PL image with simultaneous current extraction, in which high $R_s$ regions appear relatively brighter. For the non-illuminated area, the image closely resembles an EL image, and high $R_s$ regions appear relatively darker. The two partially illuminated images can be used to create two new images, in which the illuminated and non-illuminated sections of the two partially illuminated images are combined respectively. These two images are then divided to achieve a higher contrast of the $R_s$ image, as shown in Fig. C.1(e), where the top part is from the division of Fig. C.1(c) by Fig. C.1(b), while the bottom part is the reverse. This modified method further improves the quality of the resulting $R_s$ image. For comparison, the $R_s$ image measured by the method of Kampwerth *et al.* [274] is presented in Fig. C.1(f). As can be seen, the $R_s$ image obtained by the DMD-based method clearly shows the high $R_s$ regions caused by broken fingers. Meanwhile, the lifetime artefact is almost completely suppressed in Fig. C.1(e), while it is clearly visible in the data analyzed according to the original method from Kasemann *et al*. [275]. The bright busbar in Fig. C.1(e) is a measurement artefact that is a result of spurious luminescence.

## C.4 Contactless emitter sheet resistance measurement

The DMD-based PL imaging setup is then used to determine the $\rho_{she}$ of a diffused layer as proposed by Juhl *et al.* [276]. The set of samples used in this section have gone through a similar process as described in Ref. [276]. The wafers were phosphorous diffused using various conditions to create various $\rho_{she}$. After removal of the phosphor-silicate glass, the front surface was passivated by $SiN_x$ followed by full area rear aluminum metallization using screen printing and firing at 850 °C. As proposed by Juhl *et al.* [276], PL images are measured with uniform illumination across the sample, except for a circular non-illuminated region. In contrast to the earlier work, where the non-illuminated part was created by mechanically placing a long pass filter onto the sample, the capabilities of the DMD-based illumination is used here. The resulting PL image of a representative sample is shown in Fig. C.2. In this first proof of concept study, the diameter of the circular non-illuminated region is chosen to be 25.4 mm, *i.e.* the same as the diameter of the circular long pass filter used by Juhl *et al.* [276].

The method by Juhl *et al* [276] analyses the ratio of the PL intensities in the illuminated and non-illuminated regions, respectively, which is affected by the emitter sheet

resistance and by the illumination intensity. A theoretical relationship for the ratio between the maximum and minimum PL counts (MMPL) as a function of the product of the photo-generation current density ($J_L$) and $\rho_{she}$ is derived [276]. Results from the DMD-based measurement system for a range of samples with different emitter sheet resistance and illumination intensities are shown in Fig. C.2. The emitter sheet resistance of each sample was measured by 4PP and the photo-generation current density is calculated by the integration of the sample's absorptance and the spectrum of the illumination. The theoretically predicted relationship between MMPL and the $\rho_{she} \cdot J_L$ product, developed by Juhl *et al.* [276] from simulations of this particular geometry, is shown in Fig. C.2 as a solid black line. As can be seen in Fig. C.2, the results obtained by the DMD-based method agree well (within 12% for most of the points) with the predicted results. The large deviation of 26% for the sample with the highest sheet resistance is due to the sample having a non-uniform carrier lifetime. This results in lateral currents flowing in directions other than that assumed by the model of Juhl *et.al.* [276].
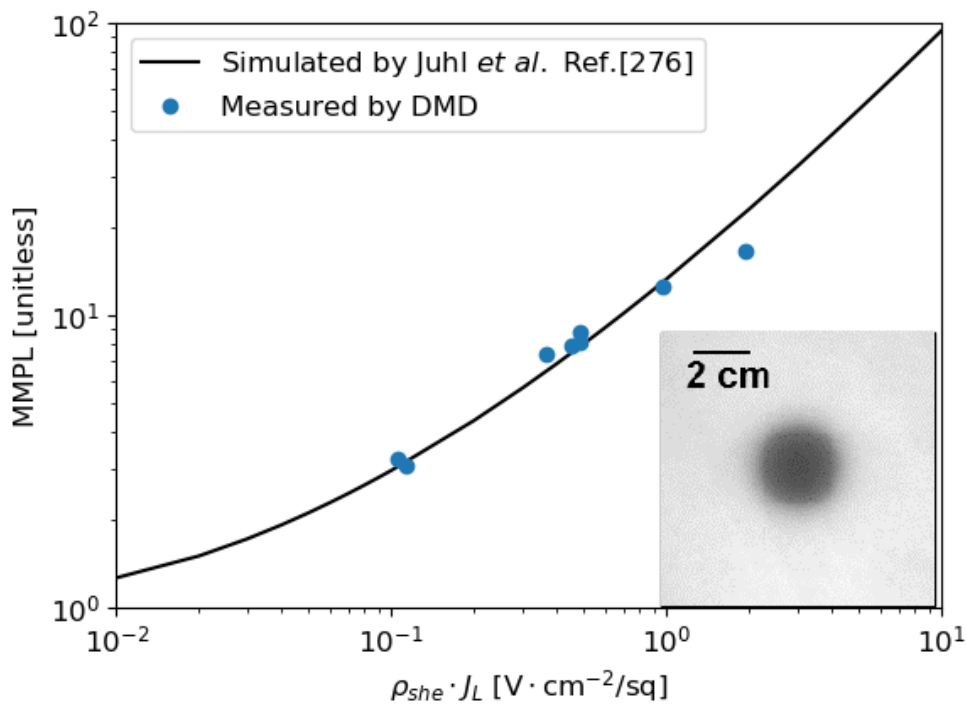


**Fig. C.2** PL intensity ratio between illuminated and non-illuminated regions (MMPL) obtained by the DMD-based method as a function of the product of $\rho_{she}$ and $J_L$, compared to the theoretical relationship from Juhl *et al.* [276]. The inset shows the non-uniformly illuminated PL image of one sample.

By using the DMD-based method, the non-uniform illumination is no longer limited by the physical dimension or shape of specific filters. A much smaller diameter can be

used and a scanning of emitter sheet resistance or even simultaneous measurement of multiple spots across a wafer can easily be implemented. The aforementioned problem of the large deviation of the last point can also be mitigated by using an illumination pattern with a smaller diameter.

## C.5 Diffusion length measurement

In the previous section, carrier drift through the emitter was the main mechanism for lateral current flows. In samples without emitter, the lateral carrier diffusion induced by non-uniform illumination can be used for the determination of the diffusion length. For silicon wafers with lifetimes in the order of milliseconds, the corresponding diffusion length is in the order of millimeters. This is long enough to be observed in PL images, such as the ones used here, with a pixel resolution of 160 μm. For shorter diffusion lengths higher spatial resolution would be required. For a silicon wafer with length and width much larger than its thickness, the impact of the edges can be ignored. For the specific case of a uniform wafer that is illuminated along one line, the decay of carriers from the illuminated area to the non-illuminated area reduces to a two dimensional problem and is then given by [281]:

$$\Delta n(x,y) = A_d e^{\frac{-x}{L_{eff}}} \left[ \frac{SRV}{D\beta} \sin(\beta y) + \cos(\beta y) \right] \tag{C.2}$$

where $x$ is the direction vertical to the edge of illumination in the surface, $y$ is the direction perpendicular to the surface, $A_d$ and $\beta$ are two constants, $L_{eff}$ is the effective diffusion length, and $D$ is the diffusivity. Under low injection, the PL intensity is given by [47]:

$$PL = C\Delta n N_{dop} \tag{C.3}$$

where $C$ is a constant. By combining Eq. (C.2) and Eq. (C.3), the correlation between the PL intensity and the effective diffusion length can be obtained:

$$\left| \frac{\partial}{\partial x} \ln PL \right| = \left| \frac{\partial}{\partial x} \ln \Delta n \right| = \frac{1}{L_{eff}} \tag{C.4}$$

To demonstrate this, a 0.6 cm wide white strip with constant intensity is projected on the wafer (the illumination intensity outside the strip being zero) and the PL decay perpendicular to the strip investigated. In this experiment, an *n*-type FZ wafer with high quality a-Si surface passivation is used. Its effective lifetime at $\Delta n$ of $1 \times 10^{15}$ cm$^3$ is

measured to be 2.81 ms using QSSPC measurements [83], indicating a diffusion length of 0.18 cm. This wafer is used as it has a weak injection dependence on the effective lifetime below 0.4 suns.

The PL image is deconvolved [282] and flat-field corrected. Fig. C.3 presents the resulting PL image and a line scan of the PL counts. The red doted box indicates the selected region used for the line scan. The black dashed lines in the graph indicate the width of the illumination strip. The two red solid lines represent the fitted data according to Eq. (C.4) of the cross section of the PL counts just outside the illuminated region. The fitting results are also presented in the figure. The orange line plotted in the right vertical axis indicates the line scan of the illumination light intensity.
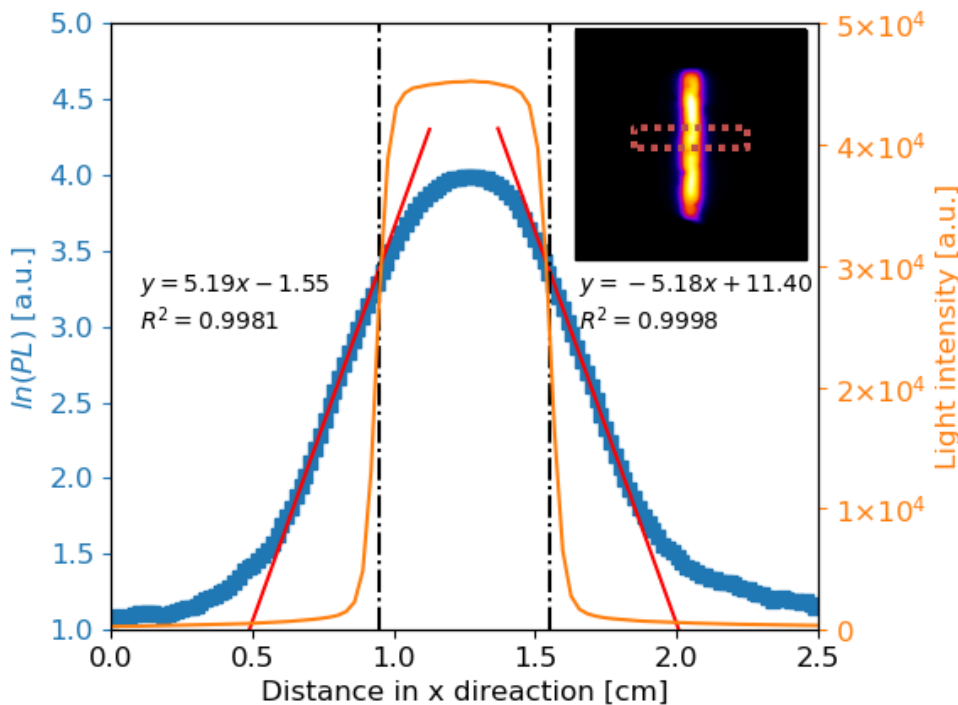


**Fig. C.3** The resulting PL image and a line scan of the PL counts. The line scan of the illumination light intensity is plotted in the right vertical axis. The red solid lines represent a linear fit of the data just outside the illuminated region.

According to Eq. (C.4) the effective diffusion length is given as the inverse of the slope. Using this method, a diffusion length of 0.19 (−0.2, 0.7) cm is calculated, which is in good agreement (in the range of 6%) with the diffusion length derived from the lifetime measurement. It is noted that the simple model applied here works only for samples with uniform minority carrier lifetime and the measurements are intended merely as a proof of concept for this measurement principle. For samples with a lower lifetime, non-uniform

lifetime or a strongly injection dependent lifetime, more complex models will need to be used.

## C.6 Summary

This appendix presented a DMD-based PL imaging setup which is able to achieve non-uniform illumination with virtually arbitrary illumination patterns. PL imaging with non-uniform illumination opens a range of quantitative analytical methods, three of which were demonstrated here. From the lateral carrier diffusion induced by non-uniform illumination, the diffusion length of a high lifetime $n$-type silicon wafer was extracted in a contactless method. The ability of the proposed method to extract series resistance images on fully processed cells and emitter sheet resistance on diffused wafers was also demonstrated.

# Reference

[1]     "List of Scientific Organizations that hold the position that Climate Change has been caused by human action." [Online]. Available: http://www.opr.ca.gov/facts/list-of-scientific-organizations.html.

[2]     J. R. Petit *et al.*, "Climate and atmospheric history of the past 420,000 years from the Vostok ice core, Antarctica," *Nature*, vol. 399, no. 6735, pp. 429–436, Jun. 1999.

[3]     D. Lüthi *et al.*, "High-resolution carbon dioxide concentration record 650,000–800,000 years before present," *Nature*, vol. 453, no. 7193, pp. 379–382, May 2008.

[4]     "National Oceanic and Atmospheric Administration." [Online]. Available: https://www.noaa.gov/.

[5]     J. L. Lean, "Cycles and trends in solar irradiance and climate," *Wiley Interdiscip. Rev. Clim. Chang.*, vol. 1, no. 1, pp. 111–122, Jan. 2010.

[6]     M. Lockwood, "Solar change and climate: an update in the light of the current exceptional solar minimum," *Proc. R. Soc. A Math. Phys. Eng. Sci.*, vol. 466, no. 2114, pp. 303–329, Feb. 2010.

[7]     R. S. Nerem, B. D. Beckley, J. T. Fasullo, B. D. Hamlington, D. Masters, and G. T. Mitchum, "Climate-change–driven accelerated sea-level rise detected in the altimeter era," *Proc. Natl. Acad. Sci.*, vol. 115, no. 9, pp. 2022–2025, Feb. 2018.

[8]     "World glacier monitoring service." [Online]. Available: https://wgms.ch/.

[9]     D. J. Wuebbles, D. W. Fahey, K. A. Hibbard, D. J. Dokken, B. C. Stewart, and T. K. Maycock, Eds., "Climate Science Special Report: Fourth National Climate Assessment, Volume I," Washington, DC, 2017.

[10]    R. Perez and M. Perez, "A fundamental look at energy reserves for the planet," *Int. Energy Agency SHC Program. Sol. Updat.*, vol. 50, pp. 2–3, 2009.

[11]    "International Energy Agency." [Online]. Available: https://www.iea.org/.

[12]    "International Technology Roadmap for Photovoltaic (ITRPV)," 2018.

[13]    P. W. Graham, J. Hayward, J. Foster, O. Story, and L. Havas, "GenCost 2018: Updated projections of electricity generation technology costs," 2018.

[14]    IEA, "Trend 2018 in photovoltauc applications," 2018.

[15]    IEA, "Technology roadmap: Solar photovoltaic energy," 2010.

[16]    J. Mandelkorn and J. H. Lamneck, "A new electric field effect in silicon solar cells," *J. Appl. Phys.*, vol. 44, no. 10, pp. 4785–4787, Oct. 1973.

[17]    M. A. Green, "The passivated emitter and rear cell (PERC): from conception to mass production," *Sol. Energy Mater. Sol. Cells*, vol. 143, pp. 190–197, 2015.

[18]    F. Feldmann, M. Bivour, C. Reichel, M. Hermle, and S. W. Glunz, "Passivated rear contacts for high-efficiency n-type Si solar cells providing high interface passivation quality and excellent transport characteristics," *Sol. Energy Mater. Sol. Cells*, 2014.

[19]    S. M. Sze and K. K. Ng, *Physics of semiconductor devices*. John wiley & sons, 2006.

[20]    D. V. Lang, "Deep-level transient spectroscopy: A new method to characterize traps in semiconductors," *J. Appl. Phys.*, vol. 45, no. 7, pp. 3023–3032, Jul. 1974.

[21]    S. Rein, *Lifetime spectroscopy: a method of defect characterization in silicon for photovoltaic applications*, vol. 85. Berlin: Springer Science and Business Media, 2006.

[22]    N. E. Grant, V. P. Markevich, J. Mullins, A. R. Peaker, F. Rougieux, and D. Macdonald, "Thermal activation and deactivation of grown-in defects limiting the lifetime of float-zone silicon," *Phys. status solidi - Rapid Res. Lett.*, vol. 10, no. 6, pp. 443–447, Jun. 2016.

[23]    D. Macdonald and A. Cuevas, "Trapping of minority carriers in multicrystalline silicon," *Appl. Phys. Lett.*, vol. 74, no. 12, pp. 1710–1712, Mar. 1999.

[24]    M. A. Green, *Solar cells: operating principles, technology, and system applications*. 1982.

[25]    Y. P. Varshni, "Band-to-Band radiative recombination in groups IV, VI, and III-V semiconductors (I)," *Phys. status solidi*, vol. 19, no. 2, pp. 459–514, 1967.

[26]    P. V. Auger, "Sur les rayons β secondaires produits dans un gaz par des rayons X," *CR Acad. Sci.*, vol. 177, p. 169, 1923.

[27]    H. Schlangenotto, H. Maeder, and W. Gerlach, "Temperature dependence of the radiative recombination coefficient in silicon," *Phys. status solidi*, vol. 21, no. 1, pp. 357–367, 1974.

[28]    W. Michaelis and M. H. Pilkuhn, "Radiative recombination in silicon p-n junctions," *Phys. status solidi*, vol. 36, no. 1, pp. 311–319, 1969.

[29]    T. Trupke *et al.*, "Temperature dependence of the radiative recombination coefficient of intrinsic crystalline silicon," *J. Appl. Phys.*, vol. 94, no. 8, pp. 4930–4937, 2003.

[30]    H. T. Nguyen, S. C. Baker-Finch, and D. MacDonald, "Temperature dependence of the radiative recombination coefficient in crystalline silicon from spectral photoluminescence," *Appl. Phys. Lett.*, vol. 104, no. 11, 2014.

[31]    P. P. Altermatt, F. Geelhaar, T. Trupke, X. Dai, A. Neisser, and E. Daub, "Injection dependence of spontaneous radiative recombination in crystalline silicon: Experimental verification and theoretical analysis," *Appl. Phys. Lett.*, vol. 88, no. 26, pp. 2004–2007, 2006.

[32]    A. R. Beattie and P. T. Landsberg, "Auger effect in semiconductors," *Proc. R. Soc. London. Ser. A. Math. Phys. Sci.*, vol. 249, no. 1256, pp. 16–29, Jan. 1959.

[33]    L. Pincherle, "One-dimensional overlap functions and their application to Auger recombination in semiconductors," *Proc. R. Soc. London. Ser. A. Math. Phys. Sci.*, vol. 258, no. 1295, pp. 486–495, Nov. 1960.

[34]    A. Haug, "Auger recombination with traps," *Phys. Status Solidi*, vol. 97, no. 2, pp. 481–490, 1980.

[35]    L. Huldt, "Band-to-band auger recombination in indirect gap semiconductors," *Phys. status solidi*, vol. 8, no. 1, pp. 173–187, 1971.

[36]    J. Dziewior and W. Schmid, "Auger coefficients for highly doped and highly excited silicon," *Appl. Phys. Lett.*, vol. 31, no. 5, pp. 346–348, 1977.

[37]    R. A. Sinton and R. M. Swanson, "Recombination in highly injected silicon," *IEEE Trans. Electron Devices*, vol. 34, no. 6, pp. 1380–1389, 1987.

[38]    A. Hangleiter and R. Häcker, "Enhancement of band-to-band Auger recombination by electron-hole correlations," *Phys. Rev. Lett.*, vol. 65, no. 2, pp. 215–218, 1990.

[39]    P. P. Altermatt, J. Schmidt, G. Heiser, and A. G. Aberle, "Assessment and parameterisation of Coulomb-enhanced Auger recombination coefficients in lowly injected crystalline silicon," *J. Appl. Phys.*, vol. 82, no. 10, pp. 4938–4944, 1997.

[40]    D. B. Laks, G. F. Neumark, and S. T. Pantelides, "Accurate interband-Auger-recombination rates in silicon," *Phys. Rev. B*, vol. 42, no. 8, pp. 5176–5185, 1990.

[41]    M. Govoni, I. Marri, and S. Ossicini, "Auger recombination in Si and GaAs semiconductors: Ab initio results," *Phys. Rev. B - Condens. Matter Mater. Phys.*, vol. 84, no. 7, 2011.

[42]    S. W. Glunz, D. Biro, S. Rein, and W. Warta, "Field-effect passivation of the SiO2-Si interface," *J. Appl. Phys.*, vol. 86, no. 1, pp. 683–691, 1999.

[43]    M. J. Kerr and A. Cuevas, "General parameterization of Auger recombination in crystalline silicon," *J. Appl. Phys.*, vol. 91, no. 4, pp. 2473–2480, 2002.

[44]    A. Richter, S. W. Glunz, F. Werner, J. Schmidt, and A. Cuevas, "Improved quantitative description of Auger recombination in crystalline silicon," *Phys. Rev. B*, vol. 86, no. 16, p. 165202, 2012.

[45]    B. A. Veith-Wolf, S. Schäfer, R. Brendel, and J. Schmidt, "Reassessment of intrinsic lifetime limit in n-type crystalline silicon and implication on maximum solar cell efficiency," *Sol. Energy Mater. Sol. Cells*, vol. 186, pp. 194–199, Nov. 2018.

[46]    E. Yablonovitch and T. Gmitter, "Auger recombination in silicon at low carrier densities," *Appl. Phys. Lett.*, vol. 49, no. 10, pp. 587–589, 1986.

[47]    T. Trupke and R. A. Bardos, "Photoluminescence: a surprisingly sensitive lifetime technique," in *31st IEEE Photovoltaic Specialists Conference*, 2005, pp. 903–906.

[48]    P. Würfel and U. Würfel, *Physics of solar cells: from basic principles to advanced concepts*. John Wiley & Sons, 2009.

[49]    H. Nagel, C. Berge, and A. G. Aberle, "Generalized analysis of quasi-steady-state and quasi-transient measurements of carrier lifetimes in semiconductors," *J. Appl. Phys.*, vol. 86, no. 11, pp. 6218–6221, 1999.

[50] D. Macdonald and A. Cuevas, "Validity of simplified Shockley-Read-Hall statistics for modeling carrier lifetimes in crystalline silicon," *Phys. Rev. B*, vol. 67, no. 7, pp. 1–7, 2003.

[51] M. A. Green, *Silicon solar cells: advanced principles & practice*. Centre for Photovoltaic Devices and Systems, University of New South Wales, 1995.

[52] K. Graff, *Metal impurities in silicon-device fabrication*, vol. 24. Springer Science & Business Media, 2013.

[53] S. Woo *et al.*, "An insight into dislocation density reduction in multicrystalline silicon," *Sol. Energy Mater. Sol. Cells*, vol. 155, pp. 88–100, Oct. 2016.

[54] G. D. Watkins, "Defects in irradiated silicon: electron paramagnetic resonance and electron-nuclear double resonance of the aluminum-vacancy pair," *Phys. Rev.*, vol. 155, no. 3, p. 802, 1967.

[55] M. Vaqueiro-Contreras *et al.*, "Powerful recombination centers resulting from reactions of hydrogen with carbon–oxygen defects in n-type Czochralski-grown silicon," *Phys. status solidi - Rapid Res. Lett.*, vol. 1700133, no. 8, pp. 6–11, 2017.

[56] J. Schmidt, A. G. Aberle, and R. Hezel, "Investigation of carrier lifetime instabilities in Cz-grown silicon," 2002.

[57] J. D. Murphy, R. E. McGuire, K. Bothe, V. V. Voronkov, and R. J. Falster, "Minority carrier lifetime in silicon photovoltaics: The effect of oxygen precipitation," *Sol. Energy Mater. Sol. Cells*, vol. 120, no. PART A, pp. 402–411, Jan. 2014.

[58] A. G. Aberle, *Crystalline silicon solar cells: advanced surface passivation and analysis*. University of New South Wale, 2004.

[59] W. Shockley and W. T. Read, "Statistics of the recombination of holes and electrons," *Phys. Rev.*, vol. 87, no. 46, pp. 835–842, 1952.

[60] R. N. Hall, "Electron-hole recombination in germanium," *Phys. Rev.*, vol. 87, no. 2, pp. 387–387, 1952.

[61] C. Sah and W. Shockley, "Electron-hole recombination statistics in semiconductors through flaws with many charge conditions," *Phys. Rev.*, vol. 109, no. 4, pp. 1103–1115, 1958.

[62] R. B. M. Girisch, R. P. Mertens, and R. F. De Keersmaecker, "Determination of Si-SiO2 interface recombination parameters using a gate-controlled point-junction diode under illumination," *IEEE Trans. Electron Devices*, vol. 35, no. 2, pp. 203–222, 1988.

[63] A. G. Aberle, S. Glunz, and W. Warta, "Impact of illumination level and oxide parameters on Shockley-Read-Hall recombination at the Si-SiO2 interface," *J. Appl. Phys.*, vol. 71, no. 9, pp. 4422–4431, 1992.

[64] R. S. Bonilla and P. R. Wilshaw, "On the c-Si/SiO2 interface recombination parameters from photo-conductance decay measurements," *J. Appl. Phys.*, vol. 121, 2017.

[65] A. R. Peaker, B. Hamilton, S. Leonard, V. P. Markevich, K. Youssef, and G. Rozgonyi, "Recombination via nano-precipitates: a new mechanism for efficiency loss in solar silicon?," in *2014 IEEE 40th Photovoltaic Specialist Conference (PVSC)*, 2014, pp. 0037–0041.

[66]    W. Kwapil, J. Sch, F. Schindler, W. Warta, and M. C. Schubert, "Impact of iron precipitates on carrier lifetime in silicon wafers in model and experiment," *IEEE J. Photovoltaics*, vol. 4, no. 3, pp. 791–798, 2014.

[67]    M. D. Negoita and T. Y. Tan, "Metallic precipitate contribution to generation and recombination currents in p-n junction devices due to the Schottky effect," *J. Appl. Phys.*, vol. 94, no. 8, pp. 5064–5070, 2003.

[68]    K. R. McIntosh, B. B. Paudyal, and D. H. MacDonald, "Generalized procedure to determine the dependence of steady-state photoconductance lifetime on the occupation of multiple defects," *J. Appl. Phys.*, vol. 104, no. 8, pp. 1–6, Oct. 2008.

[69]    Y. Hu, H. Schøn, Ø. Nielsen, E. Johannes Øvrelid, and L. Arnberg, "Investigating minority carrier trapping in n-type Cz silicon by transient photoconductance measurements," *J. Appl. Phys.*, vol. 111, no. 5, p. 053101, Mar. 2012.

[70]    Y. Zhu, M. K. Juhl, G. Coletti, and Z. Hameiri, "Reassessments of minority carrier traps in silicon with photoconductance decay measurements," *IEEE J. Photovoltaics*, vol. 9, no. 3, pp. 652–659, 2019.

[71]    D. V Lang, "Fast capacitance transient appartus: Application to ZnO and O centers in GaP p-n junctions," *J. Appl. Phys.*, vol. 45, no. 101, 1974.

[72]    T. Trupke, R. A. Bardos, M. C. Schubert, and W. Warta, "Photoluminescence imaging of silicon wafers," *Appl. Phys. Lett.*, vol. 89, no. 4, p. 44107, 2006.

[73]    J. A. Hornbeck and J. R. Haynes, "Trapping of minority carriers in silicon. I. p-type silicon," *Phys. Rev.*, vol. 97, no. 2, pp. 311–321, Jan. 1955.

[74]    J. R. Haynes and J. A. Hornbeck, "Trapping of minority carriers in silicon. II. n-type silicon," *Phys. Rev.*, vol. 100, no. 2, pp. 606–615, Oct. 1955.

[75]    F. Shimura, T. Okui, and T. Kusama, "Noncontact minority-carrier lifetime measurement at elevated temperatures for metal-doped Czochralski silicon crystals," *J. Appl. Phys.*, vol. 67, no. 11, pp. 7168–7171, 1990.

[76]    Y. Kirino, A. Buczkowski, Z. J. Radzimski, G. A. Rozgonyi, and F. Shimura, "Noncontact energy level analysis of metallic impurities in silicon crystals," *Appl. Phys. Lett.*, vol. 57, no. 26, pp. 2832–2834, 1990.

[77]    V. G. Weizer, H. W. Brandhorst, J. D. Broder, R. E. Hart, and J. H. Lamneck, "Photon-degradation effects in terrestrial silicon solar cells," *J. Appl. Phys.*, vol. 50, no. 6, pp. 4443–4449, 1979.

[78]    J. Schmidt, C. Berge, and A. G. Aberle, "Injection level dependence of the defect-related carrier lifetime in light-degraded boron-doped Czochralski silicon," *Appl. Phys. Lett.*, vol. 73, no. 15, pp. 2167–2169, 1998.

[79]    J. Schmidt and A. Cuevas, "Electronic properties of light-induced recombination centers in boron-doped Czochralski silicon," *J. Appl. Phys.*, vol. 86, no. 6, pp. 3175–3180, 1999.

[80]    D. Walz, J. P. Joly, and G. Kamarinos, "On the recombination behaviour of iron in moderately boron-doped p-type silicon," *Appl. Phys. A Mater. Sci. Process.*, vol. 62, no. 4, pp. 345–353, 1996.

[81]    H. Bleichner, P. Jonsson, N. Keskitalo, and E. Nordlander, "Temperature and injection dependence of the Shockley–Read–Hall lifetime in electron irradiated n -type silicon," *J. Appl. Phys.*, vol. 79, no. 12, pp. 9142–9148, Jun. 1996.

[82]    R. A. Sinton, A. Cuevas, and M. Stuckings, "Quasi-steady-state photoconductance, a new method for solar cell material and device characterization," in *Photovoltaic Specialists Conference, 1996., Conference Record of the Twenty Fifth IEEE*, 1996, pp. 457–460.

[83]    R. A. Sinton and A. Cuevas, "Contactless determination of current–voltage characteristics and minority-carrier lifetimes in semiconductors from quasi-steady-state photoconductance data," *Appl. Phys. Lett.*, vol. 69, no. 17, pp. 2510–2512, Oct. 1996.

[84]    S. Rein, T. Rehrl, W. Warta, and S. W. Glunz, "Lifetime spectroscopy for defect characterization: Systematic analysis of the possibilities and restrictions," *J. Appl. Phys.*, vol. 91, no. 3, pp. 2059–2070, 2002.

[85]    A. G. Aberle, "Overview on SiN surface passivation of crystalline silicon solar cells," *Sol. Energy Mater. Sol. Cells*, vol. 65, no. 1, pp. 239–248, 2001.

[86]    J. Schmidt, "Temperature-and injection-dependent lifetime spectroscopy for the characterization of defect centers in semiconductors," *Appl. Phys. Lett.*, vol. 82, no. 13, pp. 2178–2180, 2003.

[87]    B. B. Paudyal, K. R. McIntosh, and D. H. Macdonald, "Temperature dependent carrier lifetime studies on Ti-doped multicrystalline silicon," *J. Appl. Phys.*, vol. 105, no. 12, p. 124510, Jun. 2009.

[88]    A. Inglese, J. Lindroos, H. Vahlman, and H. Savin, "Recombination activity of light-activated copper defects in p-type silicon studied by injection- and temperature-dependent lifetime spectroscopy," *J. Appl. Phys.*, vol. 120, no. 12, p. 125703, Sep. 2016.

[89]    B. B. Paudyal, K. R. McIntosh, and D. H. Macdonald, "Temperature dependent electron and hole capture cross sections of iron-contaminated boron-doped silicon," in *34th IEEE Photovoltaic Specialist Conference*, 2009, pp. 1588–1593.

[90]    C. Sun, F. E. Rougieux, J. Degoulange, R. Einhaus, and D. Macdonald, "Reassessment of the recombination properties of aluminium-oxygen complexes in n- and p-type Czochralski-grown silicon," *Phys. status solidi*, vol. 253, no. 10, pp. 2079–2084, Oct. 2016.

[91]    T. U. Nærland *et al.*, "On the recombination centers of iron-gallium pairs in Ga-doped silicon," *J. Appl. Phys.*, vol. 122, no. 8, 2017.

[92]    C. Sun, A. Liu, F. E. Rougieux, and D. Macdonald, "Lifetime spectroscopy and hydrogenation of chromium in n-and p-type Cz Silicon," *Energy Procedia*, vol. 77, pp. 646–650, 2015.

[93]    A. E. Morishige *et al.*, "Lifetime spectroscopy investigation of light-induced degradation in p-type multicrystalline silicon PERC," *IEEE J. Photovoltaics*, vol. 6, no. 6, pp. 1466–1472, Nov. 2016.

[94]    C. Gemmel, J. Hensen, S. Kajari-Schroder, and R. Brendel, "4.5 ms effective carrier lifetime in kerfless epitaxial silicon wafers from the porous silicon process," *IEEE J. Photovoltaics*, vol. 7, no. 2, pp. 430–436, Mar. 2017.

[95]    C. Vargas *et al.*, "Recombination parameters of lifetime-limiting carrier-induced defects in multicrystalline silicon for solar cells," *Appl. Phys. Lett.*, vol. 110, no. 9, p. 092106, Feb. 2017.

[96]    F. E. Rougieux, N. E. Grant, C. Barugkin, D. Macdonald, and J. D. Murphy, "Influence of annealing and bulk hydrogenation on lifetime-limiting defects in nitrogen-doped floating zone silicon," *IEEE J. Photovoltaics*, vol. 5, no. 2, pp. 495–498, Mar. 2015.

[97]    N. Nampalli, T. H. Fung, S. Wenham, B. Hallam, and M. Abbott, "Statistical analysis of recombination properties of the boron-oxygen defect in p-type Czochralski silicon," *Front. Energy*, vol. 11, no. 1, pp. 4–22, 2017.

[98]    D. Bredemeier, D. Walter, S. Herlufsen, and J. Schmidt, "Understanding the light-induced lifetime degradation and regeneration in multicrystalline silicon," *Energy Procedia*, vol. 92, no. 0, pp. 773–778, 2016.

[99]    J. D. Murphy, K. Bothe, R. Krain, V. V Voronkov, and R. J. Falster, "Parameterisation of injection-dependent lifetime measurements in semiconductors in terms of Shockley-Read-Hall statistics: An application to oxide precipitates in silicon," *J. Appl. Phys.*, vol. 111, no. 11, p. 113709, 2012.

[100]   S. Bernardini, T. U. Naerland, G. Coletti, and M. I. Bertoni, "Defect parameters contour mapping: a powerful tool for lifetime spectroscopy data analysis," *Phys. Status Solidi Basic Res.*, vol. 255, no. 8, pp. 1–5, 2018.

[101]   T. U. Narland, S. Bernardini, M. S. Wiig, and M. I. Bertoni, "Is it possible to unambiguously assess the presence of two defects by temperature-and injection-dependent lifetime spectroscopy?," *IEEE J. Photovoltaics*, vol. 8, no. 2, pp. 465–472, 2018.

[102]   J. Schmidt, N. Thiemann, R. Bock, and R. Brendel, "Recombination lifetimes in highly aluminum-doped silicon," *J. Appl. Phys.*, vol. 106, no. 9, p. 93707, 2009.

[103]   S. Rein and S. W. Glunz, "Electronic properties of the metastable defect in boron-doped Czochralski silicon: Unambiguous determination by advanced lifetime spectroscopy," *Appl. Phys. Lett.*, vol. 82, no. 7, pp. 1054–1056, 2003.

[104]   F. E. Rougieux, C. Sun, and D. Macdonald, "Determining the charge states and capture mechanisms of defects in silicon through accurate recombination analyses: A review," *Sol. Energy Mater. Sol. Cells*, vol. 187, pp. 263–272, Dec. 2018.

[105]   T. Niewelt, J. Schön, J. Broisch, W. Warta, and M. Schubert, "Electrical characterization of the slow boron oxygen defect component in Czochralski silicon," *Phys. status solidi - Rapid Res. Lett.*, vol. 9, no. 12, pp. 692–696, 2015.

[106]   J. Schmidt, K. Bothe, and R. Hezel, "Oxygen-related minority-carrier trapping centers in p-type Czochralski silicon," *Appl. Phys. Lett.*, vol. 80, no. 23, pp. 4395–4397, Jun. 2002.

[107]   R. A. Bardos, T. Trupke, M. C. Schubert, and T. Roth, "Trapping artifacts in quasi-steady-state photoluminescence and photoconductance lifetime measurements on silicon wafers," *Appl. Phys. Lett.*, vol. 88, no. 5, pp. 1–3, 2006.

[108]   N. P. Harder, R. Gogolin, and R. Brendel, "Trapping-related recombination of charge carriers in silicon," *Appl. Phys. Lett.*, vol. 97, no. 11, p. 112111, Sep. 2010.

[109] R. Gogolin and N. P. Harder, "Trapping behavior of Shockley-Read-Hall recombination centers in silicon solar cells," *J. Appl. Phys.*, vol. 114, no. 6, p. 064504, Aug. 2013.

[110] D. H. Neuhaus, P. J. Cousins, and A. G. Aberle, "Trapping and junction-related perturbations of the effective excess carrier lifetime," *Proc. 3rd World Conf. Photovolt. Energy Convers.*, vol. 1, pp. 91–94, 2003.

[111] B. Hoex *et al.*, "Ultralow surface recombination of c-Si substrates passivated by plasma-assisted atomic layer deposited Al2O3," *Appl. Phys. Lett.*, vol. 89, no. 4, p. 042112, Jul. 2006.

[112] S. M. Myers, M. Seibt, and W. Schröter, "Mechanisms of transition-metal gettering in silicon," *J. Appl. Phys.*, vol. 88, no. 7, pp. 3795–3819, 2000.

[113] A. R. Peaker, V. P. Markevich, I. D. Hawkins, B. Hamilton, K. Bonde Nielsen, and K. Gościński, "Laplace deep level transient spectroscopy: Embodiment and evolution," *Phys. B Condens. Matter*, vol. 407, no. 15, pp. 3026–3030, 2012.

[114] B. Peter and J. W. Orton, *The electrical characterization of semiconductors : majority carriers and electron states*. Academic Press, 1992.

[115] G. M. Martin, A. Mitonneau, and A. Mircea, "Electron traps in bulk and epitaxial GaAs crystals," *Electron. Lett.*, vol. 13, no. 7, p. 191, 2007.

[116] A. Mitonneau, G. M. Martin, and A. Mircea, "Hole traps in bulk and epitaxial GaAs crystals," *Electron. Lett.*, vol. 13, no. 22, p. 666, 2007.

[117] A. Chantre, G. Vincent, and D. Bois, "Deep-level optical spectroscopy in GaAs," *Phys. Rev. B*, vol. 23, no. 10, pp. 5335–5359, 1981.

[118] R. Brunwin, B. Hamilton, P. Jordan, and A. R. Peaker, "Detection of minority-carrier traps using transient spectroscopy," *Electron. Lett.*, vol. 15, no. 12, pp. 349–350, 1979.

[119] F. D. Auret and M. Nel, "Detection of minority-carrier defects by deep level transient spectroscopy using Schottky barrier diodes," *J. Appl. Phys.*, vol. 61, no. 7, pp. 2546–2549, 1987.

[120] M. Takikawa and T. Ikoma, "Photo-excited DLTS: measurement of minority carrier traps," *Jpn. J. Appl. Phys.*, vol. 19, no. 7, pp. L436–L438, 1980.

[121] L. Dobaczewski, P. Kaczor, I. D. Hawkins, and A. R. Peaker, "Laplace transform deep-level transient spectroscopic studies of defects in semiconductors," *J. Appl. Phys.*, vol. 76, no. 1, pp. 194–198, Jul. 1994.

[122] L. Dobaczewski, A. R. Peaker, K. Bonde Nielsen, P. Kaczor, I. D. Hawkins, and A. R. Peaker, "Laplace-transform deep-level spectroscopy: The technique and its applications to the study of point defects in semiconductors," *J. Appl. Phys.*, vol. 96, no. 9, pp. 4689–4728, Nov. 2004.

[123] J. Mullins *et al.*, "Recombination via transition metals in solar silicon: The significance of hydrogen–metal reactions and lattice sites of metal atoms," *Phys. Status Solidi Appl. Mater. Sci.*, vol. 214, no. 7, 2017.

[124] M. Vaqueiro-Contreras *et al.*, "Identification of the mechanism responsible for the boron oxygen light induced degradation in silicon photovoltaic cells," *J. Appl. Phys.*, vol. 125, no. 18, p. 185704, May 2019.

[125] B. Mitchell, J. W. Weber, M. Juhl, D. Macdonald, and T. Trupke, "Photoluminescence imaging of silicon bricks," *Solid State Phenom.*, vol. 205–206, pp. 118–127, 2013.

[126] I. Zafirovska, M. K. Juhl, J. W. Weber, O. Kunz, and T. Trupke, "Module inspection using line scanning photoluminescence imaging," *32nd Eur. Photovolt. Sol. Energy Conf. Exhib.*, pp. 1826–1829, Jan. 2016.

[127] R. Bhoopathy, O. Kunz, M. Juhl, T. Trupke, and Z. Hameiri, "Outdoor photoluminescence imaging of photovoltaic modules with sunlight excitation," *Prog. Photovoltaics Res. Appl.*, vol. 26, no. 1, pp. 69–73, 2018.

[128] T. Fuyuki, H. Kondo, T. Yamazaki, Y. Takahashi, and Y. Uraoka, "Photographic surveying of minority carrier diffusion length in polycrystalline silicon solar cells by electroluminescence," *Appl. Phys. Lett.*, vol. 86, no. 26, pp. 1–3, 2005.

[129] T. Trupke *et al.*, "Progress with luminescence imaging for the characterisation of silicon wafers and solar cells," in *22nd European Photovoltaic Solar Energy Conference*, 2007.

[130] H. J. Leamy, "Charge collection scanning electron microscopy," *J. Appl. Phys.*, vol. 53, no. 6, pp. R51–R80, Jun. 1982.

[131] T. Wilson and E. M. McCabe, "Theory of optical beam induced current images of defects in semiconductors," *J. Appl. Phys.*, vol. 61, no. 1, pp. 191–195, Jan. 1987.

[132] H. T. Nguyen, D. Yan, F. Wang, P. Zheng, Y. Han, and D. Macdonald, "Micro-photoluminescence spectroscopy on heavily-doped layers of silicon solar cells," *Phys. status solidi - Rapid Res. Lett.*, vol. 9, no. 4, pp. 230–235, Apr. 2015.

[133] T. Trupke, B. Mitchell, J. W. Weber, W. McMillan, R. A. Bardos, and R. Kroeze, "Photoluminescence imaging for photovoltaic applications," in *International Conference on Materials for Advanced Technologies 2011*, 2012, vol. 15, pp. 135–146.

[134] H. C. Sio, S. P. Phang, T. Trupke, and D. Macdonald, "An accurate method for calibrating photoluminescence-based lifetime images on multi-crystalline silicon wafers," *Sol. Energy Mater. Sol. Cells*, vol. 131, pp. 77–84, 2014.

[135] J. A. Giesecke, M. C. Schubert, B. Michl, F. Schindler, and W. Warta, "Minority carrier lifetime imaging of silicon wafers calibrated by quasi-steady-state photoluminescence," *Sol. Energy Mater. Sol. Cells*, vol. 95, no. 3, pp. 1011–1018, 2011.

[136] D. Kiliani, G. Micard, B. Steuer, B. Raabe, A. Herguth, and G. Hahn, "Minority charge carrier lifetime mapping of crystalline silicon wafers by time-resolved photoluminescence imaging," *J. Appl. Phys.*, vol. 110, no. 5, p. 54508, 2011.

[137] S. P. Phang, H. C. Sio, and D. Macdonald, "Carrier de-smearing of photoluminescence images on silicon wafers using the continuity equation," *Appl. Phys. Lett.*, vol. 103, no. 19, p. 192112, Nov. 2013.

[138]   S. P. Phang, H. C. Sio, and D. Macdonald, "Applications of carrier de-smearing of photoluminescence images on silicon wafers," *Prog. Photovoltaics Res. Appl.*, vol. 24, no. 12, pp. 1547–1553, Dec. 2016.

[139]   "Sinton Instruments." [Online]. Available: www.sintoninstruments.com.

[140]   K. R. McIntosh and R. a. Sinton, "Uncertainty in photoconductance lifetime measurements that use an inductive-coil detector," *23rd Eur. Photovolt. Sol. Energy Conf.*, no. September, pp. 77–82, 2008.

[141]   G. K. Wertheim, "Transient recombination of excess carriers in semiconductors," *Phys. Rev.*, vol. 109, no. 4, pp. 1086–1091, Feb. 1958.

[142]   H. Y. Fan, "Effect of traps on carrier injection in semiconductors," *Phys. Rev.*, vol. 92, no. 6, pp. 1424–1428, 1953.

[143]   "Sinton Instruments WCT-120 Photoconductance Lifetime Tester: User manual," 2011.

[144]   "INSTEC." [Online]. Available: http://www.instec.com/.

[145]   S. Herlufsen, D. Hinken, M. Offer, J. Schmidt, and K. Bothe, "Validity of calibrated photoluminescence lifetime measurements of crystalline silicon wafers for arbitrary lifetime and injection ranges," *IEEE J. Photovoltaics*, vol. 3, no. 1, pp. 381–386, 2013.

[146]   M. S. Tyagi, J. F. Nijs, and R. J. Van Overstraeten, "Effect of surface recombination on the transient decay of excess carriers produced by short wavelength laser pulses," *Solid State Electron.*, vol. 25, no. 5, pp. 411–415, 1982.

[147]   J. S. Swirhun, R. A. Sinton, M. K. Forsyth, and T. Mankad, "Contactless measurement of minority carrier lifetime in silicon ingots and bricks," *Prog. Photovoltaics Res. Appl.*, vol. 19, no. 3, pp. 313–319, May 2011.

[148]   R. Lago-Aurrekoetxea, I. Tobías, C. del Cañizo, and A. Luque, "Lifetime measurements by photoconductance techniques in wafers immersed in a passivating liquid," *J. Electrochem. Soc.*, vol. 148, no. 4, p. G200, Jul. 2001.

[149]   K. Ramspeck, S. Reissenweber, J. Schmidt, K. Bothe, and R. Brendel, "Dynamic carrier lifetime imaging of silicon wafers using an infrared-camera-based approach," *Appl. Phys. Lett.*, vol. 93, no. 10, pp. 2006–2009, 2008.

[150]   T. Trupke and R. A. Bardos, "Self-consistent determination of the generation rate from photoconductance measurements," *Appl. Phys. Lett.*, vol. 85, no. 16, pp. 3611–3613, 2004.

[151]   R. A. Sinton and T. Trupke, "Limitations on dynamic excess carrier lifetime calibration methods," *Prog. Photovoltaics Res. Appl.*, vol. 20, no. 2, pp. 246–249, Mar. 2012.

[152]   D. B. M. Klaassen, "A unified mobility model for device simulation—I. Model equations and concentration dependence," *Solid. State. Electron.*, vol. 35, no. 7, pp. 953–959, Jul. 1992.

[153]   D. B. M. Klaassen, "A unified mobility model for device simulation-II. temperature dependence of carrier mobility and lifetime," *Solid State Electron.*, vol. 35, no. 7, pp. 961–967, 1992.

[154]   F. Schindler *et al.*, "Modeling majority carrier mobility in compensated crystalline silicon for solar cells," *Sol. Energy Mater. Sol. Cells*, vol. 106, pp. 31–36, 2012.

[155]   G. L. Miller, "Method and apparatus for the contactless monitoring carrier lifetime in semiconductor materials," 4,286,215, 1981.

[156]   D. Kane and R. Swanson, "Measurement of the emitter saturation current by a contactless photoconductivity decay method," in *18th IEEE photovoltaic specialists conference*, 1985, pp. 578–583.

[157]   J. Tan, D. Macdonald, F. Rougieux, and A. Cuevas, "Accurate measurement of the formation rate of iron–boron pairs in silicon," *Semicond. Sci. Technol.*, vol. 26, no. 5, p. 055019, May 2011.

[158]   P. P. Altermatt, A. Schenk, and G. Heiser, "A simulation model for the density of states and for incomplete ionization in crystalline silicon. I. Establishing the model in Si:P," *J. Appl. Phys.*, vol. 100, no. 11, 2006.

[159]   J. Giesecke, "Quantitative recombination and transport properties in silicon from dynamic luminescence," Springer, 2014.

[160]   T. Trupke, R. A. Bardos, and M. D. Abbott, "Self-consistent calibration of photoluminescence and photoconductance lifetime measurements," *Appl. Phys. Lett.*, vol. 87, no. 18, p. 184102, 2005.

[161]   J. A. Giesecke, M. C. Schubert, and W. Warta, "Self sufficient minority carrier lifetime in silicon from quasi steady state photoluminescence," *Phys. status solidi*, vol. 209, no. 11, pp. 2286–2290, 2012.

[162]   J. A. Giesecke, M. C. Schubert, W. Warta, J. A. Giesecke, M. C. Schubert, and W. Warta, "Measurement of net dopant concentration via dynamic photoluminescence," *J. Appl. Phys.*, vol. 112, no. 6, 2012.

[163]   J. A. Giesecke and W. Warta, "Microsecond carrier lifetime measurements in silicon via quasi-steady-state photoluminescence," *Prog. Photovoltaics Res. Appl.*, vol. 20, no. 2, pp. 238–245, 2012.

[164]   S. Rein and S. W. Glunz, "Electronic properties of interstitial iron and iron-boron pairs determined by means of advanced lifetime spectroscopy," *J. Appl. Phys.*, vol. 98, no. 11, p. 113711, Dec. 2005.

[165]   M. A. Green, "Intrinsic concentration, effective densities of states, and effective mass in silicon," *J. Appl. Phys.*, vol. 67, no. 6, pp. 2944–2954, Mar. 1990.

[166]   J. Raphson, *Analysis Aequationum Universalis*. London, UK: Typis Tho. Braddyll, 1702.

[167]   C. Sun, F. E. Rougieux, and D. Macdonald, "Reassessment of the recombination parameters of chromium in n-and p-type crystalline silicon and chromium-boron pairs in p-type crystalline silicon," *J. Appl. Phys.*, vol. 115, no. 21, p. 214907, 2014.

[168]   P. P. Altermatt, A. Schenk, B. Schmithüsen, and G. Heiser, "A simulation model for the density of states and for incomplete ionization in crystalline silicon. II. Investigation of Si:As and Si:B and usage in device simulation," *J. Appl. Phys.*, vol. 100, no. 11, p. 113715, 2006.

[169] R. Couderc, M. Amara, and M. Lemiti, "Reassessment of the intrinsic carrier density temperature dependence in crystalline silicon," *J. Appl. Phys.*, vol. 115, no. 9, p. 093705, Mar. 2014.

[170] R. Pässler, "Dispersion-related description of temperature dependencies of band gaps in semiconductors," *Phys. Rev. B*, vol. 66, no. 8, p. 85201, 2002.

[171] D. Yan and A. Cuevas, "Empirical determination of the energy band gap narrowing in p + silicon heavily doped with boron," *J. Appl. Phys.*, vol. 116, no. 19, p. 194505, Nov. 2014.

[172] K. Nakayashiki *et al.*, "Engineering solutions and root-cause analysis for light-induced degradation in p-type multicrystalline silicon PERC modules," *IEEE J. Photovoltaics*, vol. 6, no. 4, pp. 860–868, Jul. 2016.

[173] A. C. Wang and C. T. Sah, "Complete electrical characterization of recombination properties of titanium in silicon," *Cit. J. Appl. Phys.*, vol. 56, p. 5862, 1984.

[174] R. H. Wu and A. R. Peaker, "Capture cross sections of the gold donor and acceptor states in n-type Czochralski silicon," *Solid. State. Electron.*, vol. 25, no. 7, pp. 643–649, Jul. 1982.

[175] S. Diez, S. Rein, T. Roth, and S. W. Glunz, "Cobalt related defect levels in silicon analyzed by temperature- and injection-dependent lifetime spectroscopy," *J. Appl. Phys.*, vol. 101, no. 3, p. 033710, Feb. 2007.

[176] S. D. Brotherton and J. Bicknell, "The electron capture cross section and energy level of the gold acceptor center in silicon," *J. Appl. Phys.*, vol. 49, no. 2, pp. 667–671, Feb. 1978.

[177] J. Schmidt, R. Krain, K. Bothe, G. Pensl, and S. Beljakowa, "Recombination activity of interstitial chromium and chromium-boron pairs in silicon," *J. Appl. Phys.*, vol. 102, no. 12, p. 123701, 2007.

[178] A. A. Istratov, H. Hieslmair, and E. R. Weber, "Iron and its complexes in silicon," *Appl. Phys. A Mater. Sci. Process.*, vol. 69, no. 1, pp. 13–44, 1999.

[179] J. D. Murphy, M. Al-Amin, K. Bothe, M. Olmo, V. V. Voronkov, and R. J. Falster, "The effect of oxide precipitates on minority carrier lifetime in n -type silicon," *J. Appl. Phys.*, vol. 118, no. 21, p. 215706, Dec. 2015.

[180] J. D. Murphy, K. Bothe, M. Olmo, V. V. Voronkov, and R. J. Falster, "The effect of oxide precipitates on minority carrier lifetime in p-type silicon," *J. Appl. Phys.*, vol. 110, no. 5, p. 053713, Sep. 2011.

[181] M. Hourai, T. Nagashima, H. Nishikawa, W. Sugimura, T. Ono, and S. Umeno, "Review and comments for the development of point defect-controlled CZ-Si crystals and their application to future power devices," *Phys. Status Solidi*, vol. 1800664, p. 1800664, 2018.

[182] W. Von Ammon, "FZ and CZ crystal growth: Cost driving factors and new perspectives," *Phys. Status Solidi Appl. Mater. Sci.*, vol. 211, no. 11, pp. 2461–2470, Sep. 2014.

[183]   J. Zhao, A. Wang, M. A. Green, and F. Ferrazza, "19.8% efficient 'honeycomb' textured multicrystalline and 24.4% monocrystalline silicon solar cells," *Appl. Phys. Lett.*, vol. 73, no. 14, pp. 1991–1993, Oct. 1998.

[184]   K. Yoshikawa *et al.*, "Silicon heterojunction solar cell with interdigitated back contacts for a photoconversion efficiency over 26%," *Nat. Energy*, vol. 2, no. 5, Mar. 2017.

[185]   C. Hollemann, F. Haase, S. Schäfer, J. Krügener, R. Brendel, and R. Peibst, "26.1%-efficient POLO-IBC cells: Quantification of electrical and optical loss mechanisms," *Prog. Photovoltaics Res. Appl.*, 2019.

[186]   C. Sun, H. T. Nguyen, H. C. Sio, F. E. Rougieux, and D. Macdonald, "Activation kinetics of the boron–oxygen defect in compensated n- and p-type silicon studied by high-injection micro-photoluminescence," *IEEE J. Photovoltaics*, vol. 7, no. 4, pp. 988–995, Jul. 2017.

[187]   M. A. Jensen *et al.*, "Evaluating root cause: The distinct roles of hydrogen and firing in activating light- and elevated temperature-induced degradation," *J. Appl. Phys.*, vol. 124, no. 8, p. 085701, Aug. 2018.

[188]   K. Bothe and J. Schmidt, "Electronically activated boron-oxygen-related recombination centers in crystalline silicon," *J. Appl. Phys.*, vol. 99, no. 1, p. 013701, Jan. 2006.

[189]   N. E. Grant *et al.*, "Permanent annihilation of thermally activated defects which limit the lifetime of float-zone silicon," *Phys. status solidi*, vol. 213, no. 11, pp. 2844–2849, 2016.

[190]   W. von Ammon, R. Hölzl, J. Virbulis, E. Dornberger, R. Schmolke, and D. Gräf, "The impact of nitrogen on the defect aggregation in silicon," *J. Cryst. Growth*, vol. 226, no. 1, pp. 19–30, Jun. 2001.

[191]   T. Abe, "Generation and annihilation of point defects by doping impurities during FZ silicon crystal growth," *J. Cryst. Growth*, vol. 334, no. 1, pp. 4–15, Nov. 2011.

[192]   K. Sumino, I. Yonenaga, M. Imai, and T. Abe, "Effects of nitrogen on dislocation behavior and mechanical strength in silicon crystals," *J. Appl. Phys.*, vol. 54, no. 9, pp. 5016–5020, Sep. 1983.

[193]   C. R. Alpass, J. D. Murphy, R. J. Falster, and P. R. Wilshaw, "Nitrogen diffusion and interaction with dislocations in single-crystal silicon," *J. Appl. Phys.*, vol. 105, no. 1, p. 013519, Jan. 2009.

[194]   T. Abe and T. Takahashi, "Intrinsic point defect behavior in silicon crystals during growth from the melt: A model derived from experimental results," *J. Cryst. Growth*, vol. 334, no. 1, pp. 16–36, Nov. 2011.

[195]   V. V. Voronkov, "The mechanism of swirl defects formation in silicon," *J. Cryst. Growth*, vol. 59, no. 3, pp. 625–643, Oct. 1982.

[196]   M. A. Khorosheva, V. I. Orlov, N. V. Abrosimov, and V. V. Kveder, "Determination of the nonequilibrium concentration of vacancies in silicon crystals by measuring the concentration of nickel atoms at lattice sites," *J. Exp. Theor. Phys.*, vol. 110, no. 5, pp. 769–774, May 2010.

[197]   J. Mullins *et al.*, "Thermally activated defects in float zone silicon: Effect of nitrogen on the introduction of deep level states," *J. Appl. Phys.*, vol. 124, no. 3, p. 035701, Jul. 2018.

[198]   J. Bullock *et al.*, "Superacid Passivation of Crystalline Silicon Surfaces," *ACS Appl. Mater. Interfaces*, vol. 8, no. 36, pp. 24205–24211, 2016.

[199]   N. E. Grant *et al.*, "Superacid-treated silicon surfaces: extending the limit of carrier lifetime for photovoltaic applications," *IEEE J. Photovoltaics*, vol. 7, no. 6, pp. 1574–1583, 2017.

[200]   A. H. Mahan, J. Carapella, B. P. Nelson, R. S. Crandall, and I. Balberg, "Deposition of device quality, low H content amorphous silicon," *J. Appl. Phys.*, vol. 69, no. 9, pp. 6728–6730, May 1991.

[201]   C. H. Henry and D. V. Lang, "Nonradiative capture and recombination by multiphonon emission in GaAs and GaP," *Phys. Rev. B*, vol. 15, no. 2, p. 989, 1977.

[202]   P. T. Landsberg, "Trap-Auger recombination in silicon of low carrier densities," *Appl. Phys. Lett.*, vol. 50, no. 12, pp. 745–747, Mar. 1987.

[203]   L. C. Kimerling, "Recombination enhanced defect reactions," *Solid State Electron.*, vol. 21, no. 11–12, pp. 1391–1401, 1978.

[204]   M. Lax, "Cascade capture of electrons in solids," *Phys. Rev.*, vol. 119, no. 5, p. 1502, 1960.

[205]   P. T. Landsberg and D. J. Robbins, "The first 70 semiconductor Auger processes," *Solid State Electron.*, vol. 21, no. 11–12, pp. 1289–1294, 1978.

[206]   A. Hangleiter, "Nonradiative recombination via deep impurity levels in silicon: Experiment," *Phys. Rev. B*, vol. 35, no. 17, p. 9149, 1987.

[207]   R. M. Gibb *et al.*, "A two stage model for deep level capture," *Philos. Mag.*, vol. 36, no. 4, pp. 1021–1034, 1977.

[208]   I. Pelant and J. Valenta, *Luminescence Spectroscopy of Semiconductors*. Oxford University Press, 2012.

[209]   F. D. Heinz, T. Niewelt, and M. C. Schubert, "Experimental evidence of electron capture and emission from trap levels in Cz silicon," *Phys. status solidi*, p. e201700292, Jun. 2017.

[210]   M. Kunst and G. Beck, "The study of charge carrier kinetics in semiconductors by microwave conductivity measurements," *J. Appl. Phys.*, vol. 60, no. 10, pp. 3558–3566, 1986.

[211]   M. Kunst and G. Beck, "The study of charge carrier kinetics in semiconductors by microwave conductivity measurements. II.," *J. Appl. Phys.*, vol. 63, no. 4, pp. 1093–1098, 1988.

[212]   D. Macdonald, R. A. Sinton, and A. Cuevas, "On the use of a bias-light correction for trapping effects in photoconductance-based lifetime measurements of silicon," *J. Appl. Phys.*, vol. 89, no. 5, pp. 2772–2778, 2001.

[213] Y. Zhu, M. Juhl, G. Coletti, and Z. Hameiri, "Reassessment of minority carrier traps in silicon during 'quasi steady-state' photoconductance measurements," in *IEEE 7th World Conference on Photovoltaic Energy Conversion*, 2018, pp. 0077–0088.

[214] N. Schüler, T. Hahn, S. Schmerler, S. Hahn, K. Dornich, and J. R. Niklas, "Simulations of photoconductivity and lifetime for steady state and nonsteady state measurements," *J. Appl. Phys.*, vol. 107, no. 6, p. 064901, Mar. 2010.

[215] N. Schüler, T. Hahn, K. Dornich, and J. R. Niklas, "Spatially resolved determination of trapping parameters in p-doped silicon by microwave detected photoconductivty," in *25th European Photovoltaic Solar Energy Conference and Exhibition*, 2010, pp. 343–346.

[216] H. Conzelmann, K. Graff, and E. R. Weber, "Chromium and chromium-boron pairs in silicon," *Appl. Phys. A*, vol. 30, no. 3, pp. 169–175, 1983.

[217] S. Dubois, O. Palais, and P. J. Ribeyron, "Determination at 300 K of the hole capture cross section of chromium-boron pairs in p-type silicon," *Appl. Phys. Lett.*, vol. 89, no. 23, p. 2112, 2006.

[218] R. Boyle, "FT-IR measurement of interstitial oxygen and substitutional carbon in silicon wafers," Madison, 2008.

[219] J. O.L.Curtis, Jr., and J.H.Crawford, "Radiation-induced recombination and trapping centers in germanium. I. the nature of the recombination process," *Phys. Rev.*, vol. 124, no. 6, pp. 1731–1740, Dec. 1961.

[220] J. S. Blakemore, *Semiconductor statistics*. Courier Corporation, 2002.

[221] B. G. Streetman, "Carrier recombination and trapping effects in transient photoconductive decay measurements," *J. Appl. Phys.*, vol. 37, no. 8, pp. 3137–3144, Jul. 1966.

[222] H. J. Stein, S. K. Hahn, and S. C. Shatas, "Rapid thermal annealing and regrowth of thermal donors in silicon," *J. Appl. Phys.*, vol. 59, no. 10, pp. 3495–3502, May 1986.

[223] K. R. McIntosh, J. Guo, M. D. Abbott, and R. A. Bardos, "Calibration of the WCT-100 photoconductance instrument at low conductance," *Prog. Photovoltaics Res. Appl.*, vol. 16, no. 4, pp. 279–287, 2008.

[224] L. Johnson and H. Levinstein, "Infrared properties of gold in germanium," *Phys. Rev.*, vol. 117, no. 5, pp. 1191–1203, Mar. 1960.

[225] J. R. Barrett and G. C. Gerhard, "Negative photoconductivity in gold-doped silicon," *J. Appl. Phys.*, vol. 38, no. 2, pp. 900–902, Feb. 1967.

[226] T. Kurosu, H. Yasuda, Y. Akiba, M. Iida, and I. Y. Choe, "Transient negative photoconductivity in silicon doped with gold," *Appl. Phys. A Solids Surfaces*, vol. 43, no. 3, pp. 205–208, Jul. 1987.

[227] H. Kimura, T. Kurosu, Y. Akiba, and M. Iida, "A model for the occurrence of transient negative photoconductivity in silicon doped with gold," *Appl. Phys. A Solids Surfaces*, vol. 53, no. 3, pp. 194–197, Sep. 1991.

[228] H. Kimura, T. Kurosu, Y. Akiba, and M. Iida, "A simulation of transient negative photoconductivity in silicon doped with gold," *Jpn. J. Appl. Phys.*, vol. 32, no. 8 R, pp. 741–746, 1993.

[229] C. M. Penchina, J. S. Moore, and N. Holonyak, "Energy levels and negative photoconductivity in cobalt-doped silicon," *Phys. Rev.*, vol. 143, no. 2, pp. 634–636, Mar. 1966.

[230] M. Liao, Y. Koide, J. Alvarez, M. Imura, and J. P. Kleider, "Persistent positive and transient absolute negative photoconductivity observed in diamond photodetectors," *Phys. Rev. B - Condens. Matter Mater. Phys.*, vol. 78, no. 4, pp. 1–9, 2008.

[231] P. C. Wei *et al.*, "Room-temperature negative photoconductivity in degenerate InN thin films with a supergap excitation," *Phys. Rev. B - Condens. Matter Mater. Phys.*, vol. 81, no. 4, pp. 1–5, 2010.

[232] A. S. Chaves and H. Chacham, "Negative photoconductivity in semiconductor heterostructures," *Appl. Phys. Lett.*, vol. 727, no. 1995, p. 727, 1995.

[233] A. Serpi, "Negative photoconductivity in MoS2," *Phys. Status Solidi*, vol. 133, no. 2, pp. K73–K77, Oct. 1992.

[234] J. N. Heyman, J. D. Stein, Z. S. Kaminski, A. R. Banman, A. M. Massari, and J. T. Robinson, "Carrier heating and negative photoconductivity in graphene," *J. Appl. Phys.*, vol. 117, no. 1, 2015.

[235] F. Stöckmann, "Negative photoeffekte in halbleitern," *Zeitschrift für Phys.*, vol. 143, no. 3, pp. 348–356, Jun. 1955.

[236] R. A. Höpfel, "Extremely high negative photoconductivity in p -modulation-doped GaAs quantum wells," *Appl. Phys. Lett.*, vol. 52, no. 10, pp. 801–803, Mar. 1988.

[237] A. Rose, *Concepts in photoconductivity and allied problems*. Interscience Publishers, 1963.

[238] P. D. Altukhov, E. G. Kuzminov, and G. V. Ivanov, "Excitons and multi-exciton complexes bound to a two-dimensional hole layer at a silicon surface: the Kondo effect, the Coulomb blockade and a negative photoconductivity," *Superlattices Microstruct.*, vol. 23, no. 5, pp. 985–990, May 1998.

[239] N. V. Joshi, L. Mogollon, J. Sanchez, and J. M. Martin, "Detection of negative photoconductivity in CdxFe1−xSe system," *Solid State Commun.*, vol. 65, no. 2, pp. 151–153, Jan. 1988.

[240] C. Sun, F. E. Rougieux, and D. Macdonald, "A unified approach to modelling the charge state of monatomic hydrogen and other defects in crystalline silicon," *J. Appl. Phys.*, vol. 117, no. 4, 2015.

[241] D. Chung, B. Mitchell, M. Goodarzi, R. A. Sinton, D. Macdonald, and T. Trupke, "Uncertainty in photoluminescence metrology on multicrystalline silicon bricks and cross validation with wafers," *IEEE J. Photovoltaics*, vol. 7, no. 6, pp. 1701–1709, Nov. 2017.

[242] R. Ebner, B. Kubicek, G. Ujvari, S. Novalin, M. Rennhofer, and M. Halwachs, "Optical characterization of different thin film module technologies," *Int. J. Photoenergy*, vol. 2015, 2015.

[243] C.-Y. Peng, S.-Y. Wen, Z.-J. Ji, and C.-P. Huang, "Non-destructive displaying defects for luminescence image of photovoltaic panel arrays," in *International Conference on Advanced Robotics and Intelligent Systems (ARIS)*, 2015, pp. 1–4.

[244]  D. Macdonald, J. Tan, and T. Trupke, "Imaging interstitial iron concentrations in boron-doped crystalline silicon using photoluminescence," *J. Appl. Phys.*, vol. 103, no. 7, p. 073710, Apr. 2008.

[245]  H. Habenicht, M. C. Schubert, and W. Warta, "Imaging of chromium point defects in p-type silicon," *J. Appl. Phys.*, vol. 108, no. 3, p. 34909, 2010.

[246]  M. C. Schubert, H. Habenicht, and W. Warta, "Imaging of metastable defects in silicon," *IEEE J. Photovoltaics*, vol. 1, no. 2, pp. 168–173, 2011.

[247]  C. Shen, H. Kampwerth, and M. A. Green, "Photoluminescence based open circuit voltage and effective lifetime images re-interpretation for solar cells: The influence of horizontal balancing currents," *Sol. Energy Mater. Sol. Cells*, vol. 130, pp. 393–396, 2014.

[248]  M. Glatthaar *et al.*, "Evaluating luminescence based voltage images of silicon solar cells," *J. Appl. Phys.*, vol. 108, no. 1, pp. 1–6, 2010.

[249]  M. Glatthaar, J. Haunschild, M. Kasemann, J. Giesecke, W. Warta, and S. Rein, "Spatially resolved determination of dark saturation current and series resistance of silicon solar cells," *Phys. Status Solidi - Rapid Res. Lett.*, vol. 4, no. 1–2, pp. 13–15, 2010.

[250]  Z. Hameiri and P. Chaturvedi, "Spatially resolved electrical parameters of silicon wafers and solar cells by contactless photoluminescence imaging," *Appl. Phys. Lett.*, vol. 102, no. 7, pp. 1–4, 2013.

[251]  B. Michl, D. Impera, M. Bivour, W. Warta, and M. C. Schubert, "Suns-PLI as a powerful tool for spatially resolved fill factor analysis of solar cells," *Prog. Photovoltaics Res. Appl.*, vol. 22, no. 5, pp. 581–586, May 2014.

[252]  R. Eberle, S. T. Haag, I. Geisemeyer, M. Padilla, and M. C. Schubert, "Temperature coefficient imaging for silicon solar cells," *IEEE J. Photovoltaics*, vol. 8, no. 4, pp. 930–936, Jul. 2018.

[253]  S. Nie, S. T. Kristensen, A. Gu, T. Trupke, and Z. Hameiri, "A novel method for characterizing temperature sensitivity of silicon wafers and cells," in *46th IEEE Photovoltaic Specialists Conference*, 2019.

[254]  C. Shen, M. A. Green, O. Breitenstein, T. Trupke, M. Zhang, and H. Kampwerth, "Improved local efficiency imaging via photoluminescence for silicon solar cells," *Sol. Energy Mater. Sol. Cells*, vol. 123, pp. 41–46, 2014.

[255]  C. Shen, H. Kampwerth, M. Green, T. Trupke, J. Carstensen, and A. Schütt, "Spatially resolved photoluminescence imaging of essential silicon solar cell parameters and comparison with CELLO measurements," *Sol. Energy Mater. Sol. Cells*, vol. 109, pp. 77–81, Feb. 2013.

[256]  B. Michl *et al.*, "Imaging techniques for quantitative silicon material and solar cell analysis," *IEEE J. Photovoltaics*, vol. 4, no. 6, pp. 1502–1510, 2014.

[257]  H. Haug, R. Søndenå, A. Berg, and M. S. Wiig, "Lifetime spectroscopy with high spatial resolution based on temperature- and injection dependent photoluminescence imaging," *Sol. Energy Mater. Sol. Cells*, vol. 200, no. May, p. 109994, Sep. 2019.

[258]  F. D. Heinz, Y. Zhu, Z. Hameiri, M. Juhl, T. Trupke, and M. C. Schubert, "The principle of adaptive excitation for photoluminescence imaging of silicon: theory," *Phys. status solidi - Rapid Res. Lett.*, vol. 12, no. 7, p. 1800137, Jul. 2018.

[259] Y. Zhu, M. K. Juhl, T. Trupke, and Z. Hameiri, "Photoluminescence imaging of silicon wafers and solar cells with spatially inhomogeneous illumination," *IEEE J. Photovoltaics*, vol. 7, no. 4, pp. 1087–1091, 2017.

[260] Y. Zhu, M. K. Juhl, Z. Hameiri, and T. Trupke, "Applications of DMD-based inhomogeneous illumination photoluminescence imaging for silicon wafers and solar cells," in *IEEE 44th Photovoltaic Specialist Conference (PVSC)*, 2017, pp. 66–69.

[261] Y. Zhu, M. K. Juhl, F. D. Heinz, M. C. Schubert, T. Trupke, and Z. Hameiri, "Photoluminescence imaging at uniform excess carrier density using non uniform illumination," in *27th PVSEC, Shiga*, 2017.

[262] S. F. Ray, *Applied photographic optics : imaging systems for photography, film, and video*. Focal Press, 1998.

[263] D. N. R. Payne, M. K. Juhl, M. E. Pollard, A. Teal, D. M. Bagnall, and S. Wenham, "Evaluating the accuracy of point spread function deconvolutions applied to luminescence images," *43rd IEEE PVSC*, no. August, pp. 1585–1589, Jun. 2016.

[264] D. N. R. Payne *et al.*, "Acceleration and mitigation of carrier-induced degradation in p-type multi-crystalline silicon," *Phys. Status Solidi - Rapid Res. Lett.*, vol. 10, no. 3, pp. 237–241, 2016.

[265] "Meyer Burger." [Online]. Available: www.meyerburger.com.

[266] V. V Voronkov, R. Falster, K. Bothe, B. Lim, and J. Schmidt, "Lifetime-degrading boron-oxygen centres in p-type and n-type compensated silicon," *J. Appl. Phys.*, vol. 110, no. 6, p. 63515, 2011.

[267] B. Hallam *et al.*, "Recent insights into boron-oxygen related degradation: Evidence of a single defect," *Sol. Energy Mater. Sol. Cells*, vol. 173, pp. 25–32, Dec. 2017.

[268] J. Schmidt, K. Bothe, V. V. Voronkov, and R. Falster, "Fast and slow stages of lifetime degradation by boron-oxygen centres in crystalline silicon," *Phys. status solidi*, p. pssb.201900167, Aug. 2019.

[269] G. Coletti *et al.*, "Removing the effect of striations in n-type silicon solar cells," *Sol. Energy Mater. Sol. Cells*, vol. 130, pp. 647–651, Nov. 2014.

[270] D. Hinken, K. Ramspeck, K. Bothe, B. Fischer, and R. Brendel, "Series resistance imaging of solar cells by voltage dependent electroluminescence," *Appl. Phys. Lett.*, vol. 91, no. 18, p. 182104, Oct. 2007.

[271] K. Ramspeck, K. Bothe, D. Hinken, B. Fischer, J. Schmidt, and R. Brendel, "Recombination current and series resistance imaging of solar cells by combined luminescence and lock-in thermography," *Appl. Phys. Lett.*, vol. 90, no. 15, pp. 10–13, Apr. 2007.

[272] J. Haunschild, M. Glatthaar, M. Kasemann, S. Rein, and E. R. Weber, "Fast series resistance imaging for silicon solar cells using electroluminescence," *Phys. Status Solidi - Rapid Res. Lett.*, vol. 3, no. 7–8, pp. 227–229, 2009.

[273] T. Trupke, E. Pink, R. A. Bardos, and M. D. Abbott, "Spatially resolved series resistance of silicon solar cells obtained from luminescence imaging," *Appl. Phys. Lett.*, vol. 90, no. 9, p. 93506, 2007.

[274] H. Kampwerth, T. Trupke, J. W. Weber, and Y. Augarten, "Advanced luminescence based effective series resistance imaging of silicon solar cells," *Appl. Phys. Lett.*, vol. 93, no. 20, p. 202102, 2008.

[275] M. Kasemann, L. M. Reindl, B. Michl, W. Warta, A. Schütt, and J. Carstensen, "Contactless qualitative series resistance imaging on solar cells," *IEEE J. Photovoltaics*, vol. 2, no. 2, pp. 181–183, 2012.

[276] M. Juhl, T. Trupke, and Y. Augarten, "Emitter sheet resistance from photoluminescence images," in *39th IEEE Photovolt. Spec. Conf.*, 2013, pp. 198–202.

[277] B. Lee, "DMD 101: Introduction to digital micromirror device (DMD) technology," 2013.

[278] S. R. G. Hall, M. Cashmore, J. Blackburn, G. Koutsourakis, and R. Gottschalg, "Compressive current response mapping of photovoltaic devices using MEMS mirror arrays," *IEEE Trans. Instrum. Meas.*, vol. 65, no. 8, pp. 1945–1950, 2016.

[279] R. Gupta, O. Breitenstein, M. Planck, M. Physics, and D.- Halle, "Digital micromirror device application for inline characterization of solar cells by tomographic light beam-induced current imaging," *Proc. SPIE*, vol. 6616, pp. 66160-1-66160O–9, 2007.

[280] T. Dennis, J. B. Schlager, K. A. Bertness, S. Member, K. A. Bertness, and S. Member, "A novel solar simulator based on a supercontinuum laser for solar cell device and materials characterization," *IEEE J. Photovoltaics*, vol. 4, no. 4, pp. 1119–1127, 2014.

[281] O. V. Sorokin, "Measurement of surface recombination rates in thin semiconductor specimens with qualitatively different boundaries," *Sov. physics. Tech. phisics*, vol. 1, no. 11, pp. 2384–2389, 1956.

[282] D. Walter, A. Liu, E. Franklin, D. Macdonald, B. Mitchell, and T. Trupke, "Contrast enhancement of luminescence images via point-spread deconvolution," in *38th IEEE Photovoltaic Specialists Conference*, 2012, pp. 000307–000312.

[283] F. E. Rougieux *et al.*, "A contactless method for determining the carrier mobility sum in silicon wafers," *IEEE J. Photovoltaics*, vol. 2, no. 1, pp. 41–46, 2012.